UNIVERSITÉ DU LUXEMBOURG

PhD-FSTM-2024-023
Faculty of Life Sciences, Technology and Medicine

DISSERTATION

Presented on 8^{th} March 2024 in Esch-sur-Alzette
to obtain the degree of

DOCTEUR DE L'UNIVERSITÉ DU LUXEMBOURG EN SCIENCES DE L'INGENIEUR

by

Prasad ADHAV
Born on 31^{st} July 1993 in Pune, India

AN INNOVATIVE AND ACCURATE TECHNOLOGY FOR MULTI-PHYSICS DIGITAL TWINS IN HIGH-PERFORMANCE COMPUTING

Dissertation Defence Committee:

Prof. Dr-Ing. Bernhard PETERS (Dissertation Supervisor)
Professor, Université du Luxembourg

Prof. Dr. Andreas ZILIAN (Chair)
Professor, Université du Luxembourg

Dr. Xavier BESSERON (Vice Chair)
Université du Luxembourg

Prof. Dr. rer. nat. habil. Miriam SCHULTE
Professor, University of Stuttgart

Dr. Ralph USELDINGER
Ceratizit Luxembourg S. à r. l.

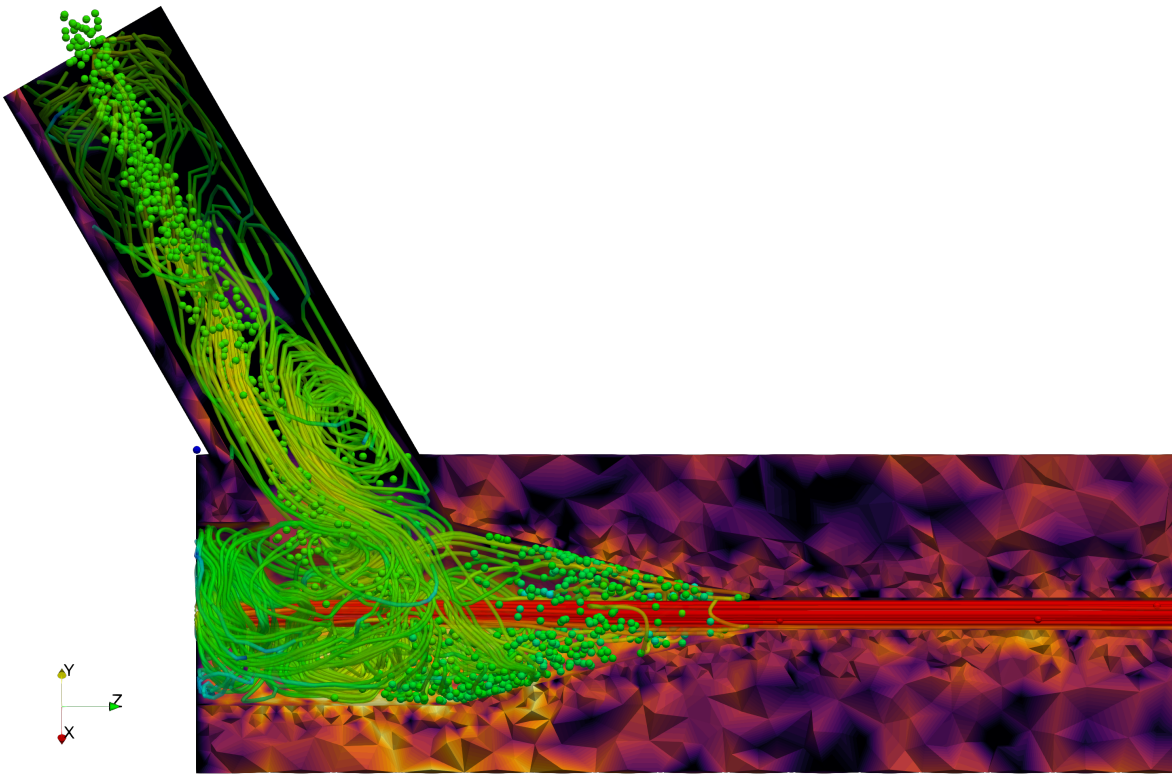

Doctoral Programme in Computational Sciences

Luxembourg XDEM Research Center

Affidavit

I hereby confirm that the PhD thesis entitled "An innovative and accurate technology for multi-physics digital twins in High-Performance Computing" has been written independently and without any other sources than cited.

Date/Location: _____ Name: _____

Acknowledgments

As I stand at this significant milestone of completing my PhD thesis, my heart is filled with gratitude for all those who have been part of this journey. The path to this accomplishment was paved with guidance, support, and inspiration from many, without whom this work would not have been possible.

First and foremost, I extend my deepest appreciation to my supervisor, Prof. Bernhard PETERS, whose unwavering support and expert guidance have been the cornerstone of my research. His invaluable advice, relentless encouragement, and inspiring mentorship have shaped my academic and personal growth in ways I could never have imagined.

I am also immensely thankful to my thesis committee members, Prof. Dr. Andreas ZILLIAN, Dr. Ralph USELDINGER, Prof. Dr. Mariam SCHULTE, and Dr. Xavier BESSERON, for their insightful feedback and constructive criticism. Their diverse perspectives and rigorous scrutiny have significantly enhanced the quality and depth of my research.

A special word of thanks to Xavier for his detailed reviews and stimulating discussions that pushed the boundaries of my research. His enthusiasm and academic rigor have been particularly motivating. I cannot emphasize enough how valuable your words of wisdom and encouragement were throughout this time. I thank you Odile, for all the administrative support, kind words, and the warmest smile, that made my Ph.D. journey smooth.

To my colleagues and friends at XDEM, especially Wahid, Brice, Muhammad, Fateme, Navid, Sina, Daniel, Vikram, Asif, and many others, your companionship and shared wisdom have been a constant source of strength. Our collaborative efforts and mutual support have made this challenging journey an enriching experience. I also owe a great deal of thanks to

my peers from the floor - Saurabh, Chintan, Jean, Raquel, Carolina, Pratik, Jinyuan (aka Henry) among others. Their daily interactions and words of encouragement have played a significant role in both my personal and professional development.

I extend my heartfelt gratitude to the preCICE team, especially Benjamin UEKERMANN, Gerasimos CHOURDAKIS (Makis), Benjamin RODENBOURG, Frederic SIMONIS, David SCHNEIDER, Kyle DAVIS, and Ishan DESAI, for their invaluable collaboration and contributions to my research. The conferences we attended together not only enriched our collaboration but also created a sense of family away from XDEM family, for which I am profoundly appreciative. Their expertise has been a cornerstone of my work. Equally, I am deeply thankful to the UL HPC team for their indispensable technical support and the comprehensive training they provided, which were crucial for my computational endeavors.

My journey would have been markedly different without the unwavering support and guidance of Tejas, who has been more than a friend to me; he has been a mentor, illuminating every path of my life with wisdom and encouragement. And to my girlfriend, Tanushree, whose love and support have been as deep and enduring as the ocean she explores. Your support has been as boundless as the ocean you love. Equally, the friendship and encouragement from my school and college friends - Mayuresh, Anurag, Sagar, Bhumik, Prasad (Mahajan), Akshay, Avnish, Kishan, Sushin, Nirali, Ekata, Shraddha, Siddhi, Yogesh, and Rutuja - have been indispensable. Despite the miles that separate us, their friendship has transcended boundaries, offering me a foundation of support and a reservoir of joy. Their unwavering presence, across different time zones and through every up and down, has been a source of comfort and motivation.

I would like to offer my deepest gratitude to my mentors and supporters in my career, Dr. B A PARATE (ARDE, Pune, IN), Dr. Chandra Shekhar PRASAD (Institute of Thermomechanics, Prague, CZ), Dr. Iona WARNEBOLDT and Dr. Pierre CHARRIER (Vibracoustic Nantes SAS, Nantes, FR).

Last, but certainly not least, my deepest gratitude to my family. Your unconditional love, sacrifice, and encouragement have been the bedrock of my perseverance and success. This achievement is as much yours as it is mine.

This thesis stands as a testament to the collective effort and spirit of all those mentioned and many unmentioned. I am deeply honored and grateful for your contributions to my journey.

Scientific Contributions

Publications

- **Adhav, Prasad**, Zetao Feng, Tao Ni, Bernhard Peters, and Xuanmei Fan. "Numerical insights into rock–ice avalanche geophysical flow mobility through CFD–DEM simulation." Computational Particle Mechanics (2024): 1-17. [1]

- Aminnia, Navid, **Adhav, Prasad**, Fateme Darlik, Muhammad Mashhood, Sina Hassanzadeh Saraei, Xavier Besseron, and Bernhard Peters. "Three-dimensional CFD-DEM simulation of raceway transport phenomena in a blast furnace." Fuel 334 (2023): 126574. [2]

- Besseron, Xavier, **Adhav, Prasad**, and Bernhard Peters. "Parallel Multi-Physics Coupled Simulation of a Midrex Blast Furnace." In Proceedings of the International Conference on High Performance Computing in Asia-Pacific Region Workshops, pp. 87-98. 2024. [3]

- Darlik, Fateme, **Adhav, Prasad**, and Bernhard Peters. "Prediction of the biomass particles through the physics informed neural network." In ECCOMAS Congress 2022-8th European Congress on Computational Methods in Applied Sciences and Engineering. 2022. [4]

Preprints

- **Adhav, Prasad**, Xavier Besseron, Alvaro A. ESTUPINAN, and Bernhard Peters. "Development and Validation of CFD-DEM Coupling Interface for Heat & Mass Transfer

Using Partitioned Coupling Approach." Available at SSRN 4668107. Accepted with revisions in International Communications in Heat and Mass Transfer. [5]

- **Adhav, Prasad**, Xavier Besseron, and Bernhard Peters. "Development of 6-way CFD-DEM-FEM momentum coupling interface using partitioned coupling approach.". Accepted after revisions in Results in Engineering. [6].

- **Adhav, Prasad**, Xavier Besseron, and Bernhard Peters. "Insights into erosion behavior of AWJC Nozzle using 6-way CFD-DEM-FEM momentum coupling". Under review in Powder Technology. [7]

In preparation/Submitted

- **Adhav, Prasad**, Xavier Besseron, and Bernhard Peters. "Performance and parameter study of partitioned coupling approach"

Conferences

- **Adhav, Prasad**, Xavier Besseron, Alban Rousset, and Bernhard Peters. "Evaluation of erosion inside AWJC Nozzle by 6-way coupling of DEM+ CFD+ FEM using preCICE." preCICE Workshop 2021, Germany (2021). [8]

- **Adhav, Prasad**, Xavier Besseron, Alban ROUSSET, and Bernhard Peters. "AWJC nozzle simulation by 6-way coupling of DEM+ CFD+ FEM using preCICE coupling library." 9th edition of the International Conference on Computational Methods for Coupled Problems in Science and Engineering (COUPLED PROBLEMS 2021) (2021). [9]

- **Adhav, Prasad**, Xavier Besseron, Alvaro Antonio Estupinan Donoso, Bernhard Peters, and Alban Rousset. "HEAT AND MASS TRANSFER BETWEEN XDEM & OPENFOAM USING PRECICE COUPLING LIBRARY." 8th European Congress on Computational Methods in Applied Sciences and Engineering (2022). [10]

- **Adhav, Prasad**. "Investigation of OpenFOAM-XDEM momentum coupling results for AWJC Nozzle using preCICE." preCICE Workshop 2023, Germany (2023). [11]

- Besseron, Xavier, **Adhav, Prasad**, Daniel Louis Louw, and Bernhard Peters. "Toward High-Performance Multi-Physics Coupled Simulations for the Industry with XDEM." In 1st conference Math 2 Product (M2P) on Emerging Technologies in Computational Science for Industry, Sustainability and Innovation. (2023). [12]

- **Adhav, Prasad**; Besseron, Xavier; Peters, Bernhard. "6-way CFD-DEM-FEM momentum & HMT coupling using preCICE". Computational Fluid Dynamics und Wärme- und Stoffübertragung (2023).

- **Adhav, Prasad**; Besseron, Xavier; Peters, Bernhard. "Investigation of CFD-DEM momentum coupling results for AWJC Nozzle using preCICE". COUPLED PROBLEMS 2023, International Conference of Computational Methods for Coupled Problems in Science and Engineering (2023).

- **Adhav, Prasad**; Besseron, Xavier; Peters, Bernhard. "6-way CFD-DEM-FEM partitioned momentum coupling using preCICE". International Conference on Data-Integrated Simulation Science (SimTech2023) (2023).

- **Adhav, Prasad**; Besseron, Xavier; Peters, Bernhard. "6-way CFD-DEM-FEM partitioned momentum coupling using preCICE". PARTICLES 2023 Conference VIII International Conference on Particle-Based Methods (2023).

- **Adhav, Prasad**; Besseron, Xavier; Peters, Bernhard. "Investigation of CFD-DEM-FEM momentum coupling results for AWJC Nozzle using preCICE". NAFEMS Multiphysics Conference 2023 (2023).

Software

- XDEM preCICE Adapter `https://gitlab.uni.lu/LuXDEM/precice-coupling/xdem-adapter`

- Modified OpenFOAM preCICE Adapter `https://gitlab.uni.lu/LuXDEM/precice-coupling/openfoam-adapter`

- OpenFOAM Solvers with preCICE fields and custom `fvOptions` `https://gitlab.uni.lu/LuXDEM/precice-coupling/of-solvers`
- Test cases and data for preCICE coupling `https://gitlab.uni.lu/LuXDEM/precice-coupling/test_cases-4-precice_coupling`
- XDEM preCICE Coupling Superbuild all assets `https://gitlab.uni.lu/LuXDEM/precice-coupling/xdem_precice_superbuild`
- Volume coupling interface PR #182 into opensource directory `https://github.com/precice/openfoam-adapter/pull/182`
- Volume coupling module PR #183 into opensource directory `https://github.com/precice/openfoam-adapter/pull/183`
- Volume coupling PR #255 into opensource directory `https://github.com/precice/openfoam-adapter/pull/255`
- Contributed to XDEM wiki page and tutorials `https://gitlab.uni.lu/LuXDEM/xdem-source/-/wikis/home`

Outreach/Seminars

- **Adhav, Prasad**. "PhD Day-Complex Particle Laden Fluid Structure Interaction.", University of Luxembourg Ph.D. day (2022). [13]
- Drouet, Luce, **Adhav, Prasad**, and Solanke, Abiodun. "Chronicles from Platform 6". In Lux:plorations A Universe of research, University of Luxembourg, November 2020. Volume 1, First Edition. `https://sciencecomics.uni.lu/comics-vol-1/`

Table of Contents

List of Figures

List of Tables

Abstract

Most of the physical phenomena encountered in engineering applications require multiple disciplines and their interaction to be completely described. Furthermore studying these complex multi-physics phenomena experimentally can be difficult or impossible. This can be due to the complex multi-physical interactions themselves, operating environments that might be hostile to sensors, or the immense scale and costs of performing such experiments. These limitations to study complex multi-physics phenomena through experiments can be overcome by utilizing numerical models.

This thesis establishes a highly flexible, multi-component multi-physics simulation environment through a partitioned coupling approach. The proposed coupling approach uses the preCICE coupling library to couple three numerical solvers: XDEM (solves for particle motion and thermodynamics), OpenFOAM (solves the fluid dynamics and thermodynamics), and CalculiX (solves for the solid deformations). A 6−way CFD-DEM-FEM momentum coupling and a 2−way CFD-DEM heat & mass transfer is established. The proposed coupling approach is verified and validated through various numerical experiments and experimental observations.

The highly flexible partitioned coupling is then used to study several large-scale complex multi-physics phenomena such as: the erosion inside abrasive water jet cutting nozzle; the drying of packed wood particle bed; frictional behavior of gravel in the presence of melting ice; the raceway region of a blast furnace; iron reduction in midrex furnace. The thesis delves deep into the analysis of results thus giving unprecedented comprehension of such complex multi-physics phenomena.

Chapter 1

Introduction

1.1 Background

In the intricate tapestry of modern engineering, the convergence of diverse disciplines has become imperative to address the challenges posed by complex real-world phenomena. From the precision of abrasive water jet cutting to the chaotic dance of rock-ice avalanches, and from the intense metal melting thermodynamics within blast furnaces to the sustainable manufacturing potentials of midrex furnaces, each chapter in this research narrative seeks to decipher the complexities at the crossroads of multiple physics, illuminating new pathways for innovation and problem-solving.

Complex multi-physics phenomena are often very difficult to study in their entirety through experimentation. Often the environment is too hostile for the sensitive instruments used to monitor the phenomena as it evolves. The applications considered in this thesis have such hostile environments that experimental study might only yield results after the process is over. Whereas the temporal evolution of the complex phenomena eludes even experimental researchers. For example, inside the abrasive water jet cutting, the abrasive particle-laden high-pressure water-jet moves at very high speeds. It even erodes the toughest metal known to mankind. On the other hand, the furnaces used in iron-making operate at hundreds of degrees Celsius. Finally, there are some large-scale phenomena such as geophysical flows seen in rock-ice avalanches, that can happen without notice in the vast mountain ranges, moving at hundreds of kilometers per hour, and with immense momentum due to sheer mass. These all show the severe limitations posed when trying to study these complex multi-physics phenomena experimentally, while not even considering the monetary and time costs involved.

Hence, it is imperative to study these complex multi-physics phenomena through numerical simulations. Various numerical methods are used to solve governing equations that model certain real-life physical phenomena. Over the years and decades, they have become specialized for solving one type of physics. Some of these are Computational Fluid Dynamics (CFD) famously used for solving fluid dynamics using Finite Volume Method (FVM) [14, 15], Finite Elements Method (FEM) is preliminarily used for solving for solid mechanics [16, 17, 18, 19], solving over a continuum. There also exist methods to solve for discrete phases

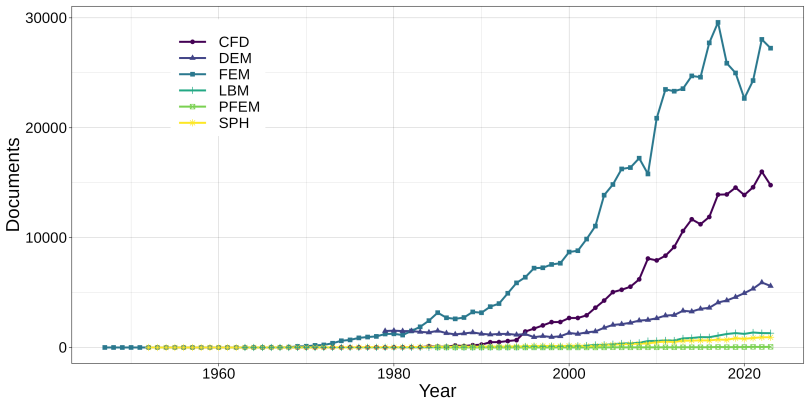

Figure 1.1: Number of citations for various single physics numerical methods over the years obtained from `https://www.scopus.com/`

such as particulate flows using the Discrete Element Method (DEM) [20], Discrete Particle Method (DPM) [21]. Additionally, there have been some methods developed such as Smoothed Particle Hydrodynamics (SPH), Lattice Boltzmann Method (LBM) [22], and Particle Finite Element Methods (PFEM) [23, 24] that are also used to solve for fluid dynamics and solid mechanics.

I used the Scopus database to understand the publication trends over the years. The database of titles, abstracts, and keywords was searched with the complete or abbreviated name of the numerical method. Then the filter was applied to limit to research articles, published in journals related to various fields in engineering only. Figure 1.1 shows the number of citations for individual numerical methods only. These methods have been quite successful in solving a lot of engineering problems, as it it evident in the number of publications over the years in figure 1.1. Some single physics numerical methods such as CFD, FEM, and DEM have been quite successful, as can be inferred from the thousands of publications each year.

Although these numerical methods have been applied only for "single" physics. There are two meanings intended here when using "single" physics, either the application purely involves only one physics in the simulation domain, for example flow of water through pipes, or when only one part of the physics is considered for simulation and other physics are ignored, for example the fluid forces acting on the pipe due to the flow of water are ignored, and only flow characteristics of the water are considered. Hence, we turn our attention to "multi" physics

applications. The multi-physics simulations are usually done by coupling single physics. There are various ways to achieve this that will be discussed later. In the figure 1.2, and 1.3, the number of publications for multi-physics studies involving coupling with fluid solvers, and particle solvers respectively. It can be seen that there are significantly less number of publications when considering multi-physics works as compared to single-physics.

There are a few reasons for this trend, the first and most important is the sheer complexity when establishing a multi-physics simulation environment. Due to this complexity engineers and researchers have tried to simplify multi-physics problems to single-physics problems and approached a partial solution. On the other hand, there have also been attempts to use simpler numerical methods. In figure 1.2, this is evident that CFD-FEM coupling has been tried to be substituted with SPH-FEM, and PFEM-FEM couplings, thus stagnating the CFD-FEM growth.

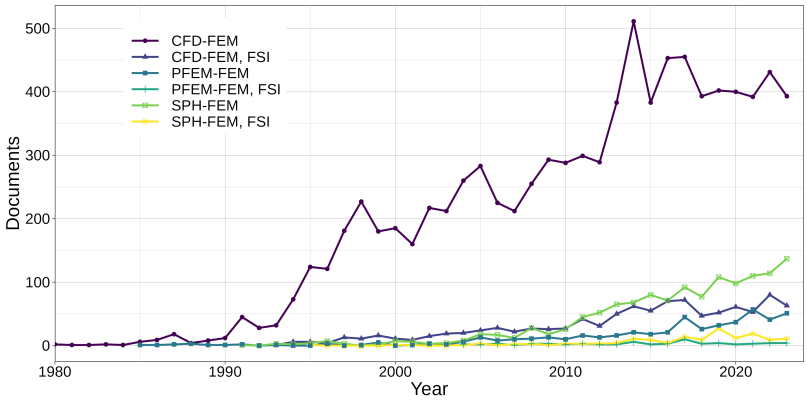

Figure 1.2: Number of citations for various numerical methods coupled with fluid solver over the years obtained from `https://www.scopus.com/`

The second most important challenge faced when trying to establish a multi-physics simulation environment is the computational cost. In figure 1.3, it can be seen that the CFD-DEM coupling publications have been increasing almost exponentially from the 2000s. This is no coincidence. Discrete methods are considered to be quite computationally costly as they track every individual particle in the simulation domain. These methods have been quite limited due to the hardware. If the figure 1.3 was to be superimposed with the transistor counts [25], the CFD-DEM trend will tend to match qualitatively with the transistor counts. Although

increased computational power has increased the capabilities of approaching multi-physics problems involving discrete media, several other factors play a role as well. Consequently, throwing supercomputers alone at a problem does not necessarily mean solving large-scale problems.

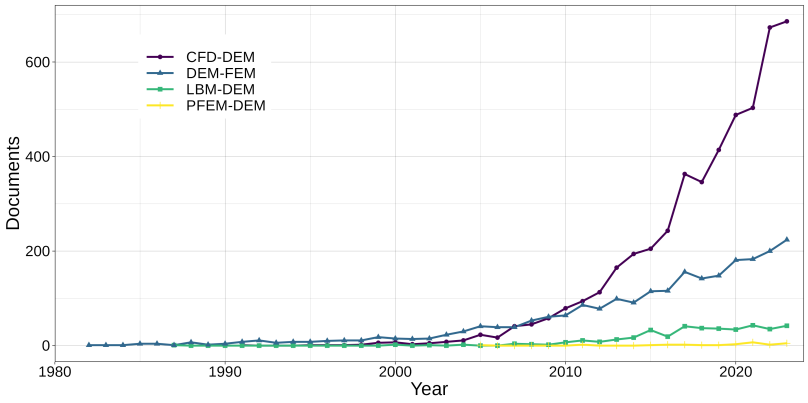

Figure 1.3: Number of citations for various numerical methods coupled with particle solver over the years obtained from `https://www.scopus.com/`

With the help of the previous three paragraphs, I wanted to showcase the two major challenges faced when establishing a multi-physics simulation environment i.e. complexity in coupling and parallelization. This thesis attempts to solve these same issues. Although the preliminary goal of the thesis will be to establish a multi-physics simulation environment, the question of solving large-scale applications by using High Performance Computing (HPC) and challenges in parallelization is also addressed.

1.2 The erosion problem of Abrasive Water Jet Cutting Nozzles

In the 1930s, the first use of narrow water jets appeared in industrial cutting, used for cutting sheets of paper, developed by Charles Fourness [26]. Although these jets of high-pressure water could only be used for cutting soft materials, soon Elmo Smith [27] added abrasive particles to cut several other soft materials. The abrasive water jet cutting operation was very slow to develop between its inception and the 1970s. Mohamed Hashish published a

series of studies experimenting with various aspects of the AWJ, and demonstrating that such abrasive-laden water jets could cut hard materials [28, 29, 30, 31, 32]. Over the years, research and development have enabled AWJC operation to not only make very small cuts but cut a 3D object using a 5-axis CNC machine, some examples are presented in figure 1.4. Additionally, the AWJC operation does not have any significant heat-affected zones, thus it does not alter the material properties and microstructure [33]. There are more advantages AWJC operation has over traditional cutting operations. The final advantage AWJC has over its counterparts is that it is environmentally friendly, and can be used in reducing emissions [34, 35].

Figure 1.4: Examples of different cutting operations achieved on different materials by Abrasive Water Jet Cutting operation [36]

Despite its numerous advantages and applications, years of research, and experimentation, one issue that came up persistently was the erosion of the AWJC nozzle itself. The majority of modern experimental, and numerical studies on the AWJ operation focus mainly on the

AWJC cut quality, cut depth etc [37, 38]. Hashish and some others have addressed this issue experimentally [39, 40, 41] Depending on the operating conditions the erosion inside the AWJC Nozzle can have various shapes. As seen in figure 1.5, the most commonly occurring erosion patterns are either of uniform type, forming a convergent or a divergent channel. On the contrary, the uneven wear seen in figure 1.5(a) forms a wavy erosion pattern along the length of the AWJC nozzle. The eroded focusing tubes are sliced in half to observe various erosion patterns seen in figure 1.6. As the internal geometry of the AWJC nozzle changes over time due to the erosion, the cut performance is lost.

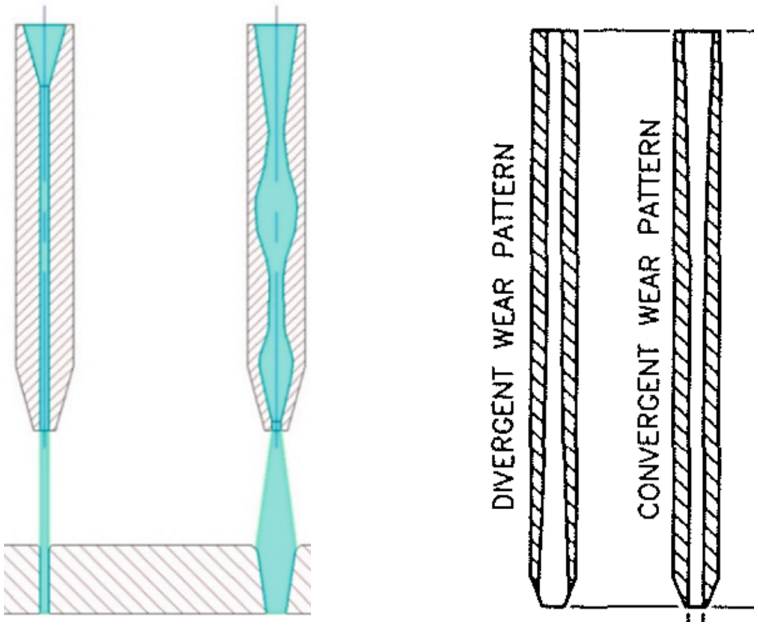

(a) New AWJC nozzle and uneven wear [42] (b) Even wear [32]

Figure 1.5: Illustration of possible types of erosion patterns inside the AWJC Nozzle/focusing tube

Very sparse literature can be found on the numerical modeling of the AWJC Nozzle itself, furthermore, the literature on the numerical predictions of the AWJC nozzle is even more rare. A relevant work done to study the temporal evolution of erosion pattern inside the AWJC nozzle was done by Pozzetti [45]. Although, the numerical results are qualitative when compared to experimental observations of the temporal evolution of erosion by Perec [42], the qualitative numerical predictions match the experimental observations. Although there

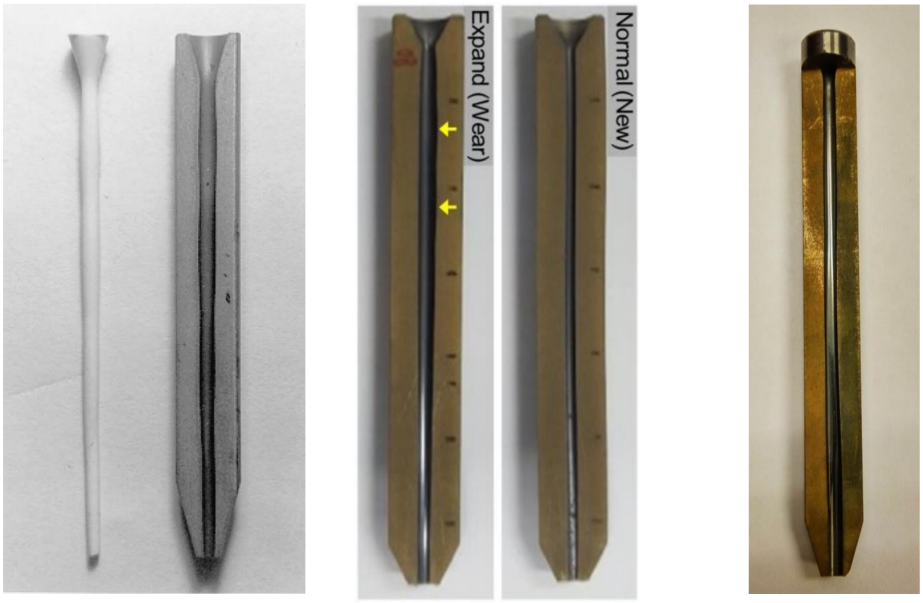

(a) Uneven wear [40] (b) Convergent wear [43] (c) Divergent wear [44]

Figure 1.6: Sliced AWJC focusing tube displaying various erosion patterns from literature

might be a way to predict erosion patterns through numerical studies, this still does help monitor the temporal evolution of wear when the AWJC is being used. To bridge this gap, several attempts have been made in the literature to use the AWJC nozzle vibrations and acoustics as a means of monitoring the wear progression [46, 47, 48, 49, 43].

Copertaro [49] has proposed a monitoring method with the use of accelerometers and microphones. Through experimentation, he demonstrates that it is indeed possible to monitor the wear progression by monitoring the first 2 or 3 eigenmodes. As the AWJC nozzle erodes from the inside, an up-shift in the eigenmode values is seen. The monitoring devices proposed are cheap and can be retrofitted to existing apparatuses. Although this technique might be a game changer in wear monitoring and can reduce operational costs significantly, there still lacks one crucial piece of information. What might be the values of these first 2 or 3 eigenmodes before and after erosion? Additionally, it is unknown how different operating conditions might affect these values.

To the best of my knowledge, there is no numerical research performed in the literature to study the mechanical response of an AWJC nozzle coupled with particles and/or fluid

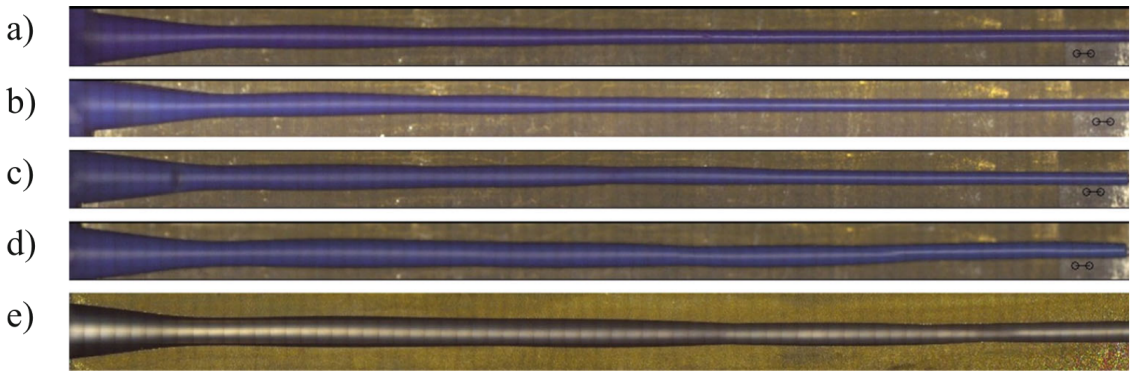

Figure 1.7: Evolution of the uneven wear inside the AWJC focusing tube over time [42] (a) after 5mins, (b) after 10mins, (c) after 15mins, (d) after 25mins, (e) after 35mins

phases. Hence, the article proposed in chapter 4 presents a 6−way CFD-DEM-FEM coupled model of AWJC nozzle. This chapter explores the erosion patterns and mechanical response of the AWJC nozzle for different operating conditions. These chapters establish and lay the foundation to obtain the mechanical response of a worn nozzle that is also coupled. This way multi-physics numerical simulations can be used to know the change in natural frequencies of the AWJC nozzle *a priori* and for different operating conditions.

1.3 Thesis Structure

This thesis is organized as a cumulative collection of articles [1, 2, 3, 5, 6, 7] submitted to international peer-reviewed journals that explore the various aspects of monolithic and partitioned coupling approach. Each of the chapters is structured as the articles are, i.e. they contain a self-containing introduction to the topic, the methodology used explaining the numerical models used thoroughly. Furthermore, as coupling is a central theme to the thesis and the articles, the coupling between different solvers is explained, followed by numerical results, discussion, and conclusion.

The thesis is roughly divided into two parts, part one explains the establishment of the multi-physics simulation environment using the partitioned coupling approach. The second part showcases the applications for the partitioned coupling approach as well as well as some applications using the monolithic coupling approach.

As discussed in the first section of the introduction, it is quite complex and difficult to couple different physics to establish a multi-physics simulation environment. A significant amount of work has been done to establish monolithic coupling between different physics, but such monolithic approaches are application-specific and quite inflexible. To incorporate the flexibility, and utilize powerful pre-existing single-physics solvers, the preCICE coupling library [50, 51] is chosen to couple different single-physics solvers.

In chapter 2, a 6−way momentum coupling between three numerical solvers, namely OpenFOAM (for the fluid phase), XDEM (for the particulate phase), and CalculiX (for the solid) is established. A preCICE adapter for XDEM is developed, while the OpenFOAM adapter [52] is modified to enable volume coupling. The CalculiX adapter is used out-of-box. The momentum coupling is explored through various numerical experiments. In the current configuration of the established coupling, the CFD or the FEM solvers/software can be swapped for other solvers/software. It is also possible for external members to couple their own DEM solver with the CFD and FEM to establish the momentum coupling.

The chapter 3, the preCICE adapter for XDEM and OpenFOAM proposed in chapter 2 are extended to incorporate heat and mass transfer. The heat and mass transfer are validated and verified against legacy monolithic coupling and experimental observations. A preliminary comparison of the performance analysis is performed for the proposed coupling with the legacy coupling. It was not possible to do a direct performance comparison for the proposed momentum coupling and legacy coupling in chapter 2, as the 6−way CFD-DEM-FEM coupling does not exist in the XDEM software suite.

In chapter 4, the 6−way CFD-DEM-FEM momentum coupling developed in chapter 2 is used to establish a fully coupled AWJC nozzle model. This chapter delves into the effects of particle-laden flow and its effects on the fluid flow, erosion pattern, and mechanical response of the AWJC nozzle for different operating conditions.

In chapter 5, the CFD-DEM momentum coupling is applied to study the dynamic changes in the frictional behavior of gravel in the presence of melting ice. This study replicates an experiment performed to better understand the rock-ice avalanche phenomena. In this chapter, the ice melting is modeled by injecting an equivalent amount of water to simplify the model.

This work only considered one combination of rock-ice ratio. This can be further expanded to estimate frictional behavior for different rock-ice mixtures. The legacy CFD-DEM coupling is used in this article as the proposed coupling from chapter 2 was not yet published. Nonetheless, the proposed coupled approach can be used to study this very disastrous phenomenon of rock-ice avalanche and is expected to yield the same results.

In chapter 6, the three-dimensional raceway of a blast furnace is modeled. This chapter uses CFD-DEM momentum, heat, and mass transfer between the fluid and particulate phases. Additionally, there are solid-solid, solid-fluid, fluid-fluid chemical reactions taking place. This chapter perfectly demonstrates how quickly multi-physics simulations can become complex. Even though this is the case, this chapter also shows performing such numerical experiments gives unprecedented insights into the complex multi-physics phenomena.

In chapter 7, the challenges faced in parallelization of the multi-physics simulations are explored for large-scale application of the eco-friendly midrex furnace. In the legacy coupling, there has been an issue of scaling up applications due to various issues, one noteworthy mention is the partitioning used. The partitioning of the simulation domain can be quite complex, the simulation domains involved in the multi-physics simulations are non-conforming. When partitioned incorrectly, the instabilities at the partition boundaries can lead to complications. Hence, a compromise has to be made to keep the simulation stable while sacrificing some performance. The partitioned coupling approach proposed in chapter 3 allows for the coupling of non-conforming simulation domains while utilizing the best partitioning for each coupled solver. Thus giving a stable numerical solution in the least possible time.

Finally, the chapter 8 draws inferences from the various works presented in the thesis, and provides insights and recommendations for future work. The thesis then comes to a close with a conclusion.

Part I

Methodology

Chapter 2

Development of 6-way CFD-DEM-FEM momentum coupling interface using partitioned coupling approach[1]

[1]The content of this chapter is under review in Results in Engineering[6]

2.1 Abstract

Fluid-particle-structure interactions (FPSI) govern a wide range of natural and engineering phenomena, from landslides to erosion in abrasive water jet cutting nozzles. Despite the importance of studying FPSI, existing numerical frameworks often simplify or neglect certain physics, limiting their applicability. This work introduces a novel 6-way CFD-DEM-FEM momentum coupling for FPSI using a partitioned coupling approach, providing a flexible and adaptable solution.

Our prototype uses the preCICE coupling library to couple three numerical solvers: OpenFOAM for fluid dynamics, eXtended Discrete Element Method (XDEM) for particle motion, and CalculiX for structural mechanics. The coupling approach extends existing adapters and introduces a novel XDEM preCICE adapter, allowing data exchange over surface and volumetric meshes.

Numerical experiments demonstrate the successful validation of the 6-way coupling, showcasing fluid-structure interactions and particle dynamics. The versatility of the partitioned coupling approach is highlighted, allowing the interchangeability of different single-physics solvers and facilitating the study of complex FPSI phenomena.

This article offers a thorough description of the methodology, coupling strategies, and detailed results, offering insights into the advantages and disadvantages of the proposed approach. This work lays the groundwork for a scalable and customizable FPSI simulation framework with a wide range of applications. [2]

2.2 Introduction

Landslides, rock-ice avalanches, erosion and fracturing of oil pipes located underground or underwater, and leakage in sewer pipes all have a few things in common, the foremost important of them is disaster and damage caused leading to economic damages or even worse loss of human life. The other common factor among the listed is they are caused by the fluid-particle-structure interactions (FPSI). Apart from the phenomena described above, there are

[2] The content of this chapter is under review in Results in Engineering

many more engineering fields requiring the study of FPSI.

The applications requiring these numerical methods can lead to great benefits, but very limited work has been done in the actual development of a coupled framework for FPSI. This is not due to the lack of motivation or resources but rather the sheer complexity involved in modeling. Many researchers have to weigh the cost of modeling such multi-scale, multi-physics phenomena partially or completely against the possible outcomes and the intended usage. Furthermore, the underlying multi-physical phenomena are complex and interact in a complex manner. Usually for the FPSI applications in consideration, the fluid and/or particle phase are the source of the momentum. These particle-laden flows then interact with a structure, that undergoes deformation due to exerted forces. This altered geometry of the structure in turn influences the flow characteristics. In some cases, such as the milling operation, the structure itself might be the source of momentum in the system.

A lot of work has been done over the years for modeling the fluid-structure interactions (FSI) using CFD-FEM [53], furthermore using immersed boundary [54], and meshfree methods [23, 55, 56]. There is an extensive choice when it comes to FSI modeling, applied to applications such as aeroelasticity [57], biomedical applications involving blood flow [58], wind turbines [59], tidal turbines [60], bridge flutter [61], liquid filled pipes [62, 63], etc.

Additionally, one can also find an abundance of particle-fluid interactions (PFI) [64, 65]. Some of the applications include pneumatic conveyor [66], blast furnace simulations [2], granular flow [67], fluidised beds [68], rock ice avalanche [69], sand ejecting fire extinguisher [70], debris flow [71], pipe flow [72] etc.

In terms of particle-structure interaction (PSI), the popular applications are erosion [73], snow-tire interactions [74], abrasive water jet cutting [75], frictional behavior [76] etc.

Although the examples provided above for FSI, PFI, and PSI are not exhaustive, they show the extensive study and research done over the last years/decades, and the potential applications of such couplings. Some of the applications mentioned above are actually involve FPSI, but one or more of the physics is not modeled for various reasons, thus leaving ample space for improvement. The examples provided above shows that indeed a good foundation for FPSI exists, but very little work is done in this field.

Some noteworthy studies done in FPSI on the impact of debris flow on barriers/structures [77, 78, 79], usually applied for studying landslide/avalanches and their effects on man-made structures. These are very important phenomena to understand and study to implement better preventive structures against such disastrous forces. These works use Discrete Element Method (DEM) for the particle phase, Finite Element Method (FEM) for the structure, although they use different approaches for modeling the fluid. Smooth Particle Hydrodynamics (SPH) is used by [79] and [77]. On the contrary, [78] uses the Lattice Boltzmann Method (LBM) for modeling the fluid phase.

The FPSI is also used to study the pipe fracturing [80], where CFD-DEM-FEM is used. In the literature, it is shown that it is important to study vibrations in pipes to better understand and prevent pipe wear, erosion, and fraction in [81, 82]. Although this research gap exists, numerical FPSI framework has yet to be applied to such applications.

Additionally, FPSI is applied in modeling mills. SPH-DEM-FEM modeling is used by [83], whereas [84] uses coupling between particle finite element method (PFEM), DEM, and FEM. Apart from modeling the mill behavior, abrasive wear on the mill is also studied in [84].

Although sparse, the literature shows attempts at FPSI modeling. The literature presented above shows, that the fluid phase is mostly modeled using SPH, PFEM, or LBM. Although these might present advantages in terms of computational costs and free surface flows, they have limitations in terms of capturing certain physics, such as incompressibility or constant pressure boundaries. In the context of FPSI coupling using CFD, only two relevant studies, [80] and [85], are found in the literature. Furthermore, the coupled environment might have all the components of FPSI, but the coupling between these components might not be established. For example, [82] ignores the impacts of the particles on the structure, [80] uses 2-way coupling method between fluid-particle interaction, but used only 1-way coupling algorithm when considering interactions between structure and fluid-particles flow.

The different fields of engineering constantly face problems involving multi-scale, multi-physics and their complex interactions. Moreover, it is known from abundant literature that developing and working with coupled problems is challenging. This prohibits engineers, researchers, and scientists from completely realizing some problems and modeling certain

multi-physics. In the FPSI literature presented above, generally, a monolithic coupling approach is utilized, with one exception [85]. In the FPSI by [85], the FSI part is implemented as a monolithic solver, whereas the interaction with particles is coupled using the partitioned approach. In a monolithic coupling approach, the different sets of segregated equations representing the different physics are solved iteratively. Such couplings are developed as a single code solver. For certain applications, the monolithic coupling approach may prove to be more robust. However, due to the nature of monolithic coupling, they are restricted to certain applications and offer little to no flexibility when modifying, extending, or adapting to new applications. Furthermore, increased fidelity in such multi-physics models implies increased requirement of computational resources, thus scaling for large, industrial, and high-fidelity applications can be a challenge [86, 87, 88, 89, 90].

In contrast to monolithic coupling, the partitioned approach couples high-level single-physics software currently available [88]. Utilizing this coupling approach allows to modify, exchange, add, or remove physics components from the multi-physics simulation environment. Thus allowing us to address the growing complexity problem. The partitioned coupling approach also allows us to leverage the parallelization capabilities of the individual software involved efficiently and better load balancing required from different applications [90]. There are several open source coupling libraries/software to achieve such partitioned coupling approach, such as OpenPALM [91], Data Transfer Kit [92], Amuse [93], MuMMI [94], MUSCLE [95], MUI [96], preCICE [50] to name a few. From a review [97] on multi-scale coupling software, one can follow the logic to choose the correct coupling software. Hence, considering the possible applications, the availability of pre-existing single-physics software along with their ready-to-use adapters as the preCICE coupling library [50] is chosen to be used to establish the partitioned 6-way coupling between fluids, particles, and structures.

The preCICE coupling library allows us to circumvent the problems faced in monolithic coupling by treating the single-physics software/solvers as a black box. It enables communication, data mappings, time interpolations, and different coupling strategies thus providing much-needed flexibility when establishing a multi-scale, multi-physics simulation framework for FPSI. This further removes the need to have access or understanding to the solver source

code, only the understanding of the usage and underlying physics is required. Additionally, due to the application programming interface (API) support for different languages such as C, C++, Python, MatLAB, Fortran, Julia, etc., solvers/software in different languages can be coupled.

The preCICE coupling library was developed originally to enable FSI [88], where the coupling is done over surface meshes. The preCICE coupling library and its adapters [52, 98] have also been used to model Conjugate Heat transfer [99] between fluid and solids over surface meshes. Fracturing in poro-elastic medium due to fluid flow is simulated over volumetric meshes, but the coupled system uses surface terms for equilibrium. Although there are more multi-scale, multi-physics applications achieved using the preCICE coupling library, they are not relevant in the context of FPSI.

In the present work, a highly flexible, modifiable, and scalable partitioned coupling approach for fluid-particle-structure interaction (FPSI) through 6-way CFD-DEM-FEM momentum coupling is proposed. To the best knowledge of the authors, such a fully partitioned coupling approach has not yet been presented in the literature. As by the nature of the partitioned coupling approach, three different numerical solver/software are used, namely OpenFOAM [100] to simulate the fluids using CFD, eXtended Discrete Element Method (XDEM) [64] suite to solve for particle motion, and CalculiX [101, 102] software is used to solve for structure deformations, stresses and vibrations. The fluid-structure and particle-structure interactions are achieved over surface meshes, whereas the fluid-particle Eulerian-Lagrangian interactions are achieved over volumetric meshes. The CFD is in the Eulerian framework, on the contrary, the DEM and FEM are in the Lagrangian framework. It should be noted that since the coupling is achieved over black box solvers/software, the single-physics software can be swapped, added, or removed altogether, as seen in figure 2.1.

To achieve the 6-way CFD-DEM-FEM partitioned momentum coupling, the pre-existing FSI coupling achieved over surface meshes is used, namely the OpenFOAM preCICE adapter [52], and CalculiX preCICE adapter [99, 98]. Our contributions, which are novel or related to the 6-way partitioned momentum coupling for FPSI are, (1) developing an original XDEM preCICE adapter (the first DEM adapter developed) to enable data exchange over surface and

volumetric meshes; (2) extending the OpenFOAM preCICE adapter to enable coupling over volumetric meshes; (3) presenting test cases to demonstrate 6-way momentum coupling, with using 2-way coupling as examples.

The article is arranged as follows: in section 2.3, the governing equations for each of the single-physics solvers involved are provided. Additionally, the mathematical model for accounting for coupled effects is also described. In section 2.4, the coupling strategies are explained more in detail along with a detailed description of the XDEM preCICE adapter. In section 2.5, the results demonstrating the coupled FPSI behavior are presented. Additionally, FPSI numerical experiments are compared to the FPSI experimental observations. In section 2.6, the results, their impacts, and insights are discussed along with the strengths and weaknesses of the proposed coupling approach. Future work and possibilities for applying the 6-way coupling are also explored. Finally, in the section 2.7, the concluding remarks are presented.

2.3 Model Description

In the partitioned coupling approach, three different software are used to establish a multi-physics environment to couple momentum between fluids, particles, and structures. These physics are simulated using CFD, DEM, and FEM respectively. The governing equations of the respective numerical methods are described below.

2.3.1 Governing equations for discrete particles

XDEM software suite [64] is used in the current work to model the discrete particle phase. XDEM models both dynamics as well as thermodynamics of the particulate system. In the current work, the main focus will be the dynamic behavior of particles interacting with fluids and structures. The particle position, velocity, and acceleration are computed with the dynamics module of the XDEM.

The discrete element method (DEM) used in the dynamics module of XDEM is based on the soft sphere model. In this method, it is assumed that the particles are deformable

and can overlap each other, where the magnitude of overlap is decided by the contact force using the force-displacement law. The hardness of the particle is expressed via Young's Modulus, while the particle energy dissipation is described with a dampener and/or dashpot. The translational and rotational movements of individual particles are tracked using classical mechanics equations. A detailed description of all the terms mentioned below can be found in previous work [103]. A summary of the translational and rotational motion equations is given below: Equations of particle motion:

$$m_i \frac{d\vec{v_i}}{dt} = m_i \frac{d^2\vec{X}_i}{dt^2} = \vec{F_i^c} + \vec{F_i^g} + \vec{F_i^{ext}} \tag{2.1}$$

where $\vec{X}_i$ is the position vector for a given particle, $\vec{\phi_i}$ is the orientation, and $\vec{u}_{p_i}$ is particle velocity. $\vec{F_i^g}$ is the force due to gravity. $\vec{F_i^{ext}}$ is the sum of all the external forces acting on the particle, such as (hydro-static) buoyancy forces $\vec{F_B}$ and (hydrodynamic) drag forces $\vec{F_D}$.

$$I_i \frac{d\vec{\omega_i}}{dt} = \vec{M}_c + \vec{M}_{ext} + \vec{M}_{roll} \tag{2.2}$$

where I_i is the moment of inertia, $\vec{M}_c$ stands for the torque acting due to inter-particle collisions, $\vec{M}_{ext}$ is the torque acting on the particles from external sources. The $\vec{M}_{roll}$ is the torque acting due to rolling friction given as follows:

$$\vec{M}_{roll} = -\mu_r |\vec{F}_n| R_i \frac{\vec{\omega}}{|\omega|} \tag{2.3}$$

where $\vec{F}_n$ is the normal force derived from the Hertz theory [104] for the normal elastic force whereas Mindlin's work [105] is used to compute the normal energy dissipation, given as follows:

$$\vec{F}_n = -\left(\frac{4}{3} E_{ij} \sqrt{R_{ij}} \delta^{\frac{3}{2}} + c_n \delta^{\frac{1}{4}} \dot{\delta}\right) \tag{2.4}$$

where c_n is the normal dissipation coefficient proposed by Tsuji et al. The normal dissipation coefficient is expressed as proposed by Tsuji et al. [106] and Zhang and Whitten [107].

The tangential forces include static and dynamic friction as follows:

$$\vec{F_t} = \min\left(k_t\delta_t + c_t\dot{\delta}_t, \mu\vec{F_n}\right) \tag{2.5}$$

The inter-particle collision forces and torques are given as follows:

$$\vec{F_i^c} = \sum_{i\neq j} \vec{F_{i,j}}(\vec{X_j}, \vec{u}_{p_j}, \vec{\phi_j}, \vec{\omega_j}) \tag{2.6}$$

$$\vec{M_i^c} = \sum_{i\neq j} \vec{M_{i,j}}(\vec{X_j}, \vec{u}_{p_j}, \vec{\phi_j}, \vec{\omega_j}) \tag{2.7}$$

where the for $\vec{F_i^c}$ stands for the collision forces between the particles, $\vec{M_i^c}$ is the torque due to collisions, $\vec{F_{i,j}}$ and $\vec{M_{i,j}}$ is the force and torque exerted by particle j on particle i respectively, $\vec{\omega}$ is the particle angular velocity. The sum $\sum_{i\neq j}$ represents the sum over all particles other than i. It should be noted that any boundaries, walls, or drums in the current work are treated as another particle. Hence, the collisions with boundaries/walls/drum are considered in the equations 2.6 and 2.7. In the equation 2.1, the term $\vec{F_i^{ext}}$ accounts for the fluid forces acting on the particle discussed further in section 2.3.4.

2.3.2 Governing equations for fluid

In the Eulerian volumetric average method, the conservation equation of mass (Eq 6.10) and momentum (Eq 6.11) are written over a representative volume. Conservation of mass

$$\frac{\partial}{\partial t}(\rho_f) + \boldsymbol{\nabla}\cdot(\rho_f\vec{u}_f) = m' \tag{2.8}$$

Conservation of momentum

$$\frac{\partial}{\partial t}(\rho_f\vec{u}_f) + \boldsymbol{\nabla}\cdot(\rho_f\vec{u}_f\vec{u}_f) = -\boldsymbol{\nabla}p + \rho_f\vec{g} + \mu_f\boldsymbol{\nabla}^2\vec{u}_f + \vec{S} \tag{2.9}$$

2.3.3 Governing equations for solid structures

The structures in the current work are modeled using the Finite Element Method (FEM). In this method, a large continuous problem (continuum) is discretized into smaller and simpler "finite elements". In this manner the underlying partial differential equations (PDEs) do not need to be solved over the complete spatial domain, but rather over a small element [16]. It is to be noted that FEM is a method to solve a set of PDEs, hence, depending on the underlying governing equations different physics can be modeled. In the current work, the displacements and the stresses of the structures are of interest.

The governing equations for displacements and stresses in a structure are derived from the principles of continuum mechanics and material behavior under consideration. The equilibrium equations express the balance of forces within the structure. They are derived from the principle of virtual work and are used to establish the equilibrium of internal and external forces. In matrix form, the equilibrium equations can be expressed as:

$$\mathbf{K} \cdot \vec{U} = -\vec{f} \tag{2.10}$$

where $\mathbf{K}$ is the global stiffness matrix, $\vec{U}$ is the vector of nodal displacements and $\vec{f}$ is the vector of applied nodal forces.

The constitutive equations relate stresses to strains for the material being analyzed. For linear elastic materials, Hooke's law is commonly used to express the relationship between stress and strain:

$$\boldsymbol{\sigma} = \mathbf{D} \cdot \boldsymbol{\varepsilon} \tag{2.11}$$

where $\boldsymbol{\sigma}$ is the stress tensor, $\mathbf{D}$ is the elasticity matrix and $\boldsymbol{\varepsilon}$ is the strain tensor.

The relationship between strains and displacements is defined based on the assumed displacement field within each finite element. This relationship is typically expressed using the strain-displacement matrix, which relates the strains to the nodal displacements within an element.

$$\boldsymbol{\varepsilon} = \mathbf{B} \cdot \vec{U} \tag{2.12}$$

where **B** is the strain-displacement matrix, that is dependent on the type of elements, and shape function used.

By combining the equilibrium equations, constitutive equations, and the strain-displacement relationship, a system of equations can be formulated to solve for the nodal displacements and subsequently calculate the stresses within the structure.

In the current work, Calculix [101, 102] an open-source, three-dimensional FEM software is used to solve the structure displacements and stresses on unstructured Lagrangian meshes. The readers are referred to the standard textbooks on FEM [16, 17, 19, 18] for further reading.

2.3.4 CFD-DEM Coupling

The CFD-DEM Eulerian-Lagrangian coupling is achieved over a volumetric mesh. In this section, the equations utilized to represent the coupled physics are presented. This work deals with single-phase as well as multi-phase fluids. Consequently, the equations presented in the following subsections, consider these different fluid conditions.

Fluid forces acting on particles

In this section, the effects of fluid forces acting on the particles are formulated. The DEM solver receives the fluid fields and properties and uses the following equations to compute the fluid forces acting on the particles. There are two types of fluid forces acting on the particles, namely hydrostatic or pressure force, and hydrodynamic or momentum exchange force. The hydrostatic force is the buoyancy force that accounts for the pressure gradient around an individual particle [108].

$$\vec{F_B} = -V_{p_i} \boldsymbol{\nabla} p \tag{2.13}$$

where $\vec{F_B}$ si the buoyancy force, V_{p_i} is the volume of particle under consideration and $\boldsymbol{\nabla} p$ is the gradient of pressure experienced by the particle.

To compute the momentum exchange or hydrodynamics forces acting on the particles, first, the porosity i.e. the space fraction occupied by particles is computed. The porosity/void

fraction of particles in fluid is given as:

$$\epsilon = 1 - \frac{1}{V_c} \sum_{i}^{n} \eta_i V_{p_i} \tag{2.14}$$

where V_c is the cell volume containing the particle, V_{p_i} is the volume of the i^{th} particle in the cell, and *eta* is the weight used for the porosity computation depending on the particle volume present inside the current cell.

In the Eulerian-Lagrangian approach, the hydrodynamic force corresponds to the fluid-particle interaction. This force depends on the relative velocity of the solid particle and fluid along with the forces acting due to the presence of neighboring particles. Several drag laws are implemented in the XDEM suite, such as Arastoopour [109], di Felice [110], Gidaspow [111], Richardson-Zaki [112], Shiller-Neumann [113], Sun-Battagli [114] and Syamal-OBrien [115]. The drag force acting on the particle due to the fluid for the CFD-DEM approach used in the current study is given as follows:

$$\vec{F_D} = \frac{\beta V_p}{(1-\epsilon)} \left(\vec{u}_f - \vec{u}_p\right) \tag{2.15}$$

The interphase momentum exchange β is predicted according to Gidsaw [111]. Although to cover all range of void fraction (ϵ), Wen and Yu [116] ($\epsilon \geq 0.8$) and Ergun and Orning [117] ($\epsilon < 0.8$) equations are included.

$$\beta = \begin{cases} 150\dfrac{(1-\epsilon)^2}{\epsilon}\dfrac{\mu_f}{d_p^2} + 1.75(1-\epsilon)\dfrac{\rho_f}{d_p}|\vec{u}_f - \vec{u}_p|, & \text{if} \quad \epsilon < 0.8 \\ \dfrac{3}{2}C_d\dfrac{\epsilon(1-\epsilon)^2}{d_p}\rho_f|\vec{u}_f - \vec{u}_p|\epsilon^{-2.65}, & \text{if} \quad \epsilon \geq 0.8 \end{cases} \tag{2.16}$$

where the drag coefficient C_d is given as:

$$C_d = \begin{cases} \dfrac{24}{Re}\left[1 + 0.15(Re)^{0.687}\right], & \text{if} \quad \text{Re} < 1000 \\ 0.44, & \text{if} \quad \text{Re} \geq 1000 \end{cases} \tag{2.17}$$

and the Reynolds number for the particle is given as:

$$Re = \frac{\epsilon \rho_f |\vec{u}_f - \vec{u}_p| d_p}{\mu_f} \tag{2.18}$$

Particle momentum source terms

Due to the nature of the momentum coupling under consideration, there are different possibilities for momentum exchange between fluids and particles as follows: the fluid can be the driving force, imparting momentum on the particles, consequently the particles offer resistance (drag source) to the fluid motion; the particles can be the source of momentum, imparting motion on the fluid by exerting acceleration on it; or lastly due to the complex nature of the application both conditions stated above can take place simultaneously in the different parts of the simulation domain. Therefore the momentum exerted by the solid particles on the fluid is treated in a semi-implicit way according to the method proposed by Xiao and Sun [118]. The explicit momentum source term $\vec{A}_c$ and implicit momentum source term Ω_c are as given in Eq 6.30

$$\vec{A}_c = \frac{1}{\rho_f V_c} \widetilde{\sum}_i B_i \vec{u_{p_i}}, \quad \Omega_c = \frac{1}{\rho_f V_c} \sum_{i=1}^{c_n} B_i \tag{2.19}$$

where the coefficient B_i [118] depends on the particle velocity $\vec{u_p}$, fluid velocity for the cell containing the particle $\vec{u_{f_c}}$, drag coefficient C_d and particle diameter d_p. Thus giving the source term to be injected in equation 6.11 as follows:

$$\vec{S} = \rho_f \vec{A}_c - \rho_f \Omega_c \vec{u}_{f_c} \tag{2.20}$$

Alternatively, if the application demands it, the particles can be represented in the fluid phase only as a drag source term S_i. The drag source is computed based on the Darcy–Forchheimer law [119, 120] for porous media, which is comprised of a viscous loss term and an inertial loss term. This creates a pressure drop proportional to the fluid velocity

and velocity squared, respectively.

$$\vec{S} = -\left(\mu_f D + \frac{1}{2}\rho \vec{u_f} F\right) \vec{u_f} \tag{2.21}$$

where D and F are Darcy–Forchheimer coefficients computed as follows:

$$\begin{aligned} D &= \frac{d_p^2}{150}\frac{\epsilon^3}{(1-\epsilon)^2} \\ F &= \frac{d_p}{3.5}\frac{\epsilon^3}{(1-\epsilon)} \end{aligned} \tag{2.22}$$

where d_p is the mean particle diameter assuming that the porous media is comprised of spherical particles, and ϵ is the volume porosity defined in equation 6.9.

2.3.5 CFD-FEM and DEM-FEM Coupling

The CFD-FEM and DEM-FEM coupling is achieved over a surface mesh. The structure is usually a moving boundary patch in the CFD domain. The pressure field of the fluid acting over the structure surface is used to compute the forces exerted by fluid, thus computing pressure over the CFD cell face area. These forces are communicated over to the nodes of the structure.

The DEM solver uses STL to represent the structure in the DEM simulation domain. This STL wall is treated as just another particle, and thus it is possible to capture the inter-particle interactions. However in this case the particle forces acting on the triangles of the STL file are captured. The forces are then distributed over the three points of the triangles. These forces on the STL "nodes" are then communicated to the FEM solver.

The FEM solver receives fluid/particle forces as an input. These forces are then summed up. The forces are then applied as Neumann boundary conditions.

Neumann boundary conditions specify the applied forces or traction on the boundaries of the domain [16], given as follows:

$$t_i = t_{i,0} \quad \text{for } i \in \Gamma_t \tag{2.23}$$

where t_i is the traction on the i^{th} degree of freedom, $t_{i,0}$ is the prescribed value of traction and Γ_t is the set of degrees of freedom on which the Neumann boundary conditions are applied.

Once the FEM solver receives the forces exerted by the CFD/DEM solver, and they are applied as Neumann boundary condition using the `*CLOAD` card in CalculiX, the FEM solver then solves for the displacements in the structure. These displacements are then communicated to the CFD and the DEM solvers.

The CFD solver represents the structure as a moving wall, hence the CFD mesh is moved according to the displacements. On the contrary, as DEM is a mesh-less method, and the structure is represented as an STL wall, the displacements are directly applied to the STL wall and it is deformed. This is equivalent to changing the shape of a particle.

2.4 Coupling approach

The preCICE coupling library uses high-level APIs to minimize the invasion in the solver code base by using adapters. In the context of the current work an "adapter" is what is referred to as this preCICE integration into the solver [98]. Furthermore, an API for a well-developed solver, be it open-source, internally developed, or otherwise, is typically available. On the contrary, if one wishes to couple an in-house solver, due to indigenous development, the code base is well understood and ad-hoc API can be implemented. The adapter can be easily implemented and compiled as a separate library that the solver calls during runtime by using the API from the solver and preCICE, which keeps the solver code intact. In a coupled simulation, the adapter receives the necessary data from the solver and relays it to the other coupled solver(s) via preCICE (MPI ports or TCP/IP sockets). An outline for the partitioned coupling is presented in figure 2.1.

2.4.1 OpenFOAM adapter for preCICE coupling

The preCICE coupling library provides an OpenFOAM adapter [52] that can handle surface coupling preliminarily used for Fluid-Structure interaction (FSI) and Conjugate Heat Transfer (CHT). The adapter out of the box is not equipped to handle volume coupling but rather

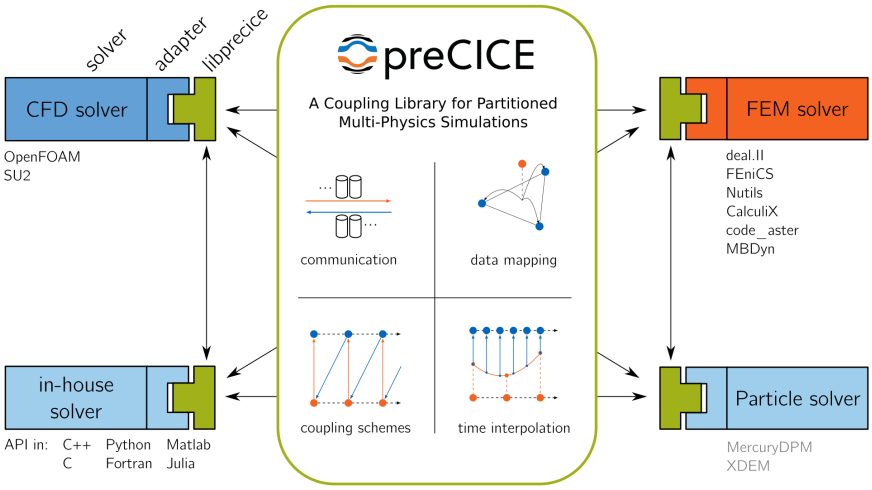

Figure 2.1: A schematic outlining the coupling procedure [121] (reproduced with permission)

extended by the users [52]. The OpenFOAM adapter does not have all the fields required for the CFD-DEM volume coupling intended for momentum exchange, some that are available, are defined over the surface mesh. Hence, it was necessary to implement and develop this part for the adapter.

To enable the volume coupling, a new coupling interface is implemented in the OpenFOAM adapter consisting of two modules, namely, Fluid Properties and Momentum Transfer. A simplified class UML diagram is presented in the figure 2.2, illustrating the new additions and modifications in the OpenFOAM adapter (represented using a solid outline, whereas the dashed outline is a pre-existing implementation). The muted colors represent pre-existing classes, whereas the bright colors show the modifications added to the current work.

As described in section 2.3.4, fluid fields such as fluid velocity, density, viscosity, pressure gradient, and phase volume fraction gradient are required for computing the fluid forces/effects on the particles. Hence, these fields are implemented in the Fluid Properties module, as they are not tied to CFD-DEM coupling per-say rather they are the data fields available for volume coupling representing the fluid state. As the class structure exists, one may add further fluid fields. The data fields coming from the DEM are added to the Momentum Transfer module. These fields represent the particle momentum contribution in the fluid phase as described in section 2.3.4. They consist of volume porosity, acceleration,

omega, and particle diameter. Depending on the type of flow, different particle representation is used. For example, packed beds offer only drag (or pressure drop) to the fluid. Hence, in such cases, the volume porosity can be used to compute the drag based on Darcy–Forchheimer law. On the contrary, moving particles may offer drag or acceleration to the fluid, in such case, acceleration and omega, semi-implicit momentum source term is used.

Irrespective of the drag representation used, the drag is injected or represented in the fluid phase using the `fvOptions` dictionary (renamed as `fvModels` since OpenFOAM v9). Hence, there is no need for any invasive modifications in the CFD solver code base. In a broader scope, OpenFOAM provides various solvers representing different flow conditions and utilizes different algorithms for solving the governing equations. Irrespective of the solver used, the same fields can be used for representing the particles in the fluid phase.

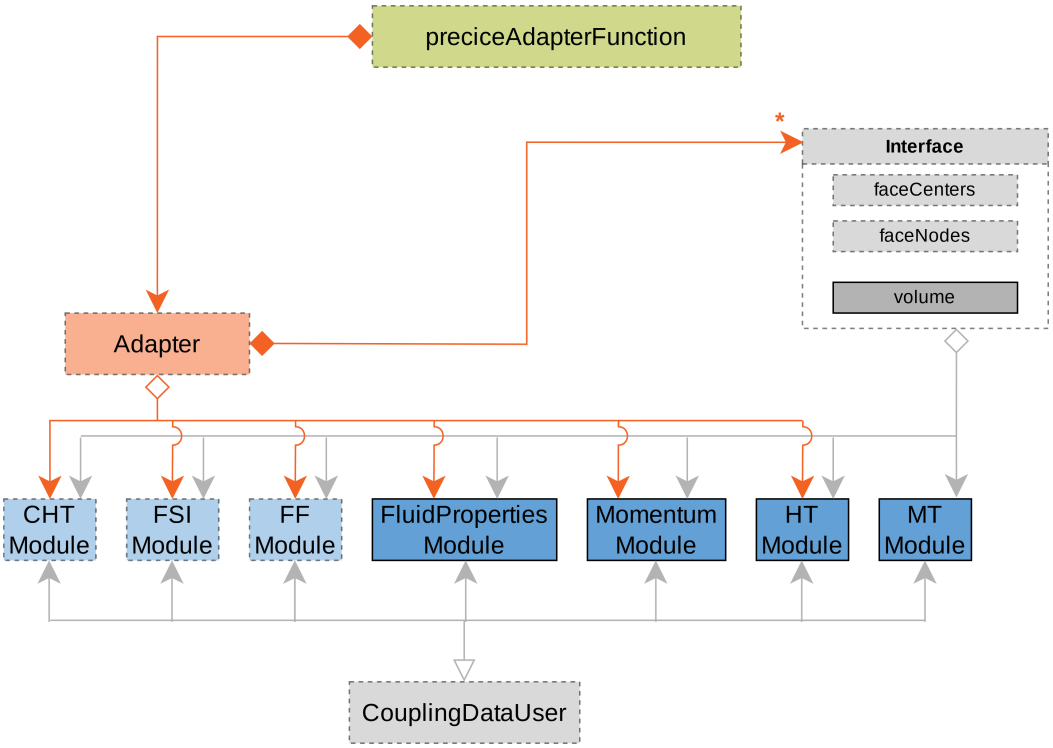

Figure 2.2: A simplified class UML diagram for the modified OpenFOAM adapter

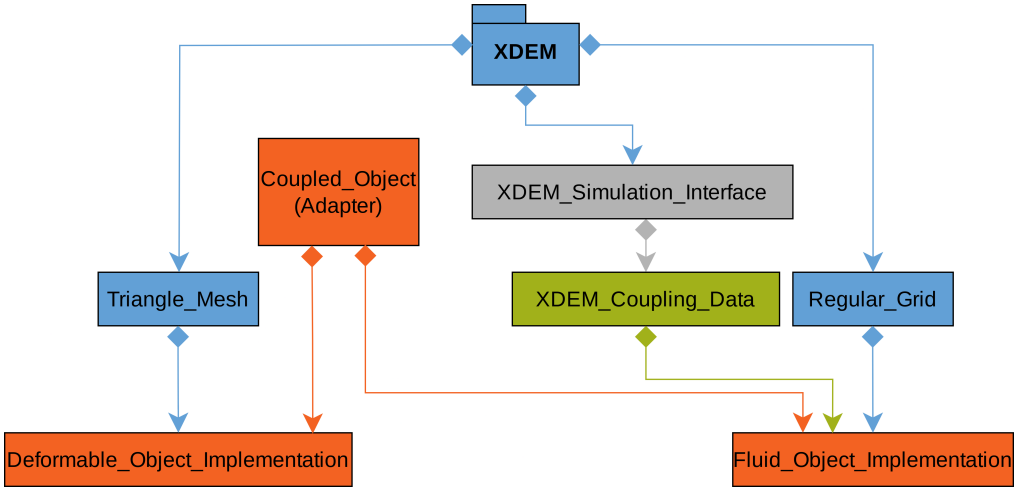

Figure 2.3: A simplified class UML diagram for the XDEM adapter

2.4.2 XDEM adapter for preCICE coupling

The XDEM software suite is implemented in C++, thus when the XDEM preCICE adapter is also implemented in C++. The C++ API of preCICE is used to call and utilize the coupling library. It is to be noted that such API is also provided in various programming languages such as C, MatLAB, Python, Fortran, Julia, etc. Thus, when implementing an adapter for an in-house solver written in the above-mentioned programming languages is straightforward using the API for the respective language.

The XDEM adapter is implemented to be flexible for diverse types of applications, following the guidelines from the preCICE coupling library. A simplified class UML diagram for the XDEM adapter is presented in figure 2.3, illustrating the adapter structure. The XDEM software suite consists of several solvers, purpose-built for certain applications. The `xdem-adapter` thus is compiled just as another XDEM solver. The XDEM solvers usually expect only one argument, i.e. the input file name, but in the case of the XDEM preCICE adapter, it also needs the name of the preCICE configuration file as an argument. As the adapter handles all the simulation types, it checks which simulation types are needed using the preCICE configuration and XDEM input file. Depending on this it will create `Coupled_Object` for each of the coupling done. The XDEM preCICE adapter allows the selection and use of any data fields. Additionally, if a field is required but not exchanged it will

set default values for that field, implemented in the `Deformable_object_Implementation` and `Fluid_object_Implementation`. The XDEM adapter also provides a summary of the exchanged data fields and the possible type of simulation being run based on the data fields used.

The XDEM adapter receives several fluid fields describing the flow conditions. Based on these fields the fluid forces (drag) on the particles are computed and applied as external forces. Several drag laws are available in XDEM, as described in section 2.3.4, that utilize the fluid fields to compute the fluid drag acting on the particles.

Additionally, using the particle state, either the volume porosity or the seim-implicit momentum source is computed and transferred by XDEM through the XDEM adapter. This reduces the computation cost of the fluid solver.

2.4.3 Volume Coupling

The XDEM software suite is based on the discrete element method, which is a mesh-less method. This poses the largest challenge when coupling such mesh-less methods with mesh-based methods. In the current work, although the DEM solver is a mesh-less method, due to the computational costs a lot of work has been done to parallelize the solver and improve performance [89, 86, 122, 90, 12]. Due to the requirement of parallelization, the mesh-less domain is divided into several small parts thus providing a pseudo mesh/structure. For the volume coupling, this pseudo mesh is used to exchange the coupling data.

In figure 2.4, a side view of the volumetric mesh is shown for the flow through channel case as presented in section 2.5.2. More details on the simulation set are available in the mentioned section, as only the current section focuses only on the volume coupling itself. The XDEM simulation domain is initially just a box, where the particle position is tracked, if the particle leaves this spatial domain it is deleted from the simulation. The figure 2.5 (a), shows this XDEM simulation domain is discretized, with the crosses showing the centers of the volumes. The figure 2.5 (b) shows the meshed fluid domain. As the CFD uses finite volume methods, the mesh volumes and cell centers are already available and represented here as squares.

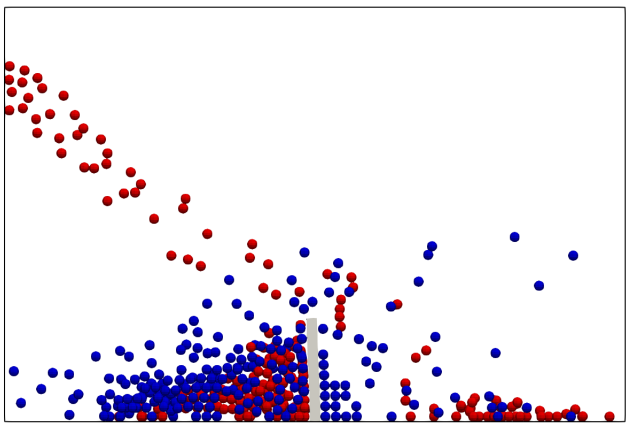

Figure 2.4: DEM simulation domain displaying the particle positions of heavy (red) and light (blue) particles

These volume/cell centers are used to exchange the coupling data. As it can be seen in figure 2.5 the DEM and the CFD mesh do not entirely conform. This is because in the DEM domain, the structure is treated just like another particle, but with some additional properties, represented with a STL file. On the contrary, in the CFD, only the fluid domain is present, while the space for the structural domain is left out. Even though the CFD and DEM domains have non-conforming meshes, it is not an issue due to the data mapping schemes available. These data mapping schemes will interpolate the data between the cell centers that do conform.

In the figure 2.5, an example of scalar data mapping is shown from DEM to the CFD domain. The particles may be represented in the fluid domain as a drag source using porosity. The same is seen in figure 2.5, where Volume porosity represents the particles. XDEM computes this volume porosity, a scalar, and stores these values at the cell centers. When comparing the particle positions shown in figure 2.4 and the volume porosity shown in figure figure 2.5 (a), it can be seen that it represents the particle positions well. The XDEM grid can be refined further to capture the variables better, in this case, the volume porosity. Nonetheless, the data mapping strategies allow for mapping the data well. Due to the nature of the volume coupling used along with the data mapping, this type of volume coupling offers flexibility in choosing the CFD mesh size and the particle size used in the unresolved

CFD-DEM coupling.

Figure 2.5 (b), illustrates the volume porosity after it is mapped onto the CFD mesh. Th figure 2.5 (a) and (b) only show the volume porosity values at the volume/cell centers. To further illustrate the data mapping, a slice of the fluid domain with the XDEM cell centers and volume porosity is shown in figure 2.6. Similarly, all the other fields are transferred and mapped using these volume/cell centers in both directions of the coupling. Additionally, if the CFD data is made available on the CFD volume centers, then theoretically any given CFD software tool/package can be used to achieve this CFD-DEM partitioned volume coupling.

2.4.4 Surface Coupling

The CFD-FEM surface coupling used in the current study is standard out of the box. It is well described and validated in the literature [123, 52] using the Turek-Horn FSI2 and FSI3 benchmarks [124]. Thus the surface coupling between fluid and structure is not discussed further in the current work.

The surface coupling did not exist between the DEM and the FEM solver. However, the FEM preCICE adapter is used out of the box for this coupling. The FEM solver is not specified in this case as any FEM solver with the preCICE adapters can be used as the fields required for such coupling are common among the existing FEM preCICE adapters, namely forces and displacements.

To achieve the particle-structure interaction, only two data fields are needed. These data fields are exchanged over nodes of the FEM mesh. Figure 2.7 (a) shows a FEM structure with its mesh along with the nodes that are used to share data. Hence, for this particular DEM-FEM coupling, it is crucial to have a mesh good enough to capture the particle impacts.

As described in section 2.3.1, equation 2.6, the $\vec{F_i^c}$ is the collision force between particles. In the XDEM software suite, the structure wall is treated just as another particle. This particle uses an STL file to represent the geometry needed. The triangles are sub-shapes forming the particle. The particle impacts on these triangles it captured and interpolated onto the nodes. The force interpolation is based on the virtual work equivalent to ensure consistent nodal forces for the Finite Element Method (FEM). This approach allows the work

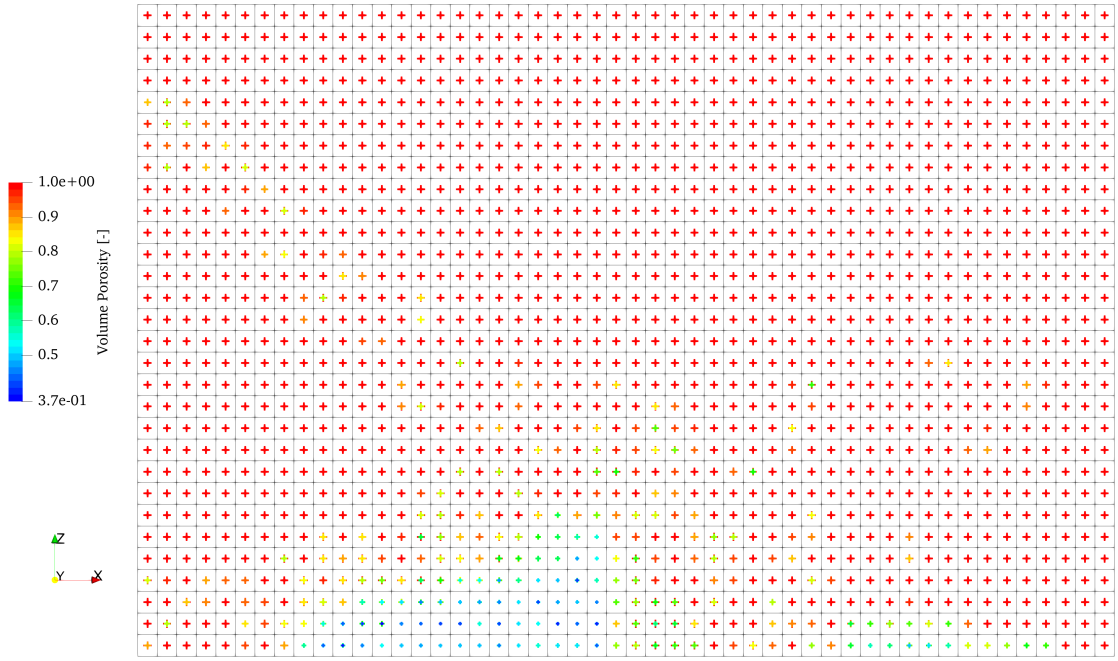

(a) XDEM discretized domain

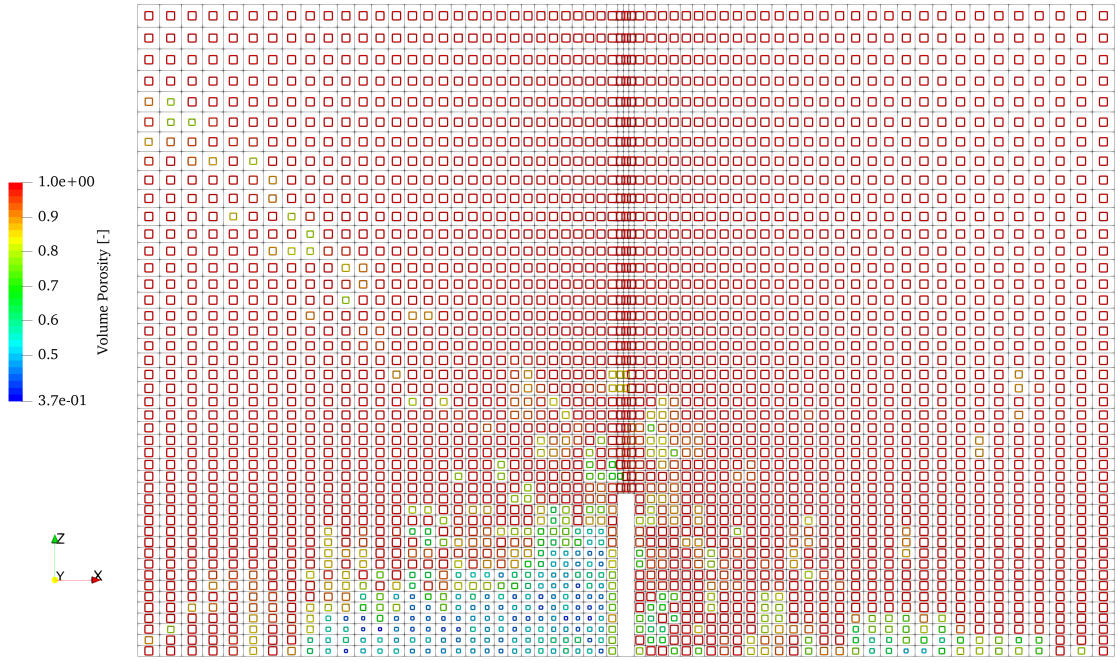

(b) Fluid Mesh

Figure 2.5: DEM and fluid domain with their volume and cell centers respectively, colored and scaled using the volume porosity

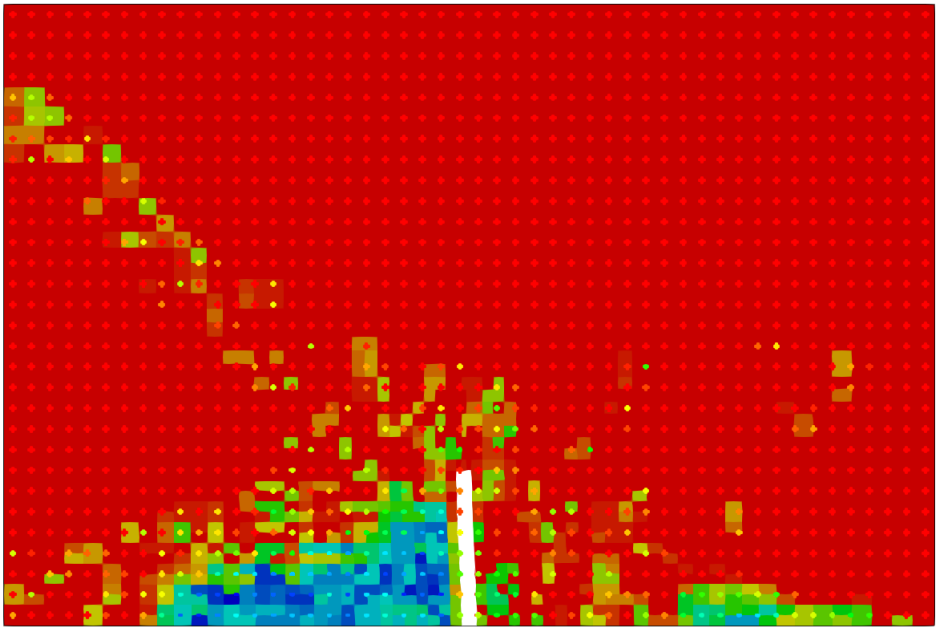

Figure 2.6: Fluid slice showing volume porosity field with the XDEM cell centers

of the particle force paired with the interpolated displacement to equal the work achieved by the nodal forces and nodal displacement, ensuring an accurate representation of the forces on the triangles [125]. A detailed description of the contact prediction and interpolation algorithm can be found in the literature [126, 127, 125].

As these forces are interpolated onto the nodes of the STL, they communicated with the FEM solver. The preCICE coupling library uses data mapping schemes to apply these point loads onto the nodes. The point loads coming from particles and the fluid are summed up when necessary, mainly depending on the coupling exchange time step. The FEM solver then solves for the displacements of the structure and communicates the displacements to the other participants in the partitioned coupling. XDEM then deforms (or rather translates) the STL in its domain as per the displacements applied. This moves the STL wall within the DEM domain, thus representing the structure movement.

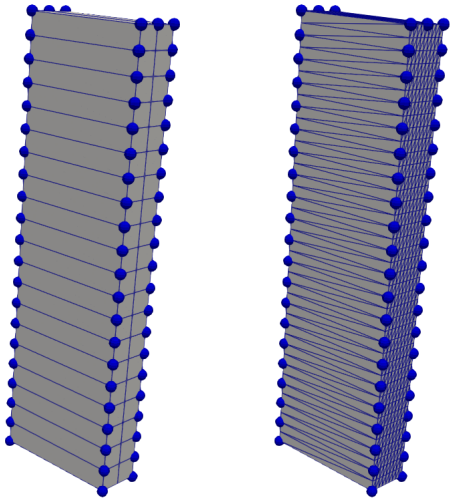

(a) FEM mesh with nodes (b) XDEM STL wall with nodes

Figure 2.7: FEM mesh with the nodes used to exchange data

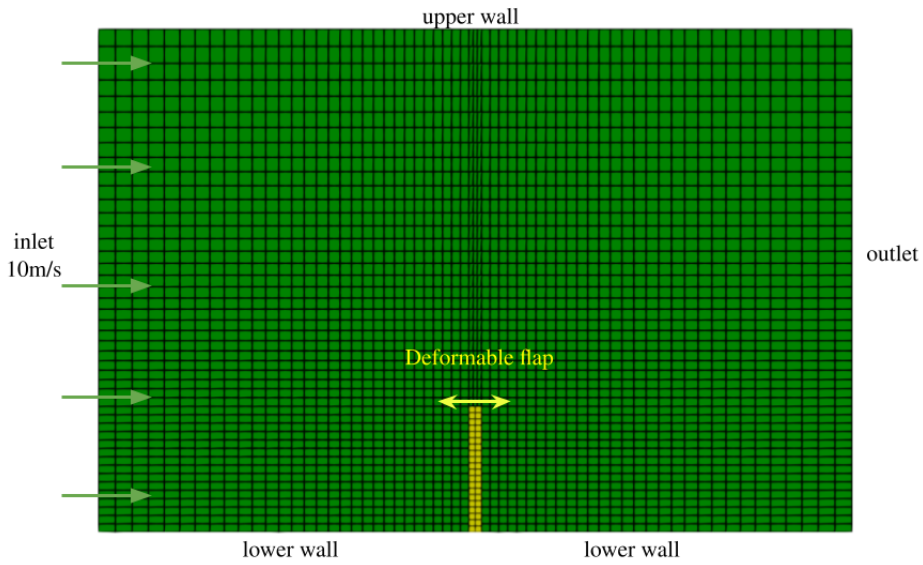

Figure 2.8: Case setup and boundary conditions for fluid-structure interaction case

2.5 Results

In the Methods 2.3 and Coupling 2.4 section, we established how the coupling between different single-physics black box solvers is achieved. Although one can model a 6−way CFD-DEM-FEM coupling at this point, the multi-physics partitioned model needs to be tested.

To establish that this 6−way coupled modelling is correct certain physical phenomenon are tested individually. Hence, in the results section, we will first go through coupling between two software and test out the 2−way coupling. This study will ascertain if the 2−way coupled physics works properly. And finally we study the 6−way coupling. This step-by-step study of the coupled model not only reveals the strengths but also pushes the model to its limitations.

For each type of coupling, a format is followed, where we start with a general description of the test case, the goals to be achieved with the given case, simulation setup including individual physics boundary conditions (BC) and coupling parameters, and finally we see the results for the given case.

In the literature [128], usually a coupling CFD-DEM coupling is considered 2−way coupling, and inter-particle momentum exchange is also considered as 2−way coupling between individual particles. Hence the case presented here is usually known as a 4−way coupling. But as the focus of the current work is coupling of two different physics, we consider this type of cases as a 2−way coupling.

2.5.1 2-way CFD-FEM Coupling Case: Flow through channel

The first test case provided by the preCICE team [121], that is a pesudo 2D version of FSI case from [129]. In this case, there is a flexible perpendicular flap in a channel. This case demonstrates Fluid-Structure Interaction (FSI). Furthermore, this setup is used to expand and add particle physics as well.

A pseudo two-dimensional fluid flow through a channel is modelled [121]. A deformable flap is placed in the centre of this channel. The perpendicular flap deforms and oscillates due to the fluid flow.

Simulation Setup

The fluid domain is 6 m long in the x-direction, and 4 m in the y-direction. The deformable flap is 1 m long in the y-direction, and 0.1 m thick in x-direction. The fluid inlet is located on the left side as seen in figure 2.8, where the fluid enters the simulation domain at 10 m/s. The upper and lower side as enclosed and treated as wall boundaries. The deformable flap is treated as a moving boundary. Finally, the outlet is on the right side of the simulation domain. As this a pseudo two-dimensional fluid flow, the front and back are empty boundaries.

The fluid mesh consists of 3150 hexahedrons as seen in figure 2.8. As the CFD uses finite volume method (FVM), it needs a volume, hence the z-direction consists of one cell of arbitrary length. The deformable flap is divided in 20 equidistant divisions in the y-direction, 2 divisions parts in the x-direction, and 1 division in the z-direction. The FEM model uses $C3D8$ element [102]. A Dirichlet boundary condition is applied on the nodes at the bottom restricting the displacements to zero using the `*BOUNDARY` card, whereas a Neumann boundary condition is applied on the rest of the nodes, where point forces are applied using the `*CLOAD` card.

The fluid density (ρ_f) is 1 kg/m^3, and the deformable flap density (ρ_s) is 3000 kg/m^3. The fluid kinematic viscosity $\nu_f = 1$ m/s^2. The deformable flap's Young's Modulus E = 4×10^6 kg/ms^2, and the Poisson ration $\nu_s = 0.3$.

The CFD uses a time-step of 10^{-4} s, FEM uses a time-step of 10^{-2} s, whereas the coupling time-step between the CFD and FEM is set to 10^{-2} s. The `nearest-neighbor` mapping scheme is used for data mapping from CFD to FEM, whereas `nearest-projection` mapping scheme is used for data mapping from FEM to CFD.

Results for 2-way Coupling Case

The flexible perpendicular flap moves because of the fluid flow acting on it. A point on the flap is monitored for displacements and this displacement is plotted overtime, presented in figure 2.10. Additionally, the normalized forces acting at the tip in the x-direction are presented in the figure 2.11. An oscillatory behaviour in the displacement can be clearly seen in the 2.10 due to the pressure built up.

Figure 2.9, the a slice of 2D fluid field showing the fluid velocity as well as the deformable flap show displacements are presented for different instances in the simulation. The figure 2.10, and figure 2.11 can be used to cross verify the fluid-structure interaction.

This section establishes the FSI, where fluid is the momentum source causing the displacements in the deformable flap.

2.5.2 6-way CFD-DEM-FEM Coupling Case: Flow through Channel

In the section 2.5.1, the FSI case with a fluid flow through channel is established. In the current section, the same case is extended so as to include the effects of particles on the fluid flow as well as structure deformation. In this case, the fluid momentum is still the main driving force.

Simulation Setup

The simulation setup for the fluid and the structure remains the same as described in section 2.5.1. The only change made is to the structure solver is that the FEM solver time step is reduced from 10^-2 s to 10^-4 s. This change is made so as to capture the particle impacts with sufficient temporal resolution.

The DEM simulation time-step used is 10^{-5} s. This is much lower than the other two counterparts so as to allow detection of particle collisions. The Hertz-Mindlin collision model is used, as described in the section 2.3.1. The gravity is pointing in the negative z-direction, with $\vec{g} = 9.81$ m/s^2.

There are two type of particles, heavy and light injected into the simulation domain as shown in figure 2.12. The mechanical properties of these particles is given in the table 2.1. These particles are used so as to demonstrate different effects of fluid forces acting on the particles. The heavy particles as injected using a particle source located at $(-3, 0.15, 3.25)$ m. The particle source size is 0.05×0.25 m. The heavy particles are injected with an initial velocity of 1 m/s, with a particle rate of 50 particles/s, with a time-step of 10^{-5} s. The coupling time-step between the DEM and FEM is set to 10^{-3} s. The coupling time-step between the DEM and CFD is set to 10^{-3} s.

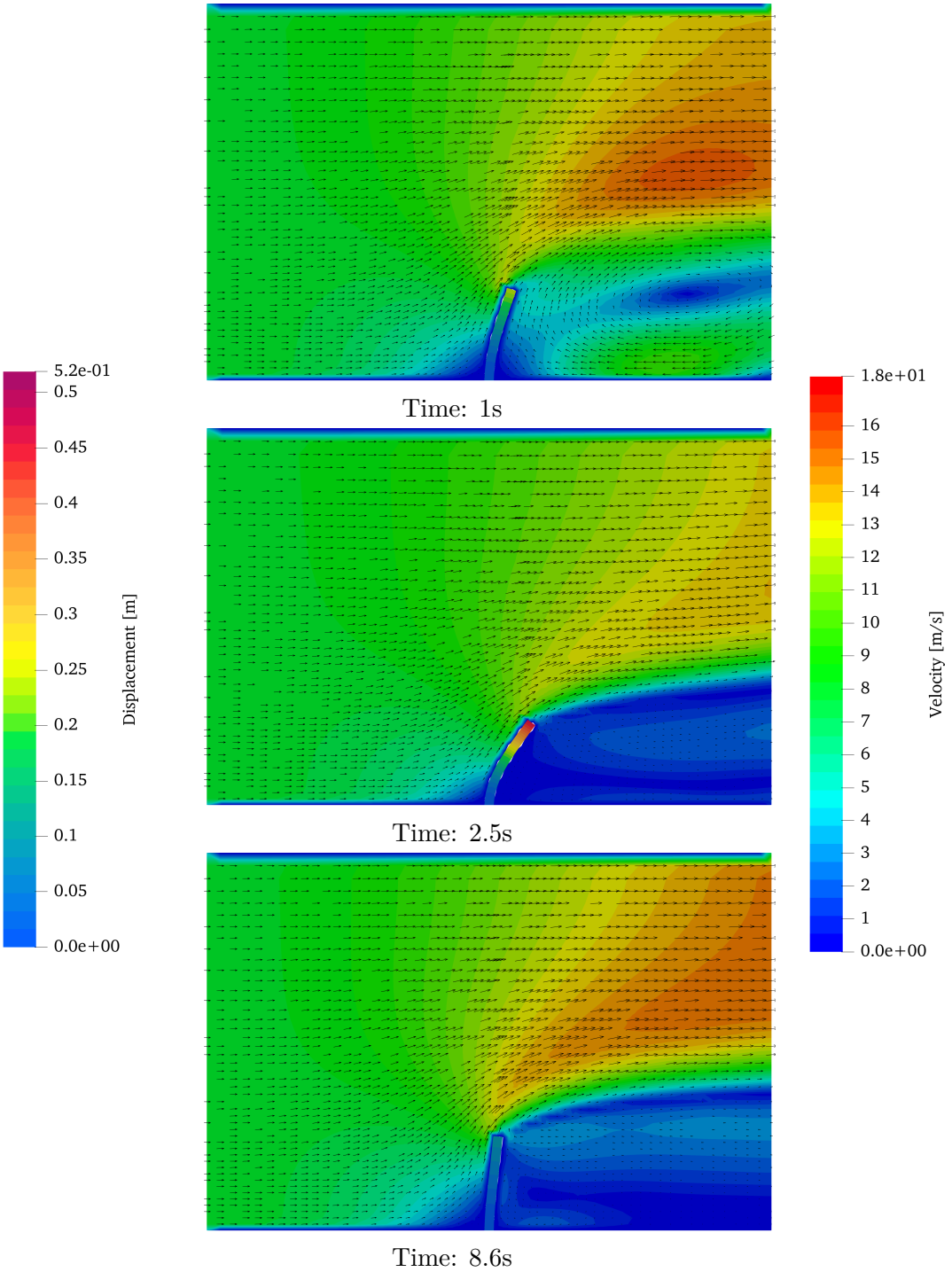

Figure 2.9: Fluid flow through the channel deforming the perpendicular flap

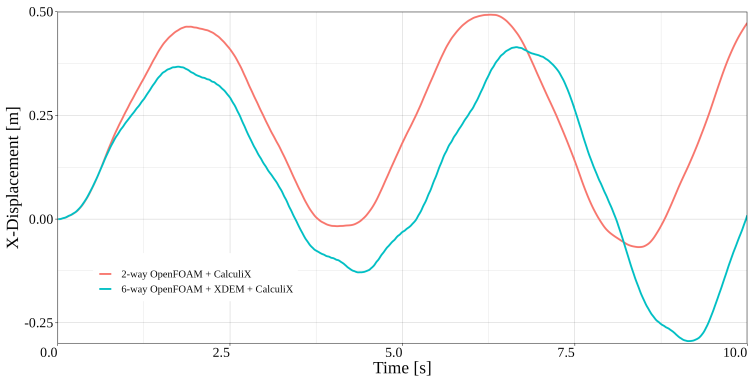

Figure 2.10: Displacement of flap tip monitored over time caused due to FSI and FPSI

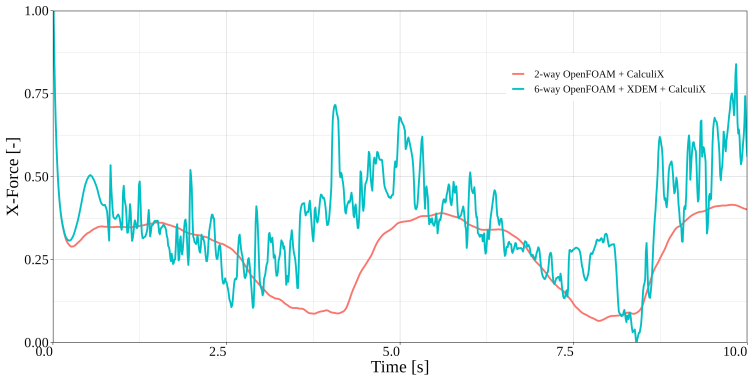

Figure 2.11: Normalised x-direction forces acting on the deformable flap tip

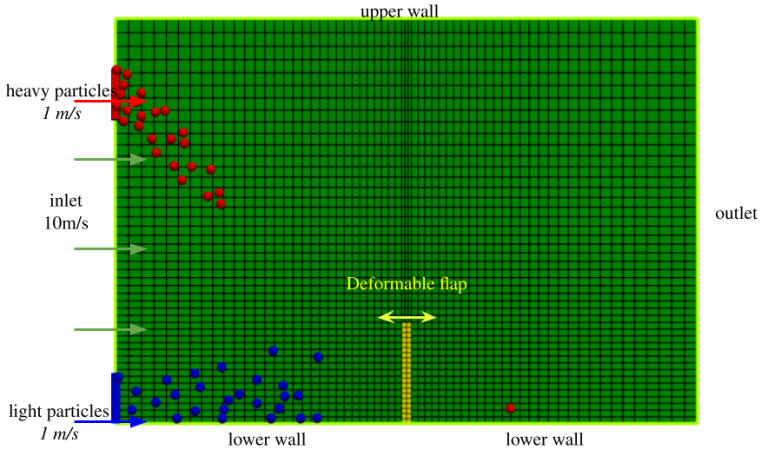

Figure 2.12: Case setup and boundary conditions for fluid-structure interaction case

Properties	Heavy particles	Light Particles
Density ρ (kg/m^3)	50	0.5
Young's Modulus (Pa)	5×10^5	5×10^5
Poisson Ratio [-]	0.45	0.45
Spring Stiffness [N/m]	1×10^5	1×10^5
Coefficient of Restitution	0.5	0.5
Coefficient of Static Friction	0.8	0.8
Coefficient of rolling friction	0.15	0.15

Table 2.1: Physical and Mechanical properties of the particles used in the DEM model

Results for 6-way Coupling Case

As seen in the previous section, the fluid is the main momentum source in this simulation as well. The fluid transfer momentum on the particles as well as the deformable flap. In the figure 2.13, both the heavy and light particles are transported in the direction of the fluid flow.

In the current example, there are two types of particles being used in the simulation domain, heavy and light. As the name suggests, they are either heavier or lighter than the fluid. This not only allows to check for momentum transfer but also the buoyancy forces acting on the particles. The figure 2.13, shows temporal evolution, where the heavy particles are observed to be transported in the fluid flow direction, as well as they sink in the fluid domain due to being heavier than the fluid. On the contrary, the lighter particles are seen to rise as they are being transported bu the fluid. This demonstrates that the buoyancy forces are working correctly.

The fluid velocity field seen as time 1 s in figure 2.9 and figure 2.13, are similar, as the particles have yet to alter the fluid flow. The fluid velocity field in the figure 2.13, additionally shows the drag offered by the particles to the fluid flow. A consistent lower velocity is observed just at the particle injection points due to the consistent presence of the particles. As the simulation progresses, the particles start filling up the space left of the deformable flap. As opposed to the unrestricted fluid flow seen to the left side of the deformable flap in figure 2.9, due to the blockage caused by particles, the fluid flow is heavily restricted. Due to this particle blockage, the fluid flow is changed quite drastically for the 6−way FPSI coupled

scenario as compared to the 2-way FSI case, especially observed in at time 8.6 s in figure 2.9 and figure 2.13 respectively.

The figure 2.10, further confirms this altered flow through the displacement of the the deformable flap tip. The flap tip displacement for the FSI case 2.5.1, is oscillatory in nature and has a consistent amplitude over time. On the contrary, for the 6−way FPSI case, although some oscillatory behaviour is seen for the flap tip displacement, it is clearly altered. The reason behind this altered behaviour, is further confirmed from figure 2.11, illustrating the x-direction forces acting at the flap tip. For the FSI case, as only fluid forces are acting on the flap represented in red, the forces are seen to acting in an oscillatory manner, thus resulting in the oscillatory displacements. On the contrary, the forces acting on the flap tip for the 6−way FPSI case, the forces are a lot more erratic in nature. This is because the forces acting on the flap included the fluid as well as the particle forces. Although these forces are very erratic, if a time-averaged force is plotted, it can be seen that there is still an oscillatory pattern. Additionally, due the clumping of particles on the deformable flap, a higher over-all force is acting on the flap leading to more deformation compared to 2−way case, as seen in figure 2.10.

2.5.3 6-way CFD-DEM-FEM Coupling Case: Particle flow

In the section 2.5.2, a 6−way CFD-DEM-FEM momentum coupling was presented, where fluid flow is the driving force. Conversely, in the current section, the fluid is stand-still, and the particles are injected in the simulation domain at high velocity. The particle induces momentum on fluid, that indirectly moves the perpendicular flap.

Simulation Setup

The simulation setup is similar as described in section 2.5.2. The only change to the fluid simulation setup is, that the inlet velocity is set to zero. The light particles are not injected, while the heavy particles are injected at 10 m/s.

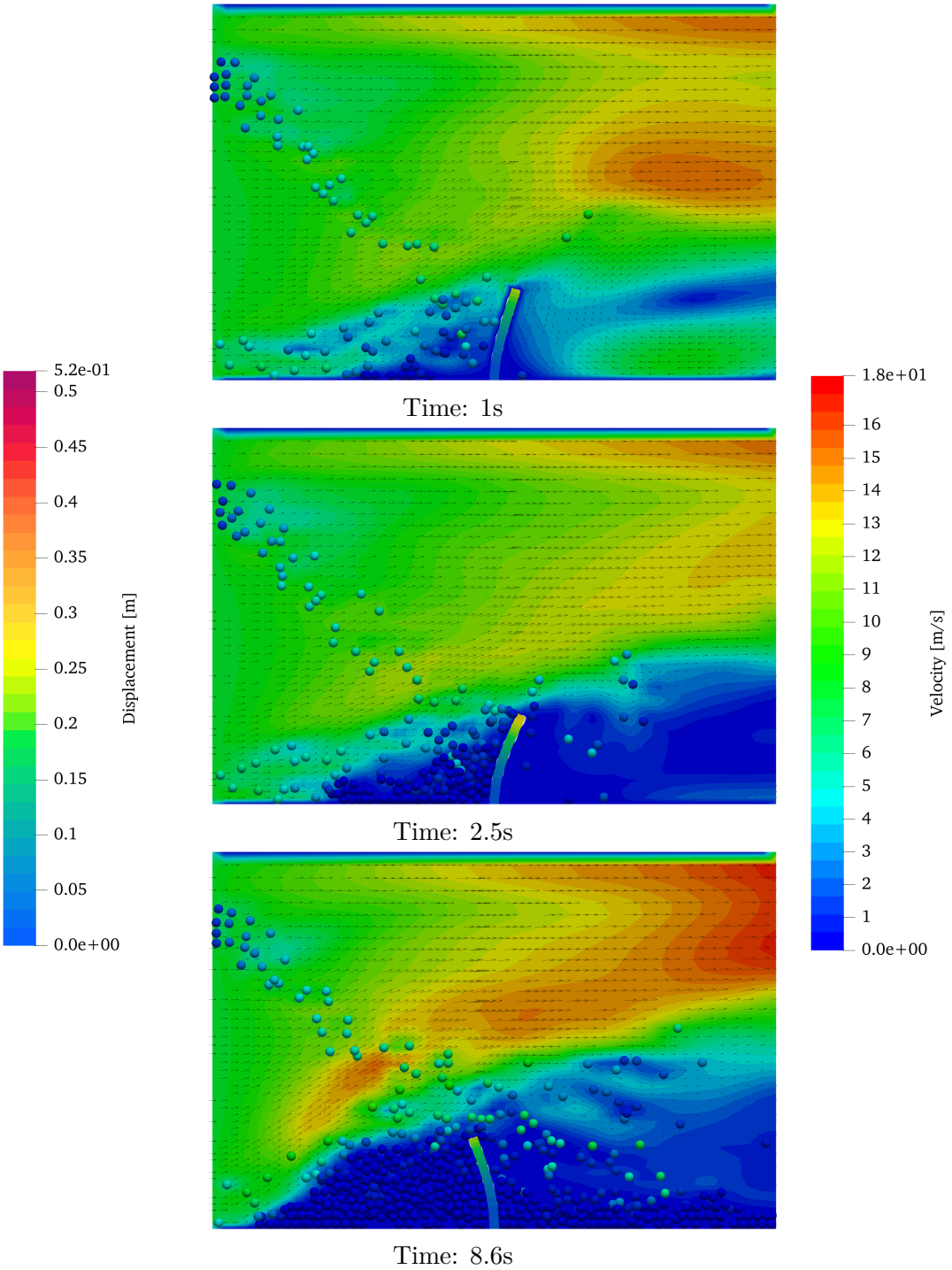

Figure 2.13: Fluid flow through the channel deforming the perpendicular flap

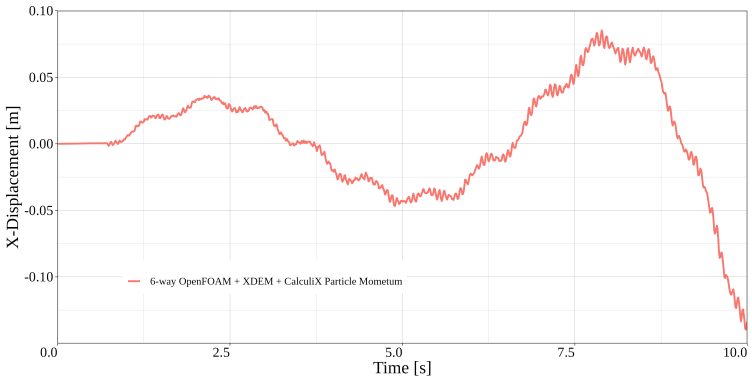

Figure 2.14: Displacement of flap tip caused due to indirect interaction with the particle flow

Results for 6-way Coupling Case: Particle flow

The figure 2.15, illustrates the temporal evolution of the fluid velocity field as the particles are injected in the simulation domain. As the particles are injected and the fluid is at a stand still, the semi-implicit momentum source term is injected (as described in equation 6.30), a fluid flow is established. The momentum exchange and the fluid drag forces exerted on the particles makes them lose their initial velocity, thus dropping to the bottom as they are about to reach the right extreme of the simulation domain.

The fluid velocity in the section 2.5.1 and section 2.5.2, was 10 m/s. In the current numerical experiment, although the particles have an initial velocity of 10 m/s, the fluid does not move at the same velocity. Additionally, only the fluid directly in the path of particles is affected the most, where as the rest of the flow is established due to indirect interactions. Due to these factors, the deformable flap does not move as much as seen in figure 2.14. This numerical experiment established the direct and indirect momentum exchange between the particles, fluid and structure.

2.6 Discussion

The partitioned coupling approach presents a lot of benefits and flexibility as compared to the monolithic coupling approach. The literature contains a lot of work done to enable partitioned coupling approach through the use of external libraries [50, 91, 93, 94, 95, 96].

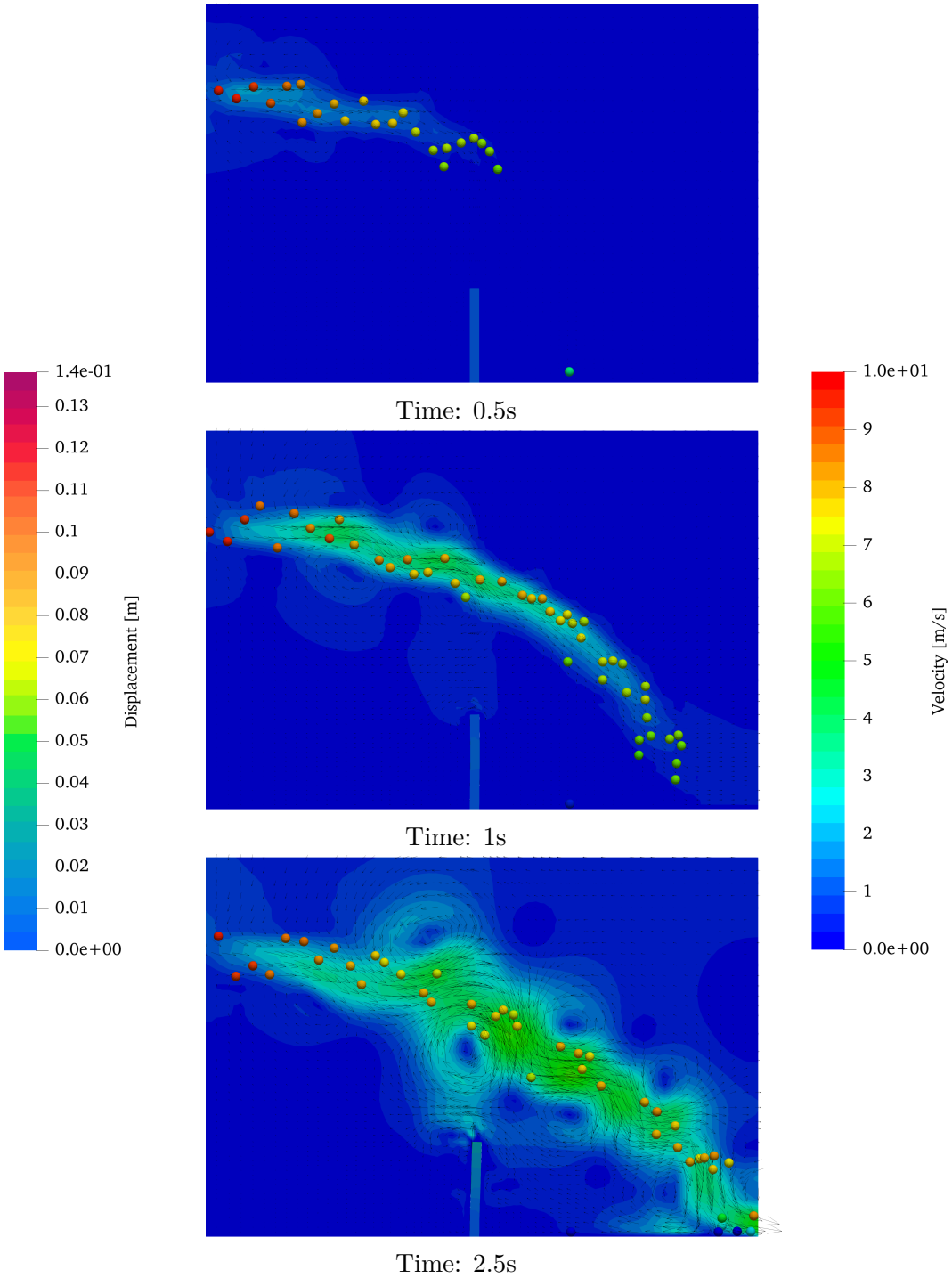

Figure 2.15: Fluid flow through the channel deforming the perpendicular flap

Although, these are applied to or restricted to only certain types of applications. In the context of fluid-particle-structure interaction, the literature is sparse, and it is even more so when considering the partitioned coupling approach used for FPSI.

The section 2.4, an in-depth description of the partitioned coupling approach is presented. This section delves into the development process of the preCICE adapters for single physics solvers. The mathematical formulations to consider the effects of different physics are presented thoroughly in the section 2.3.4 and section 2.3.5. Thus the authors believe that the current work provides a complete concept and notion of achieving a 6-way CFD-DEM-FEM momentum coupling via a partitioned coupling approach. This approach allows for the exchange/swap of any of the single physics solvers involved thus allowing engineers and researchers to easily couple a single physics solver/software to achieve FPSI.

The results section 2.5, presents numerical experiments involving a preliminary 2−way CFD-FEM coupling (FSI). This case successfully validates the fluid-structure interaction, with additional FSI validation available in literature [52]. This case demonstrates the oscillatory displacement of the perpendicular flap tip due to the influence of fluid flow. The fluid forces acting on the tip further support this displacement pattern.

This 2−way CFD-FEM coupling is expanded to include particle physics, thus turning it into 6−way CFD-DEM-FEM coupling. In the section 2.5.2, the fluid remains the primary source of momentum. This momentum is successfully transferred to particles along with the flap. The different density particles also demonstrate the fluid buoyancy acting on the particles. The deformable flap is affected by both fluid and particle forces acting on it, demonstrated by the forces acting on the tip. Furthermore, the flap tip displaces in an oscillatory manner, similar to in the 2−way CFD-FEM case, but the displacement amplitudes and temporal evolution are heavily influenced due to the presence of particles. On the contrary, in the section 2.5.3, particles indirectly displacement the perpendicular flap, still displaying an oscillatory displacement pattern, but with much lower amplitude due to the lower fluid velocities. This case also successfully demonstrates the bi-directional nature of the coupling between the different single physics solvers.

The current CFD-DEM coupling established is of an un-resolved type, hence only a global

interaction can be achieved. The intricate particle-fluid interaction cannot be resolved with the unresolved coupling. Although, this is a limitation of the unresolved CFD-DEM coupling rather than the partitioned coupling approach. Another caution when using this coupling is to have FEM and STL resolved enough to capture the particle impacts correctly. This is because the particle impact is captured on the triangular sub-shape of the STL file representing the structure in the DEM domain. These forces are distributed on the three nodes of the triangle, that are applied as point loads on the FEM mesh. If these triangles are too big, the forces might be applied too far from the actual point of impact thus leading to erroneous behaviour. Similarly, when representing the structure deformations in the DEM domain, the STL nodes are "displaced" according to the displacements computed by FEM. If the STL mesh is not fine enough to represent the deformations computed by the FEM mesh, this might lead to the structure deformations represented incorrectly in the DEM domain.

This coupling is developed to solve real-world problems, such as erosion predictions and erosion monitoring inside the abrasive water jet cutting nozzle [9, 11] that is currently being developed. The results presented in the current work only consider single-phase fluid, whereas a multi-phase fluid is being considered and developed as described in [9, 11]. Additionally, the partitioned CFD-DEM coupling approach has been developed [5] and applied to steel-making processes such as Midrex blast furnace [90].

There are many more engineering applications, that involve fluid, structure, and particle interactions. But often one of the interactions, or even worse one of the physics is entirely ignored to reduce complexity. The partitioned coupling approach presented in the current work is very flexible and can be used or extended to involve even more physics.

2.7 Conclusion

In conclusion, this work introduces a comprehensive and novel approach to achieve a $6-$way CFD-DEM-FEM momentum exchange using the partitioned coupling approach. This method is important because it is flexible enough to allow researchers and engineers to couple different single physics solvers for fluid, particle, and structure interactions interchangeably.

The developed preCICE adapters facilitate the coupling of single physics solvers, enabling a seamless momentum exchange between different single physics solvers to achieve fluid-particle-structure interactions (FPSI). The successful fluid-particle-structure interactions are demonstrated via numerical experiments. The foundation for a strong and adaptable coupling framework is laid by the mathematical formulations shown in the coupling equations, which demonstrate the methodical consideration of various physics.

Through sequential testing, the numerical experiments validate the partitioned coupling approach. Fluid-structure interactions (FSI) are successfully captured by the first 2−way CFD-FEM coupling, which has been verified against previous research. Particle dynamics are introduced by extending this coupling to a 6−way CFD-DEM-FEM scenario, illustrating the intricate interaction between fluid, particles, and deformable structures.

In conclusion, the developed 6-way CFD-DEM-FEM momentum coupling, facilitated by a partitioned coupling approach, provides a flexible framework with wide-ranging applications across various engineering domains in addition to aiding in the understanding of FPSI. The successes and insights that have been demonstrated open up new avenues for the study of complex coupled physics phenomena.

Nomenclature

	Physical constants/Greek symbols
β	Inter-phase momentum exchange $(kg/(m^3.s))$
ϵ	Porosity
μ_f	Dynamic viscosity $(Pa.s)$
μ	Sliding friction (-)
μ_r	Rolling Friction (-)
η	Weight of particle for porosity calculation
Ω_c	Implicitly treated drag term $(1/s)$
ρ	Density (kg/m^3)
	Operators
∂	Differential operator (-)
Δ	Difference (-)
∇	Nabla operator (-)

	Scalars
A	Surface Area
C_d	Drag Coefficient (-)
d	Particle diameter (m)
I_i	Moment of inertia $(kg.m^2)$
m	Mass (kg)
p	Pressure (Pa)
r, R	Radius (m)
Re	Reynolds number (-)
t	Time (s)
T_{final}	Length of simulation (s)
V	Volume (m^3)

	Subscripts
c	Cell, collision
d	Drag
eff	Effective values
f	Fluid
g	Gravity
i, j	Particle
n	Normal direction
p, P	Particle
s	Solid
t	Tangential direction

	Superscripts
n	Geometry exponent
(n)	n^{th} (time) step
$(n+1)$	n^{th} (time) step +1

	First order tensors (vectors)
$\vec{A_c}$	Acceleration on fluid cell due to explicitly treated drag term (m/s^2)
$\vec{g}$	Gravitational acceleration (m/s)
$\vec{F^c}$	Contact Forces (N)
$\vec{F^g}$	Gravitational Force (N)
$\vec{F^{ext}}$	External Forces (N)
$\vec{F_B}$	Buoyancy Force (N)
$\vec{F_D}$	Drag Force (N)
$\vec{M}$	Torque $(N.m)$
$\vec{v}$	Velocity
$\vec{X_i}$	Positional vector (m)
$\vec{\omega}$	Rotational velocity (rad/s)
$\vec{\phi}$	Orientation (deg)

Table 2.2: Nomenclature

Chapter 3

Development and validation of CFD-DEM coupling interface for Heat & Mass Transfer using partitioned coupling approach [1]

[1] The content of this chapter is under review in International Communications in Heat and Mass Transfer [5]

3.1 Abstract

This work demonstrates the rapid development of a simulation environment to achieve Heat and Mass Transfer (HMT) between Discrete Element Method (DEM) and Computational Fluid Dynamics (CFD). This coupling holds potential for simulating various processes like drying, pyrolysis, combustion, melting, and solid-fluid reactions, finding applications in biomass furnaces, boilers, heat exchangers, and flow through packed beds among others. To accurately model these applications, diverse CFD features and solvers must integrate with DEM to capture intricate physics.

The proposed method employs the preCICE coupling library on volumetric meshes, uniting CFD-DEM through an Eulerian-Lagrangian approach for HMT. The prototype uses eXtended Discrete Element Method (XDEM) for DEM calculations and OpenFOAM for CFD. XDEM receives key CFD data fields through preCICE, setting particle boundary conditions based on fluid domain properties and flow conditions. Heat and mass source terms computed by XDEM are fed into the CFD solver, representing the particle contributions.

This coupling framework, comprising preCICE, XDEM, and its adapter, accommodates a wide array of applications involving convective heat transfer between particles and fluids. Validation includes comparisons with experiments and a specialized solver, affirming the accuracy of predicted numerical results across heat transfer, drying, and pyrolysis cases. Additionally, the study delves into the computational costs associated with different coupling approaches, offering valuable performance insights.

3.2 Introduction

The field of engineering faces problems related to multi-phase media, which may include a continuous phase such as fluids, and a discrete phase such as powders, granular media, etc. Furthermore, these phases can behave and interact on multiple scales. The engineering applications involving such complexities are very difficult to study through experimentation. Therefore, such complex multi-physics, multi-scale problems are usually studied via numerical simulations.

The problems involving such mixed media, cannot be resolved well by only a continuous or a discrete phase alone. Such problems need to account for both continuous and discrete media along with their interactions with each other [64]. Such an approach is known as the Combined Continuum and Discrete Model (CCDM) [130]. In the present work, we will deal with the Heat and Mass Transfer (HMT) between the continuous fluid phase and discrete particles phase. HMT between fluid and particles can be used to describe processes such as drying, pyrolysis, combustion, gasification, and melting. These processes have a wide variety of applications in industrial sectors such as mining, energy production, waste management, pharmaceuticals, manufacturing & production, and process industries. Due to the challenges in performing experiments, it is desirable to have an HMT multi-physics simulation environment between particles and fluids to better capture these phenomena.

Such novel and rapidly evolving applications demand a rapid development of a simulation environment. In the literature, to achieve CFD-DEM coupling either commercial CFD software such as ANSYS Fluent®[131, 132, 133, 134, 135, 136] is coupled with commercial, open-source or in-house DEM software such as Rock-DEM® [137]. Open-source software such as CFDEM (OpenFOAM + LIGGGHTS) [138] are also utilized extensively for HMT applications [139, 140].

The CFD-DEM couplings mentioned above are achieved by solving different sets of segregated equations iteratively. This is ordinarily achieved by a single code coupling, where all physics models are implemented in one code also known as the monolithic coupling approach. Or they are coupled using a partitioned coupling approach, that couples existing single-physics software on a high level [88].

The monolithic coupling approach can be more robust when applied to specific applications. Additionally, years of extensive research and development are required to achieve such a simulation environment for a specific application. An extensive review [128] of developments in CFD-DEM coupling approaches for different applications demonstrates the same. Even with these developments, a lot more research remains to be done. However, due to the intrinsic nature of the monolithic coupling approach, it is rigid in its implementations. Moreover, such approaches rarely allow easy modifications or adaptions to make the model closer

to reality, or adapt for different applications. However, the partitioned coupling approach allows such modifications or exchange of physical components.

In addition to the limitations mentioned above, due to the nature of CFD-DEM coupling, the over-lapping domain (often the entire computational domain) is affected, and it is important to exchange the information for coupling [89]. Furthermore, these simulations are very computationally expensive. Hence, it is very important to parallelize such pieces of software. To tackle these problems a co-located partitioning strategy is proposed [86, 89]. Although this strategy solves the problems mentioned above, it also has limitations when dealing with non-conforming meshes due to the mesh/grid alignments. The unresolved CFD-DEM coupling further adds restrictions on the smallest CFD cell size, based on the largest particle size.

To circumvent the constraints of the monolithic coupling approach and offer more flexibility, we employ the preCICE coupling library [50] to develop a partitioned multi-physics simulation environment. In the partitioned coupling approach, a multi-physics problem is decomposed into multiple single physics parts and solved separately. The preCICE coupling library can be then used to couple these new or existing (highly specialized, optimized, purpose-built) single physics solvers/software to achieve the said multi-physics problem [121].

The preCICE coupling library treats these solvers/software as black-box and enables communication, and data mapping strategies. This type of coupling approach only needs nodal information from the black box. Subsequently, only standard Dirichlet and Neumann boundary conditions are applied [88].

Hence, there is no need to have access to source code, furthermore, no need to have expert knowledge of the source code of each of the solvers/software used in the partitioned multi-physics simulation. This also allows us to couple of solvers/software implemented in different languages (where currently supported languages are C++, Python, MatLAB, Fortran, and Julia). Although, to enable this communication and data mapping, a "preCICE coupling adapter" needs to be developed. Such a development requires a basic understanding of the solver/software along with its API. Hence the development of a preCICE adapter is a fairly accessible and achievable task.

The preCICE coupling library [50] and its adapters [52, 141] have been used to model Conjugate Heat Transfer (CHT) [99] between fluid and solid. Volume coupling has been utilized to simulate fracturing in a poro-elastic medium due to fluid flow [142]. Although the physical nature of coupling in this work is volumetric, the coupled system uses surface terms for equilibrium. The state-of-art on the CFD-DEM coupling is quite vast[128]. Some related works using OpenFOAM and XDEM monolithic coupling include [103, 143, 144, 145, 146, 89], where the heat and mass transfer is modeled for various applications.

To rapidly establish an HMT simulations environment, our prototype couples OpenFOAM [100] with eXtended Discrete Element Method (XDEM) [64] to achieve Heat & Mass Transfer between CFD and DEM. Although either of the software mentioned can be replaced with an alternative due to the modular nature of the coupling.

Our contributions, which are novel or related to the CFD-DEM coupling strategies, are (1) a flexible partitioned CFD-DEM coupling approach achieved by (a) developing an original preCICE adapter for XDEM (first DEM preCICE adapter), (b) extending the OpenFOAM preCICE adapter [123] to enable coupling over volumetric meshes, and mass transfer; (2) the verification against monolithic coupling and validation against experimental observations of the proposed partitioned CFD-DEM coupling approach; (3) preliminary performance analysis of monolithic versus partitioned coupling approach.

The paper is organized as follows: in section 3.3 we present the mathematical modeling of CFD and DEM. In section 3.4, the partitioned coupling strategies and software development are described. In section 3.5, we present and compare numerical simulation results with experimental observations, these cases include heating up, drying, and pyrolysis processes. In section3.6, we compare and discuss the performance of the partitioned coupling approach with the monolithic coupling approach. Finally in section 3.7 we discuss the development followed by conclusions.

3.3 Model Description

In the following section, the governing equations for continuum fluids and discrete particles are presented. In the partitioned coupling, we couple two single-physics software, namely CFD and DEM to achieve the multi-physics CFD-DEM environment. These are presented in section 3.3.2 and 3.3.1 respectively. The partitioned coupling approach is described in the section 3.4. The partitioned coupling approach is compared with a legacy monolithic coupling approach. Consequently, the reader is referred to the literature for a detailed description of the XDEM + OpenFOAM legacy coupling [145, 146, 147].

3.3.1 Governing equations for discrete particles

XDEM predicts both the thermodynamics and dynamics of the particulate system. In the current work, the main focus will be the thermodynamics of such particulate systems. The particle position, velocity, and acceleration are computed with the *dynamics* module of the XDEM, whereas the temperature and chemical processes are computed with the *conversion* module.

Conversion module

The conversion module of XDEM handles the heat and mass transfer within the particles and between the particles. It also accounts for various processes such as drying, gasification, combustion, etc. describing the inflow and outflow of the gas mixture. The detailed model description of the conversion module can be found in [148, 64], a summary of the governing equations for the fluid present in the porous regions within particles is given below.
Mass conservation equation for fluids in particle pores:

$$\frac{\partial}{\partial t}\left(\epsilon_f \rho_f\right) + \vec{\nabla} \cdot \left(\epsilon_f \rho_f \vec{v_f}\right) = m'_{s,f} \tag{3.1}$$

where $m'_{s,f}$ is the sum of all individual species' mass production or consumption rates due to chemical reactions, ϵ_f denotes the porosity within individual particles occupied by fluid(s).

The fluid species transport within this porous space of the particle obeys Darcy's law:

$$-\frac{\partial p}{\partial r} = \frac{\mu_f \epsilon_f}{K}(\vec{v_f}) \tag{3.2}$$

One-dimensional transient energy conservation equations for spherical particles:

$$\frac{\partial \rho c_p T}{\partial t} = \frac{1}{r_n}\frac{\partial}{\partial r}\left(r^n \lambda_{eff}\frac{\partial T}{\partial r}\right) - r^n\left(\vec{v}\rho_f c_{p_f} T\right) + \epsilon_f \sum_{k=1}^{l} \dot{\omega_k} H_k \tag{3.3}$$

The mass balance and transport equation of individual fluid species within the particle pores:

$$\frac{\partial}{\partial t}\left(\epsilon_f \rho_{f,i}\right) + \nabla \cdot \left(\epsilon_f \rho_{f,i}\vec{v_f}\right) = \frac{1}{r_n}\frac{\partial}{\partial r}\left(r^n \epsilon_f D \frac{\partial \rho_{f,i}}{\partial t}\right) + m'_{s,f,i} \tag{3.4}$$

The following boundary conditions apply to the governing equations mentioned above:

$$-\lambda_{eff}\frac{\partial T}{\partial r}\bigg|_{r=0} = 0 \tag{3.5}$$

$$-\lambda_{eff}\frac{\partial T}{\partial r}\bigg|_{r=R} = \alpha(T_R - T_\infty) + q''_{rad} + q''_{cond} \tag{3.6}$$

$$-D_{i,eff}\ \frac{\partial \rho_i}{\partial r}\bigg|_{r=R} = \beta_i\left(\rho_{i,R} - \rho_{i,\infty}\right) \tag{3.7}$$

In the Eq 3.6, q''_{cond} and q''_{rad} are conduction and radiation heat sources respectively from the neighboring particles. A detailed description of the conduction and radiation between particles is given by B. Peters in [148].

To solve for heat & mass transfer within the particle, the particle radius is discretized. This radial discretization can be uniform or non-uniform, as shown in fig 3.1. In the present work, uniform radial discretization is used. The non-uniform radial discretization allows for having a smaller cell length near the particle surface that allows the model to capture the sharp temperature and mass flow gradients.

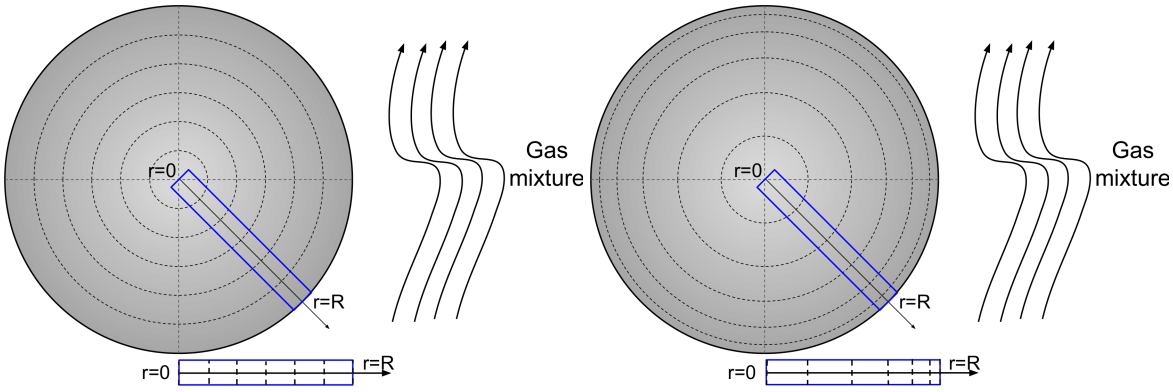

(a) Uniform discretization (b) Non-Uniform discretization

Figure 3.1: Radial discretization for heat & mass transfer calculations within a particle

Dynamics module

The discrete element method used in the dynamics module of XDEM is based on the soft sphere model. In this method, it is assumed that the particles are deformable and can overlap each other, where the magnitude of overlap is decided by the contact force using the force-displacement law. The hardness of the particle is expressed via Young's Modulus, while the particle energy dissipation is described with a dampener and/or dashpot. The translational and rotational movements of individual particles are tracked using classical mechanics equations. A detailed description can be found in [103].

The scope of the present work is heat and mass transfer, hence the cases chosen for this study do not have particle(s) in motion. However, if the fluid velocities were to be increased, particles could move due to the momentum transfer. The fluid velocity is modeled as one of the external forces F_i^{ext}. An example of such a case can be found in the modeling of a raceway zone in a blast furnace [2].

A summary of the translational and rotational motion equations is given below:
Equations of particle motion, where $\vec{F_i^{ext}}$ is the sum of all the external forces acting on the particle, such as buoyancy forces $\vec{F_B}$ and drag forces $\vec{F_D}$:

$$m_i \frac{d\vec{v_i}}{dt} = m_i \frac{d^2\vec{X}_i}{dt^2} = \vec{F_i^c} + \vec{F_i^g} + \vec{F_i^{ext}} \tag{3.8}$$

$$I_i \frac{d\vec{\omega}_i}{dt} = \sum_{j=1}^{n} \vec{M}_{i,j} \tag{3.9}$$

3.3.2 Governing equations for fluid

In the Eulerian volumetric average method, the conservation equation of mass (Eq 3.10), momentum (Eq 3.11) and energy (Eq 3.12) are written over a representative volume.

Conservation of mass:

$$\frac{\partial}{\partial t}(\rho_f) + \nabla \cdot (\rho_f \vec{v}_f) = m' \tag{3.10}$$

Conservation of momentum:

$$\frac{\partial}{\partial t}(\rho_f \vec{v}_f) + \nabla \cdot (\rho_f \vec{v}_f \vec{v}_f) = -\nabla p + \rho_f \vec{g} + \mu \nabla^2 \vec{v}_f + \vec{S} \tag{3.11}$$

Conservation of energy:

$$\frac{\partial}{\partial t}(\rho_f h_f) + \nabla \cdot (\rho_f \vec{v}_f h_f) = \frac{\partial p}{\partial t} + \vec{v}_f \cdot \nabla p + q' \tag{3.12}$$

Mass conservation equation for chemical species i in CFD is given as follows in Eq 3.13

$$\frac{\partial}{\partial t}\rho_{f,i} + \nabla \cdot (\rho_{f,i} \cdot \vec{v}_f) = m'_i \tag{3.13}$$

In the XDEM + OpenFOAM legacy coupling [145, 146, 147], all the terms in the governing equations 6.11, 6.12, 6.13 of the fluid are multiplied with the term ϵ (porosity), where porosity (ϵ Eq 6.9)refers to the interstitial space between the solid particles. The porosity calculation in brief is as follows:

$$\epsilon = 1 - \frac{1}{V_c} \sum_{i}^{n} \eta_i V_i \tag{3.14}$$

where V_c is the volume of the cell in consideration, V_i is the volume of each particle multiplied by η_i denoting the amount of particle volume present in the current volume.

The key differences in the fluid governing equations between the legacy coupling and the proposed partitioned coupling approach is that the porosity term described in equation 6.9

is not directly included in the current CFD model. This is because the fluid solver needs to be modified and tested thoroughly. Additionally, the heat, mass, and species sources from the particles are directly injected into the respective fluid governing equation. This process is highly intrusive and defeats the rapid development of the HMT simulation environment. As the fluid governing equations are not modified to consider the porosity, it is considered within XDEM when computing the heat source (q'), mass source (m'), and species source (m'_{specie}).

Furthermore, this porosity is exchanged as a field. Subsequently, it is used to model the drag offered by the particles to the fluid as follows [21]:

$$\kappa = \frac{d_{p_{mean}}^2 \epsilon^3}{150(1-\epsilon^2)} \tag{3.15}$$

where $d_{p_{mean}}$ is the mean particle diameter.

$$C = \frac{1.75(1-\epsilon)}{d_{p_{mean}} \epsilon^3} \tag{3.16}$$

$$drag = \frac{\mu}{\kappa} + \rho C \vec{v}_f \epsilon \tag{3.17}$$

The fluid solvers do not need to be modified to model the effects of particles, as these are injected as source terms into the fluid governing. Further explained in section 3.4.

3.4 Partitioned Coupling Implementation with preCICE

A flexible multi-physics simulation environment is achieved through the preCICE coupling library due to its minimal invasion of the solvers through the usage of high-level API (Application Programming Interface). This integration of preCICE into the solver is known as an "adapter" [98], seen in a schematic in figure 2.1. For a well-developed in-house, open-source, or any other kind of solver, an API for the solver is generally available. Alternatively, solvers developed in-house are well understood and can be developed to facilitate data field communication through preCICE. By utilizing the API from the solver and preCICE, the

solver code remains unchanged, and the adapter can be easily implemented and compiled as a separate library called by the solver during runtime. During coupled simulation, the solver passes the required data via its adapter to preCICE, which in turn communicates it to the other coupled solver(s) using MPI messages or TCP/IP sockets. A list of data fields exchanged for the HMT CFD-DEM coupling for the current work is presented in table 3.1.

3.4.1 OpenFOAM Adapter for preCICE coupling

The OpenFOAM adapter [123] is already available for coupling over surfaces [149]. It is used in different examples and applications such as Conjugate Heat Transfer (CHT) and Fluid-Structure Interactions (FSI) that can be achieved when coupled with other software. Although the default adapter contains all the fluid fields required to achieve HMT between CFD-DEM, they are described on surfaces.

To enable CFD-DEM volume coupling, a new coupling interface is implemented in the OpenFOAM adapter. Four different modules are implemented. These modules enable an exchange of different data fields related to Fluid Properties, Momentum Transfer, Heat Transfer (HT), and Mass Transfer (MT). Depending on the type of simulation these modules can be switched on or off (similar to the pre-existing modules).

Data fields such as fluid density, viscosity, thermal conductivity, and specific heat are added to the Fluid properties module. The fluid temperature and heat source fields are added to the HT module, whereas chemical species mass fractions, mass source, and species mass source are added to the MT module. Fluid velocity, pressure, and porosity fields are exchanged via the Momentum transfer module. The user is free to select which data fields they want to exchange, and what modules to use. Depending on the simulation type, these data fields are communicated via preCICE and the adapters to the other solver(s) and make them available for calculation.

In addition, OpenFOAM adapter receives various source fields such as heat (q'), mass (m'), species (m_i'), and porosity (ϵ) through their respective modules. These source fields are then injected into the respective governing equations through the finite volume plug-in `fvOptions` of OpenFOAM. The drag offered by the particles is computed using the porosity

field implemented through `codedSource` in the `fvOptions`. This drag source in injected into the momentum equation of the solver. As the presence of particles in the fluid is only represented by source terms in the finite volume options, there is no need to modify any of the OpenFOAM solvers to accommodate this CFD-DEM coupling. In the present work, `rhoPimpleFoam` (HT) and `reactingFoam` (HT & MT) solvers provided by OpenFOAM are used.

In practice, when using OpenFOAM, one only needs to change the CFD solver name in `controlDict`, and execute the solver. If this solver has the fields required as mentioned in table 3.1, no more work is required to run a CFD-DEM multi-physics simulation. In broad scope, it is also possible to switch between different OpenFOAM versions seamlessly to avail of different functionalities and solvers. With some more effort, one can also implement an adapter for an in-house CFD solver, and couple it with the needed solver (XDEM in this case).

Data Fields	CFD →DEM	DEM →CFD
Fluid Temperature	✓	
Fluid Viscosity	✓	
Fluid Conductivity	✓	
Fluid Specific Heat	✓	
H_2O	✓	
O_2	✓	
N_2	✓	
⋮	✓	
species n	✓	
Heat Source (q')		✓
Mass Source (m')		✓
Heat Transfer Coefficient		✓
Volume Porosity (ϵ)		✓
source H_2O (m'_{H_2O})		✓
source O_2 (m'_{O_2})		✓
source N_2 (m'_{N_2})		✓
⋮		✓
source species n (m'_n)		✓

Table 3.1: The data fields that are exchanged for the heat and mass transfer coupling

3.4.2 XDEM Adapter for preCICE coupling

Similar to preCICE, XDEM is also implemented in C++, thus when implementing the XDEM adapter for preCICE, we utilize C++ API of preCICE. An XDEM coupling interface class is implemented and then utilized to access data fields from the XDEM adapter.

XDEM adapter is developed to be flexible for diverse types of simulation. Similar to some other preCICE adapters provided by preCICE, the XDEM adapter is developed so that one can choose what fields are to be exchanged. If required fluid fields are not exchanged, default values are used for required calculations. XDEM adapter provides a summary of the data fields exchanged and possible types of simulation being run based on the data fields used. XDEM adapter receives several fields describing fluid properties and flow conditions. These values are then used as boundary conditions on the particles. In the context of current work, XDEM offers several HT laws and MT laws [150, 151, 152, 153]. These are set through the XDEM input file. These HT and MT laws are then utilized to compute the heat, mass, and chemical species source terms. Depending on the species mass concentrations and fluid flow conditions, XDEM also computes species transport and Solid-Fluid reactions.

These source terms are then transferred to the CFD solver through preCICE. The XDEM coupling interface class and the XDEM adapter are designed in such a way that ideally we can switch between any desired CFD solver/software. It does not make an assumption the kind of CFD solver used, rather it just assumes it receives and sends some specific fields that can be configured. Thus providing flexibility in choosing a CFD solver based on the application.

3.4.3 Mapping methods over Volumetric mesh

In the current work, we achieve the HMT coupling over volumetric meshes. Normally, we already have a volumetric mesh for the CFD. In contrast, DEM is a mesh-less method. In the XDEM suite, the DEM simulation domain is defined by a simple box, and individual particles are tracked within this box. An example of such a domain can be seen in figure 3.14 (b). However, due to DEM methods being costly, they require some parallelization. To this end, the simple box in the XDEM suite can be discretized over the three axes. Figure 3.15 (b)

shows the DEM domain discretized. The domain is sliced to reveal the cells and cell-centres. Consequently, the CFD cell size does not depend on the largest particle diameter for the unresolved coupling presented in this work.

The numerical experiments presented to use the default mapping offered by the preCICE coupling library. The `nearest projection` mapping method is applied when mapping data from CFD to DEM. In contrast, `nearest neighbor` mapping method is applied when mapping data from DEM to CFD. The `nearest-projection` mapping method is mostly a second-order method. This method first projects the data onto the mesh and uses linear interpolation within each element [51]. An illustration of this method can be seen in the top half of figure 3.2. This method requires the mesh connectivity information. The `nearest neighbor` mapping method is a first-order method as presented in the lower half of the figure 3.2. The cases under consideration do not warrant complex mapping methods such as `nearest neighbor gradient` or `radial basis function`. Although these mapping methods are available in the preCICE coupling library.

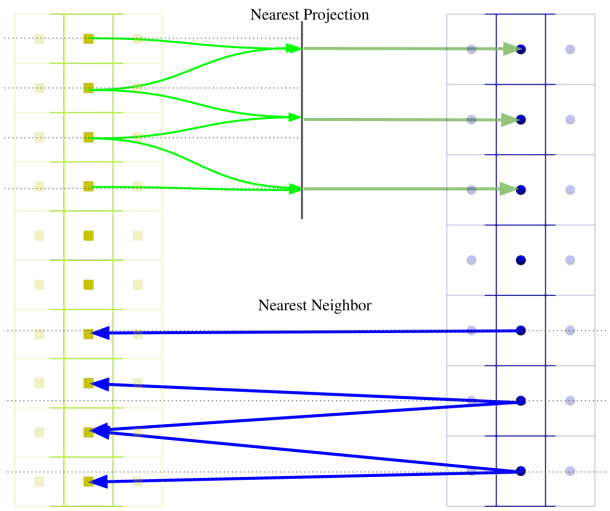

Figure 3.2: A schematic showing the two data mapping strategies used

Further, the mappings have two different types of constraints so as to account for mapping between non-conforming meshes. These are `consistent` and `conservative` [51]. The `conservative` mapping constraint aggregates the data to be mapped such that the total

amount of data coupled is the same on the two meshes. In the present work, we apply the `conservative` mapping constraint when mapping data from DEM to CFD. This ensures that the exactly same amount of heat, mass, and/or species source generated by the particles is injected into the CFD domain. Although, one has to be careful with non-conforming meshes. More discussions on how this mapping constraint affects the simulation results are in sections 3.5.4 and 5.6. The `consistent` mapping constraint is applied when mapping data from CFD to DEM. This constraint is applied for physical quantities such as temperature or velocities. This mapping constraint will apply the exact value seen on the originating mesh. In the applications under consideration, this mapping constraint can be very useful as the CFD-DEM coupling is unresolved. Depending on the mesh size differences, it can be enough to know the fluid conditions corresponding to the CFD cell center closest to the particle center.

This constraint can be quite limiting if the mesh size difference between CFD and DEM is large. This mapping constraint can also be limited if we see large gradients in physical values over a distance shorter than particle diameter. These limitations can be counteracted by employing the `radial basis function` mapping instead of either methods mentioned above. Although this method will give more accurate mapping and, thus more accurate simulation results, this method is more costly. In the current work, the CFD and DEM cell size disparity is almost non-existent (for single particle cases) or very minor (for packed bed case).

3.4.4 Coupling Strategies

It is very important to consider the type of coupling needed for a given problem. A further restriction of the monolithic coupling approaches is that the application hence the type of coupling strategies are predefined. This can lead to two issues, either the coupling strategy used is okay but might lead to additional costs or the coupling strategy is ill-suited for a new problem.

In this section, we briefly discuss the coupling strategies available for the presented partitioned coupling. There are two main distinct coupling strategies available for partitioned

coupling approaches, broadly known as explicit and implicit. The explicit coupling strategy executes and calls the coupled solvers for a set number of coupling time steps, whereas the implicit coupling strategy is used when either the numerical solution is unstable or there is a need to completely capture the coupled solution. The reader is referred to the literature for in-depth reading [51, 88]. In the numerical experiments presented in the next sections, we only use the explicit coupling strategy. However, using the implicit coupling strategies could be used just as easily without any additional work.

3.4.5 Execution Strategies

Although parallelization and scalability are not the primary focus of this work, due to the computational costs involved in discrete methods, this issue is bound to come up. The current partitioned coupling approaches allow for the rapid development of heat and mass transfer simulation environments. Although this might allow to establish a multi-physics simulation environment required for a certain application, it is also important that it is scalable for the intended application. These simulations can be quite large when considering industrial scale applications.

In the classical monolithic coupling approach, each set of equations describing one of the physics involved is executed consecutively or serially. These equations might be parallelized, but their execution is serial. This leads to the computing resources being idle. The different execution strategies are illustrated in figure 3.3. Figure 3.3 (a) and (b) illustrates respectively the execution of the monolithic coupling and the serial execution of partitioned solvers. In terms of solving the equations, they tend to behave similar to each other. However, in our monolithic approach, the two physics are coupled into a single executable, they share the data on the memory, that is used to exchange the information between the solvers. On the contrary, for the partitioned execution, the exchange of data is handled through the preCICE coupling library leading to extra memory copies and communications. Another downsides to partitioned coupling approach when considering data exchange, is that the data for the entire coupled domain needs to be transferred as opposed to exchanging data only where particles are located in the monolithic approach. This is discussed further in section 3.6.

Figure 3.3 (a) and (b), in terms of the execution, there is not much difference apart from the way the information is shared. The big difference comes in the parallelization of individual solvers. In the monolithic approach, as the equations are intermingled, the domain needs to be divided exactly the same way for both the solvers, so as to ensure solver stability and reduce inter-processor communication times. Hence the co-located partitioning approach [86] is used for the monolithic solver. In contrast, for the partitioned coupling approach, the domains for each solver can be divided as the need arises. The communication between each rank is computed and only relevant ranks are connected via preCICE [88]. This feature plays an important role when there are non-conforming domains/meshes involved in the coupling, which is the case for most real-world applications.

Furthermore, figure 3.3 (a) and (b) demonstrates another fatal flaw of this type of execution, i.e. wasting computing resources by idling. As the solvers execute one after the other, one solver always has to wait for the other solver to finish. Consequently, a parallel execution strategy can be utilized to avoid this problem, as illustrated in figure 3.3 (c). Here, both solvers are executed simultaneously. In this example, we see that the DEM solver requires more time, hence the CFD solver computing resources stay idle, but the overall idle time as compared to the serial execution is less. This problem of idling can also be solved by further load balancing.

3.5 Results

In the present work, we use simple fundamental test cases to demonstrate the robustness of the partitioned HMT coupling between CFD and DEM. Along with the simple cases, we also study the drying process of a packed bed [154] to demonstrate the coupling with a large number of particles. To validate and verify the coupling, we compare the simulation results from the current coupling methodology with experimental results and simulation results from legacy CFD-DEM (XDEM). The current work only focuses on convective heat transfer between particles and fluid, as inter-particle heat transfer has been extensively studied in previous work [147, 21].Conduction and radiation between particles and fluid can also

be modeled similarly, but for the current cases their contribution is insignificant, hence we ignore these heat sources.

The XDEM + OpenFOAM preCICE coupling uses OpenFOAM v7 [100]. However, XDEM + OpenFOAM legacy coupling uses FOAM-Extend v3.2 [155], which is a fork of OpenFOAM. This different implementation might lead to minor numerical differences in the results, however the underlying physical models are identical. The software used for legacy coupling are a modified version of foam-extend 3.2 (git hash $3912d19b$) and XDEM (git hash $fd06b8a0$). The preCICE coupling uses OpenFOAM 7, XDEM (git hash $a6f0b7f9$) and preCICE 2.5.0. The simulations are carried out on the *Aion* cluster at the University of Luxembourg that offers 354 computing nodes, consisting of two AMD Epyc ROME 7H12 2.6Ghz processors accounting for 128 cores per computing node, each equipped with 256 GB of memory.

3.5.1 Heat Transfer only: Single particle heat-up

In the heat transfer only case, we consider one particle at room temperature heating up due to the hot air surrounding it. The CFD domain is $0.02 \times 0.02 \times 0.1$ m in size, discretized into 5 cells in the vertical direction only (uniform 3D Grid $1 \times 1 \times 5$). The air inside the fluid domain is at 1123 K and atmospheric pressure is $1e+05$ Pa. The air enters from the bottom of the CFD domain with 0.38 m/s and a temperature of 1123 K, mimicking the experimental setup in [156]. The air exits the CFD domain from the top.

The DEM domain contains a dry spherical Beech wood particle of diameter 0.02 m, with wood properties found in Table 3.2 [144]. The particle is discretized radially into 30 uniform segments for 1D HMT computations within the particle. The particle is at 300 K at the beginning of the simulation. The particle is located at $(0.01, 0.01, 0.05)$ m and it remains stationary throughout the simulation.

In this numerical experiment, the Wakao [153] model is used to compute the heat transfer coefficient.

Properties	**Beech wood** [154]	**Fir wood** [157]
Density ρ (kg/m^3)	750	330
Porosity ϵ (-)	0.64	0.6
Pore diameter	50×10^{-6}	50×10^{-6}
Specific Heat c_p (J/kg K)	2551.3	1733
Conductivity λ (W/m K)	0.47	0.2

Table 3.2: Physical properties of the wood particles

Heat transfer case results

Figure 3.4, we see the temporal evolution of the CFD domain and particle surface temperature. Figure 3.4 and 3.5 show that the particle uses thermal energy from fluid to heat up. This drain of thermal energy leads to a drop in the air temperature downwind. As the particle heats up, the rate of heat transfer drops, and we see that the air temperature downwind gradually increases, although it remains somewhere between the CFD inlet temperature and the particle surface temperature. From figure 3.5, we see that the particle surface temperature comes close to the fluid temperature. These results demonstrate how two-way HMT coupling works, as we see the effects of fluid conditions on the particle and the effect of the particle on the fluid temperature field. Figure 3.5 also shows the drop in fluid outlet temperature. The sudden initial drop-off in fluid outlet temperature is because the results for fluid are recorded every 10 s, starting at 10 s.

Figure 3.5 and 3.6 show the particle surface and center temperature evolution over time. The current results are compared with the XDEM-OpenFOAM legacy coupling which has been thoroughly verified and validated against experimental results. Figure 3.5 and 3.6 shows that the temperature evolution of the particle for XDEM + OpenFOAM preCICE coupling is in good agreement with XDEM + OpenFOAM legacy coupling.

We can see that the temperature profile is in very good agreement, but we see a minor difference in the numerical results. This is because we use different OpenFOAM versions.

Figure 3.5 and 3.6 shows that the XDEM + OpenFOAM preCICE coupling simulation results, specifically the particle surface and particle center temperatures are in good agree-

ment.

As there is no experimental data for the heating up of a single wood particle, we use the experimental results by Petek [156]. The simulation setup mimics the experimental setup, the only difference being the current case does not simulate any chemical reactions (pyrolysis). In figure 3.7, the simulated surface temperature of the particle closely follows the experimental observations, but the numerical results under-estimate the particle surface temperatures. This is to be expected as the majority of the chemical reactions are taking place within the particle as compared to on the particle surface. On the contrary, the numerical results presented here are only for particle heating. The numerical model assumes spherically symmetric temperature distribution, using one dimensional model for temperature distribution in radial direction. Due to this assumption the particle is uniformly heated in the numerical simulation, thus showing lower surface temperatures between 0 s and 75 s as compared to experimental observations.

Furthermore, as the presented case is simple, we utilize the same initial and boundary conditions and get an analytical solution for the heat-up of the particle. As this is an analytical solution, and the particle diameter is not discretized as shown in figure 6.1, thus we only have the analytical solution for the overall particle temperature. The numerical result of the mean particle temperature is compared with the analytical solution in figure 3.7. The numerical results are in good agreement with the analytical solution.

3.5.2 Heat & Mass Transfer: Drying of Fir wood particle

In the previous section, we establish that the $2-$way heat transfer between the CFD and DEM is working well. In the current section, we want to see the effects of this heat transfer on the composition of the particle. Particle drying is selected to validate the mass transfer as the moisture content in the particle and water vapor after evaporation stays stable, i.e. does not react with the surrounding fluid. Thus it is easy to track, in experiments as well as in simulations.

In this numerical experiment, the Wakao [153] model is used to compute the heat, mass, and specie transfer coefficient.

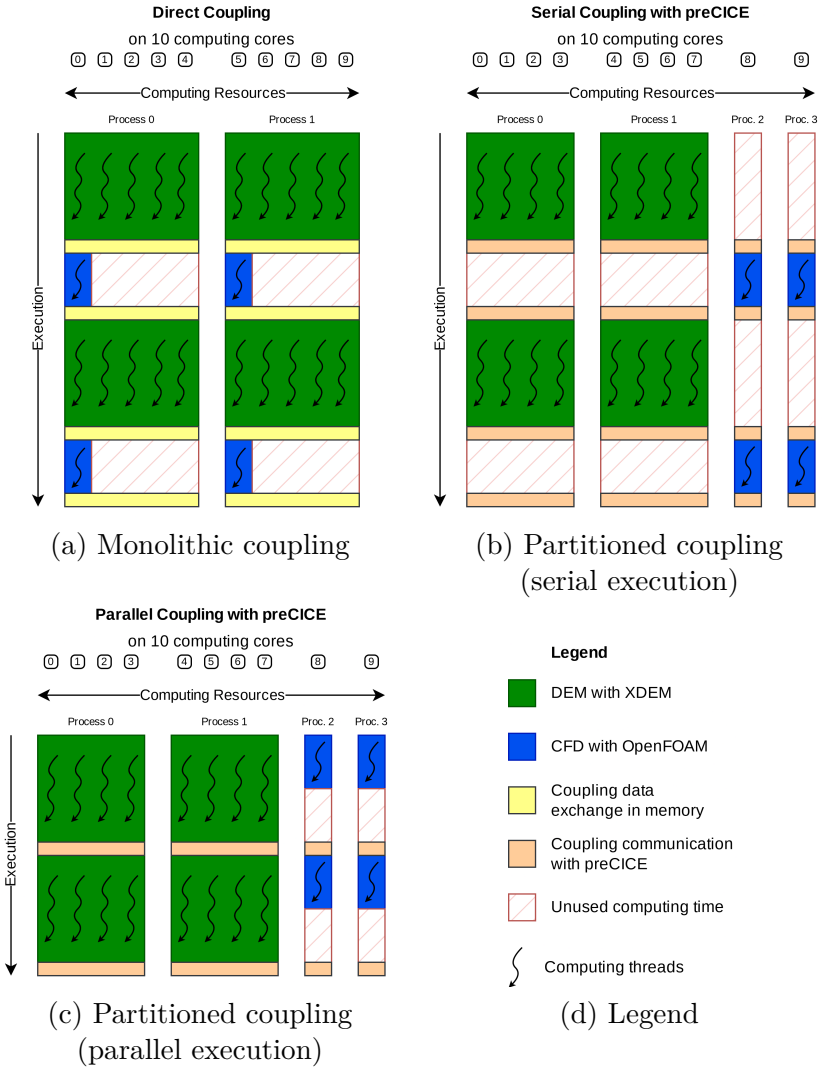

(a) Monolithic coupling

(b) Partitioned coupling (serial execution)

(c) Partitioned coupling (parallel execution)

(d) Legend

Figure 3.3: Comparison of the coupling and execution strategies

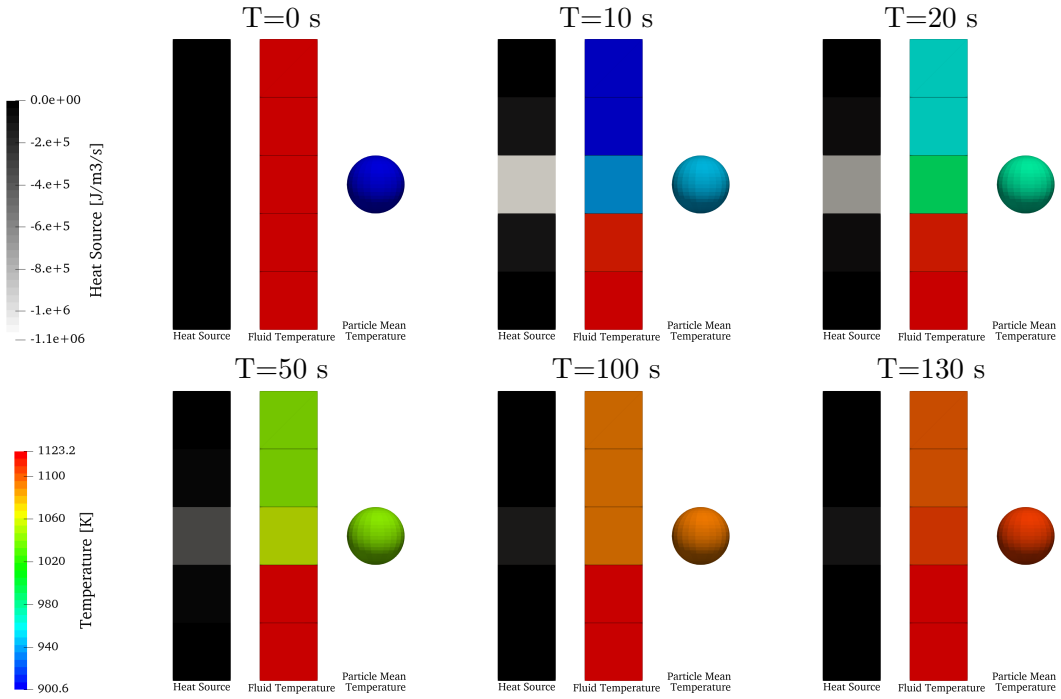

Figure 3.4: Fluid fields demonstrate the effect of the presence of cold particle heating-up

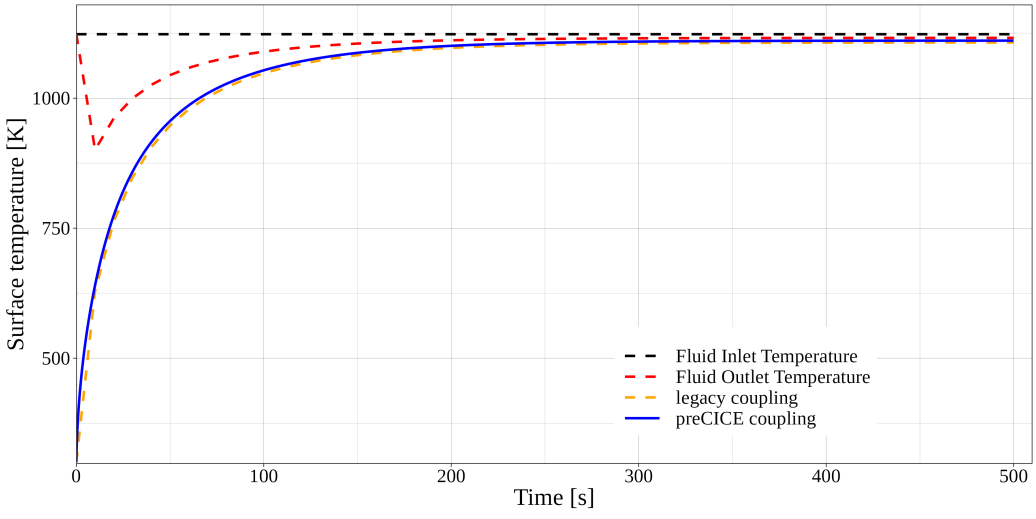

Figure 3.5: Influence on fluid temperature due to the presence of particle plotted along with the surface temperature of the particle

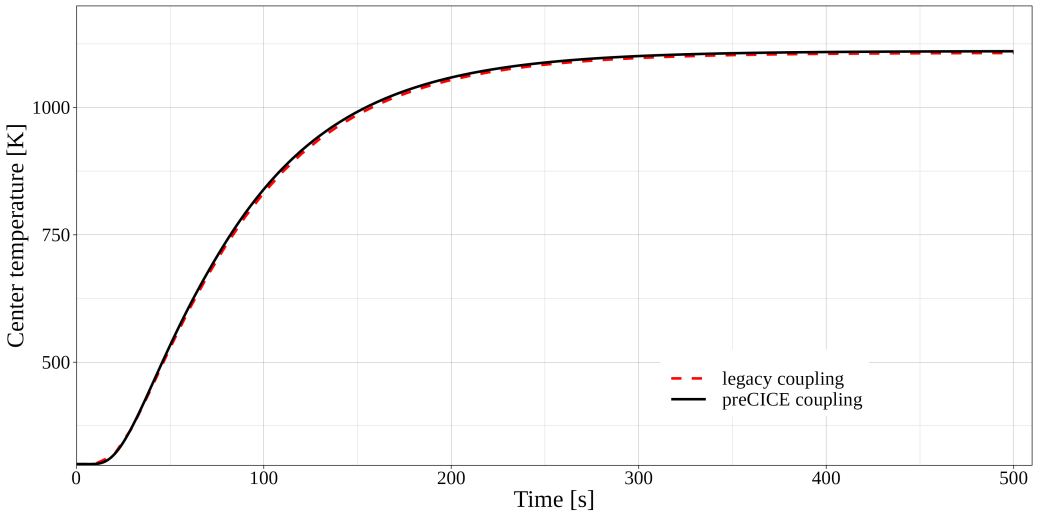

Figure 3.6: Temperature at the center of the particle compared for two different couplings

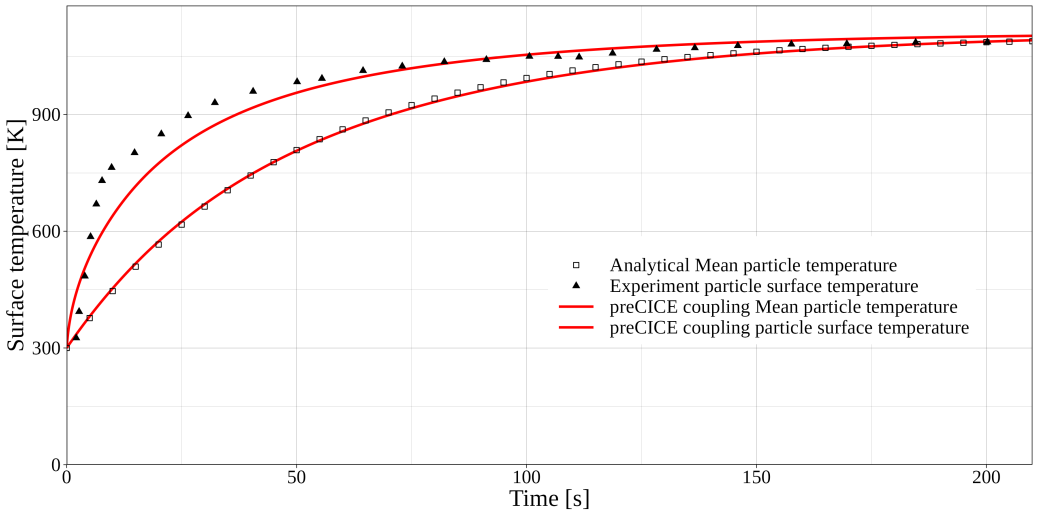

Figure 3.7: Particle surface and mean temperatures compared against experimental observations [156] and analytical solution resp.

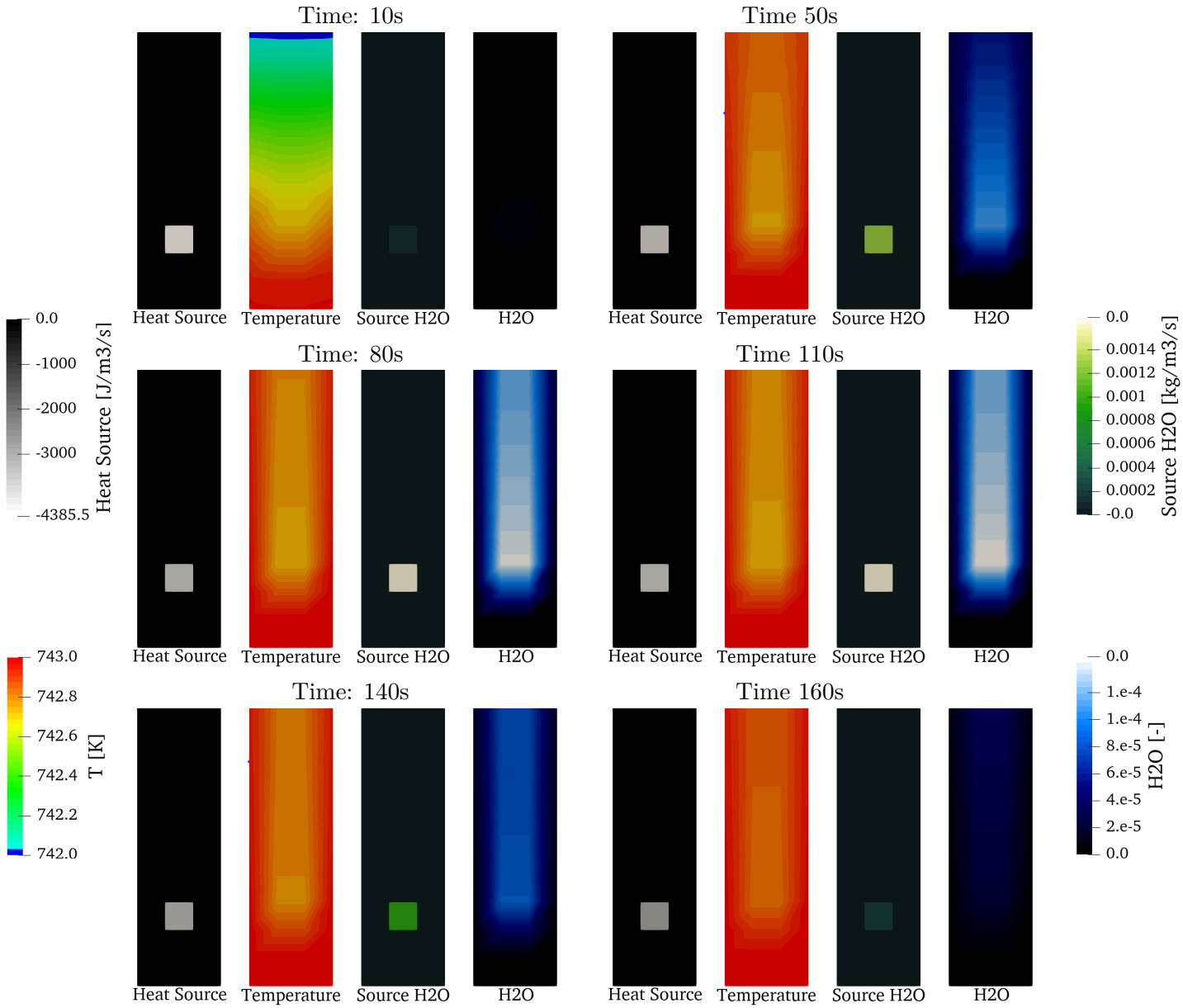

Figure 3.8: Evolution of heat source, fluid temperature, water vapor source, and water vapor mass fraction over time in the CFD domain showing drying process of wet particle.

In the heat and mass transfer case, we consider drying a spherical Fir wood particle with properties given in Table 3.2 [157] with some moisture content. The simulation set-up conditions mimic the experimental setup by B. Peters [157]. The experiments were performed with Fir wood particles with 33% and 66% moisture content. In the current work, we perform two simulations with these two different initial moisture content. The CFD domain is $0.15 \times 0.15 \times 0.5$ m in size, discretized uniformly as $3 \times 3 \times 10$. The air inside the fluid domain is at 743 K and atmospheric pressure is $1e+05$ Pa, air enters from the bottom of the CFD domain with 0.28 m/s and a temperature of 743 K. The air exits the CFD domain from the top.

The DEM domain contains a Fir wood particle of diameter 0.008 m, located at $(0.075, 0.075, 0.125)$ m. The particle is discretized radially into 21 uniform segments for 1D HMT computations within the particle. The particle is at 297 K at the beginning of the simulation.

In the current study, the heat sink model (constant evaporation model) is applied for the calculation of drying rate [154, 157]. The model is described as follows:

$$\dot{w}_{H_2O} = \begin{cases} \frac{(T-T_{evap})\rho c_p}{H_{evap}\delta t} & \text{if } T \geq T_{evap} \\ 0 & \text{if } T \leq T_{evap} \end{cases} \tag{3.18}$$

where ρ and c_p are the density, and thermal capacity of the dry wood, H_{evap} is the evaporation enthalpy. In this drying model, the evaporation temperature T_{evap} is utilized for evaporation without distinguishing between free and bound water.

Heat and mass transfer: Drying case results

Figure 3.9 shows a comparison of the moisture content of numerical simulation with experimental observations for the Fir wood particle. In figure 3.9, the triangles and the circles represent the experimental results [157]. The solid and small dashed lines represent the moisture content of the particle for the XDEM + OpenFOAM preCICE coupling over time. Drying is described as evaporation due to energy balance in conjunction with a given evaporation temperature for the current work. We see that these simulated moisture contents of the wood particle is in good agreement with the experimental results. Whereas for the case with

66% initial moisture, as seen in the figure 3.9, the mean particle temperature goes beyond the water evaporation temperature (373K at atmospheric pressure) and remains their from $\sim$ 75 s to $\sim$ 175 s. Because of this we initially see comparatively lower evaporation in the simulated results as compared to the experimental observations. Finally, at around 175 s, the evaporation of water matches the experimental observations, but we see comparatively accelerated evaporation due to higher mean particle temperature. Although the residual moisture mass fraction does not exactly match the simulated results for the 66% initial moisture content, the results are in good agreement as the overall evaporation time and profile are similar.

We also compare the XDEM + OpenFOAM preCICE coupling to XDEM + OpenFOAM legacy coupling and we see that the results are almost identical. In Figure 3.10, the mean temperature of the particle is compared for the different coupling approaches. We can see that the temperature profile for 33% moisture content in the particle is almost identical for the different coupling methods, and the temperature profile for 66% moisture content in the particle is in very good agreement for $2/3^{rd}$ of the simulated time, with minor differences towards the end.

In Figure 3.8, we see various fluid fields at different stages of time. A negative heat source is seen on the fluid side, which denotes that thermal energy from the fluid is siphoned off to heat the particle. This is confirmed by the drop in air temperature downstream of the particle location. As the particle heats up, the thermal energy is used to evaporate the water in the wood particle. This water vapor is being injected into the fluid domain. We confirm the injection of water vapor from the particle into the fluid domain by observing the transport and diffusion of the water vapor downstream.

3.5.3 Heat & Mass Transfer: Pyrolysis of Beechwood particle

In the two previous sections, it is thoroughly established that the 2-way Heat & Mass Transfer coupling between CFD and DEM works well. In the previous section, where we simulate the drying process, although the particle loses mass, there are no changes in the chemical composition of the particle. In the current case, this is exactly what is achieved. The CFD domain is $0.02 \times 0.02 \times 0.1$ m in size, discretized into 5 cells in the vertical direction only

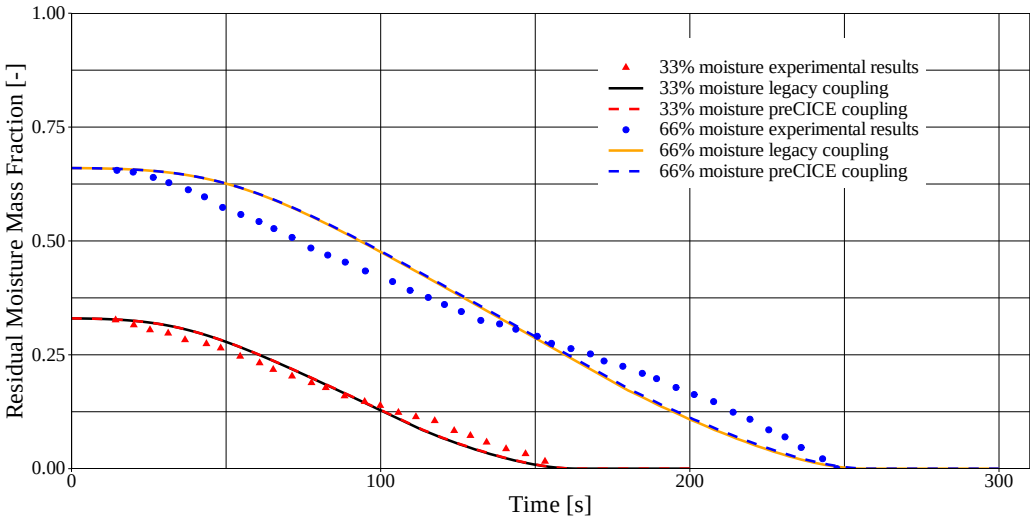

Figure 3.9: Particle drying simulations compared with experimental drying observations for different initial moisture content in the particle

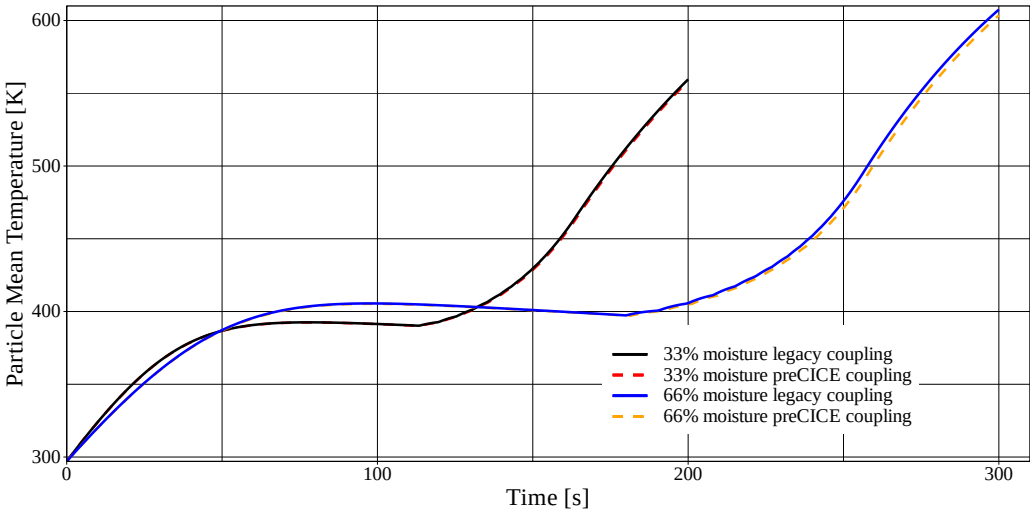

Figure 3.10: Comparison of the evolution of particle mean temperature over time for different coupling and different initial particle moisture content

(uniform 3D Grid $1 \times 1 \times 5$). The air inside the fluid domain is at 1123 K and atmospheric pressure is $1e + 05$ Pa. The air enters from the bottom of the CFD domain with 0.38 m/s and a temperature of 1123 K, mimicking the experimental setup by Petek [156]. The particle undergoes chemical conversion described in the chemical reactions 3.19, 3.20 and 3.21. The air exits the CFD domain from the top.

In this numerical experiment, the Yang [152] model is used to compute the heat transfer coefficient, where as Wakao [153] model is used to compute the mass and species transfer coefficients.

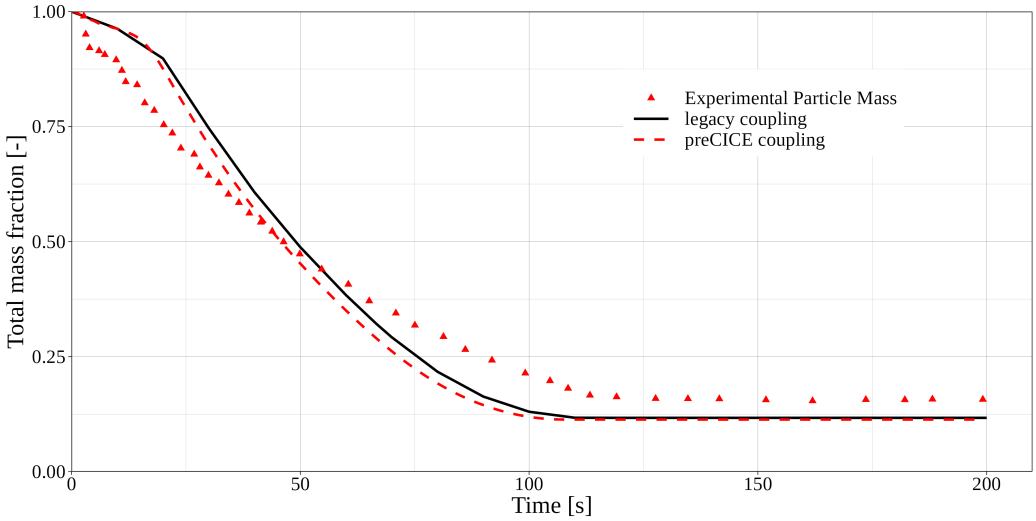

Figure 3.11: Comparison of the evolution of particle mass overtime for different coupling validated against experimental results of Petek [156]

Chemical reactions

In the present work, pyrolysis of a wood particle is simulated and validated against the experiments performed by Petek [156]. Pyrolysis is described with three independent reactions 3.19, 3.20 and 3.21 expressing the decomposition of wood into its main products char, tar and gases [147].

$$Wood \rightarrow Char \tag{3.19}$$

$$Wood \rightarrow Tar \tag{3.20}$$

$$Wood \rightarrow 0.156 \cdot CO + 0.271 \cdot CO_2 + 0.521 \cdot H_2O + 0.021 \cdot H_2 + 0.031 \cdot CH_4 \tag{3.21}$$

Heat and mass transfer: Pyrolysis case results

The simulation results for particle mass loss due to pyrolysis are presented in figure 3.11 and validated against the experimental observations. The predicted particle mass loss is in good agreement with the experimental observations. The particle surface temperature and centre temperature simulation results are compared with the experimental observations in figure 3.12 and figure 3.13 respectively. The predicted particle surface and center temperatures are in good agreement with the experiments.

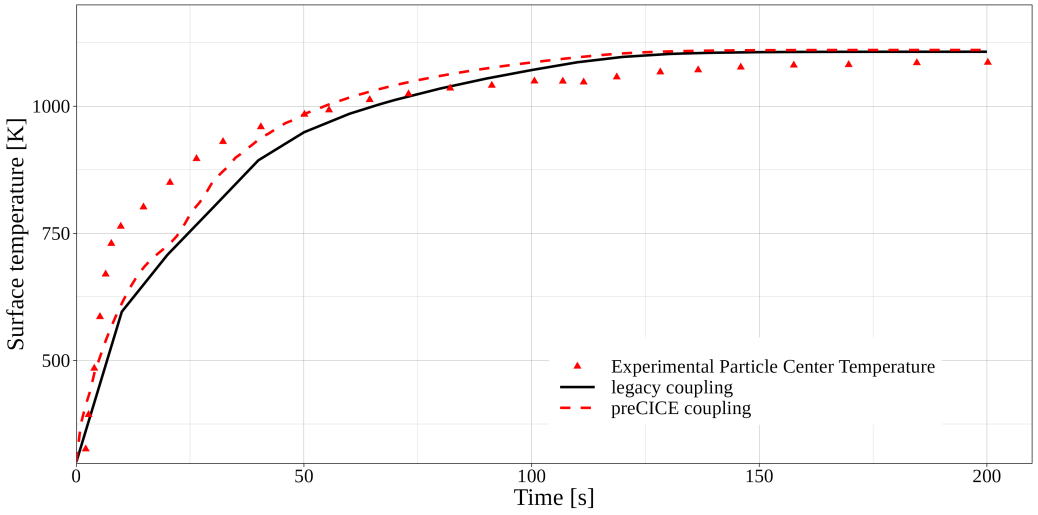

Figure 3.12: Comparison of the evolution of particle surface temperature over time for different coupling validated against experimental results of Petek [156]

From figure 3.12, it can be seen that the particle surface temperature for numerical simulation rises slowly as compared to the experimental observations, from 0 s to $\sim$ 80 s. The particle in the experiments experiences comparatively higher fluid velocities than the numerical simulations, as the particle in the numerical simulation occupy a comparatively lower

volume in the fluid flow. This is because the particles in the current numerical simulations are not fully resolved in the fluid domain. This higher fluid velocity leads to faster heat up during this initial time.

The two different simulations presented use two different coupling and dtata exchnge strategies. For the XDEM + OpenFOAM legacy coupling, the CFD-DEM coupled solver is developed specifically for such applications. In this specialized solver, the particles are represented as porosity (eq 6.9). Whereas for the XDEM + OpenFOAM preCICE coupling particles are represented as drag source term, in this case, momentum source term. As can be seen from the figure 3.12, XDEM + OpenFOAM legacy coupling has slightly different temperature than XDEM + OpenFOAM preCICE coupling. This can be caused due to the different way the effects of particles is modeled or due to the slight differences in the OpenFOAM implementations. We also see a similar phenomenon for the particle center temperature in figure 3.13.

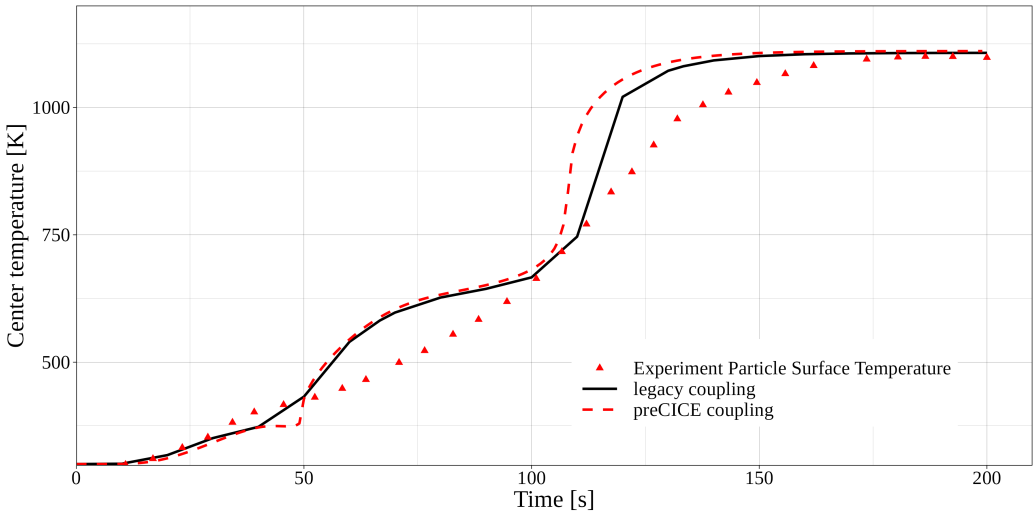

Figure 3.13: Comparison of the evolution of particle center temperature over time for different coupling validated against experimental results of Petek [156]

As the particle surface temperatures are higher for the legacy coupling, we also see a similar phenomenon for the particle center temperature in figure 3.13.

3.5.4 Heat & Mass Transfer: Drying of packed bed

The experimental data used for validation in the current case was obtained by Peters [154] on the test reactor Pantha. The reactor was set up to investigate heating-up, drying, and pyrolysis of packed beds. The experiments were carried out on around 2kg of air-dried $10\times10\times10$ mm^3 cubical Beech wood containing about 10% moisture by mass. The Beechwood is placed in a cylindrical bed of 250 mm diameter and 190 mm height. The simulation model is based on the experimental setup, a detailed description of the experimental setup is available in reference [154]. The experiments were performed using cubical particles, which are modeled as spheres of equal volume (particle radius = 6.2 mm). Thus the bed is filled with 2667 particles.The drying model described in equation 3.18 is utilized for the drying of the packed bed. In addition to the convective heat transfer, the particles also experience heat transfer through conduction.

In this numerical experiment, the Achenbach [150] model is used to compute the heat, mass and specie transfer coefficient.

The CFD simulation mesh can be seen in figure 3.14 (a) and the DEM simulation domain with particles within it can be seen in the figure 3.14 (b). An additional height of 80 mm and 60 mm on the top and bottom respectively.

The dimensions for the CFD domain are same as those mentioned above for the DEM model. The air enters the CFD domain from the top of the cylindrical, with a temperature of 423 K and a velocity of 0.113 m/s. The air exits the CFD domain at the bottom of the cylinder.

In the figure 3.15, the CFD domain and DEM domain are presented. These meshes are sliced to expose the cell centers that are used to exchange data.

Heat and mass transfer: Drying of packed bed case results

In the experiments [154], as the beech wood particles were heated up and dried, they were measured at certain time intervals to measure the mass loss. The evaporated moisture was also collected in a cold tube and weighed. These measurements were used for the mass balance in the experiments, are are to be used for validation of the current numerical simulation

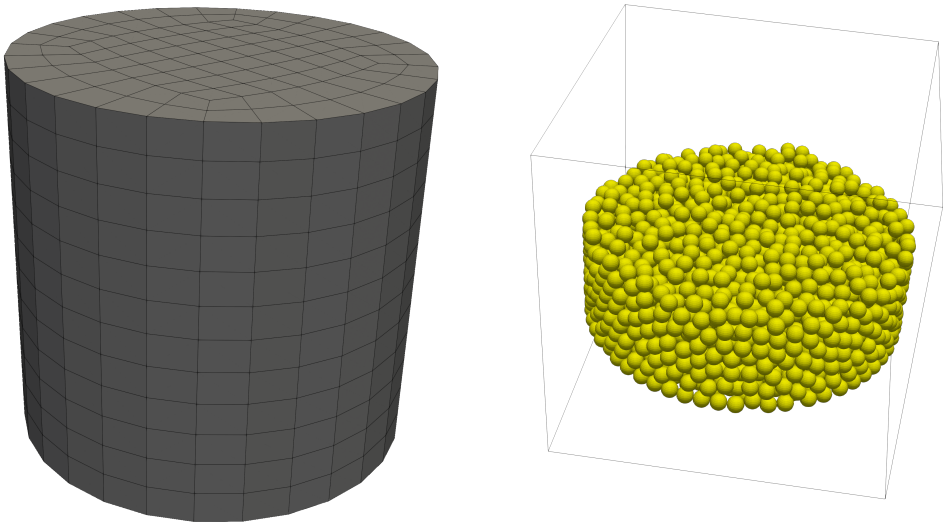

(a) CFD Mesh (b) DEM domain with wood particles

Figure 3.14: Simulation model for drying of packed bed

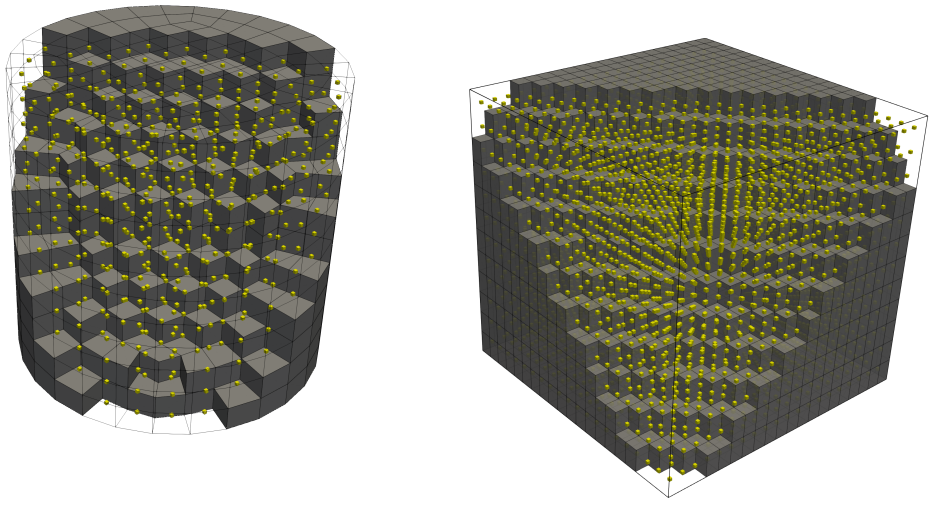

(a) CFD Mesh (b) DEM domain

Figure 3.15: CFD and DEM mesh sliced to show the cells and cell centers used for volume coupling

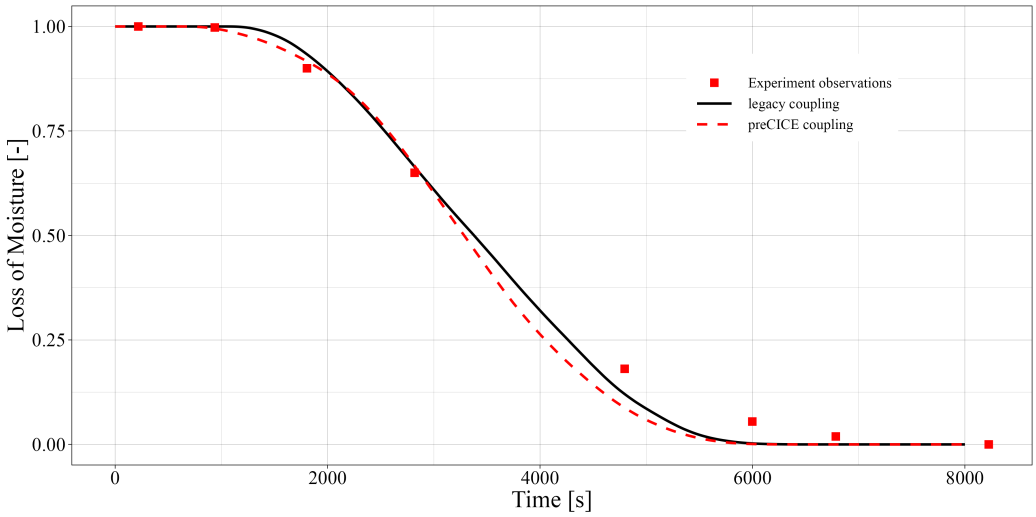

Figure 3.16: Comparison of the numerical simulation moisture content with the experimental observations

results.

The particle weights in the numerical simulation are integrated for each time step, so we have one value for the mass (or mass loss) of the entire packed bed. This is possible as we track the information for all the particles. Finally, in figure 3.16 we compare the dimensionless moisture loss from the current partitioned coupling strategy to the legacy CFD-DEM coupling as well as the experimental results. There is good agreement between the partitioned coupling approach numerical results with the experimental observations. We also see that the numerical simulation results from the current work agree with the experimental observations better as compared to the legacy coupling.

Additionally, the evolution of the moisture content (left column) and the mean temperature (right) of the packed bed is presented in figure 3.17 and 3.18 over 8000 s (same as experiment time). It is observed that the particles at the very edge start heating up more as compared to the particles in the center. Consequently, we see the drying of these particles first, as the particle temperature goes over the evaporation temperature. These initial pockets of concentrated heat in figure 3.17 are observed due to the `conservative` mapping constraint. This mapping constraint aggregates the heat source at the edges into the near wall, thus heating the particles at the edges faster than the centrally located particles. But

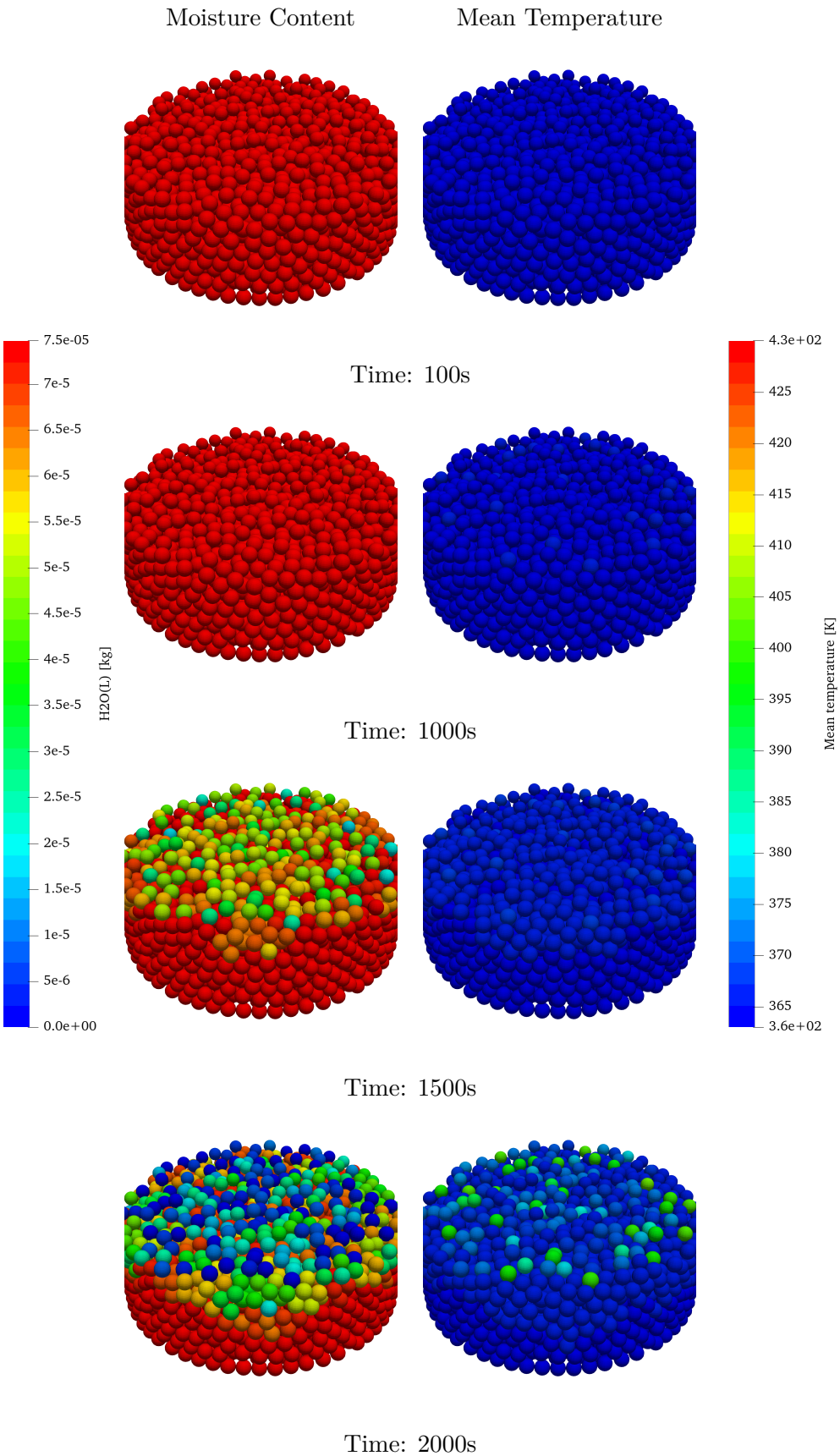

Figure 3.17: Evolution of particle moisture content and particle mean temperature from 100 s to 2000 s

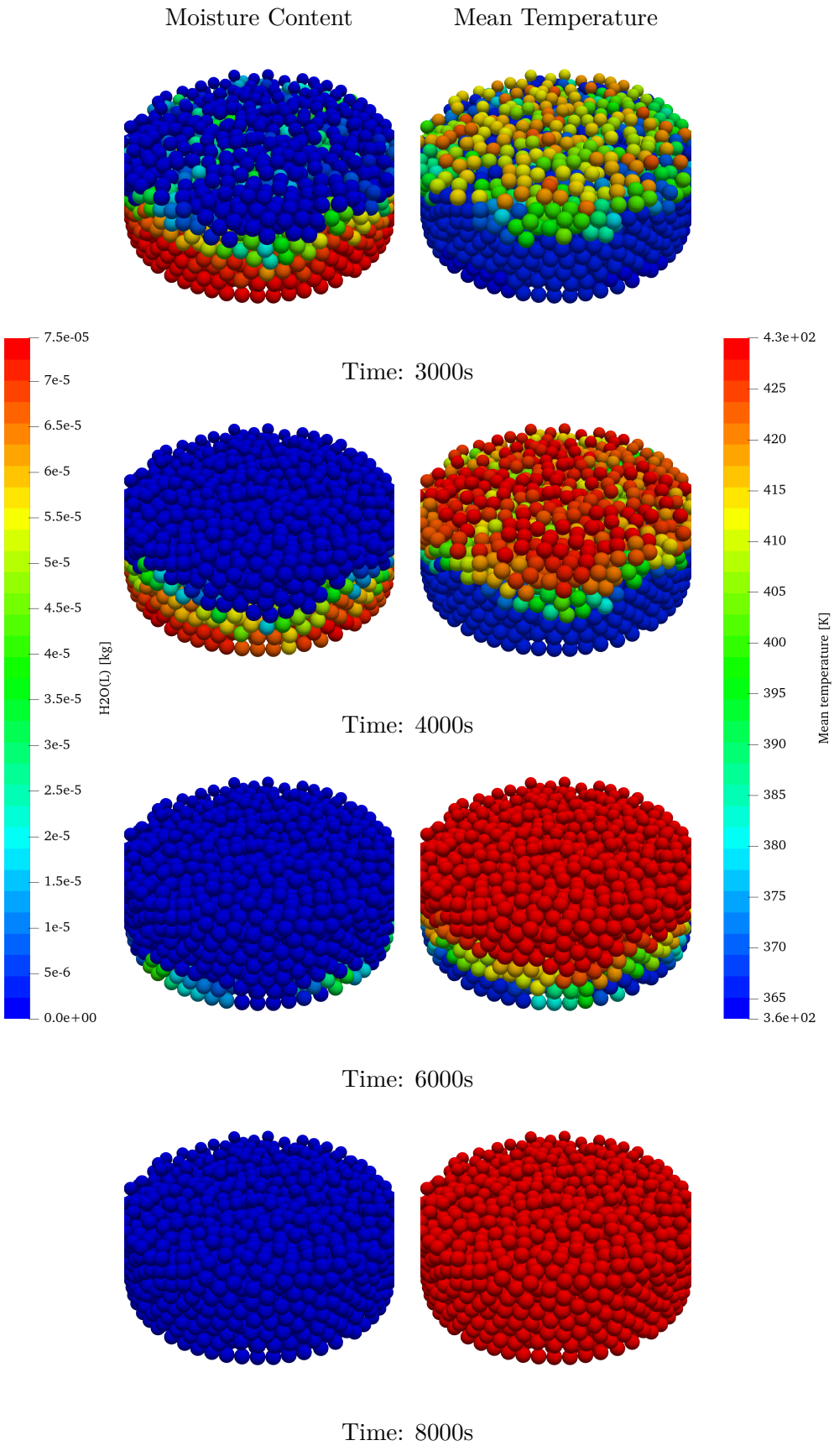

Figure 3.18: Evolution of particle moisture content and particle mean temperature from 2000 s to 8000 s

as time progresses, and the particles in the pockets on the edge reach a temperature similar to fluid temperature, the rest of the bed starts heating up. This behavior is similar to that we see in the numerical results presented in the literature [145]. As the particles

3.6 Performance study

The previous sections of the article sufficiently demonstrate that the CFD-DEM HMT coupling works well and the results agree with the experimental observations. Although the scope of this study is only the development and validation of the proposed partitioned coupling approach, the authors believe a brief performance study will round out the completeness and inform the reader well when choosing between monolithic and partitioned coupling approaches.

The XDEM suite allows two kinds of parallelization: coarse-grain parallelism with MPI and fine-grain parallelism with OpenMP. On their side, foam-extend and OpenFOAM only support MPI parallelization. The preCICE coupling library allows different coupling strategies: `serial` vs `parallel` and `explicit` vs `implicit`, as explained in the section 3.4.5 and illustrated in the figure 3.3. The `serial` type of couplings refers to staggered execution of the coupled solvers. On the contrary, the `parallel` type coupling allows the coupled solvers to execute simultaneously, allowing functional parallelism. The `explicit` type of coupling only executes once per coupling time step whereas `implicit` refers to the type of coupling where the coupled solvers execute until convergence. In the present work, `serial-explicit` and `parallel-explicit` coupling schemes are utilized. To summarise, the legacy coupling implementation behaves in the same way as `serial-explicit` preCICE coupling, where each coupled solved is executed in a staggered way.

Furthermore, it is to be noted that the load balancing is dependent on the case and its configuration. To illustrate this point, we present a performance study for the Pantha case in its original form and the Pantha case where the number of particles and CFD cells are increased. For the performance study, we only simulate 100 s, as this is enough to get performance behavior. This is because we have a constant number of particles throughout

the simulation, and they do not move.

3.6.1 Performance evaluation of packed bed

In the Pantha simulation case presented in section 3.5.4, the packed bed contains only 2667 particles, thus the use of a single computing node with 128 cores for XDEM is sufficient. On the CFD side, the CFD mesh is composed of 1260 cells, hence it does not warrant using parallel execution and it is executed sequentially.

In the figure 3.19, we compare the legacy coupling with the preCICE coupling. In the figure 3.19 (a), (b) and (c), the XDEM is executed using 16 OMP threads, whereas in the figure 3.19 (d), (e) and (f), XDEM is executed using 64 OMP threads. The blue column in all the plots signifies the execution time needed for XDEM, whereas the green column represents the execution time for the OpenFOAM. As the legacy coupling is implemented as a monolithic solver, the CFD and DEM solvers are executed one after the other. The data exchange or the coupling is done over a shared memory. Hence, we do not record a separate coupling time, it is included in the XDEM execution time. However, the execution times for XDEM can be assumed to be same for both couplings, and be used to get the coupling time.

On the contrary, for the preCICE coupling, the execution time for XDEM, OpenFOAM, and total time are recorded. The red column representing preCICE contains all the time not spent on XDEM and/or OpenFOAM execution. Consequently the red column representing preCICE cost, includes data exchange, data communication through sockets/network, interpolation of data between meshes, mapping data, and synchronization between the solvers/processes. The time required for the mapping for the `serial-explicit` and `parallel-explicit` are the same. However, it should be noted that the synchronization time, hence the preCICE time also includes the time a solver is waiting for the other solver to finish and proceed.

It is apparent from these figures that for the case under consideration, preCICE coupling costs are quite significant. For this case, preCICE coupling takes almost twice as much time as required by the legacy coupling. It is to be noted that although the original case set-up remains identical for the two couplings, the legacy coupling uses the CFD mesh for coupling (containing 1260 cells), whereas preCICE considers both CFD mesh and DEM

domain discretized as seen in figure 3.15, which has 4800 cells. This issue is addressed in the next section.

In figure 3.19 (c) and (f), the OpenFOAM and XDEM are executed simultaneously using the `parallel` coupling, hence they are plotted side-by-side. The light colors for each solver signify the idle/waiting time for the respective solver. It can be seen in the figure 3.19 (c), XDEM takes more time overall than OpenFOAM, hence the OpenFOAM ends up waiting for XDEM. In contrast, when we use more computing cores for XDEM, as seen in figure 3.19 (f), XDEM ends up waiting for OpenFOAM. Due to the nature of the computational load, we see a minor performance gain when using `preCICE-parallel` as opposed to `preCICE-serial`.

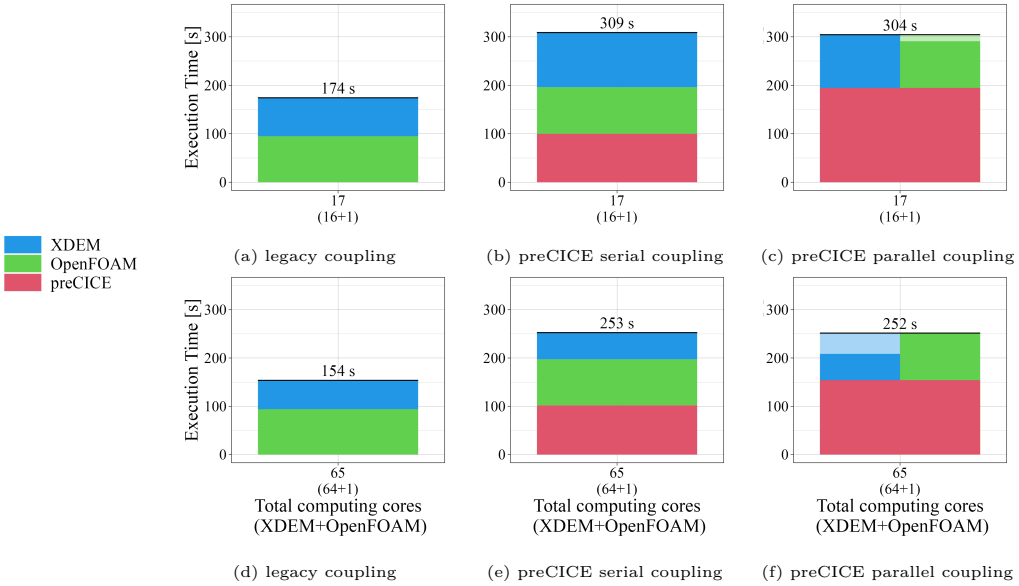

Figure 3.19: Performance comparison of the Pantha case for the legacy coupling vs the preCICE serial and parallel coupling

3.6.2 Performance evaluation of large packed bed

Through the literature [90], it is known that load balancing for the multi-physics coupled simulations is challenging and dynamic depending on various factors. In the previous section 3.6.1, it seems like preCICE is performing poorly as opposed to the legacy coupling. Hence, we extend the Pantha drying case to have more particles and CFD cells for a numerical

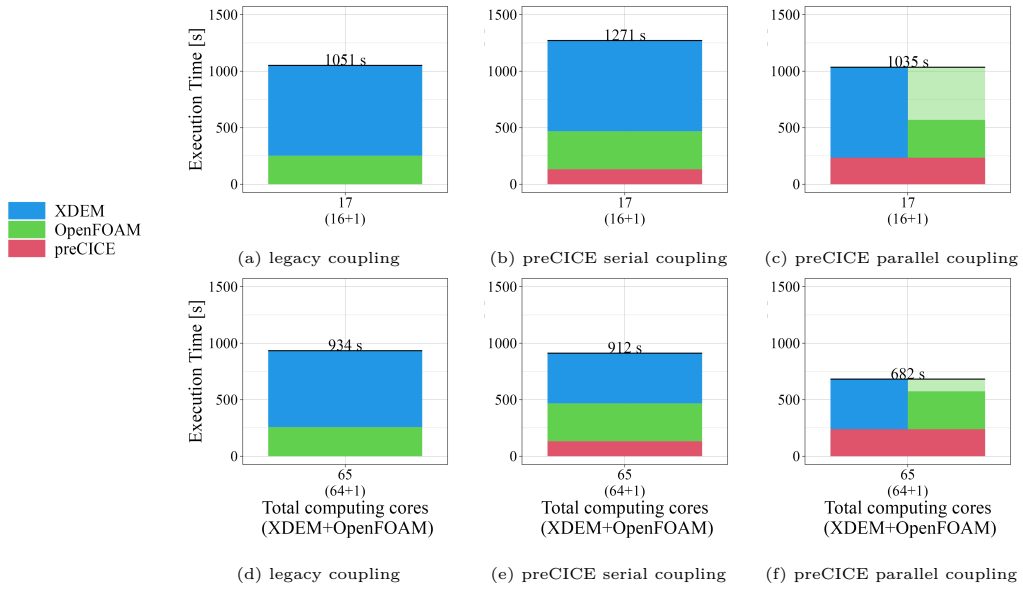

Figure 3.20: Performance comparison of the large case for the legacy coupling vs the preCICE serial and parallel coupling

experiment. This still keeps the underlying physics the same while allowing the study of performance for a computationally heavier case. The particle sizes are reduced, and we pack $23,999$ particles in the domain. The CFD mesh is further discretized to have $4,800$ cells.

The legacy coupling only uses the CFD mesh to exchange data (only 1260 cells previously). On the contrary, the preCICE coupling has to map data between CFD mesh (1260 cells) and DEM grid (4800 grid cells), thus incurring more cost in data mapping/exchange. Hence giving a hidden advantage to the legacy coupling. In the current section, due to the finer CFD mesh, the data mapping/data exchange costs for the legacy and preCICE coupling can be said to be similar as they both have to use a CFD mesh with 4800 cells.

Figure 3.20 shows the performance for the different coupling. The first notable observation when comparing figure 3.20 (a) versus (b) and (d) versus (e), is that with the scaled-up cases, the legacy coupling and preCICE serial coupling are closely matched. Furthermore, the increased load shows the disparity between staggered and simultaneous execution. The figure 3.20 (c) and (f), shows that the simultaneous execution of the solver gives a substantial performance advantage. As the CFD load is still quite small compared to the DEM load, it

can be seen that the CFD solver spends a lot of time idling, especially in figure 3.20 (c). As the number of computing resources is increased, this idling time is reduced in figure 3.20 (f), but still present.

An additional note regarding the execution times for the OpenFOAM solvers in figure 3.19(a,d) & (b,e) and figure 3.20(a,d) & (b,e), differ slightly as the implementations for the different versions of OpenFOAM are different, although they capture the underlying physical similar or same as each other. This slight difference in implementation is considered to be the reason for differences in execution times.

3.7 Discussion

The results presented in the sections 3.5, illustrate beyond any doubt that the partitioned coupling approach presented in this work can capture the multi-physics behavior. The minor differences in the numerical results between the legacy coupling and the proposed partitioned coupling are to be expected due to the different implementations of the OpenFOAM used along with the different data mapping strategies.

In our study, we compared the results of the partitioned coupling approach to experimental data, as well as with the numerical simulation results obtained using the monolithic legacy coupling. The results are in good agreement with the experimental observations as well as the legacy coupling. This is the case for simple single-particle cases as well as packed beds. Although the monolithic coupling approach is more robust, the partitioned coupling approach is able to capture the same physics with similar accuracy.

The volumetric coupling employed uses a simple grid on the DEM solver to exchange data to and from to the CFD solver. Hence, even when employing unresolved CFD-DEM coupling, the CFD mesh size is no longer dependent on and limited by the largest particle. This opens up avenues to explore applications in need of refined CFD mesh smaller than the particles without the need to use resolved CFD-DEM coupling.

Along with the verified and validated numerical results, this type of coupling gives us the advantage of modularity and flexibility. As the solvers are not intermingled, one solver can

be easily swapped out for the other. Furthermore, we would like to point out that now the software language is also no more a restriction. Highly optimized solvers are usually developed in C++, whereas experimental and research implementations are done in MatLAB or Python, or similar high-level language. Using the preCICE coupling library these solvers implemented in different programming languages can be coupled without any intrusion. Although it is possible to implement monolithic solvers with some functionalities presented in the coupling section 3.4, the amount of work needed to do so is substantial. This work demonstrates that single-physics numerical solvers can now be coupled with another single-physics software to achieve a coupled multi-physics simulation environment.

Additionally, the performance study for a packed bed is presented. With the two cases presented, we show that the performance is dependent on case to case, and the computational resources allocated. It is also shown that the partitioned coupling approach scales well, and performs just as well as the legacy coupling or even better when executing the solvers simultaneously. Hence, the proposed coupling approach can be utilised for large scale simulations without suffering additional costs for coupling (data interpolation, mapping, exchange etc.).

There are also restrictions on partitioning when using monolithic coupling. Often in the monolithic coupling approach, there domain decomposition of the involved solvers needs to conform. This limits the size of subdomains, and requires collocated domain partitioning strategy [86]. Apart from the issue of non-conforming meshes, as presented in section 3.6 there might be cases where the partitioning and resource allocation needs of the two involved solvers are different. When employing partitioned coupling, the parallelization capabilities of the individual solvers can be utilised to the fullest. The best domain decomposition for each involved solver can be used, imposing no restrictions on subdomain size or collocation. The subdomains for each rank in the first solver are directly connected to the respective ranks in the second solver [88].

The monolithic coupling approach solves the set of equations in the same solver. This means that the easiest steering strategy is for both the solvers involved have to use the same time-step. This time-step is usually dictated by the unstable solver, where reducing the time-step size leads to stability. However, due to this simple approach, one solver is

executed at lower time steps and penalized in computational time due to the unstable solver. It is indeed possible to do additional implementations so that the individual models/solver can utilize independent time-steps, but this requires significantly more work on part of the developer/researcher. When using the preCICE library for partitioned coupling approach, the individual solver time steps are independent of each other, however, they cannot be more than the coupling time-step i.e. the time-step used to exchange data. This way, the stable solver can retain its time-step, while the unstable solver can utilize a lower time-step for stability. Furthermore, more computational resources can be allocated to the solver with a lower time-step, to balance the computational load.

The current approach solves several issues faced in the state of the art for the development of coupled simulation environment. With this work, the authors intend to demonstrate the capabilities and flexibility of using the partitioned coupling approach. We believe that our findings will be useful for researchers and practitioners working in the field of particulate matter processes, particularly those interested in modeling CFD-DEM multi-physics simulations.

As a part of future work, this HMT coupling is to be applied to large-scale applications such as blast furnaces and biomass furnaces. A thorough study of the performance and the load balancing challenges using this partitioned coupling approach is to be done [90]. These cases also involve the motion of the particles along with the heat and mass transfer processes.

3.8 Conclusion

In this work, we present the rapid development of the simulation environment for HMT coupling between CFD and DEM. With the flexibility from preCICE, a user can switch the CFD solver for a preferred one or they can modify OpenFOAM solvers for preferred functionality. In any scenario, this kind of coupling allows the user to test out HMT coupling between particles and fluids. The user may use their own tested, proven, validated CFD or DEM solver to replace the software used in this work to achieve CFD-DEM coupling and simulate desired HMT processes. With the presented results, it is seen that the flexible

CFD-DEM black box coupling has similar if not the same results as a specialized CFD-DEM solver. The numerical results are in good agreement with the experimental observations.

Heat and mass transfer modules are added to the XDEM and OpenFOAM adapters with relevant required data fields to be exchanged. This enables the rapid development of a multi-physics environment for HMT between particles (DEM) and fluids (CFD). Simple cases are employed to prove that the HMT coupling is working properly. The numerical simulation results are validated against the experimental results, and they are in good agreement. Thus proving HMT coupling using preCICE works i.e. two-way HMT coupling between CFD (OpenFOAM) and DEM (XDEM). This opens up opportunities for the simulation of HMT processes such as drying, gasification, combustion, and pyrolysis.

In the HMT validation case, we use chemical species H2O, O2, N2, but our adapter also supports other species such as CH4, CO2, CO, H2, Tar commonly used in the biomass combustion process, or iron making processes. Although these species cover a wide range of applications, one might still need to use many different chemical species. We are working on automating the exchanged species based on fields defined in the preCICE configuration. This work was limited to HMT applications involving gaseous fluid mixtures. To simulate processes such as melting, and phase change, the OpenFOAM adapter, XDEM adapter, and XDEM have to be updated to handle multi-phase Euler-type CFD solvers. The proposed partitioned coupling approach performs just as well or better than the legacy coupling for large-scale simulations. Thus this type of coupling is scalable and applicable to large-scale applications. In future work, we validate individual processes such as gasification, and combustion similar to the drying and pyrolysis process in the current work. Complex cases such as biomass furnaces and blast furnaces are being investigated using the current implementation and are being validated.

3.9 Nomenclature

	Scalars
c_p	Specific Heat $(J/(Kg.K))$
d	Particle diameter (m)
I_i	Moment of inertia $(kg.m^2)$
m	Mass (kg)
m'	Mass source $(kg/m^3.s)$
p	Pressure (Pa)
q'	Heat source (W/m^2)
q''	Heat flux (W/m^2)
r, R	Radius (m)
t	Time (s)
T	Temperature (K)
T_{final}	Length of simulation (s)

	First order tensor (vectors)
$\vec{g}$	Acceleration due to gravity (m/s)
$\vec{F^c}$	Contact Forces (N)
$\vec{F^g}$	Gravitational Force (N)
$\vec{F^{ext}}$	External Forces (N)
$\vec{F_B}$	Buoyancy Force (N)
$\vec{F_D}$	Drag Force (N)
$\vec{M_{i,j}}$	torque generated by inter-particle forces $(N.m)$
$\vec{S}$	Momentum source due particles
$\vec{v}_f$	Fluid velocity field
$\vec{X_i}$	Positional vector (m)
$\vec{\omega}$	Rotational velocity (rad/s)

	Greek symbols
α	Heat transfer coefficient $(W/(m.K))$
β	Momentum exchange $(kg/(m^3.s)$
∂	Differential operator (-)
ϵ	Volume Fraction/Porosity (-)
μ	Kinematic viscosity $(Pa.s)$
∇	Nabla operator (-)
ρ	Density (kg/m^3)

	Subscripts
c	Cell
$cond$	Conduction
eff	Effective values
f	Fluid
i, j	Particle
n	Normal direction
p, P	Particle
rad	Radiation
t	Tangential direction

Part II

Applications

Chapter 4

Erosion Unveiled: A 6−way Coupled CFD-DEM-FEM Analysis of Abrasive Water Jet Cutting Nozzle [1]

[1] The content of this chapter are submitted to Powder Technology[7]

4.1 Abstract

The ability of Abrasive Water Jet Cutting (AWJC) to cut a wide variety of materials with high precision and minimal thermal effects makes it a versatile and environmentally friendly machining process that is widely used in various industries. This study addresses the persistent issue of nozzle erosion in AWJC, an issue that has received less attention in numerical modeling than the AWJ cutting process itself. While experimental studies on nozzle erosion exist, a comprehensive numerical analysis of the AWJC nozzle, especially using Finite Element Method (FEM), is lacking in the literature.

This work utilizes a 6-way CFD-DEM-FEM coupled model of the AWJC nozzle using a partitioned coupling approach. The model incorporates Computational Fluid Dynamics (CFD), Discrete Element Method (DEM), and Finite Element Method (FEM) solvers to capture interactions between the multi-phase fluid, abrasive particles, and the solid structure. The contributions of this study include the establishment of the coupled model of the AWJC nozzle, qualitative prediction of erosion patterns similar to experimental observations, monitoring of displacements under different operating conditions, and vibrational analysis of the AWJC nozzle.

The results showcase the mechanical response of a new AWJC nozzle and lay the foundation for future investigations into the mechanical behavior of worn nozzles. This study provides insights into erosion patterns for various operating conditions, contributing to a better understanding of the complex multi-physics problems associated with AWJC. The findings hold significant implications for the industry, where monitoring nozzle wear is crucial for maintaining cut quality. The presented approach, combining CFD, DEM, and FEM, offers a comprehensive tool for studying the erosion phenomena in AWJC nozzles, contributing to advancements in process optimization and equipment durability. [2]

[2]The content of this chapter are submitted to Powder Technology[7]

4.2 Introduction

A gentle river flow, some stuck pebbles, and a few thousand years have given rise to a beautiful geological formation of the largest natural potholes in a small village called Nighoj in the state of Maharashtra, India. These potholes or Giant's kettles are formed due to pebbles swirling in a helicoidal pattern in the cracks of the basalt river bed due to the river currents [158]. Abrasive water-jet cutting (AWJC) can be said to use the same phenomenon but on different spatio-temporal scales. AWJC process utilizes a high-pressure, high-velocity water jet, entrained with abrasive particles. The abrasive particles impinge on the workpiece and accelerate the wear and erosion at the impact site thus making a cut [30].

AWJC can be used to cut soft materials like paper, textile, organic tissue, food, leather, rubber, foam, plastics [159], composites [31, 160], wood [28] and hard materials such as metals [30], stones, concrete [29], glass [32], ceramics, etc [161, 162, 163, 164, 165]. Additionally, AWJC can be used to cut very precise and small components, with cuts with features as small as 50 μm to 100 μm [166]. Due to the small kerf or cuts possible, there is a huge reduction in scrap produced during machining. Furthermore, due to the nature of the erosion and wear-cutting mechanism, there are no residual thermal stresses or heat-affected zones thus avoiding warping or changes in material micro-structures [33] as opposed to traditional chipping or shearing. Additionally, there are no fumes generated (hazardous or otherwise), thus making it safe for operators. The cut surface also demonstrates excellent fatigue life [167]. Finally, depending on the material, it can be cut up to various depths with a good-quality surface finish.

The above-mentioned advantages, and versatility of the AWJC operation, it has diverse applications in, the automotive industry, aerospace, biomedical, mining, energy, etc. Additionally, it is eco-friendly as compared to its counterparts [34, 35]. A lot of research has been done since the 1970s on abrasive water jets investigating various aspects [37, 38]. As the abrasive particles erode and wear the workpiece, they do the same to the nozzle/focusing tube used to form the particle-laden jet. Thus, the erosion of the AWJC nozzle itself has plagued this operation since its inception.

Plethora of experimental studies can be found in the literature to study the cutting quality, and parameters affecting it [37, 38]. On the contrary, the erosion of the AWJC nozzle has been studied albeit sparsely as compared to the aforementioned. Some notable studies give the erosion pattern, such as the convergent and divergent erosion pattern was observed [39]. Then a wave-like structure along the nozzle axial length is observed [40]. The inlet angle of the particles plays an important role in the erosion, studied experimentally [168]. Finally, an experimental study showing the erosion of the focusing tube over time [42].

Abrasive water jet operation presents very complex multi-physics problems with a lot of variables to consider. Hence, it is no surprise the literature on the numerical model of AWJC and related processes is limited. Moreover, similar to the experiments, the numerical modeling related to the cutting process is found abundantly as compared to the numerical modeling of the AWJC nozzles. Due to the low computational cost, and comparative simplicity, the Smoothed Particle Hydrodynamics (SPH), and when modeling kerf characteristics can be seen to be favored when modeling erosion of workpiece [169, 170, 171]. Often the previously mentioned SPH model is coupled with FEM to study the kerf or erosion on the workpiece [172, 166]. CFD is also used to study the kerf pattern [173]. Some works also study the fluid flow inside and outside the nozzle, stagnation phenomena of the AWJ operation [174, 175, 176, 177].

The works related to the numerical study of erosion inside the AWJC nozzle are sparse but present. A one-way coupling approach is used between CFD and particle solver to study the particle flow inside the AWJC Nozzle [178]. Only particle flow trajectories and particle velocities were investigated. A CFD-DPM model is used to study the erosion on the cone and focusing tube [41, 168], where excessive erosion is observed at the transition from cone to tube geometry. This study also conducted experiments to compare and validate the erosion concentrations estimated numerically. Another CFD-DPM model of the AWJC nozzle is used to get the optimum nozzle geometry [179], which showed a very smooth transition from the cone to the tube leads to less erosion with optimal cutting performance. Finally, a CFD-DEM model is used to predict the erosion patterns in the AWJC model [45].

It is clear from the literature that the erosion of the nozzle/focusing tube is a persistent

issue in the industry. Furthermore, monitoring the erosion inside the AWJC nozzle is difficult and adds operational costs [180, 181]. An approach for monitoring wear progression was proposed using the operational vibrations of the AWJC nozzle [181, 49]. In this approach the vibrational response of the AWJC nozzle, the first mode frequency to be specific changes (increases) over time due to the erosion. This change is intended to be used as an indicator of erosion. The erosion of the AWJC nozzle is important to monitor as the cut quality severely depends on the integrity of the focusing tube and particle-laden water jet flowing out due to the nozzle geometry.

The literature demonstrates attempts, and further need for further numerical studies of the AWJC nozzle to understand the complex erosion phenomena of the AWJC nozzle. Furthermore, to the best knowledge of the authors, no FEM study of the AWJC nozzle has been performed (literature shows FEM studies of the AWJC footprints on the workpiece). Additionally, if the AWJC nozzle vibrational response is to be used as an inline indicator of erosion, this further prompts a study that includes the FEM model of the AWJC nozzle.

The current study intends to address some of the gaps in the literature mentioned above. In the proposed work, a partitioned coupling approach is used to couple CFD, DEM, and FEM solvers, to establish 6-way CFD-DEM-FEM momentum coupling [6]. This high-fidelity numerical model allows us to track interactions between the multi-phase fluid (water, air), particles, and the solid. The current study contributions, that are novel or related to the numerical study of AWJC Nozzle are, (1) establishing a 6-way CFD-DEM-FEM coupled model of AWJC nozzle using a partitioned coupling approach [6], (2) erosion pattern predictions are qualitatively similar to those seen in the experiments in the literature [40], (3) displacements monitoring of the AWJC nozzle tip for different operating conditions, (4) vibrational analysis of AWJC nozzle before and during the presence of water jet, and particles, (5) insights into erosion patterns for different operating conditions for the same amount of simulated time.

The current work delves into the mechanical response of a new (unworn) AWJC nozzle when fully coupled with fluid and particle physics. This work lays the foundations to study the mechanical response of worn nozzles in the future. The current article is organized as follows: in section 4.3, the governing equation for the three involved physics are described as

well as the erosion model used. In section 4.3.4, 4.3.4, and 4.3.5, the coupling is explained in brief, as the coupling approach is described in detail in a previous publication [6]. In the section 4.4, the results for the 6-way coupled AWJC nozzle are presented. The results for each of the physics involved are explored individually to focus on the important aspect of that particular solver. Additionally, the results are analyzed, followed by a discussion of the results in section 4.5. Finally, we see the conclusion in section 4.6.

4.3 Model Description

The partitioned coupling approach establishes momentum coupling between fluids, particles, and structures by creating a multi-physics environment using three different software programs. CFD, DEM, and FEM are the methods used to simulate these physics, respectively. Below is a description of the governing equations for each numerical method.

4.3.1 Governing equations for discrete particles

The discrete particle phase is modeled in the current work using the XDEM software suite [64]. The particulate system's thermodynamics and dynamics are both modeled by XDEM. The dynamic behavior of particles interacting with fluids and structures will be the main focus of the current work. Using the XDEM dynamics module, the particle's position, velocity, and acceleration are calculated.

The soft sphere model serves as the foundation for the discrete element method (DEM) utilized in the XDEM dynamics module. This method assumes that the particles are deformable and have the ability to overlap, with the contact force determining the extent of overlap through the application of the force-displacement law. Young's Modulus is used to express the particle's hardness, and a dampener or dashpot can be used to describe the particle's energy dissipation. Equations from classical mechanics are used to track each particle's translational and rotational movements. A thorough explanation of every term listed below can be found in earlier research [103]. The following is an overview of the equations for

translational and rotational motion: Equations of particle motion:

$$m_i \frac{d\vec{v_i}}{dt} = m_i \frac{d^2\vec{X}_i}{dt^2} = \vec{F_i^c} + \vec{F_i^g} + \vec{F_i^{ext}} \tag{4.1}$$

where $\vec{X}_i$ is the position vector for a given particle, $\vec{\phi_i}$ is the orientation, and $\vec{u}_{p_i}$ is particle velocity. $\vec{F_i^g}$ is the force due to gravity. $\vec{F_i^{ext}}$ is the sum of all the external forces acting on the particle, such as (hydrostatic) buoyancy forces $\vec{F_B}$ and (hydrodynamic) drag forces $\vec{F_D}$.

$$I_i \frac{d\vec{\omega_i}}{dt} = \vec{M}_c + \vec{M}_{ext} + \vec{M}_{roll} \tag{4.2}$$

where I_i is the moment of inertia, $\vec{M}_c$ stands for the torque acting due to inter-particle collisions, $\vec{M}_{ext}$ is the torque acting on the particles from external sources. The $\vec{M}_{roll}$ is the torque acting due to rolling friction given as follows:

$$\vec{M}_{roll} = -\mu_r |\vec{F}_n| R_i \frac{\vec{\omega}}{|\omega|} \tag{4.3}$$

where $\vec{F}_n$ is the normal force derived from the Hertz theory [104] for the normal elastic force whereas Mindlin's work [105] is used to compute the normal energy dissipation, given as follows:

$$\vec{F}_n = -\left(\frac{4}{3} E_{ij} \sqrt{R_{ij}} \delta^{\frac{3}{2}} + c_n \delta^{\frac{1}{4}} \dot{\delta}\right) \tag{4.4}$$

where c_n is the normal dissipation coefficient proposed by Tsuji et al. The normal dissipation coefficient is expressed as proposed by Tsuji et al. [106] and Zhang and Whitten [107].

The tangential forces include static and dynamic friction as follows:

$$\vec{F}_t = \min\left(k_t \delta_t + c_t \dot{\delta}_t, \mu \vec{F}_n\right) \tag{4.5}$$

The inter-particle collision forces and torques are given as follows:

$$\vec{F_i^c} = \sum_{i \neq j} \vec{F_{i,j}} (\vec{X}_j, \vec{u}_{p_j}, \vec{\phi_j}, \vec{\omega_j}) \tag{4.6}$$

$$\vec{M}_i^c = \sum_{i \neq j} \vec{M}_{i,j}(\vec{X}_j, \vec{u}_{p_j}, \vec{\phi}_j, \vec{\omega_j}) \tag{4.7}$$

where the for $\vec{F}_i^c$ stands for the collision forces between the particles, $\vec{M}_i^c$ is the torque due to collisions, $\vec{F_{i,j}}$ and $\vec{M}_{i,j}$ is the force and torque exerted by particle j on particle i respectively, $\vec{\omega}$ is the particle angular velocity. The sum $\sum_{i \neq j}$ represents the sum over all particles other than i. It should be mentioned that in the current work, walls, boundaries, and drums are all treated as another particle. Therefore, the equations 4.6 and 4.7 take into account collisions with boundaries, walls, and drums. The fluid forces acting on the particle, which are further discussed in section 4.3.4, are taken into account by the term $\vec{F_i^{ext}}$ in equation 4.1.

4.3.2 Governing equations for fluid

In the Eulerian volumetric average method, the conservation equation of mass (Eq 4.8) and momentum (Eq 4.9) are written over a representative volume. The turbulent scales involved in the AWJC nozzle fluid flow vary significantly over space and time. It is not feasible to resolve the turbulence in its entirety, hence the Large Eddy Simulation (LES) is used to model turbulence in the current work. The main idea behind LES is to use low-pass filtering of the Navier-Stokes equations to reduce the computational cost by ignoring the smallest length scales, which are the most computationally expensive to resolve [182]. Conservation of mass

$$\frac{\partial}{\partial t}(\rho_f) + \boldsymbol{\nabla} \cdot (\rho_f \vec{u}_f) = m' \tag{4.8}$$

Conservation of momentum

$$\frac{\partial}{\partial t}(\rho_f \vec{u}_f) + \boldsymbol{\nabla} \cdot (\rho_f \vec{u}_f \vec{u}_f) = -\boldsymbol{\nabla} p + \rho_f \vec{g} + \mu_f \boldsymbol{\nabla}^2 \vec{u}_f + \vec{S} \tag{4.9}$$

Multi-phase fluid model

In the current work, we also simulate a multi-phase fluid system. These multi-phase fluids are represented with the Volume of Fluid (VOF) method described by [183]. The local fluid

phase density and viscosity are given as follows:

$$\rho_f(\vec{x}) = \rho_1\alpha(\vec{x}) + \rho_2\alpha(1-\alpha(\vec{x})), \mu_f(\vec{x}) = \mu_1\alpha(\vec{x}) + \mu_2\alpha(1-\alpha(\vec{x})) \tag{4.10}$$

$$\begin{aligned} \rho_f(\vec{x}) &= \rho_1\alpha(\vec{x}) + \rho_2(1-\alpha(\vec{x})), \\ \mu_f(\vec{x}) &= \mu_1\alpha(\vec{x}) + \mu_2(1-\alpha(\vec{x})) \end{aligned} \tag{4.11}$$

where α is the fluid phase volume fraction defined as follows:

$$\alpha = \frac{1}{V_c}\int_V X(\vec{x})d\vec{x} \tag{4.12}$$

$$X = \begin{cases} 1, & if\ first\ fluid \\ 0, & if\ second\ fluid \end{cases} \tag{4.13}$$

4.3.3 Governing equations for solid structures

The Finite Element Method (FEM) is used to model the structures in the current work. This approach discretizes a large continuous problem (continuum) into more manageable and straightforward "finite elements". This way, the underlying partial differential equations (PDEs) can be solved over a small element [16] instead of over the entire spatial domain. It should be noted that FEM is an approach to solve a collection of PDEs; hence, depending on the underlying governing equations different physics can be modeled. The displacements of the solid is of interest in the current work.

The material behavior and continuum mechanics concepts under consideration provide the governing equations for stresses and displacements in a structure. In matrix form, the equilibrium equations can be expressed as:

$$\mathbf{K}\cdot\vec{U} = -\vec{f} \tag{4.14}$$

where $\mathbf{K}$ is the global stiffness matrix, $\vec{U}$ is the vector of nodal displacements and $\vec{f}$ is the vector of applied nodal forces.

The constitutive equations relate stresses to strains for the material being analyzed. For linear elastic materials, Hooke's law is commonly used to express the relationship between stress and strain:

$$\boldsymbol{\sigma} = \mathbf{D} \cdot \boldsymbol{\varepsilon} \tag{4.15}$$

where $\boldsymbol{\sigma}$ is the stress tensor, $\mathbf{D}$ is the elasticity matrix and $\boldsymbol{\varepsilon}$ is the strain tensor.

The relationship between strains and displacements is defined based on the assumed displacement field within each finite element. This relationship is typically expressed using the strain-displacement matrix, which relates the strains to the nodal displacements within an element.

$$\boldsymbol{\varepsilon} = \mathbf{B} \cdot \vec{U} \tag{4.16}$$

where $\mathbf{B}$ is the strain-displacement matrix, that is dependent on the type of elements, and shape function used.

It is possible to create a system of equations that solves for the nodal displacements and then determines the stresses inside the structure by combining the equilibrium equations, constitutive equations, and the strain-displacement relationship.

In the current work, Calculix [101, 102] an open-source, three-dimensional FEM software is used to solve the structure displacements and stresses on unstructured Lagrangian meshes. The readers are referred to the standard textbooks on FEM [16, 17, 19, 18] for further reading.

4.3.4 CFD-DEM Coupling

The CFD-DEM Eulerian-Lagrangian coupling is achieved over a volumetric mesh. The equations used to represent the coupled physics are given in this section. This work deals with multi-phase fluids. Consequently, the equations presented in the following subsections, consider these different fluid conditions.

Fluid forces acting on particles

In this section, the effects of fluid forces acting on the particles are formulated. The DEM solver receives the fluid fields and properties and uses the following equations to compute the

fluid forces acting on the particles. There are two types of fluid forces acting on the particles, namely hydrostatic or pressure force, and hydrodynamic or momentum exchange force. The hydrostatic force is the buoyancy force that accounts for the pressure gradient around an individual particle [108].

$$\vec{F_B} = -V_{p_i} \boldsymbol{\nabla} p \tag{4.17}$$

where $\vec{F_B}$ si the buoyancy force, V_{p_i} is the volume of particle under consideration and $\boldsymbol{\nabla} p$ is the gradient of pressure experienced by the particle.

To compute the momentum exchange or hydrodynamics forces acting on the particles, first, the porosity i.e. the space fraction occupied by particles is computed. The porosity/void fraction of particles in fluid is given as:

$$\epsilon = 1 - \frac{1}{V_c} \sum_{i}^{n} \eta_i V_{p_i} \tag{4.18}$$

where V_c is the cell volume containing the particle, V_{p_i} is the volume of the i^{th} particle in the cell, and eta is the weight used for the porosity computation depending on the particle volume present inside the current cell.

In the Eulerian-Lagrangian approach, the hydrodynamic force corresponds to the fluid-particle interaction. This force depends on the relative velocity of the solid particle and fluid along with the forces acting due to the presence of neighboring particles. Several drag laws are implemented in the XDEM suite, such as Arastoopour [109], di Felice [110], Gidaspow [111], Richardson-Zaki [112], Shiller-Neumann [113], Sun-Battagli [114] and Syamal-OBrien [115]. The drag force acting on the particle due to the fluid for the CFD-DEM approach used in the current study is given as follows:

$$\vec{F_D} = \frac{\beta V_p}{(1-\epsilon)} \left(\vec{u}_f - \vec{u}_p\right) \tag{4.19}$$

The interphase momentum exchange β is predicted according to Gidsaw [111]. Although to cover all range of void fraction (ϵ), Wen and Yu [116] ($\epsilon \geq 0.8$) and Ergun and Orning [117]

($\epsilon < 0.8$) equations are included.

$$\beta = \begin{cases} 150\frac{(1-\epsilon)^2}{\epsilon}\frac{\mu_f}{d_p^2} + 1.75(1-\epsilon)\frac{\rho_f}{d_p}|\vec{u}_f - \vec{u}_p|, & \text{if} \quad \epsilon < 0.8 \\ \frac{3}{2}C_d\frac{\epsilon(1-\epsilon)^2}{d_p}\rho_f|\vec{u}_f - \vec{u}_p|\epsilon^{-2.65}, & \text{if} \quad \epsilon \geq 0.8 \end{cases} \tag{4.20}$$

where the drag coefficient C_d is given as:

$$C_d = \begin{cases} \frac{24}{Re}\left[1 + 0.15(Re)^{0.687}\right], & \text{if} \quad \text{Re} < 1000 \\ 0.44, & \text{if} \quad \text{Re} \geq 1000 \end{cases} \tag{4.21}$$

and the Reynolds number for the particle is given as:

$$Re = \frac{\epsilon\rho_f|\vec{u}_f - \vec{u}_p|d_p}{\mu_f} \tag{4.22}$$

Particle momentum source terms

The fluid can be the driving force, imparting momentum on the particles, which causes the particles to offer resistance (drag source) to the fluid motion; the particles can be the source of momentum, imparting motion on the fluid by exerting acceleration on it; or finally, due to the complex nature of the application, both conditions stated above can occur simultaneously in the various regions of the simulation domain. These possibilities arise from the nature of the momentum coupling under consideration. Therefore the momentum exerted by the solid particles on the fluid is treated in a semi-implicit way according to the method proposed by Xiao and Sun [118]. The explicit momentum source term $\vec{A_c}$ and implicit momentum source term Ω_c are as given in Eq 4.23

$$\vec{A_c} = \frac{1}{\rho_f V_c}\widetilde{\sum}_i B_i\vec{u_{p_i}}, \quad \Omega_c = \frac{1}{\rho_f V_c}\sum_{i=1}^{c_n} B_i \tag{4.23}$$

where the coefficient B_i [118] depends on the particle velocity $\vec{u_p}$, fluid velocity for the cell containing the particle $\vec{u_{f_c}}$, drag coefficient C_d and particle diameter d_p. Thus giving the

source term to be injected in equation 4.9 as follows:

$$\vec{S} = \rho_f \vec{A_c} - \rho_f \Omega_c \vec{u}_{f_c} \tag{4.24}$$

4.3.5 CFD-FEM and DEM-FEM Coupling

The CFD-FEM and DEM-FEM coupling is achieved over a surface mesh. The structure is usually a moving boundary patch in the CFD domain. The pressure field of the fluid acting over the structure surface is used to compute the forces exerted by fluid, thus computing pressure over the CFD cell face area. These forces are communicated over to the nodes of the structure.

The DEM solver uses STL to represent the structure in the DEM simulation domain. This STL wall is treated as just another particle, and thus it is possible to capture the inter-particle interactions. However in this case the particle forces acting on the triangles of the STL file are captured. The forces are then distributed over the three points of the triangles. These forces on the STL "nodes" are then communicated to the FEM solver.

The FEM solver receives fluid/particle forces as an input. These forces are then summed up. The forces are then applied as Neumann boundary conditions.

Neumann boundary conditions specify the applied forces or traction on the boundaries of the domain [16], given as follows:

$$t_i = t_{i,0} \quad \text{for } i \in \Gamma_t \tag{4.25}$$

where t_i is the traction on the i^{th} degree of freedom, $t_{i,0}$ is the prescribed value of traction and Γ_t is the set of degrees of freedom on which the Neumann boundary conditions are applied.

Once the FEM solver receives the forces exerted by the CFD/DEM solver, and they are applied as Neumann boundary condition using the `*CLOAD` card in CalculiX, the FEM solver then solves for the displacements in the structure. These displacements are then communicated to the CFD and the DEM solvers.

The CFD solver represents the structure as a moving wall, hence the CFD mesh is moved

according to the displacements. On the contrary, as DEM is a mesh-less method, and the structure is represented as an STL wall, the displacements are directly applied to the STL wall and it is deformed. This is equivalent to changing the shape of a particle.

4.3.6 Erosion Model

The erosion model proposed by Oka-Yoshida [184] has been adopted to study erosion caused by particle impacts [45]. This model takes two different wear mechanisms into account. The first is the orthogonal impact to the surface, although it rarely happens in AWJC nozzle that the impacts will be perfectly orthogonal to the nozzle, hence the sine component of the impact is consider as the orthogonal contribution, given as follows:

$$E_{Repcoll} = E_{90} \sin\theta^{n_1} \tag{4.26}$$

where θ is the impact angle, E_{90} is a function of Vickers hardness of the material given in equation 4.27. The equation 4.26 accounts for the brittle damage caused due to repeated plastic deformation.

$$E_{90} = K(H_v)^{k_1} \left(\frac{||\vec{u_p}||}{u_{ref}} \right)^{k_2} \left(\frac{D_p}{D_{ref}} \right)^{k_3} \tag{4.27}$$

where $\vec{u_p}$ is the particle velocity, D_p is the particle diameter. As the proposed erosion model was calibrated for aluminium-sand, and no parameters for tungsten-garnet exist in the open literature, the original parameters are adopted for the current study, given in table 4.1. This suggests that erosion damage found in this contribution should be interpreted more as a measure of erosion intensity than as a volume loss predictor. The tungsten carbide-specific erosion model should be utilized in conjunction with the numerical method described in this paper to provide quantitative predictions of the volume loss inside the nozzle caused by particle erosion. Because of this, we discuss a non-dimensional erosion damage in the result section, which is calculated by normalising the erosion E_{Oka} values.

The cut mechanism is also account for in this model. The cut erosion arises due to

u_{ref}	104 [m/s]	H_v	1.049 GPa	k_1	-0.790 [-]	n_1	0.7148 [-]
D_{ref}	326 [μm]	K	81.714 [-]	k_2	2.3042 [-]	n_2	2.2945 [-]
				k_3	0.1900 [-]		

Table 4.1: The parameters used for the erosion model [184, 45]

particles sliding on the nozzle. The model considering both damages is given as follows:

$$E_{Oka} = E_{Repcoll}(1 + H_v(1 - \sin\theta))^{n_2} \tag{4.28}$$

4.4 Results

In this section, the results for the AWJC Nozzle are discussed. The momentum exchange is demonstrated in the previous work [6], along with the explanation of the partitioned coupling approach. Hence, in the current section, only the 6−way CFD-DEM-FEM coupled case and its results are explored. In the following sub-sections, the simulation setup for each of the involved single-physics solvers is described, followed by the parameters for the coupling.

4.4.1 CFD Simulation setup

Figure 4.1 shows the fluid mesh. The fluid mesh is generated using an open-source software Salome® using a Python script from the literature [45]. The mesh discretization can be controlled through the script. The performance analysis for different mesh sizes is presented in figure A.1. In the current chapter, the mesh of $374,850$ hexahedral cells is used. Since this work is developed from the literature [175], a mesh independence study has already been performed for the mesh used. The diameter of the mixing chamber is 0.00412 m, whereas the diameter of the outlet is 0.000726 m. The length of the Nozzle is 0.08282 m.

The VOF method is used to model the different phases involved. In the current work, the fluid domain contains water and air. The water feed and water pressurization are not simulated, as it is irrelevant to the current work. It is assumed that the water feed provides water at a certain velocity.

The boundary conditions prescribed in the literature [175] are used. The fluid domain

consists of 4 boundaries, namely the water inlet, air inlet, wall, and outlet. A uniform Dirichlet boundary is applied to the water inlet, prescribing the water inlet velocity of 300 m/s in the z-direction. A convective boundary along with mesh coarsening is applied at the outlet. A Neumann boundary condition for pressure is applied at the wall and the inlet region. As the outlet is open to the atmosphere, atmospheric pressure is imposed at the outlet.

The sapphire orifice ensures that only water enters the mixing chamber, hence a uniform Dirichlet condition is imposed on the volume fraction at the water inlet. A switch is imposed on the volume fraction at the outlet based on the flow direction. If the velocity is directed outwards, a Neumann boundary condition is imposed, whereas if it is directed into the Nozzle, a Dirichlet condition is applied enforcing the incoming phase to be air.

The OpenFOAM [100] open-source CFD toolbox is used. An incompressible VOF solver known as `interFoam` is used. The Large Eddy Simulation (LES) is used to model the turbulence. The time-step is set to be $10^{-}7$ s, but it is allowed to vary based on the Courant number to ensure stability. The gravity 9.81 m/s^2 is acting in the positive z-direction.

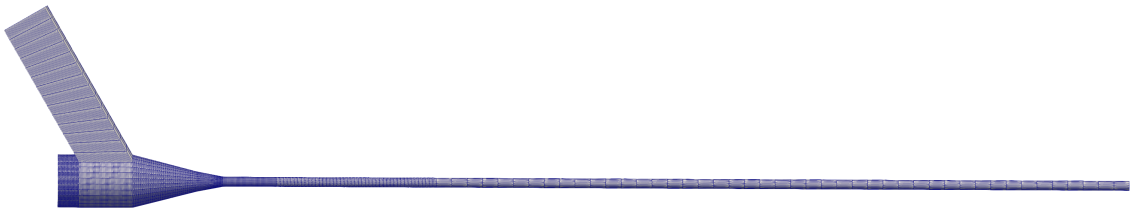

Figure 4.1: CFD mesh of the AWJC Nozzle/Focusing tube

4.4.2 FEM Simulation setup

Figure 4.2, shows the tetrahedral mesh used for the FEM solver. The FEM domain is built around the CFD mesh described above. The outer diameter of the solid part of the Nozzle is 0.00702 m, from the origin (0,0,0) until a length of 0.0716 m. The nozzle then tapers at a 15° angle, making the outer diameter at the other end of the nozzle 0.00112 m. The hopper solid part has an average thickness of around 0.02 m.

The unstructured tetrahedral mesh is generated using Salome®. The FEM mesh has $121,729$ `C3D4` tetrahedral elements. The `C3D4` is a $4-$node general purpose tetrahedral ele-

ment with one integration point [17]. As seen in the figure 4.2, the inside of the nozzle solid part is much more refined than the outer part. This is because all the forces acting on the nozzle come from the fluid or particles that travel through the solid part. The base of the FEM mesh is fixed, along with a restriction of displacements on the hopper. The restriction on the hopper is applied to avoid simulation crashes due to unexpected high-velocity particle impacts. The forces coming from the fluid and the particles are applied on the inner nodes as the Neumann boundary condition. Concentrated loads in CalculiX [102] are applied using the `*CLOAD` card.

The rest of the Nozzle does not have any constraints or boundary conditions applied to it and is free to move. Two points are monitored for displacement namely, Monitor point 1 with coordinates $(-0.000307839, 0.000479724, 0.08282)$ m, and Monitor point 2 with coordinates $(-0.0032341, 0.00151178, 0.0716238)$ m. A fixed time-step of 10^{-6} s is used because it is necessary to capture and resolve the effects of particle impacts sufficiently.

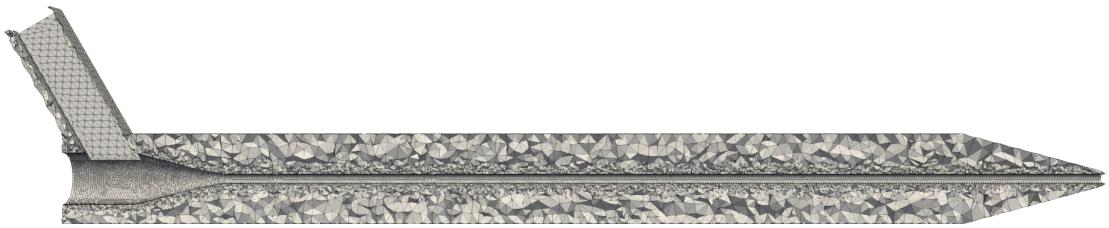

Figure 4.2: CFD mesh of the AWJC Nozzle

4.4.3 DEM Simulation setup

Figure 4.3 shows the DEM simulation domain along with the STL wall representing the Nozzle solid part. The DEM simulation domain is a box of dimensions $0.0186 \times 0.0186 \times 0.0908$ m. Although DEM is a meshless method, the XDEM divides the domain to enable parallelization. The domain is uniformly divided into 100, 100, and 200 parts in x, y, and z directions respectively.

The gravity 9.81 m/s^2 is acting in the positive z-direction. A time-step of 10^{-7} s is used for the dynamics module.

The particles are injected using a box source located at $(-0.00825, 0.00825, -0.0015)$ m,

Label	x-component [m/s]	y-component [m/s]	z-component [m/s]	Magnitude [m/s]
Vel. 1	1	-1	0.7	1.58
Vel. 2	2	-2	1.41	3.16
Vel. 3	3	-3	2.12	4.74
Vel. 4	4.47	-4.47	3.16	7.07
Vel. 7	7	-7	4.9	11.04

Table 4.2: Different inlet velocities used for the erosion study with their case label

with all the box sides of 0.0015 m. The particle mass flow rate is set to be 10 gm/s, with a time-step of 10^{-7} s. The particles injected are spherical with a constant diameter of 150 μm. There are five different cases considered for this study with different particle inlet velocities as given in table 4.2.

The Hertz-Mindlin impact model is used [104, 105]. The erosion is estimated using the Oka-Yoshida erosion model [184].

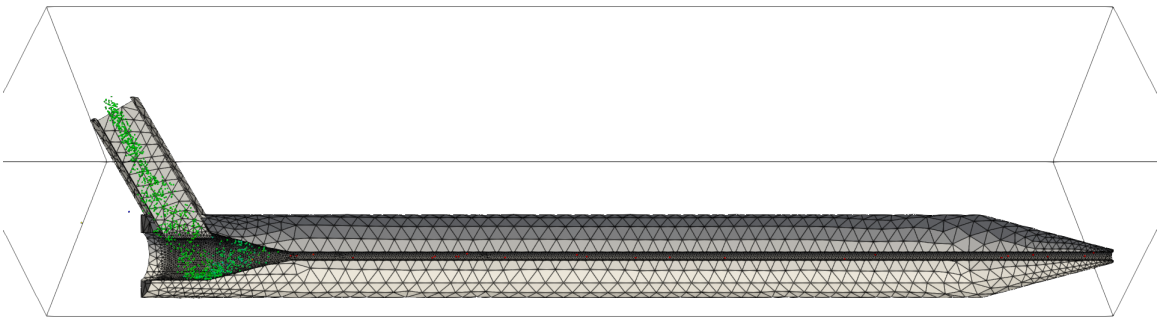

Figure 4.3: DEM STL mesh ad domain of the AWJC Nozzle

4.4.4 Coupling parameters

The coupling time step between each pair of the solver is 10^{-6} s. When writing data from DEM solver to CFD and FEM solvers respectively, `conservative` constraint is applied while using the `nearest-neighbor` mapping scheme. On the contrary, when writing the data from CFD and FEM to DEM, the `consistent` constraint is applied while using the `nearest-projection` mapping scheme. The CFD to FEM data mapping is done using

Properties	Particles	Solid
Material Name	Garnet	Tungsten Carbide
Density ρ (kg/m^3)	2500	15570
Young's Modulus (Pa)	5×10^5	705×10^9
Poisson Ratio [-]	0.45	0.31
Spring Stiffness [N/m]	1×10^5	1×10^5
Coefficient of Restitution	0.5	–
Coefficient of Static Friction	0.8	–
Coefficient of rolling friction	0.15	–

Table 4.3: Physical and Mechanical properties of the particles used in the DEM model

the `nearest-projection` mapping scheme, using the `consistent` constraint. The FEM to CFD data transfer uses `nearest-projection` mapping scheme while using the `conservative` constraint. The `parallel-explicit` coupling scheme is used.

4.4.5 AWJC Nozzle Results

In the following section, the results of the 6−way CFD-DEM-FEM coupled results are studied for the AWJC Nozzle are discussed. The results presented in the following sections are from coupled simulations, but they are presented individually wherever necessary, to delve deep into each of the single-physics involved.

CFD Results

In this section, the CFD results are studied, which are the most important part of the AWJC Nozzle model, as they are the driving force.

The figure 4.4 shows the temporal evolution of the water-jet inside the nozzle. As the water-jet approaches the junction between the cone and focusing tube seen in figure 4.4(b), the air is pushed back towards the water-jet inlet. The air phase usually has lower velocities moving erratically in the mixing chamber as seen in figure 4.4(c) and (d). On the contrary, the entrained air in the focusing tube flows with higher velocities and in a comparatively organized way.

The figure 4.4(e) and (f) show the developing and stabilized water-jet. It takes 0.0003 s for

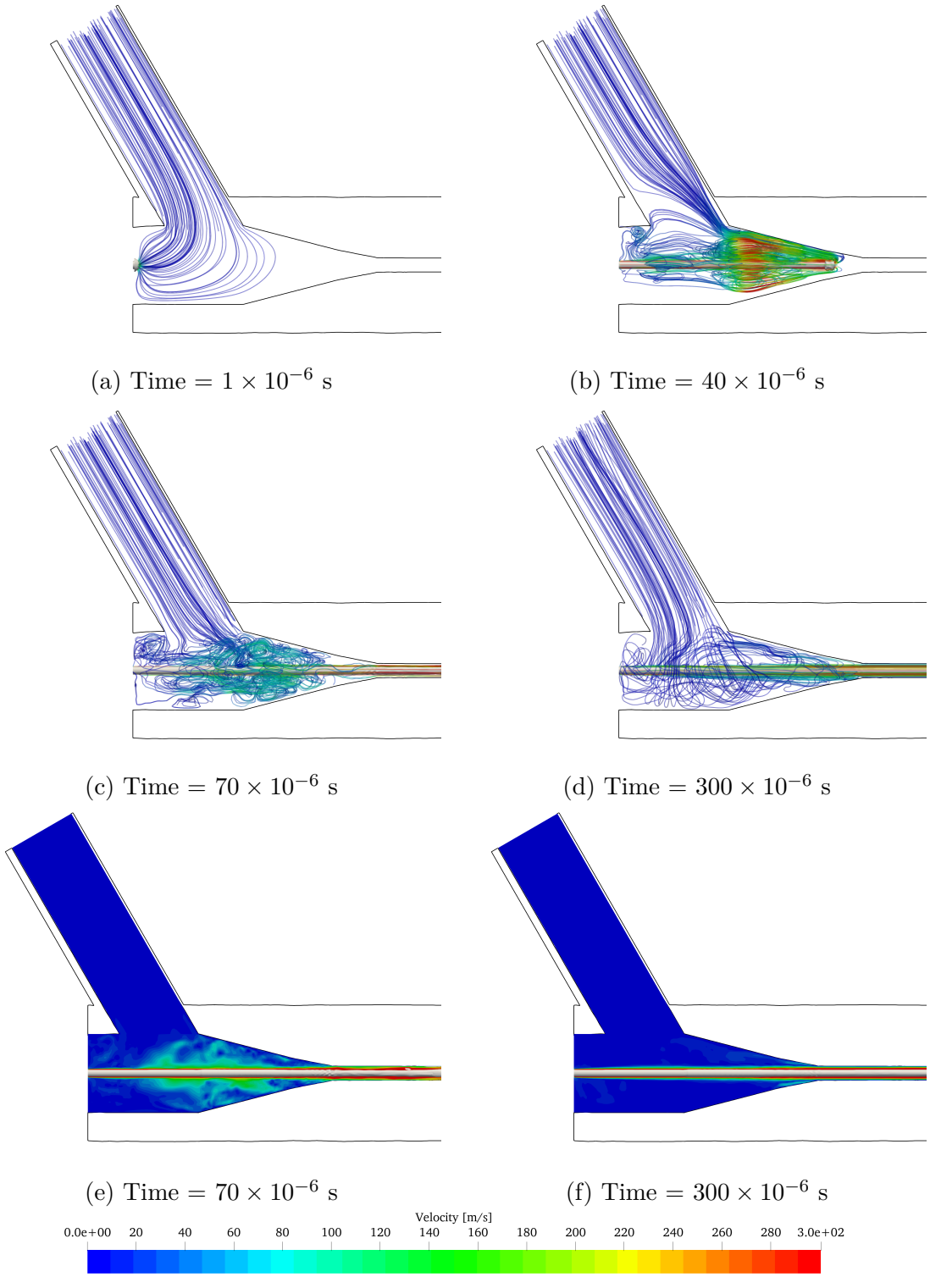

(a) Time = 1×10^{-6} s

(b) Time = 40×10^{-6} s

(c) Time = 70×10^{-6} s

(d) Time = 300×10^{-6} s

(e) Time = 70×10^{-6} s

(f) Time = 300×10^{-6} s

Figure 4.4: Temporal evolution of water-jet through the mixing chamber accompanied with streamlines to illustrate the modeled turbulence in the mixing chamber

the water-jet to reach the nozzle exit, at this stage, the flow inside the mixing chamber and the focusing tube are considered to be stabilized. The water-jet structure is represented with a clip of the phase field ($\alpha = 0.5$). As the water jet traverses across the mixing chamber and conical zone, it decelerates, thus giving rise to the classical water-jet head structure, followed by an oscillatory structure in the jet. Such oscillatory structures can lead to jet rupture, but in the current study, this is not the case. Such behavior might be caused due to the advection scheme at the air-water interface, which is known to lead to such spurious currents. These results are consistent with the literature relating to the CFD simulation of the multi-phase flow inside AWJC Nozzle [175]. Although the fluid flow is established inside the nozzle at 0.0003 s, the particles are injected only after 0.003 s, to ensure water-jet stability. In real life, it takes longer for the water-jet to completely stabilize due to the various components involved.

The interaction between the fluid and particles is quite complex, thus only some snapshots are presented demonstrating the fluid-particle interactions. The FEM model results are not included here, but it is coupled, and the results are presented in a later section. In the figure 4.5, the streamlines are presented illustrating the turbulence modeled in the nozzle. The fluid flow presented is for the Vel. 4 case prescribed in table 4.2. In the case of Vel. 4, the particles are pressure injected, as opposed to falling under gravity seen in the case of Vel. 1. This case is chosen to show the effects of fluid on particles as well as the effects of particles on the fluid. Although this can be observed in other cases as well, only one is presented here. As the particles as moving at around 7 m/s (resultant magnitude), the particles are seen to impose momentum on the fluid. Thus the fluid is accelerated, as seen in the slice fluid velocity field. Additionally, it can be seen that the particles alter the fluid flow substantially, as seen from the changes in the streamlines over time. This is especially evident when comparing the fluid low without particles as seen in figure 4.4(d). As the particles approach the mixing chamber, they experience the increased turbulent airflow, thus dispersing, as seen in figure 4.5(c). Finally, as the particles come close to the water-jet, they are propelled towards the exit at very high velocities. Due to the trajectories of the particles, the propelled particles will be either transported directly through the focusing tube, or they

can bounce off of the conical section.

DEM Results

The high-velocity, high-pressure water-jet is the driving force in the abrasive water jet cutting operation. The main mechanism of particle transport is through the entrainment of the particles in the small air layer surrounding the water-jet.

The figure 4.6 shows the Oka-Yoshida [184] erosion estimation and particle impacts for the five different particle inlet conditions. These simulations were run for 0.0225 s. The purpose of these numerical experiments is to demonstrate the impact of erosion due to the different operating conditions. In the literature [45], the simulation is run for 1 s to get good estimates of erosion progression over time, but this was done for only one operating condition. On the contrary, the results presented here show the effect of different operating conditions on erosion. The results in figure 4.6(a) demonstrate that the faster the inlet velocity of the particles, the faster the erosion.

The maximum erosion is observed where the converging part meets the long focusing tube. Figure 4.6(a) also shows a cyclic pattern in the erosion along the length of the focusing tube, where the strength of erosion reduces along the length. This observation is consistent with the literature [45]. Additionally, there is additional erosion observed near the exit of the focusing tube. There are several reasons for this increased erosion near the exit. First of all, the focusing tube is not only used to entrain the particles in the air but also to transfer the momentum from the water-jet. As the particles are reaching the outlet of the nozzle, they are moving at very high velocities. Additionally, to model the effect of water-jet opening up to the atmosphere a coarse fluid mesh near the outlet region is used. This in turn displaces the particles causing a higher number of impacts just near the outlet of the nozzle as seen in figure 4.6(b).

Figure 4.6(b) shows the particle impacts along the length of the nozzle. The maximum number of impacts are observed in the mixing chamber and the converging part of the nozzle. It can be observed that the number of impacts for the different particle inlet velocities is similar in the above-mentioned zone. It is very important to note that, even though the

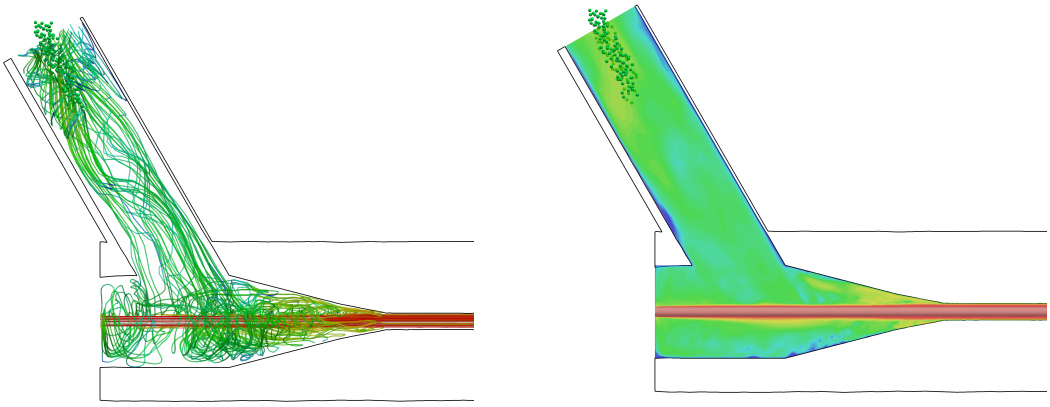

(a) t = 0.0035 s

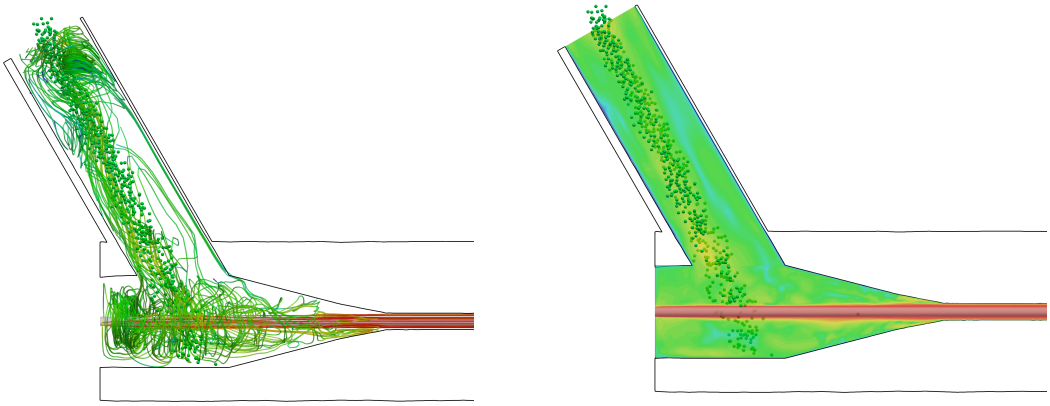

(b) t = 0.0050 s

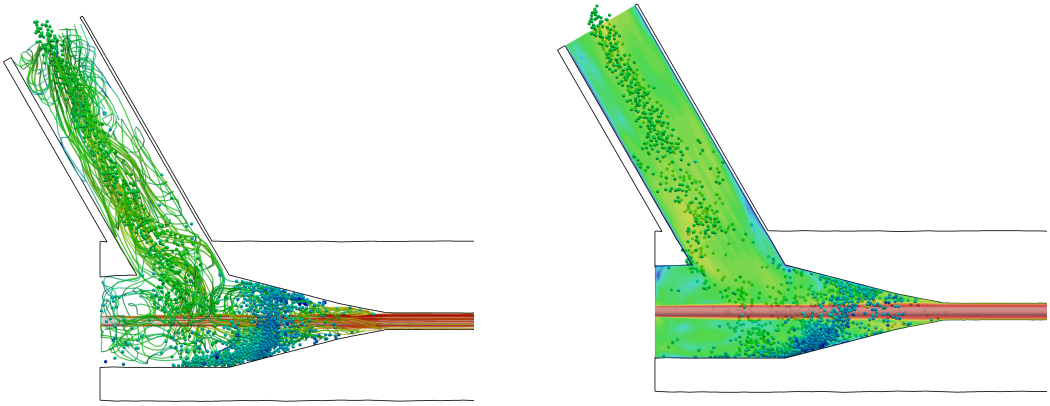

(c) t = 0.0100 s

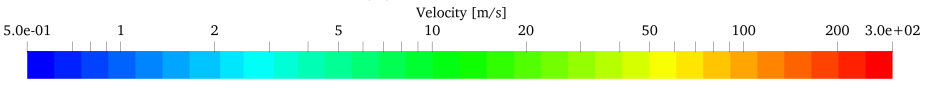

Figure 4.5: Fluid velocity field, Streamlines and particles illustrating fluid-particle interaction and 2−way alteration in flow for particles injected with Vel. 4 case

number of impacts is similar, the erosion observed for the different particle velocities is very different. This is because the particle velocities significantly affect the erosion rate. Additionally, it can be noted from figure 4.6(b), that the higher the particle inlet velocity, the higher the number of impacts observed along the length of the focusing tube.

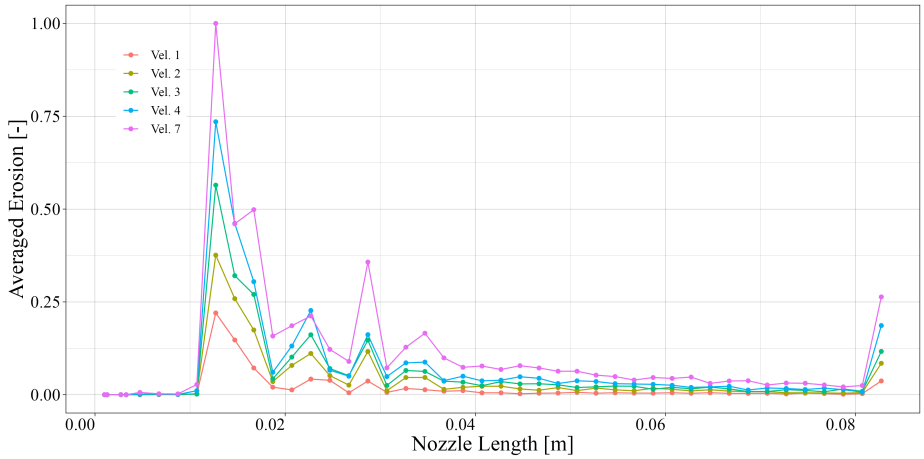

(b) Accumulated Oka erosion over the length of the Nozzle

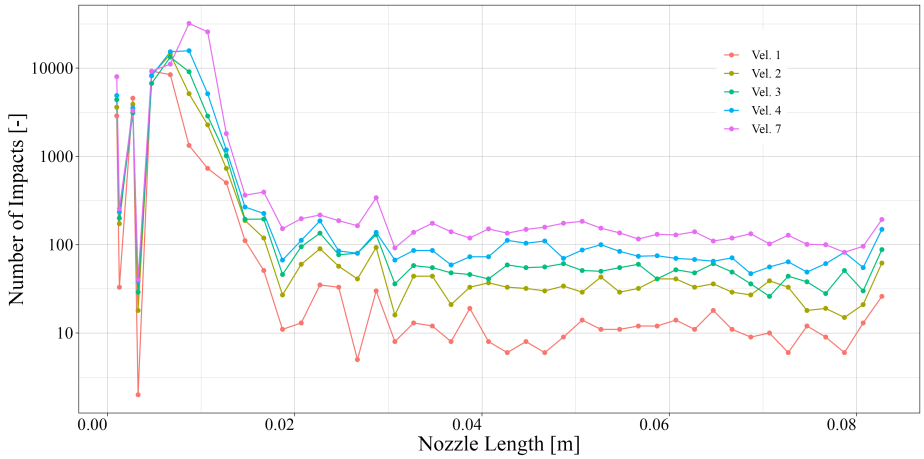

(b) Number of particle impacts [-] over Nozzle length

Figure 4.6: Particle results at the end of 0.0245 s simulated time studied over the AWJC nozzle axial direction

The figure 4.7 shows the erosion on the STL file. A threshold of 10^{-4} to 1 is applied to the normalized erosion. The amount of volume lost might seem very small, but these are non-zero values for erosion computed over a simulated time of 0.0225 s. As the actual erosion

might take several hours, the current study can only present qualitative results for the erosion patterns. Figure 4.7(b) shows the erosion pattern colored for the number of impacts. This erosion pattern demonstrates the swirling helicoidal movement of the particles in the mixing chamber along the converging part of the nozzle. The highest erosion can be seen at the joint of the converging part and the focusing tube. Additionally, zones of high erosion can be observed along the length of the focusing tube occurring at regular intervals with decreasing areas. This cyclic pattern is in alignment with the literature [40].

FEM Results

In this section, the FEM results of the solid part of the AWJC Nozzle are presented. The most interesting parameter to analyze first is the displacement of the two monitor points on the nozzle. Figure 4.8 shows the temporal evolution of the displacement (perpendicular to the nozzle axis) recorded at the two monitor points for the different particle inlet velocities. The literature shows the FEM model of the AWJC Nozzle has been ignored in the multi-physics model. The current sections add to the knowledge body significantly by considering the solid part of the nozzle in the multi-physics model.

The first observation to be made from the figure 4.8, is the impact times for the different particle inlet velocities. The lowest particle velocity case "Vel. 1" in figure 4.8(a), shows it takes a significantly long time for particles to impact the nozzle, get entrained in the air surrounding the water-jet and traverse to the end, thus causing the perturbations of the monitor points. On the contrary, the other cases considered show similar time taken for the perturbations of the monitor points. In the figure 4.8(b) and figure 4.8(e), it can be seen that the displacement of the monitor points increase in magnitude and stay at similar magnitudes throughout the rest of the simulations. In stark contrast, figure 4.8(a), (c), and (d) display the displacement magnitude increasing severely over time. This behavior can be attributed to the frequencies of particle impacts aligning with the natural frequency of the nozzle.

As the AWJC nozzle material is tungsten, which has very high yield strength, the actual displacement magnitudes are quite small. CalculiX uses a percentile convergence criteria of 0.01% of the field solved for, hence even though the displacements are quite small, sufficient

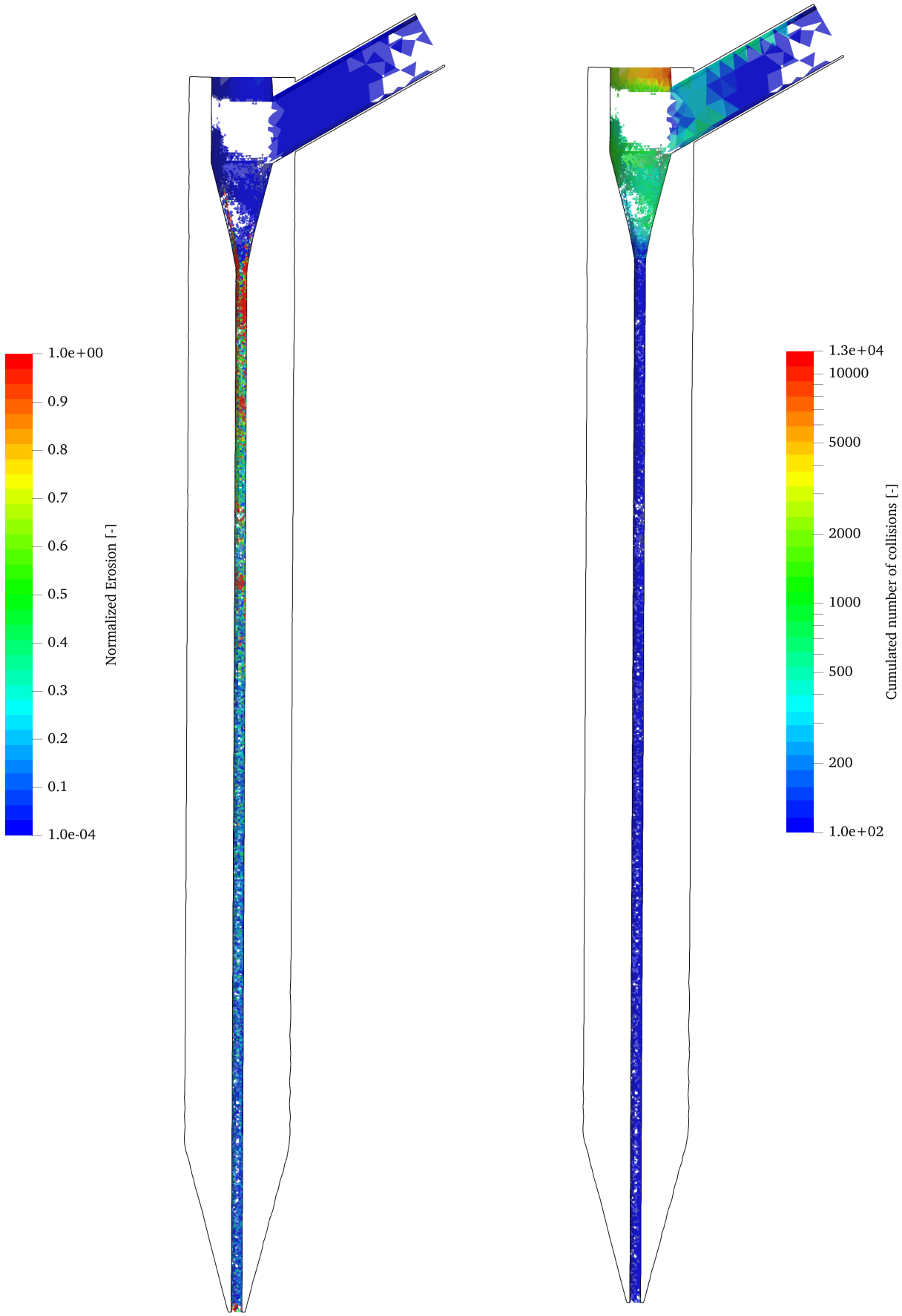

Figure 4.7: AWJC nozzle STL wall showing triangles normalized erosion and number of impacts at the end of 0.0245 s simulated time

convergence criteria are used.

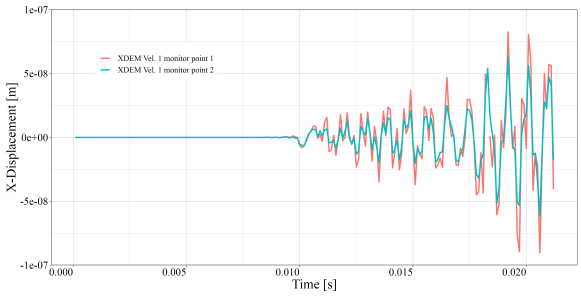

(a) Velocity $(1, -1, 0.7)$ m/s

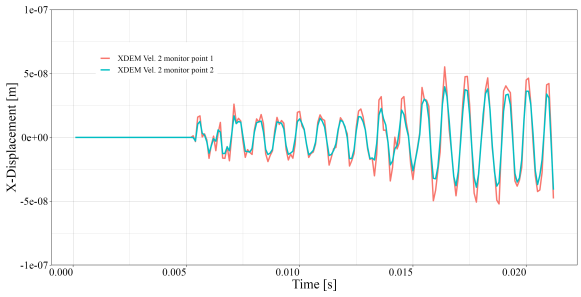

(b) Velocity $(2, -2, 1.41)$ m/s

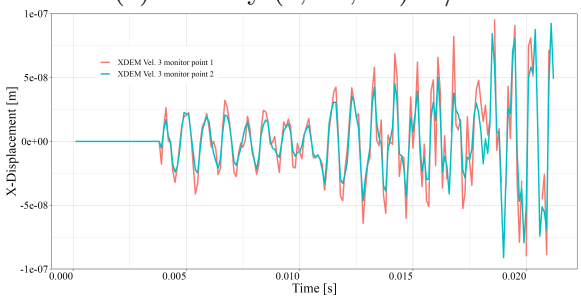

(c) Velocity $(3, -3, 2.12)$ m/s

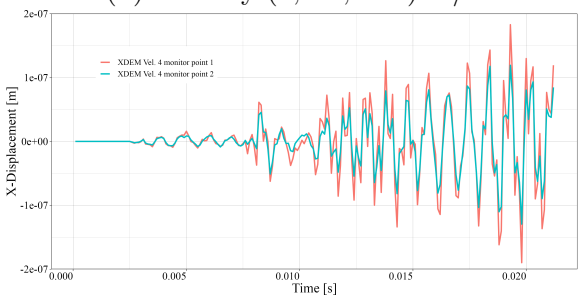

(d) Velocity $(4.47, -4.47, 3.16)$ m/s

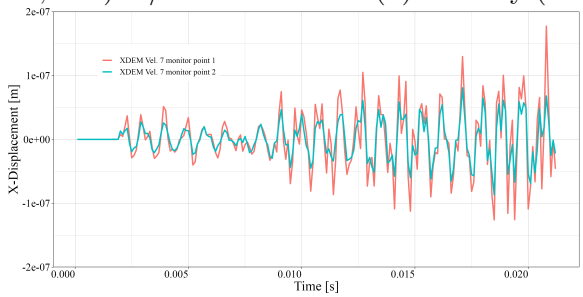

(e) Velocity $(7, -7, 4.9)$ m/s

Figure 4.8: Temporal evolution of displacements at 2 monitor points on the Nozzle FEM for different particle inlet velocities

The figure 4.9 presents the (magnified) displacement field for the nozzle solid part, sliced in the middle. It can be seen that the tip can displace quite a lot as compared to the rest of the nozzle. This is because the particles are at their highest velocities as they are approaching the nozzle exit, thus the impacts are at very high velocities. Furthermore, due to the clamping near the hopper, the tip acts as the free end of a cantilever beam. In the current study, only the leftmost nodes are fixed. Additionally, the monitor point on the outside can also be seen to be displaced in the snapshots presented above.

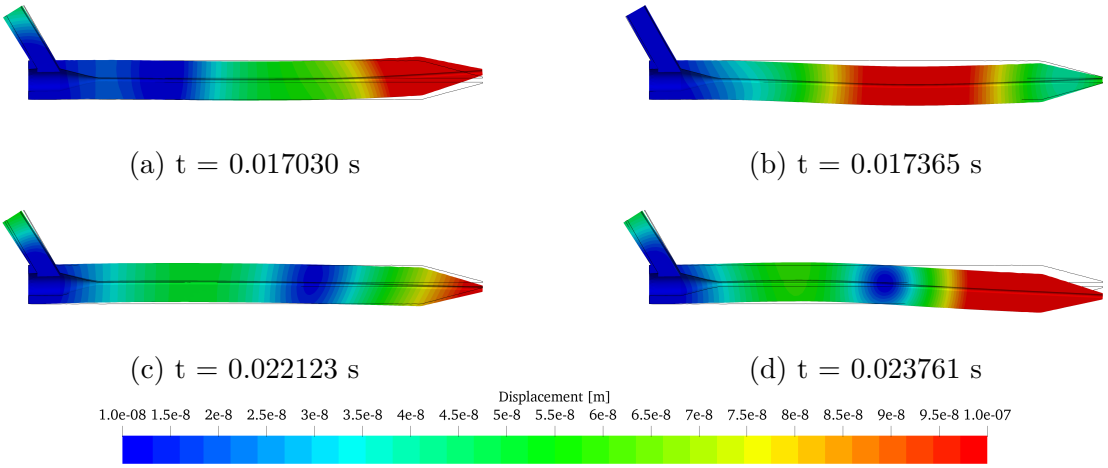

Figure 4.9: 3D AWJC Nozzle sliced to show the displacement for Vel. 7 case

In the figure 4.10, the frequency analysis is done for the nozzle. The results show the natural frequencies of the nozzle fixed at one end and unconstrained. The natural frequencies seen here are higher than seen in experiments [49]. This is because in the experiments, only the focusing tube is used, whereas in the current study, the focusing tube, mixing chamber, and hopper are modeled as one solid body. If these there components forming the nozzle are modeled as separate components in the FEM analysis, with their respective material properties, the natural frequencies obtained will be closer to experimental observations.

In the figure 4.10, mode shapes are also seen with dimensionless displacements. The mode shapes in figure 4.10(a) and (b) for the AWJC nozzle fixed at one end, are correctly predicted and are similar to the analytical mode shapes seen for cantilever beams. Similarly, the mode shapes for unconstrained AWJC nozzle are correctly predicted and match to the analytical mode shapes observed for an unconstrained beam. Due to the slightly non-symmetrical geometry, the mode shapes are seen to be a bit different, but this is to be expected.

4.5 Discussion

The current study models the complex fluid-particle-structure interaction inside the AWJC nozzle. This model is then used to simulate the flow of entrained abrasive particles inside the

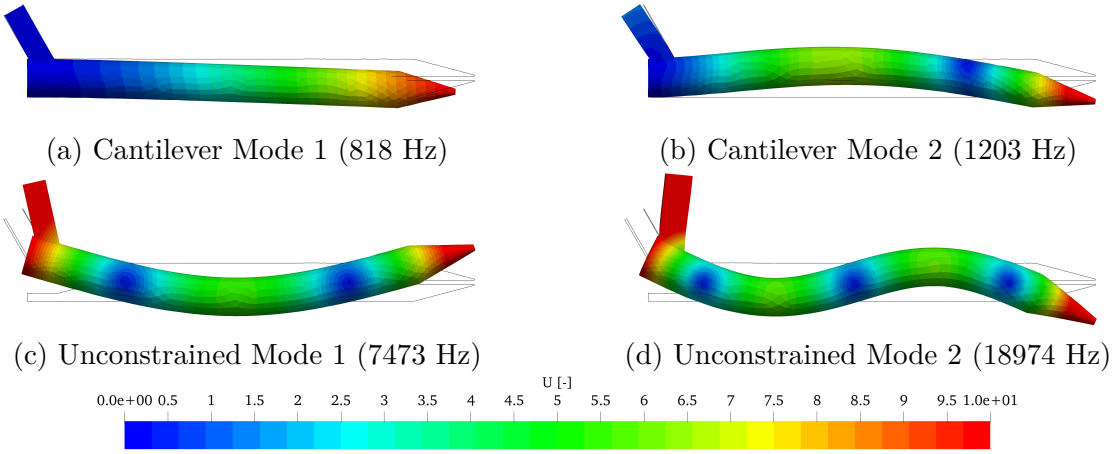

(a) Cantilever Mode 1 (818 Hz)

(b) Cantilever Mode 2 (1203 Hz)

(c) Unconstrained Mode 1 (7473 Hz)

(d) Unconstrained Mode 2 (18974 Hz)

Figure 4.10: Modal analysis of Cantilever and unconstrained AWJC Nozzle

AWJC nozzle along with the multi-phase fluid flow and the mechanical response of the AWJC nozzle for different operating conditions. The presented results can capture the different fluid-particle flow patterns thus resulting in erosion patterns along with displacements. These results demonstrate well that the 6−way CFD-DEM-FEM momentum coupled model can capture the various physics under different conditions very well.

The study aimed to gain insights into and predict the erosion inside the AWJC nozzle. The "complete" erosion of an AWJC nozzle usually happens over several hours. Hence, as we only simulate for a short time, only qualitative analysis of the erosion prediction could be done. Nonetheless, the erosion rates are known from the experiments from literature as well as numerical simulations. If one does wish to get the actual erosion, thus the actual loss of mass or volume, the erosion can be accelerated through the erosion rates. However, using the current approach, the qualitative erosion patterns and mechanical response for different operating conditions, different AWJC nozzle geometries, and different abrasive particle sizes can be estimated very well. Such studies can inform engineers and researchers about the AWJC nozzle characteristics, and help improve the abrasive water jet cutting process.

It is a known fact in the industry that the AWJC nozzle is going to wear down and needs to be replaced. Nonetheless, predicting when a nozzle might wear is important to know as the cutting quality is directly related to the focused water-jet, which in turn is directly

dependent on the interior geometry of the nozzle. The erosion inside an AWJC nozzle leads to poorly formed water-jet entrained with abrasive particles, thus leading to poor quality cutting finish. It is apparent though that monitoring the cut quality is not a reliable way to monitor nozzle wear, as it might waste the raw workpiece. There were experimental studies [181, 49] performed that intended to use the AWJC nozzle vibrations as a means of monitoring wear progression inside the nozzle, to avoid the problem mentioned above. The study used accelerometers and microphones to record the displacements of the AWJC nozzle and the noise. As the nozzle is eroded, the natural frequency up-shifts and increases gradually. The proposed device has the potential to monitor AWJC nozzle wear in-line. However, the results presented were for a specific focusing tube and operating condition.

The current study helps find the missing piece of the puzzle. The current study can successfully capture particle-laden flow for different operating conditions. Additionally, it provided the erosion pattern, that can be coupled with the erosion rate to find "true" loss of mass. As a future work, it is intended to then remove the mass from inside the nozzle based on the above results, and get a mechanical response of the nozzle. Hence, the eroded vibrational response of the nozzle can be known *a priori* through numerical simulation rather than performing expensive and time-consuming experiments. Additionally, such recommendations of the mechanical response of new, and worn focusing tubes can be made available along with a live monitoring method proposed in the studies mentioned above [181, 49].

The FEM solver used in the current study, CalculiX, provides a way to add or remove elements from a given mesh. Thus, it is indeed possible to "erode" the FEM model of the AWJC nozzle. However, it is to be noted that in the current simulations, the mesh points and the calculations required for data interpolations are only done once, at the beginning of the coupled simulation. If the geometry of any of the coupled models changes, these calculations need to be done for each coupling time step, adding severe overhead. Additionally, based on the monitoring approach mentioned above, the mechanical response for a "new" and "worn" nozzle is needed. Thus it is to only perform coupled simulations for the "new" AWJC nozzle, modify the geometry according to the erosion, and perform a second coupled simulation for the "worn" nozzle, to save computational costs.

4.6 Conclusion

A fully 6−way coupled model of the abrasive water jet cutting nozzle is established. The coupling is achieved between, CFD, DEM, and FEM solvers using a partitioned coupling approach by employing the preCICE coupling library. Due to the nature of the coupling, there is flexibility when using the individual solvers.

The influence of the fluid on the particle movements and the effects of particles on the fluid flow are explored. These results show that the fluid-particle interaction is captured correctly. Additionally, the turbulence inside the AWJC nozzle is modeled and demonstrated, showcasing multi-phase fluid flow in agreement with the observations in the literature.

The erosion patterns inside the AWJC nozzle for different operating conditions are presented. The erosion patterns can capture the different erosion phenomena correctly and are seen to be in agreement with experimental observations. The mechanical response of the AWJC nozzle is presented, demonstrating the effects of different operating conditions. Additionally, a vibration analysis of the AWJC nozzle is performed. The 3D erosion patterns are also presented on an STL geometry of the AWJC nozzle.

Nomenclature

	Physical constants/Greek symbols
β	Interphase momentum exchange $(kg/(m^3.s))$
ϵ	Porosity
μ_f	Dynamic viscosity $(Pa.s)$
μ	Sliding friction (-)
μ_r	Rolling Friction (-)
η	Weight of particle for porosity calculation
Ω_c	Implicitly treated drag term $(1/s)$
ρ	Density (kg/m^3)
	Operators
∂	Differential operator (-)
Δ	Difference (-)
∇	Nabla operator (-)

	Scalars
A	Surface Area
C_d	Drag Coefficient (-)
d	Particle diameter (m)
I_i	Moment of inertia $(kg.m^2)$
m	Mass (kg)
p	Pressure (Pa)
r, R	Radius (m)
Re	Reynolds number (-)
t	Time (s)
T_{final}	Length of simulation (s)
V	Volume (m^3)

	Subscripts
c	Cell, collision
d	Drag
eff	Effective values
f	Fluid
g	Gravity
i, j	Particle
n	Normal direction
p, P	Particle
s	Solid
t	Tangential direction

	Superscripts
n	Geometry exponent
(n)	n^{th} (time) step
$(n+1)$	n^{th} (time) step +1

	First order tensors (vectors)
$\vec{A_c}$	Acceleration on fluid cell due to explicitly treated drag term (m/s^2)
$\vec{g}$	Gravitational acceleration (m/s)
$\vec{F^c}$	Contact Forces (N)
$\vec{F^g}$	Gravitational Force (N)
$\vec{F^{ext}}$	External Forces (N)
$\vec{F_B}$	Buoyancy Force (N)
$\vec{F_D}$	Drag Force (N)
$\vec{M}$	Torque $(N.m)$
$\vec{v}$	Velocity
$\vec{X_i}$	Positional vector (m)
$\vec{\omega}$	Rotational velocity (rad/s)
$\vec{\phi}$	Orientation (deg)

Table 4.4: Nomenclature

Chapter 5

Numerical insights into Rock-Ice Avalanche Geophysical Flow Mobility through CFD-DEM simulation [1]

[1] The content of this chapter is published in Computational Particle Mechanics [1]

5.1 Abstract

Geophysical flows like rock-ice avalanches have high mobility and destructive potential, causing global loss of life and property. Water, often from melted ice, significantly impacts their mobility. Experimental investigations of debris friction in a rotating drum with melting ice show reduced friction due to water. However, experimental limitations hinder extensive testing. Employing a numerical model can overcome this, facilitating the study of various scenarios in understanding such calamitous geophysical flows.

In the current work, we numerically replicate the rotating drum experiment using Eulerian-Lagrangian CFD-DEM coupling. We focus on the initial and final states, considering a 30% gravel and 70% ice mixture ($B12-070$). We don't model the ice melting, rather we inject equivalent water over time. Our simulation captures changes in the frictional behavior of the gravel bulk and flow height profile, closely aligning with experimental observations.[2]

5.2 Introduction

Geophysical flows, which encompass various types such as debris flows, rock avalanches, and rock-ice avalanches, often exhibit remarkable mobility and destructive potential, resulting in significant loss of human life and property around the world [185, 186]. In February 2021, a series of catastrophic rock-ice avalanches swept through the Ronti Gad Valley and neighboring valleys in Chamoli, India. These avalanches had a devastating impact, leading to the destruction of two hydropower projects as detailed by the research of Shugar et al.(2021) [187] and Fan et al.(2022)[188].

Modeling the run-out distance of geophysical flows and predicting their dynamics can provide insights into avalanche propagation mechanisms and aid in estimating the potential extent of the affected area [189, 190]. Currently, available simulation methods for geophysical flows are primarily based on continuum approaches, falling into three main categories: single-phase models, mixed-phase models, and multi-phase models [191]. Savage and Hutter [192] employed the single-phase model to simulate dry granular flows, which was subsequently

[2]The content of this chapter is published in Computational Particle Mechanics [1]

extended for both dry granular flows [193, 194, 195, 195], and debris flows [196, 197]. The mixed-phase model assumes homogenization of both the fluid and solid, neglecting interactions between the phases [198, 199, 200], similar to the single-phase model [191]. Multi-phase models, introduced by Pitman [201], Pudasaini [202], and Pudasaini [203], account for phase interactions. Expanding on this foundation, Pudasaini [204] extended the approach by introducing additional governing equations for phase separation, enabling the simulation of the influence of debris flow surge front and lateral levees on the mobility of geophysical flows. Despite their computational efficiency and user-friendliness, continuum-based methods tend to overlook crucial particle phase attributes, such as particle shape, gradation, collision, fragmentation, segregation, and more. To address this absence of granular-level details, supplementary constitutive relations are often introduced [205].

The fundamental challenges of continuum mechanical modeling for geophysical flows stem from the spatial and temporal variations in macroscopic material behavior, arising from localized grain rearrangements and concurrent pore-fluid pressure development [206]. In recent years, parallel to advancements in computational capabilities, fluid-solid coupling techniques have made significant progress in geophysical flow simulation. These techniques naturally simulate particle characteristics and particle-fluid interactions without necessitating additional governing equations or assumptions. This method has been employed to simulate solid-liquid interactions in geophysical flows, covering wave surges [207, 208, 209], underwater particle column collapses [210], dam breaches [211], flume experiments [212], and evaluation of flexible protective netting [213, 214]. However, the study of particle-fluid interaction related to geophysical flow motion in the drum test through the CFD-DEM method remains insufficient.

In this study, we numerically replicated the motion of water-particle mixtures in a rotating drum experiment of rock-ice avalanches [215] under fully melted ice conditions using the CFD-DEM coupled system [216]. The results yielded numerical insights that harmonized closely with experimental observations, notably concerning factors like the friction coefficient of the gravel bulk and the profile of flow heights. This investigation delves into the fluid-particle interaction and the emerging debris flow. We investigate in depth the frictional behavior of the gravel (and water) bulk.

5.3 Experimental Methods

In the current work, we model the large rotating drum of 3.99 m diameter located at Berkeley. A detailed description of the experiments performed can be found at reference [215], figure 4.

Appropriate sizes for the gravel and ice were selected in the study through initial experimentation. Before each run, the drum was cooled down with 40 kg of ice. This ensured the inner temperature of the drum to be 0°C which prevented rapid melting of the ice in the initial stages of the experiment. The drum rotates at a constant speed of 2.09 m/s.

The experiment in question aimed to study the frictional characteristics of different gravel-ice mixtures. The large drum was equipped with a laser sensor (for flow depth), a load cell (for normal force), two pore-water pressure sensors (pwp), temperature measurement, and a video camera inside the drum In the current work, we aim to study and compare the frictional behavior only. Hence, the ice melting is not modeled, rather we inject an equivalent volume of water into the drum. The following formulations are used to compute the bulk friction coefficient, which are used in the original work [215].

$$\mu_{bulk}(t) = \tan\left(\arcsin\left(\frac{X_{COM}(t)}{r}\right)\right) \tag{5.1}$$

As the current work uses CFD-DEM coupling to numerically model the gravel behavior, the center of the mass of gravel bulk and water is to be computed as follows:

$$X_{COM}(t) = \left(\frac{\sum(X_{i,gravel} * V_{i,gravel} * \rho_{gravel}) + \sum(X_{i,water} * V_{i,water} * \rho_{water})}{\sum V_{gravel} * \rho_{gravel} + \sum V_{water} * \rho_{water}}\right) \tag{5.2}$$

where X_{COM} is the X component of the centroid of the particle bulk, $X_{i,gravel}$ is the the X position for the i^{th} particle, $V_{i,gravel}$, is the volume of for the i^{th} particle, ρ_{gravel} is the density of the gravel. The CFD cells containing water are extracted, this gives $V_{i,water}$ the volume of the cell and $X_{i,water}$ is the X component of the CFD cell centroid.

5.4 Model Description

In this section, we introduce the numerical model used for the simulation of the gravel flow in the rotating drum (as done in the experiments). In the current article, as we want to study the effects of the presence/addition of water due to melting ice in the gravel, the water is simulated as a continuum phase whereas the gravel is modeled as a discrete phase. In this article, we use the XDEM [64] platform which provides the Eulerian-Lagrangian CFD-DEM coupling. The Computational Fluid Dynamics coupling is achieved by using the OpenFOAM® software platform.

5.4.1 Governing equations for granular phase

XDEM predicts both dynamics as well as thermodynamics of the particulate system. In the current work, the main focus will be the dynamic behavior of such particulate systems. The particle position, velocity, and acceleration are computed with the dynamics module of the XDEM.

Dynamics module

The Discrete Element Method (DEM) used in the dynamics module of XDEM is based on the soft sphere model. In this method, it is assumed that the particles are deformable and can overlap each other, where the magnitude of overlap is decided by the contact force using the force-displacement law. The hardness of the particle is expressed via Young's Modulus, while the particle energy dissipation is described with a dampener and/or dashpot. The translational and rotational movements of individual particles are tracked using classical mechanics equations. A detailed description can be found in [103]. A summary of the translational and rotational motion equations is given below:
Equations of particle motion:

$$m_i \frac{d\vec{u}_{p_i}}{dt} = m_i \frac{d^2\vec{X}_i}{dt^2} = \vec{F_i^c} + \vec{F_i^g} + \vec{F_i^{ext}} \tag{5.3}$$

where $\vec{X}_i$ is the position vector for a given particle, $\vec{\phi}_i$ is the orientation, and $\vec{u}_{p_i}$ is particle velocity. $\vec{F}_i^g$ is the force due to gravity. $\vec{F}_i^{ext}$ is the sum of all the external forces acting on the particle, such as (hydrostatic) buoyancy forces $\vec{F}_B$ and (hydrodynamic) drag forces $\vec{F}_D$.

$$I_i \frac{d\vec{\omega}_i}{dt} = \vec{M}_c + \vec{M}_{ext} + \vec{M}_{roll} \tag{5.4}$$

where I_i is the moment of inertia, $\vec{M}_c$ stands for the torque acting due to inter-particle collisions, $\vec{M}_{ext}$ is the torque acting on the particles from external sources. The $\vec{M}_{roll}$ is the torque acting due to rolling friction given as follows:

$$\vec{M}_{roll} = -\mu_r |\vec{F}_n| R_i \frac{\vec{\omega}}{|\omega|} \tag{5.5}$$

where $\vec{F}_n$ is the normal force derived from the Hertz theory [104] for the normal elastic force where as Mindlin's work [105] is used to compute the normal energy dissipation, given as follows:

$$\vec{F}_n = -\left(\frac{4}{3} E_{ij} \sqrt{R_{ij}} \delta^{\frac{3}{2}} + c_n \delta^{\frac{1}{4}} \dot{\delta}\right) \tag{5.6}$$

where c_n is the normal dissipation coefficient proposed by Tsuji et al. The normal dissipation coefficient is expressed as proposed by Tsuji et al. [106] and Zhang and Whitten [107].

$$c_n = \ln e_n \sqrt{\frac{5 m_{ij} k_n}{\pi^2 + \ln e_n^2}} \; with \; k_n = \frac{4}{3} E_{ij} \sqrt{R_{ij}} \tag{5.7}$$

where $R_{ij} = 1/R_i + 1/R_j$, E_{ij}, v stand for the reduced radius, effective young modulus and impact velocity, respectively. The effective young modulus of a particle pair in contact is evaluated as

$$E_{ij} = \frac{1 - \nu_i^2}{E_i} + \frac{1 - \nu_j^2}{E_j} \tag{5.8}$$

The tangential forces include static and dynamic friction as follows:

$$\vec{F}_t = \min\left(k_t \delta_t + c_t \dot{\delta}_t, \mu \vec{F}_n\right) \tag{5.9}$$

where the tangential stiffness is written as follows:

$$k_t = 8G_{ij}\sqrt{R_{ij}\delta_t} \tag{5.10}$$

The effective shear modulus is defined as

$$\frac{1}{G_{ij}} = \frac{2-\nu_i}{G_i} + \frac{2-\nu_j}{G_j} \tag{5.11}$$

and the tangential dissipation coefficient c_t is correlated with the tangential coefficient of restitution by the following formula:

$$c_t = \ln e_t \sqrt{\frac{5\left(4m_{ij}k_t\right)}{6\left(\pi^2 + \ln e_t^2\right)}} \tag{5.12}$$

The collision forces and torques are given as follows:

$$\vec{F_i^c} = \sum_{i \neq j} \vec{F_{i,j}}(\vec{X_j}, \vec{u}_{p_j}, \vec{\phi_j}, \vec{\omega_j}) \tag{5.13}$$

$$\vec{M_i^c} = \sum_{i \neq j} \vec{M_{i,j}}(\vec{X_j}, \vec{u}_{p_j}, \vec{\phi_j}, \vec{\omega_j}) \tag{5.14}$$

where the for $\vec{F_i^c}$ stands for the collision forces between the particles, $\vec{M_i^c}$ is the torque due to collisions, $\vec{F_{i,j}}$ and $\vec{M_{i,j}}$ is the force and torque exerted by particle j on particle i respectively, $\vec{\omega}$ is the particle angular velocity. The sum $\sum_{i \neq j}$ represents the sum over all particles other than i. It should be noted that any boundaries, walls or drum in the current work are treated as another particle. Hence, the collisions with boundaries/walls/drum are consider in the equations 5.13 and 5.14. In the equation 6.1, the term $\vec{F_i^{ext}}$ accounts for the fluid forces acting on the particle. In this work, a semi-empirical drag law is utilised, given as follows:

$$\vec{F_{ext}} = \vec{F_{drag}} = \beta(\vec{u}_f - \vec{u}_p) \tag{5.15}$$

where $\vec{u}_f$ and $\vec{u}_p$ are the fluid and particle velocities respectively and β is given as follows:

$$\beta = \beta(\vec{u}_f - \vec{u}_p, \rho_f, \rho_p, d_p, A_p, \mu_f) \tag{5.16}$$

where ρ_f, ρ_p are fluid and particle densities respectively, d_p, A_p are the characteristic length and area and μ_f is the fluid density. The β for the current work is chosen to be the Schiller-Naumann [113] given as follows:

$$\beta = 0.75 C_d \epsilon (1-\epsilon) \rho_f \tag{5.17}$$

where the drag coefficient C_d is given as follows:

$$C_d = max\left(24\frac{(1+0.15Re^{0.687})}{Re}, 0.44\right) \tag{5.18}$$

5.4.2 Governing equations for fluid phase

In the coupled CFD-DEM model, the fluid phase is treated as a continuum on the macroscopic level using the Eulerian volumetric average method. In this model the conservation equation of mass (Eq 6.10), and momentum (Eq 6.11) are written over a representative volume. For representing the multiple fluids, we adopt the Volume of Fluid (VOF) method described by [183]. The changes proposed by [217] are used for the porous cases. The local fluid phase density and viscosity are given as follows:

$$\rho_f(\vec{x}) = \rho_1 \alpha(\vec{x}) + \rho_2(1-\alpha(\vec{x})), \quad \mu_f(\vec{x}) = \mu_1 \alpha(\vec{x}) + \mu_2(1-\alpha(\vec{x})) \tag{5.19}$$

where α is the fluid phase volume fraction defined as follows:

$$\alpha = \frac{1}{V_c}\int_V X(\vec{x}) d\vec{x} \tag{5.20}$$

where X is defined as follows:

$$X = \begin{cases} 1, & if\ first\ fluid \\ 0, & if\ second\ fluid \end{cases} \tag{5.21}$$

For the current study, $X = 1$ is considered to water and $X = 0$ is considered to be air. The volume fraction is considered as a scalar transported by the fluid flow

$$\frac{\partial \alpha}{\partial t} + \nabla \cdot (\alpha \vec{u}_f) + \nabla \cdot (\alpha(1-\alpha)\vec{u}_c) = 0 \tag{5.22}$$

where $\vec{u}_c$ is the relative velocity between the two phases. Conservation of mass for incompressible fluid:

$$\frac{\partial}{\partial t}(\rho_f) + \nabla \cdot (\ \rho_f \vec{u}_f) = m' \tag{5.23}$$

Conservation of momentum:

$$\frac{\partial}{\partial t}(\epsilon \rho_f \vec{u}_f) + \nabla \cdot (\epsilon \rho_f \vec{u}_f \vec{u}_f) = -\nabla p + \vec{T}_D + \epsilon \rho_f \vec{g} + \epsilon \mu \nabla^2 \vec{u}_f + \vec{S} \tag{5.24}$$

where $\vec{T}_D = \Gamma C \vec{n} \delta_\Gamma$ is the surface tension force. Each fluid phase must satisfy incompressibility constraint while also taking into consideration the void fraction

$$\nabla . \epsilon \vec{u}_f = -\frac{\partial \epsilon}{\partial t} \tag{5.25}$$

$\vec{S}$ is the semi-implicit momentum source term used to inject momentum effects from particles into the fluid. This source term consists of explicit and implicit parts [118] as shown below:

$$\vec{S} = \epsilon \rho_f \vec{A}_c - \epsilon \rho_f \Omega_c \vec{u}_{f_c} \tag{5.26}$$

where $\vec{u}_{f_c}$ is the fluid velocity in the concerned cell, the explicit momentum source term $\vec{A}_c$ is acceleration on the fluid cell and the implicit momentum source term Ω_c is the drag.

$$\vec{A}_c = \frac{1}{\rho_f V_c} \sum_i^n B_i \vec{u}_{p_i}, \qquad \Omega_c = \frac{1}{\rho_f V_c} \sum_i^n B_i \tag{5.27}$$

where the coefficient B_i depends on the particle velocity $\vec{u}_p$, fluid velocity for the cell containing the particle $\vec{u}_{f_c}$, drag coefficient C_d and particle diameter d_{p_i}.

In the CFD-DEM coupling modeled in XDEM [145, 146, 147], the governing equations of the fluid contain a term ϵ (porosity), V_c is CFD cell volume, V_i is the volume of i^{th} particle in the CFD cell and η is the weight for the porosity calculation depending on the particle volume present inside the current cell. The porosity calculation in brief is as follows:

$$\epsilon = 1 - \frac{1}{V_c} \sum_{i}^{n} \eta_i V_i \tag{5.28}$$

5.4.3 CFD-DEM Coupling

In the current study, we utilize the unresolved CFD-DEM coupling. The fluid mesh and the fluid data on this mesh is made available to the DEM solver. The particles are modeled as semi-implicit momentum source terms in the fluid, as described in equation 5.4.2, whereas the fluid is modeled as drag forces, hydro-static and hydro-dynamic forces acting on the particles. The reader erred to the literature for indepth information about the coupling approach [147, 216].

The particle finds the cell it belongs to using its centre. The fluid data on the cell is extracted for the CFD cell with the particle in consideration. The relevant fluid data fields are then used to compute the effects of fluid forces acting on the particle, as described in the equations 5.15.

The multi-phase flow information is available through the fluid density and viscosity fields as described in equation 5.19. Furthermore, to model the effects of air-water interface on the particles, the gradient of pressure and gradient of α are computed. These gradients are taken into consideration when computing the fluid forces acting on the particles. These gradients are zero if the CFD cell only contains one fluid. Otherwise, for the cells containing both fluids (i.e. at the fluid1 - fluid2 interface) will have a non-zero value for the gradients.

5.5 Results

In this section, we describe the model setup for the rotating drum. We have two parts in the model, one is the CFD part and the other is the DEM part. In the experiments section 5.3, 25 mm PVC pipes are used to prevent sliding on the smooth drum. However, in the present numerical model, we do not model these PVC risers to keep the model simple and reduce computational costs.

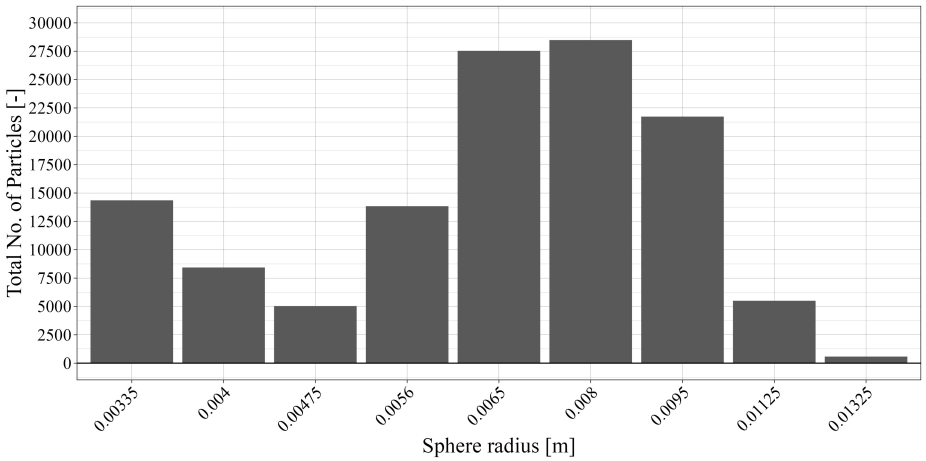

Figure 5.1: Gravel radius distribution

The DEM model domain is of dimensions $0.8 \times 3.99 \times 3.99$ m^3. The DEM is a mesh-less method and hence does not have any discretization. Rather, as described in section 5.4, each particle is tracked individually in the domain. In the present work, we want to study the rounded basalt gavel, this gravel is modeled as spherical particles with a range of different radii. This mixture is designated as $B12 - 070$ in the article describing the experimental results [215]. In the chart 5.1, the number of particles for each radius are plotted. The gravel was sifted and sieved to remove very fine particulate matter (mud and clay-forming particles). This left gravel of certain radii in the experiments, we try to keep the radius of the particles within the same range as the experiments. The material properties for these particles can be found in the table 5.1. The parameter calibration tests for the gravel (and ice particles) was performed by Schneider et al. [215], thus giving coefficient of restitution and the coefficient of friction for the gravel particles. However, as we model the friction offered by risers as

Properties	Gravel [215]
Density ρ (kg/m^3)	2740
Young's Modulus (Pa)	1×10^5
Poisson Ratio [-]	0.45
Spring Stiffness [N/m]	1×10^5
Porosity ϵ (-)	0.6
Pore diameter	50×10^{-6}
Coefficient of Restitution	0.5
Coefficient of rolling friction	0.15

Table 5.1: Physical and Mechanical properties of the gravel used in the DEM model

numerical friction coefficient offered by the drum, we perform numerical experiments so as to calibrate the friction coefficient of the drum, as presented in the figure 5.3. The friction coefficient for the drum is chosen such that the bulk friction coefficient is closest to the experimental observation at the beginning (dry phase). Particles are initially populated at the centre of the domain and packed in the drum.

To model the rotating drum, a cylindrical STL file is used as seen in figure 5.2. This rotating drum is treated numerically as another particle in the model, thus tracking interactions and collisions with other particles. The drum modeled with the STL file in the DEM domain is rotating at 2.09 m/s counter-clockwise. To prevent sliding and improve gravel

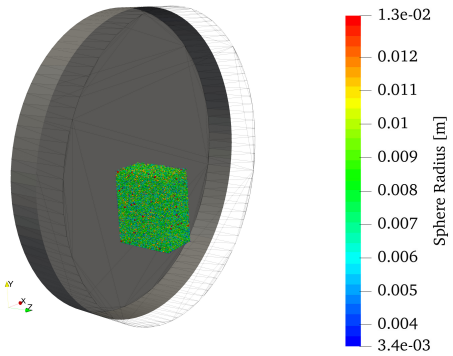

Figure 5.2: DEM simulation model for large Rotating drum

movement, the drum is modeled with friction. With this simplification, the computational

cost is reduced drastically as we avoid collision detection between hundreds and thousands of particles with tens of risers while preventing sliding on smooth surfaces. With the assumptions and simplifications made in the geometry and since the data for the friction coefficient of the drum is not available in the literature, numerical experiments were conducted with different friction coefficients as seen in figure 5.3. The experiments start with a "dry" ice and

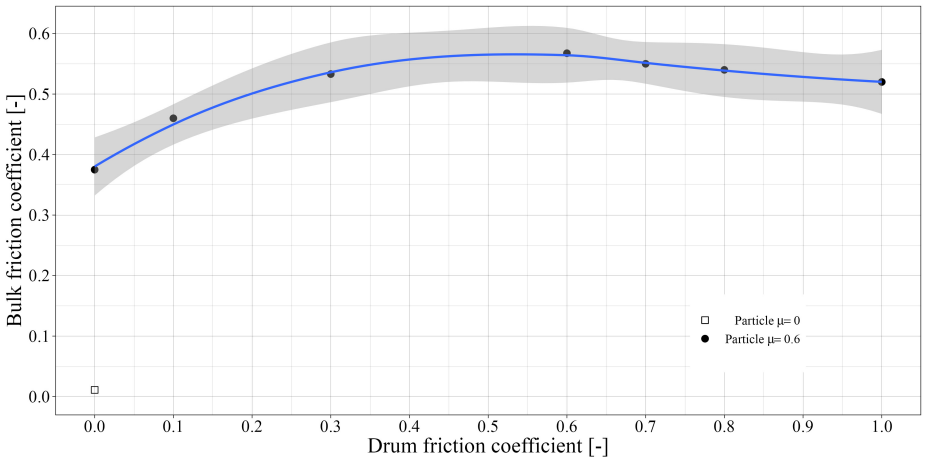

Figure 5.3: Comparison of different friction coefficient

gravel mixture with a bulk friction coefficient of 0.51. The bulk friction coefficient of the simulation is closer to the experimental value when drum friction is 1 seen in figure 5.3, but due to the excessive friction, the particles are transported too much throughout the drum. This gravel transport is not in line with the flow observed in the experiments. Considering the gravel bulk behavior, a drum friction coefficient of 0.6 is selected as seen in figure 5.3.

It should be noted that, as we do not model the ice-melting process we are primarily comparing the simulation results to the experimental observations at the initial time (T = 0 minutes) and the end time (T = $\sim$ 37 minutes) as seen in figure 5.4. As no ice has melted, we refer to the simulations run for the initial state as the dry run. For the end state, as all the ice has melted we refer to the simulations run for this state as the wet run.

The CFD model is made up of a cylinder with the same dimensions as the drum in the experiments, with a diameter of 3.99 m and thickness of 0.8 m. The CFD mesh can be seen in figure 5.5 with fairly similar-sized 2000 hexahedral cells throughout the CFD domain.

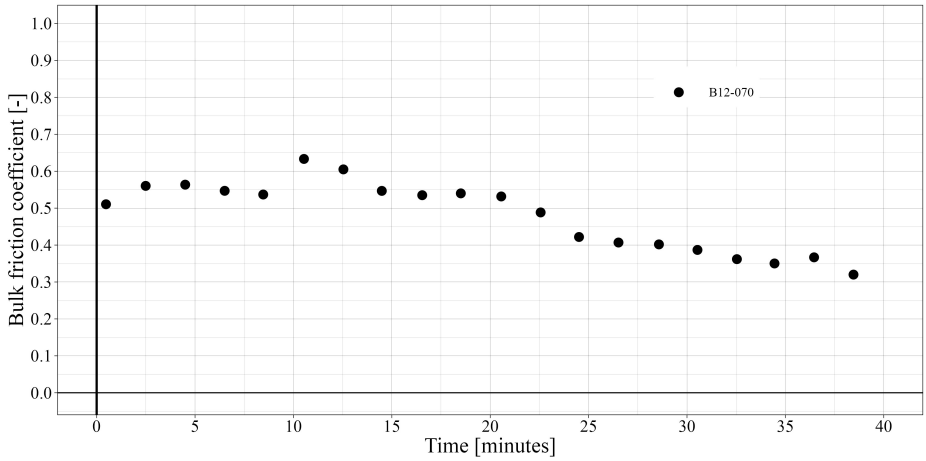

Figure 5.4: Evolution of the bulk friction coefficient for $B12-070$ [215] over time

The CFD domain is divided into 5 equally sized cells in the z-direction. The central block (which looks similar to a square) is discretised in 20×20. The surrounding blocks have 10 discretisation along the radial direction. The smallest CFD cell height is 0.092 m, whereas the maximum CFD cell height seen at the drum edge is 0.1 m. In the CFD model, we have two patches on top that are open to the atmosphere. For the rest of the side wall, we have no slip condition. As we model the water added due to melting ice in the gravel-ice mixture, we have two patches on either side of the wall to inject water into the rotating drum. As the melting phenomenon is at its peak at the top front of the gravel flow, these inlet patches are placed in the location as seen in figure 5.5. The cylindrical wall has a velocity of 2.09 m/s in the counterclockwise direction. As we do not model the 25 mm risers in the CFD domain as well, the mesh near the cylindrical wall can be kept simple and coarse thus saving computational cost on the CFD side of the coupled simulation.

The VOF method is used to model the air and water phases. In the current work, we only wish to study the change in frictional behavior due to the presence of water introduced due to melting ice. Hence, we do not actually model the ice particles melting, although this is possible to do with the XDEM suite [103]. Instead, the water (of an equivalent mass of ice) is injected into the domain for 20 s. As we know the gravel-ice mixture ratio used in the experiments, we inject the same amount of water (by mass) as the ice that was present for

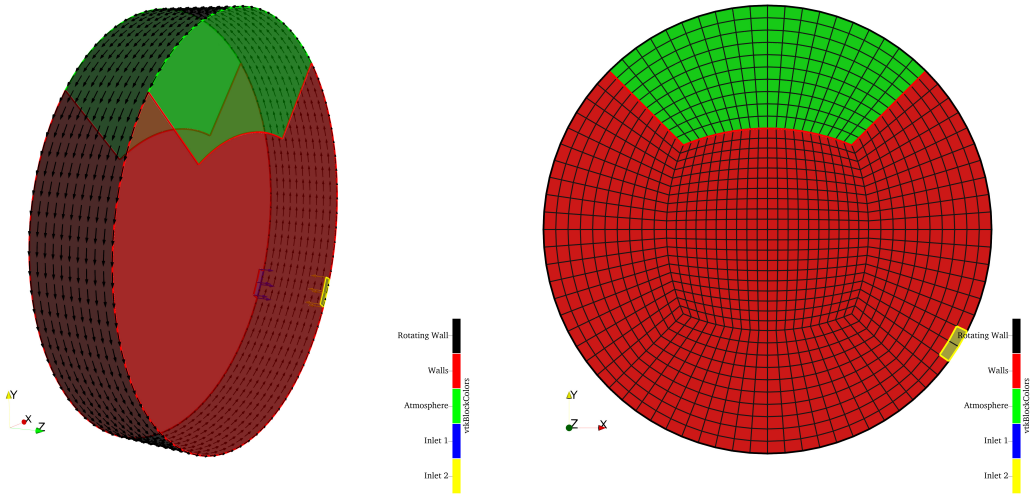

Figure 5.5: CFD simulation model for large Rotating drum

the experiments. This further reduces the computational burden on the model and allows us to explore more possibilities with commonly available computational tools.

Although the experiments took place over a significant amount of time, with the current coupled CFD-DEM model we can simulate similar behavior but accelerated over time. We plan to compare experimental and numerical results by computing the friction coefficient for the gravel (and water) as a singular bulk. This is computed as described from equation 5.1 and 5.2 in section 5.3.

In the following subsections, we see the results for the frictional behavior of gravel in the rotating drum in the absence and presence of water.

5.5.1 Dry run with particle packing, and stability with constant friction coefficient: $\mu_{drum} = 0.6$ *and* $\mu_p = 0.6$

As seen in figure 5.2, the particles are populated in the center of the domain. These particles are packed in the rotating drum. This is done as it is not easy to replicate the gravel populated at the bottom of the drum before the experiment starts. For the first simulation, the particles are allowed to pack and come to a steady condition. In the figure 5.6, after 30 s the particles achieve this steady condition represented by the bulk friction coefficient of the particles. No

water is added to this simulation as we want to achieve a steady state condition before the ice starts melting as per the experiments.

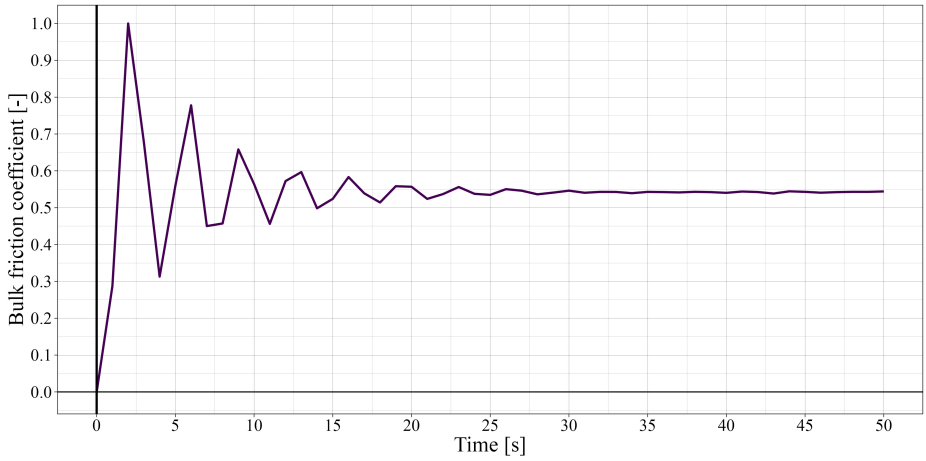

Figure 5.6: Evolution of the bulk friction coefficient for dry gravel over time

This final steady state condition at the end of the dry simulation is used as the initial condition for the following numerical simulations Water is added to model the ice melting.

As we do not model the ice particles for the dry run, we do not have the same bulk mass, hence we do not have the same friction coefficient as seen in the experiments. The bulk friction coefficient at the start of the experiments is ~ 0.51 [215], whereas it is around 0.53 for the numerical simulation. It should also be noted that the experiments for each gravel and ice weight combination, only have one observation. Hence, we do not know the variations in the observations. The bulk friction coefficient is overestimated by around 4% in the numerical simulations as compared to the experimental observations.

In figure 5.7 the gravel packing is seen. As it drops it is transported by the rotating drum upwards and drops back down. These gravel bulk oscillations can be seen in the form of the bulk friction coefficient in figure 5.6. As the gravel bulk achieves a steady flow condition within the rotating drum, the gravel bulk rotates through the drum in a consistent manner.

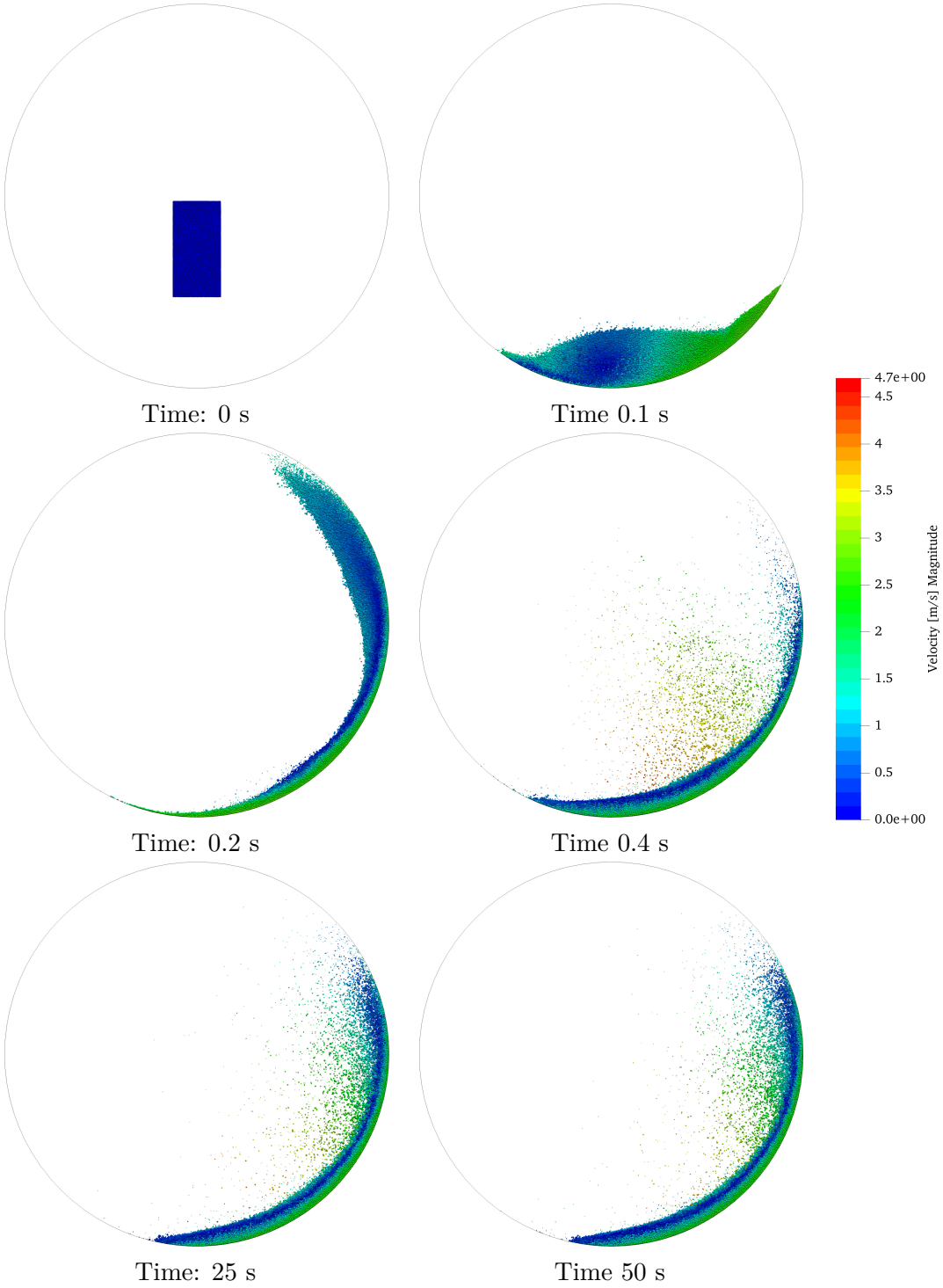

Figure 5.7: Evolution of the gravel flow in the rotating drum after the initial packing

5.5.2 Wet run with constant friction coefficient: $\mu_{drum} = 0.6$ *and* $\mu_p = 0.6$

In this section, the results of the frictional behavior of gravel when water is injected in the drum are presented. In the current section, the drum friction coefficient $\mu_{drum} = 0.6$, and the friction coefficient for the particles is $\mu_p = 0.6$, and these values stay constant over the duration of the simulation.

For the current work, we are considering the gravel-ice mixture of 30% gravel and 70% ice respectively (B12 – 070) [215]). We inject the equivalent mass of water in the CFD domain over a period of 20 s. The simulation is allowed to run until 50 s so as to allow for the gravel flow to come to a new steady state after the introduction of water.

When calculating the bulk friction coefficient for the gravel-water system, we need to consider the bulk mass of both gravel and water to get the correct value. This is defined in the equation 5.2. In figure 5.8, the evolution of the bulk friction coefficient is presented over time. It can be seen that as water is introduced in the coupled simulation, the frictional behavior of the gravel is affected immediately. Some oscillations in the bulk friction coefficient can be observed, indicating the movement of the gravel bulk in the rotating drum. For the bulk friction coefficient calculations, we only consider the water mass in the bulk after injecting the total water.

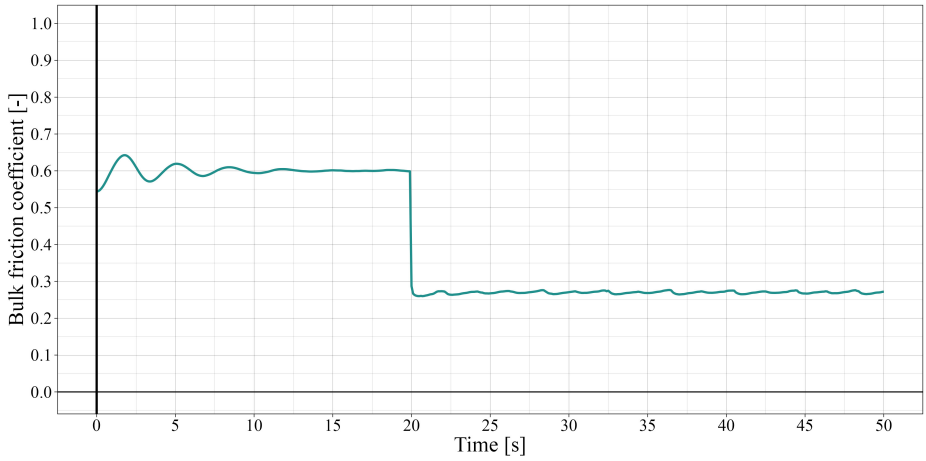

Figure 5.8: Evolution of the gravel bulk friction coefficient over time after introducing water (constant $mu = 0.6$)

This is because we are injecting water towards the right side of the drum (and the center of Mass of the gravel bulk). Hence the center of mass of water being injected skews the bulk friction coefficient. But as water injection stops and it has spread out in the drum as expected, we consider the water in the bulk mass for computing the bulk friction coefficient. This is why a sudden change in the bulk friction coefficient can be seen at 20 s in figure 5.8. The bulk friction oscillates for some duration and then stabilizes over time. Although the final value of the bulk friction coefficient is a bit low as compared to the experimental results. The experimental bulk friction coefficient at the final time is ~ 0.3, whereas the bulk friction coefficient for the simulation is ~ 0.275.

We can also compare the profile of the gravel-water distribution in the drum with the experimental results as seen in figure 5.12. the height profiles at the final time steps are similar. It is to be noted that, we do have replicates for the same experimental setup. Hence the slight mismatch in the height profile should be considered within the acceptable limit. In figure 5.9, the temporal evolution of the gravel frictional behavior can be seen as water is introduced. As water is added it increases the mobility of the gravel. Furthermore the gravel spreads out over the domain. Additionally, the velocity of the particles show that we have a rotary churning flow of gravel as compared to the dry run. This is an expected behavior due to the increase in the mobility of the gravel bulk due to the presence of water.

5.5.3 Changes in frictional behavior during the water injection

In the previous sections 5.5.1 and 5.5.2, the initial and final state of the numerical simulation respectively, is close to that of the experimental observations. In the numerical simulations, we do not model wetting and change in friction coefficient due to the wetting/lubricating of the particle surface. It is known from the literature described in the introduction, that mobility increases in the gravel due to the hydrodynamic forces introduced by the melting ice. This is also observed in the results presented in the previous sections. However, the frictional behavior during the water injection (ice melting)is not fully representative. The change in frictional behavior observed in the previous sections is purely due to the momentum exchange between CFD-DEM. It is hypothesized that the descending bulk friction coefficient seen in

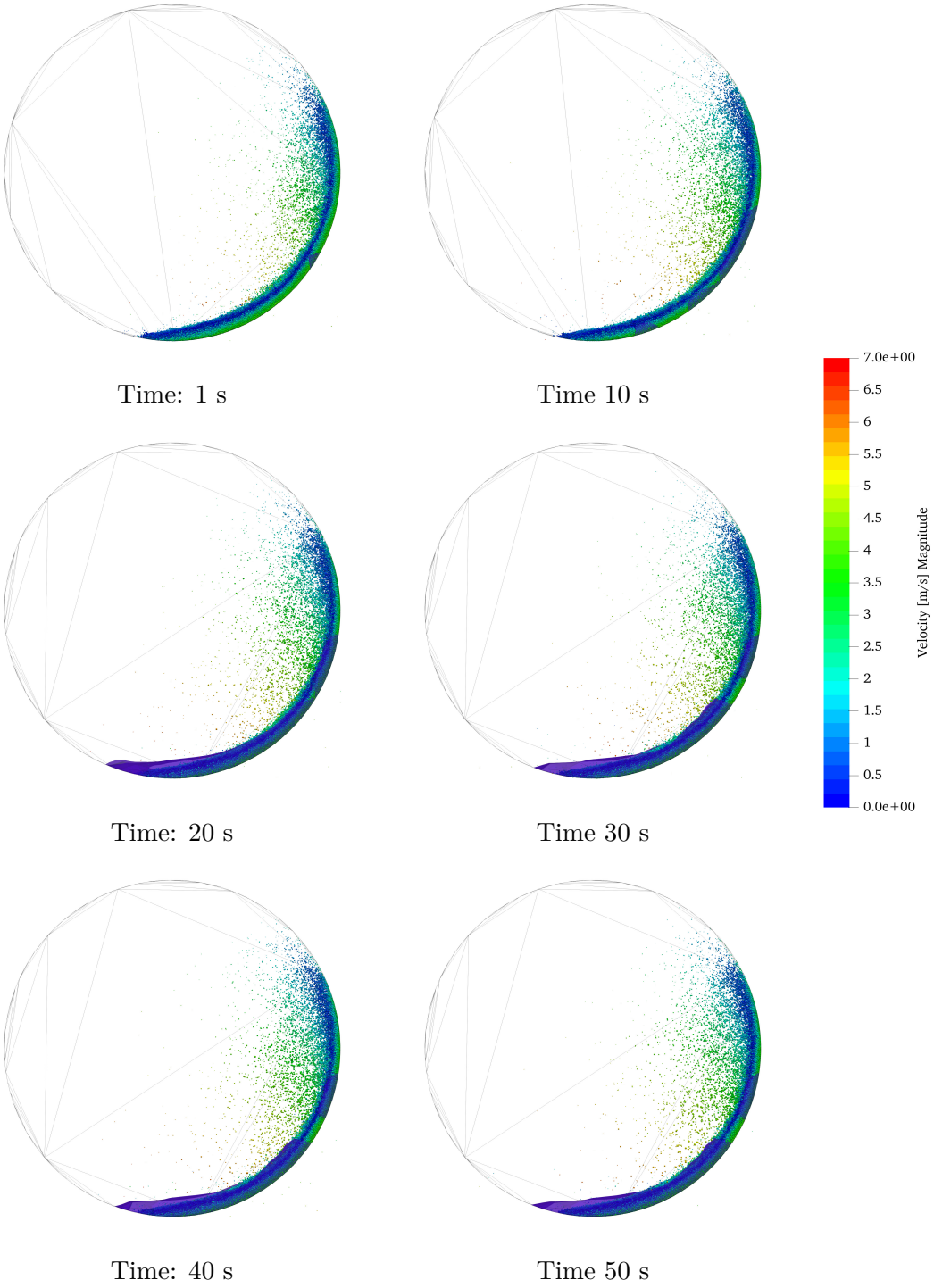

Figure 5.9: Evolution of the gravel flow in the rotating drum after injecting water

figure 5.4 can be modeled by varying the friction coefficient of the gravel and/or drum during the period over which we inject water.

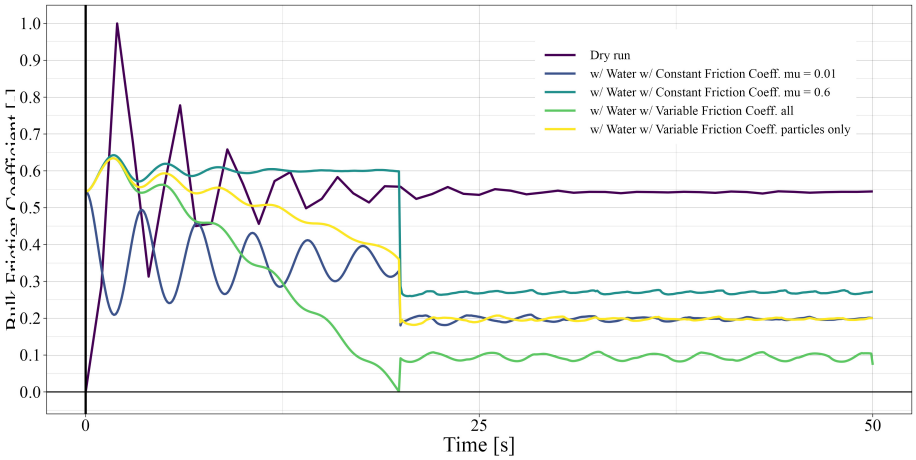

Figure 5.10: Evolution of the gravel flow in the rotating drum after injecting water

In this section, we plan to capture the dynamic behavior of the gravel bulk as the ice melts (water is injected). This can be achieved by varying the particle and/or drum friction coefficient linearly over a certain time to simulate the wetting and the lubrication of the gravel and drum. The friction coefficient is varied linearly for the same duration of time as that of injecting the water, assuming that the wetting takes place immediately after introducing the water. The particle friction starts at 0.6, and finally stays constant at 0.01 after the water injection is completed. Similarly, the friction coefficient of the drum starts at 0.6 and reduces to 0.01 as the water is injected and then stays constant for the rest of the simulated time. The reduced friction coefficient of 0.01 signifies the wetting and lubrication of the particles and/or drum. We use a simple expression $\mu(t) = -a * t + \mu_i$, where μ_i is the starting friction coefficient for drum or particle, a is the slope calculated according to the final time t used for injecting water.

In figure 5.10, the "Dry run" is the initial simulation run in section 5.5.1. The "w/Water w/ Constant Friction Coeff. mu = 0.6" is the simulation with water being injected, as presented in section 5.5.2. The "w/Water w/ Constant Friction Coeff. mu = 0.01" is same as the the case in section 5.5.2, but the friction coefficient of particles is 0.01. The case "w/Water

w/ Variable Friction Coeff. particles only", has a linear temporal variation of the particle friction coefficient. The case "w/Water w/ Variable Friction Coeff. all", has a linear temporal variation of the friction coefficient of both particles and the drum. In figure 5.10, the friction coefficient for the dry run is presented. As the initial condition for the wet runs is the end (stable) condition of the dry run, all the subsequent wet run's bulk friction coefficients start at the same value of ~ 0.53. For the constant friction coefficient cases i.e. $\mu_p = 0.6$ and $\mu_p = 0.01$, the friction coefficient oscillates around a constant value and stabilizes over time.

Whereas the bulk friction coefficient in the figure 5.10, it is illustrated that the gravel bulk behaves more dynamically for the duration of water injection. By varying the friction coefficient, the bulk friction coefficient also declines linearly. Similar behavior seen in the experiments[215] (figure 5.3). However, it can be seen that the final bulk friction coefficient for the cases where we vary the friction coefficient for particles/drum, the bulk friction coefficient is much lower than the experimental observation of ~ 0.31.

5.5.4 Comparison between dry and wet run

The numerical model of the rotating drum allows us to track and study various parameters of the individual particles. This includes instantaneous velocities of all the particles in the bulk. As this cannot be done in the experiments, it is very interesting to compare the results from the dry run i.e. no water added to the gravel versus when we have added water to the gravel bulk. From the dynamic bulk friction coefficient results seen in figure 5.10, it is clear that the mobility of the gravel bulk increases with the addition of water (melting ice). To better demonstrate this increase in mobility, we compare the dry (section 5.5.1) and wet run (section 5.5.2) side by side in figure 5.11.

In figures 5.11(a) and (b), a slice of 0.2 cm of the particles at the center of the drum in the z-direction is taken. The velocity vector for every 50^{th} particle is rendered. In figures 5.11(a) and (b), the particles closest to the drum wall move upwards, travel along the edge to the heights possible location, and fall back down. These particles fall back down and travel towards the bottom of the drum. If we compare the velocity vectors at the wall of the drum, the particles in the presence of water (figure 5.11(b)) clearly have higher mobility. The

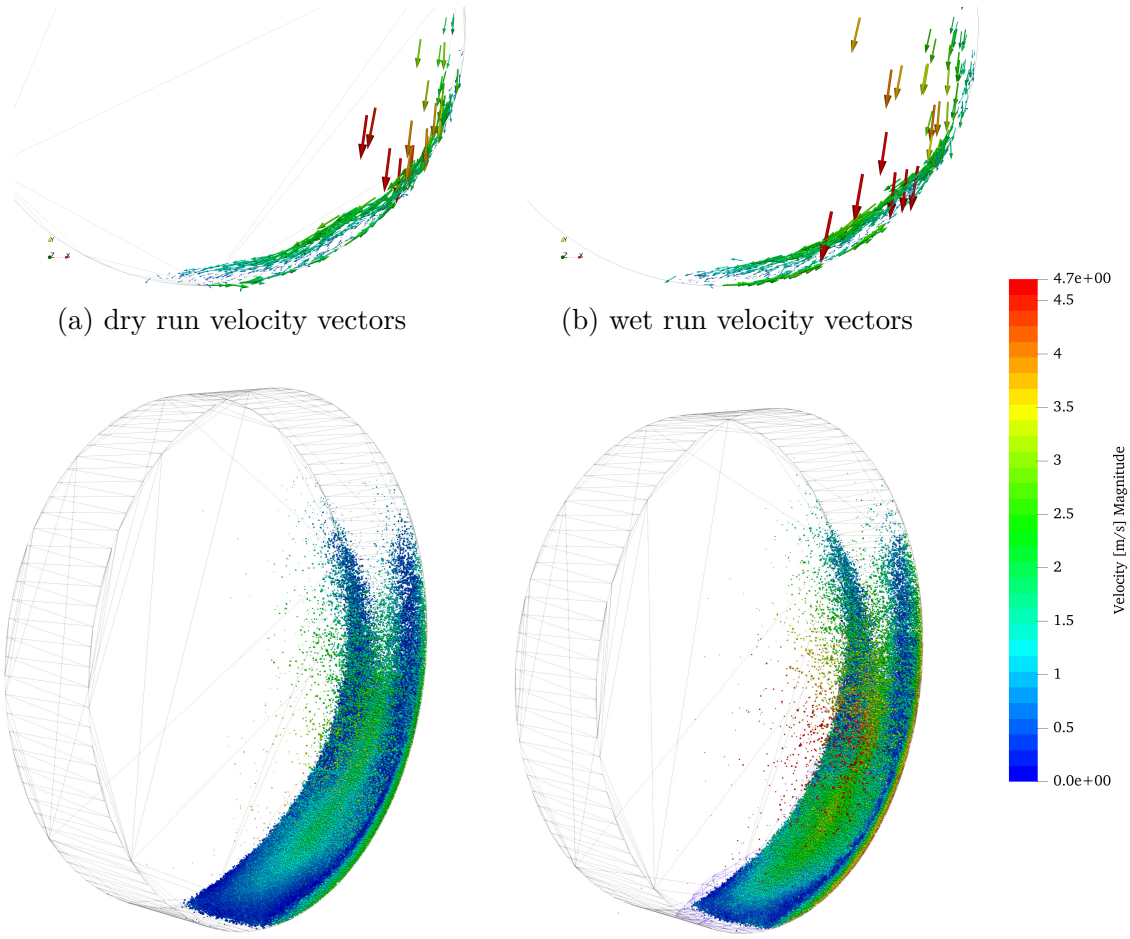

(a) dry run velocity vectors

(b) wet run velocity vectors

(c) dry run particle velocities

(d) wet run particle velocities

Figure 5.11: Comparison of gravel flow pattern using individual particle velocities

hydro-static and hydrodynamics forces acting on the particles clearly help more particles to be transported to the top of the drum. The particle bulk is rotating in a counter-clockwise manner. The gravel towards the bottom moves along with the rotating drum towards the top of the bulk. After nearing the top, due to various forces acting on the particles such as the gravitational and the force applied by the rotating drum, they rise to the top of the bulk i.e. away from the drum wall. As more and more particles fall, the top part of the layer starts moving. Thus a huge bulk of particles traverse towards the bottom of the drum. As they approach the bottom they still keep going beyond the central and the lowest points towards the left of the drum due to inertia. Subsequently, these particles are pulled down and toward the top of the bulk by the drum. A small layer in the middle with very low velocities shows behavior similar to the boundary layer i.e. transferring momentum from the fast-moving top and bottom layer to the particles inside.

In figures 5.11(c) and (d), the particle velocities for the dry and wet run respectively are presented. Both the results are scaled for the same velocity scale. This comparison shows the drastic increase in the gravel mobility when affected by the water. Furthermore, the wet gravel bulk cycles in the drum as a fluid, whereas the dry gravel bulk has significantly more stagnant areas, with only the central portion contributing to the gravel mobility.

In figure 5.12, the height profile for the gravel bulk at the initial stage (dry run) and final stage (wet run) are presented. The height profiles recorded by laser sensor are extracted from the original article [215]. To extract the height profiles of the numerical simulation, the post-processing tool ParaView [218]. The particles are rendered as spherical glyphs, visualized from the side, and colored with a single color. Then the opacity of the particles is reduced, thus revealing the particle bed. A poly-line source was used to then match the particle bed. The different in height profiles before and after introducing water, demonstrating the increased gravel bulk mobility. The height profiles from the CFD-DEM simulations are in good agreement with experimental observations. We would like to again highlight that as only one experimental observation is available it is difficult to quantify the accuracy.

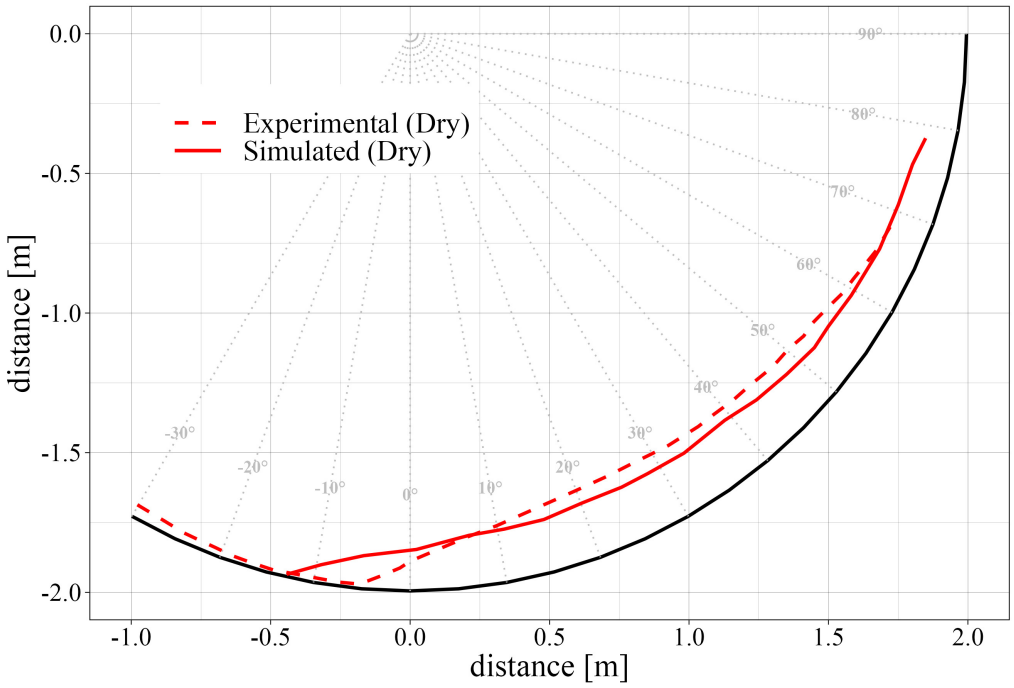

(a) Initial time (dry run)

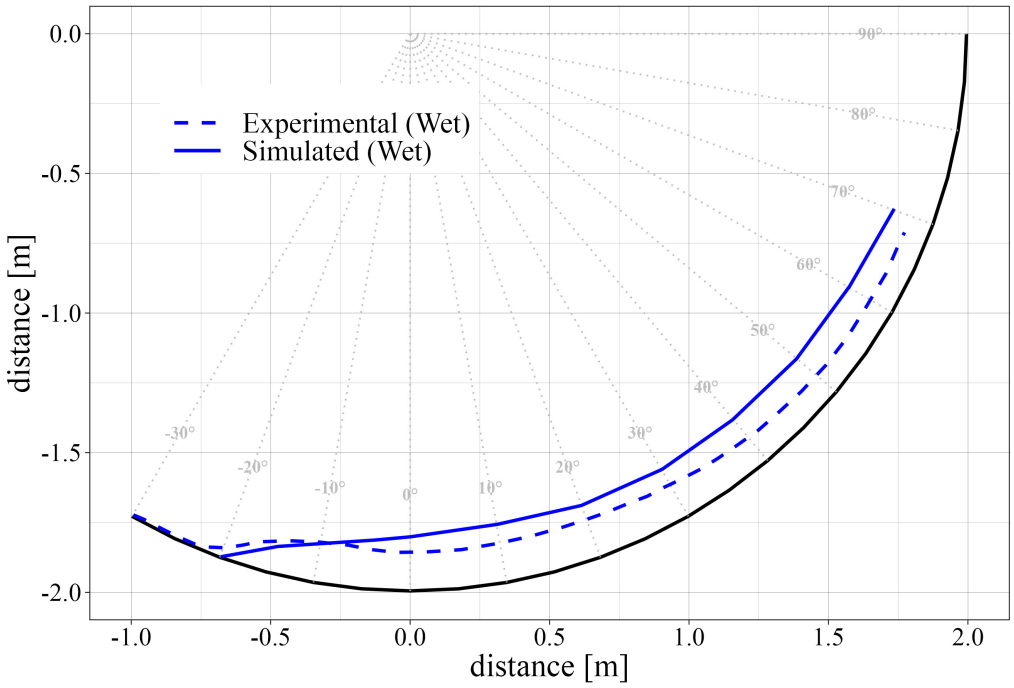

(b) Final Time (wet run)

Figure 5.12: Comparison of gravel height observed in experiment and computed in the simulations for the initial and final time

5.5.5 Insights into the numerical experiments of the rotating drum

In presented work, several numerical experiments were performed. In the previous sections, the numerical results are validated against the experimental observations. In this section, further insights are provided into the numerical experiments.

Insights on Segregation

The numerical experiments performed model particles of various radii. Thus it was interesting to investigate the segregation of the particles. Throughout all the numerical experiments,the particles of different radii are mixed quite thoroughly. Although, it is interesting to investigate the distribution of the particles with different radii.

In the figure 5.13, different threshold values are applied on the particle radii, thus showing lowest radius particles to the highest radius particles from left to right. The particles with lower radius thus lower weights, are transported the highest and the farthest into the rotating drum. In contrast, the particles with the higher radius are transported much closer to the drum wall. This demonstrates that due to the weight differences of the particles, they traverse different distances. It is also interesting to see how densely packed the higher radii particles are towards the lower part of the drum, especially the larger the particle the lower the position. Additionally heavier particles are transported higher, when they are closer to the side walls of the drum. The particles with radii of the middle values are thoroughly distributed in the rotating drum, although they as well do not traverse too much into the drum like the smallest particles. In summary, although the maximum possible distance is traversed by the smallest particles and vice versa, a thorough segregation of the particle of different radii is not observed.

Insights on modeling risers in the drum

In the presented work, numerical simulations are performed so as to replicate and investigate the experiments performed by Schneider et al. [215]. In these experiments the drum is originally smooth, and thus it is fitted with PVC pipe risers so as to provide physical hindrance to the gravel, thus increasing the friction offered by the drum to the particles and increase the

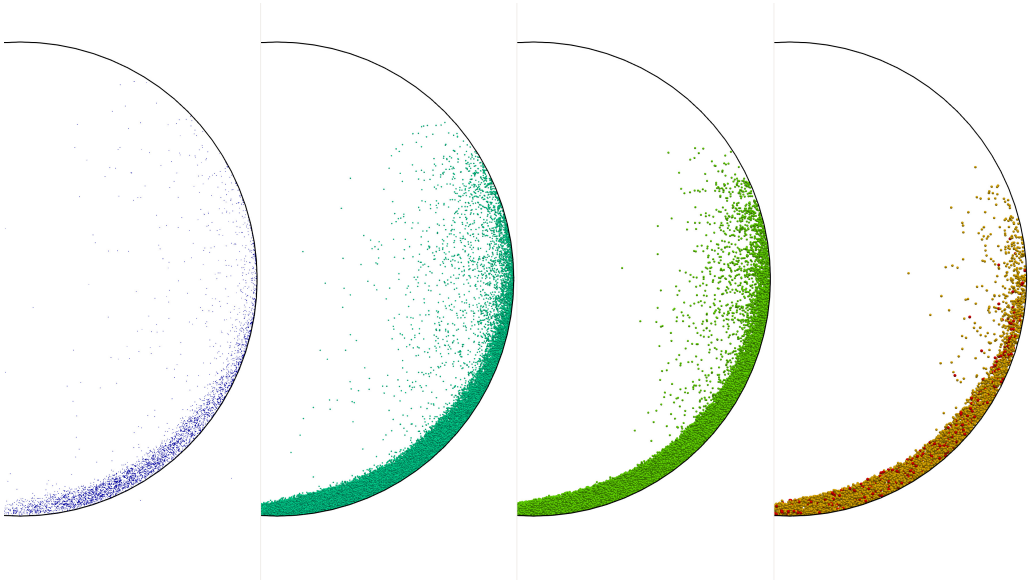

(a) Particle distribution viewed from the side

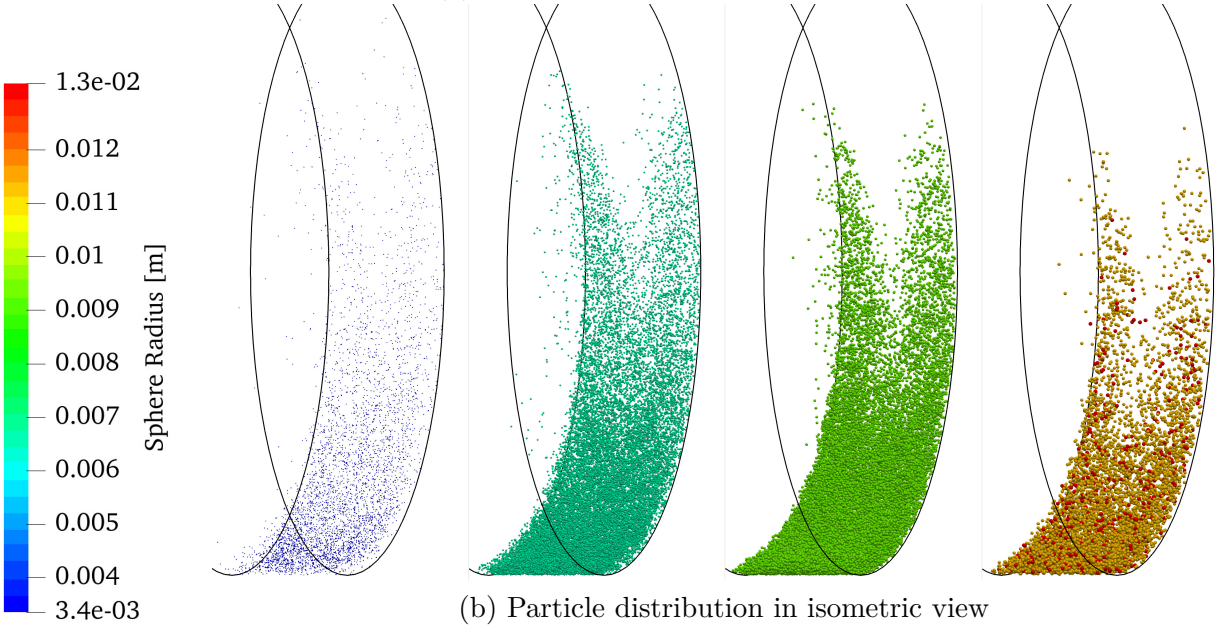

(b) Particle distribution in isometric view

Figure 5.13: Comparison of gravel height observed in experiment and computed in the simulations for the initial and final time

overall flow. In the current work, presented in previous sections, the drum is modeled without any such risers. The numerical model presented, instead models the friction numerically. In the section 5.5.4, this model shows that the simplified model yields results that are in good agreement with the experimental observations.

In this section, we provide an insight on numerical experiment performed on drums with risers. As described in the literature [215], the risers are square shaped with a length of 0.025 m. The numerical simulation conditions are identical to the ones presented in 5.5.1, except for the drum STL file. The numerical experiment starts similar to the dry run with the particle bed at the centre of the drum. Then, the particles are allowed to pack in the drum as before (similar 5.7). The particles are allowed to achieve a stability condition. The particle positions for for the drum with and without risers are presented in the figure 5.14. The particles in the drum with risers travel lot farther than the particles in the drum without risers. This is expected as the time step for the simulation with risers is inadequate to take into account for the higher velocities experienced by the particles. Furthermore, it can be seen that the particles constantly occupy the space between the height of the risers. It should be noted that the average height of the particle bed is 0.2 m, which is much higher than the risers. In the figure 5.15, a transparent view of the particle bed in the drum is illustrated. The transparency allows visualisation of the particle packing, and obscures the particles under free fall. Thus, the particle bed height can be measured for the two numerical experiments. In the figure 5.15, it can be see that the particle bed height for the drum with and without risers is almost the same.

The particle behaviour for the drum with the risers is correct given the simulation conditions. If the simulation parameters are adjusted and water is introduced, the gravel flow will be closer to the flow observed in the experiments. The introduction of risers, as discussed in the current section, significantly impacts computational demands. While keeping other simulation parameters constant, the incorporation of these elements elevates the computational load substantially, resulting in a five-fold increase in wall time.

The results presented here are only considering the dry run, i.e. we do not couple the particles with the fluid. If the coupling is need with the fluid, the fluid mesh will need to

account for the risers. Furthermore, as the risers are modeled explicitly, the CFD mesh will need to rotate as well, further complicating the model and increasing the computational cost.

This elevated computational burden is of particular relevance in the broader context of the intended application—simulating rock-ice avalanches. As these simulations inherently involve substantial computational resources, the current work aims to present a proof of concept by demonstrating the efficacy of the proposed Computational Fluid Dynamics-Discrete Element Method (CFD-DEM) model in approximating the frictional behavior of gravel in the presence of water. The model showcases promising results with reduced computational cost, laying the groundwork for scalability in larger-scale applications.

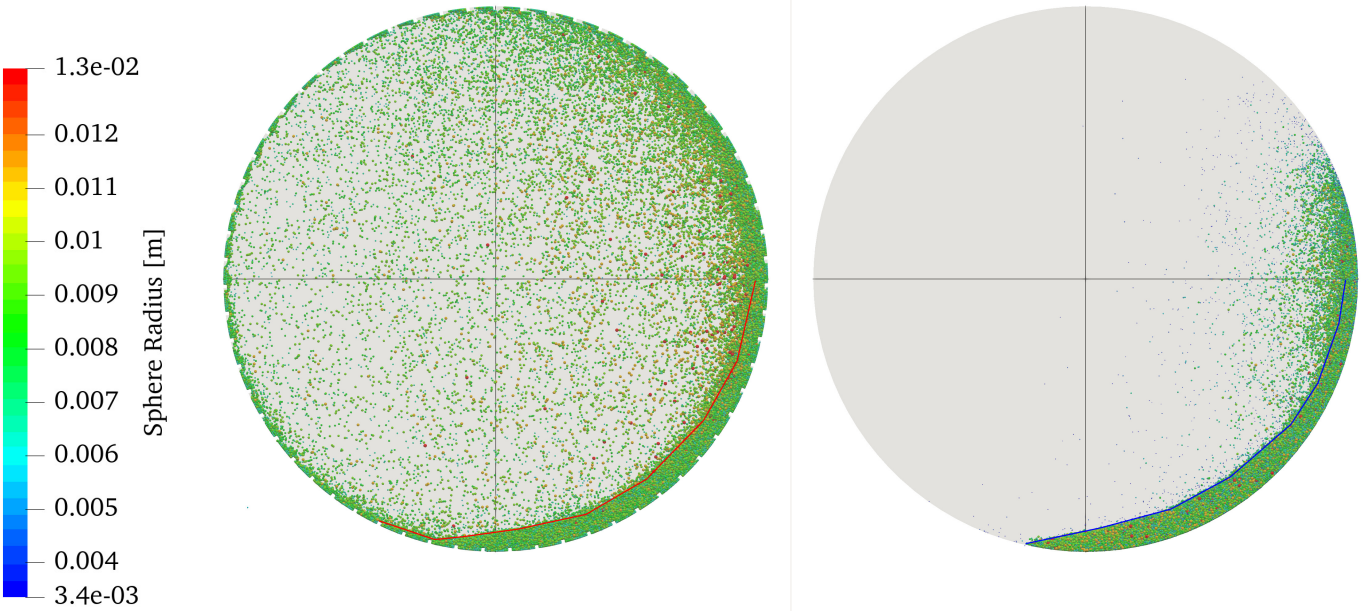

Figure 5.14: Comparison of the particle bed distribution within the drum with and without risers

Insights into varying friction coefficient for dynamic gravel behavior

In this section, we delve deeper into the numerical insights gained from the numerical experiments presented in the the section 5.5.3, particularly focusing onthe dynamic behavior

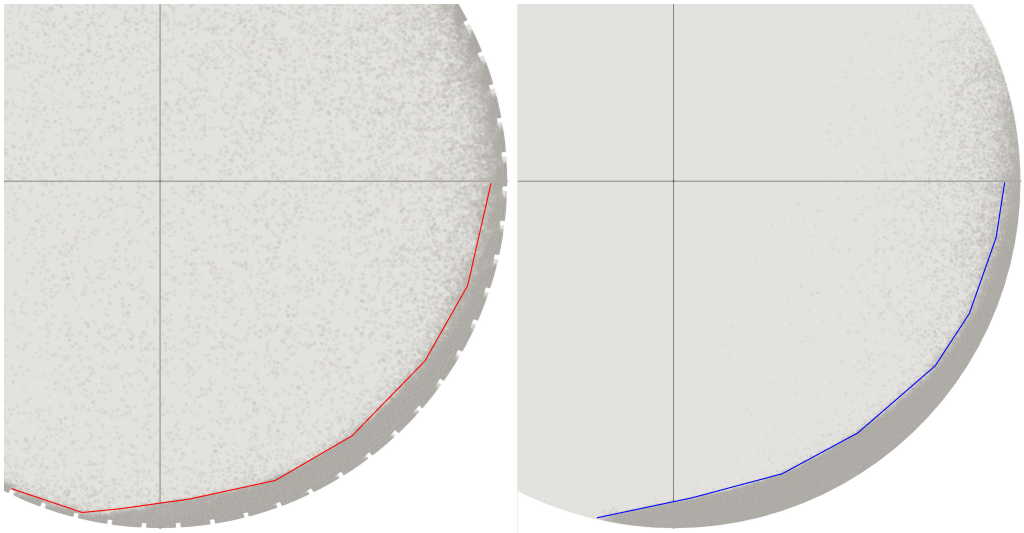

Figure 5.15: Comparison of the particle bed height for drum with (red) and without risers(blue)

of the gravel bulk during the water injection. The numerical simulations were performed by ad-hoc modification of the particle friction coefficients so as to emulate the wetting and lubrication effects. The final results i.e. the bulk friction coefficient obtained deviate from the experimental observations. Nevertheless, the insights obtained are valuable for understanding the complex interplay between particle interactions and hydrodynamic forces during the ice melting process.

It is crucial to emphasize that our approach of substituting the complex Volume of Fluid (VoF) model with reduced particle-particle friction, is distinct from conventional methods. The VoF model typically reduces friction through additional drag, whereas the ad-hoc friction variation model retains particle dynamics but directly alters friction coefficients. The decision to modify two distinct aspects of contact physics, particle dynamics and friction, stems from our intention to achieve comparable global flow behavior in the absence of a detailed wetting model.

Despite the discrepancies, the insights gained from our simulations provide valuable understanding of the interplay between wetting, friction, and hydrodynamic forces during ice melting. Future work could involve refining the friction variation model, exploring non-linear

variations, or incorporating more detailed wetting models to better replicate experimental observations.

5.6 Discussion

The rotating drum at Berkley [215] is modeled in the current work. For the dry gravel presented in section 5.5.1, the bulk friction coefficient is 0.53, which is a 4% overestimation as compared to the experimental observations. When water is added to model the melted ice presented in section 5.5.2, the final bulk friction coefficient is 0.275, which is a 11% underestimation as compared to the experimental observations. A dynamic change in bulk frictional behavior by varying the friction coefficient of the particles and/or drum, as presented in section 5.5.3. The current CFD-DEM rotating drum with gravel model is in good agreement with the experimental observations as demonstrated in section 5.5.4. It should be noted that only one experimental observation is available for the current ice-rock mixture, hence it is difficult to judge the exact accuracy of the simulation results.

This work demonstrates that the CFD-DEM model is robust to model debris flow and the effects of water (melted ice) on its flow characteristics. With the model presented in this work, we can vary the gravel-ice mixture ratios as has been done in the experiments [215]. In the future, we can study the same phenomenon for different-sized and shaped gravel, and make predictions on the frictional behavior of such gravel-ice mixture and its implications on rock-ice avalanches. Thus giving an insight into debris flow under different conditions.

The robustness of the CFD-DEM model in simulating debris flow and its response to water (melted ice) highlights the potential of this approach. The flexibility to manipulate gravel-ice mixture ratios, akin to the experiments [215], offers a platform to investigate various conditions. This model can be extended to diverse gravel shapes and sizes, yielding predictions on frictional behavior and implications for rock-ice avalanches, providing valuable insights into debris flow dynamics under diverse conditions.

Future directions propose employing the XDEM suite's particle melting capabilities [103] to simulate ice particles melting within the gravel model. This will introduce a more realistic

ice-melting rate, enhancing the fidelity of the simulation. Additionally, the incorporation of risers, although mirroring experiment conditions, might yield similar bulk friction coefficient outcomes, considering the consistent frictional behavior demonstrated by the current simplified model.

To further improve the current model the CFD mesh around the water can be refined. This will allow us to capture the water interface more accurately. Thus improving the results obtained for the height profile of the gravel and water mixture at the end of the simulation (to be seen in figure 5.12). However one must weigh the computational cost against the possible gain in the accuracy of the numerical predictions. We believe that the coarse mesh used in the current study provides good results with low computational cost.

5.7 Conclusion

The current study successfully models the large rotating drum experiment done by Schneider et al. [215]. The numerical study presented encompasses several scenarios, demonstrating the intricate dynamics of the geophysical flows impacted due to the presence of water (originating from melting ice). The changes in the frictional behavior observed are in line with the experimental observations. The Eulerian-Lagrangian CFD-DEM coupling replicates the initial and final states of the rotating drum experiment, effectively capturing changes in frictional behavior. Although experimental constraints hinder comprehensive testing, our numerical approach offers a scalable alternative to explore diverse scenarios. This research opens avenues for deeper understanding and mitigation strategies for catastrophic geophysical flows, contributing to enhanced safety and risk management worldwide.

5.8 Nomenclature

	Scalars
c_p	Specific Heat $(J/(Kg.K))$
d	Particle diameter (m)
I_i	Moment of inertia $(kg.m^2)$
m	Mass (kg)
m'	Mass source $(kg/m^3.s)$
p	Pressure (Pa)
q'	Heat source (W/m^2)
q''	Heat flux (W/m^2)
r, R	Radius (m)
t	Time (s)
T	Temperature (K)
T_{final}	Length of simulation (s)

	First order tensor (vectors)
$\vec{g}$	Acceleration due to gravity (m/s)
$\vec{F^c}$	Contact Forces (N)
$\vec{F^g}$	Gravitational Force (N)
$\vec{F^{ext}}$	External Forces (N)
$\vec{F_B}$	Buoyancy Force (N)
$\vec{F_D}$	Drag Force (N)
$\vec{M_{i,j}}$	torque generated by inter-particle forces $(N.m)$
$\vec{S}$	Momentum source due particles
$\vec{v}_f$	Fluid velocity field
$\vec{X_i}$	Positional vector (m)
$\vec{\omega}$	Rotational velocity (rad/s)

	Greek symbols
α	Heat transfer coefficient $(W/(m.K))$
β	Momentum exchange $(kg/(m^3.s)$
∂	Differential operator (-)
ϵ	Volume Fraction/Porosity (-)
μ	Kinematic viscosity $(Pa.s)$
∇	Nabla operator (-)
ρ	Density (kg/m^3)

	Subscripts
c	Cell
$cond$	Conduction
eff	Effective values
f	Fluid
i, j	Particle
n	Normal direction
p, P	Particle
rad	Radiation
t	Tangential direction

Chapter 6

Three-dimensional CFD-DEM simulation of raceway transport phenomena in a blast furnace[1]

[1]The content of this chapter is published in Fuel [2]

6.1 Abstract

Improving energy efficiency in a blast furnace (BF) has a significant effect on energy consumption and pollutant emission in a steel plant. In the BF, the blast injection creates a cavity, the so-called raceway, near the inlet. On the periphery of the raceway, a ring-type zone is formed which is associated with the highest coke combustion rate and temperatures in the raceway. Therefore, predicting the raceway size or in other words, the periphery of the ring-type zone with accuracy is important for estimating the BF's energy and coke consumption. In the present study, Computational Fluid Dynamics (CFD) is coupled to Discrete Element Method (DEM) to develop a three-dimensional (3D) model featuring a gas-solid reacting flow, to study the transport phenomena inside the raceway. The model is compared to a previously developed two-dimensional (2D) model and it is shown that the assumptions associated with a 2D model, result in an overestimation of the size of the raceway. The 3D model is then used to investigate the coke particles' combustion and heat generation and distribution in the raceway. It is shown that a higher blast flow rate is associated with a higher reaction rate and a larger raceway. A 10% increase in the inlet velocity (from 200 m/s to 220 m/s) caused the raceway volume to grow by almost 40%. The DEM model considers a radial discretization over the particle, therefore the heat and mass distributions over the particle are analyzed as well.[2]

6.2 Introduction

The ironmaking industry produces 7% of the world's total carbon dioxide emissions [219]. The most frequent ironmaking process is the blast furnace (BF), accounting for more than 70% of total energy consumption in the ironmaking industry [220] and 90% of the $CO2$ emission [221]. As a result, lowering energy usage and gas pollution in the BF ironmaking operations has received a lot of attention [222].

The region inside the furnace which is created by injecting hot blast air into the coke bed is called the raceway. Its shape is affected by different parameters such as blast velocity,

[2]The content of this chapter is published in Fuel [2]

the geometry of the nozzles, and operational circumstances [223]. Therefore, the study of the raceway is vital to analyze the gas species distributions and heat supplies which, directly have an impact on the furnace's productivity and efficiency. As a result, the raceway has been comprehensively studied, especially the principles of the particle scale. Experimental and computational methods have been used extensively to study raceway phenomena over the past few decades. As a consequence of the severe operating circumstances within the actual BF process (e.g., high temperature and pressure situations), measurement during an experimental test is difficult to undertake and only a few studies have worked on this with very limited data, such as gas species distributions [224]. For example, Matsui et al. [225] used microwave reflection gunned via a tuyere to study the BF raceway formation under heavy coal injection rate circumstances. Sastry et al. [226] studied the particle system in a two-dimensional (2D) cold model. In another study, Sastry et al. [227] conducted experimental research in a packed bed and found that the characteristics of coke particles had a significant impact on cavity development and breakdown. Zhang et al.[228] used an image-based flame detection approach to investigate the combustion characteristics of a BF raceway and discovered that the raceway temperature profile could fluctuate considerably. These experimental studies despite helping us gain a better picture of how raceways work can only explain BF functioning at the macro-scale information such as pressure and temperature in the local spots and are not able to obtain the micro-scale information such as inter-particle/phase interactions, raceway shape/size, heat transfer, coke combustion.

In light of the limitations of experimental research and the difficulty of performing accurate measurements, numerical simulations are generally employed to study raceway phenomena. Numerical simulations are divided into two common categories: Eulerian-Eulerian and Eulerian-Lagrangian. Mondal et al. [229] studied the influences of the air blast velocity on the shape and size of the raceway zone in a BF by using the Eulerian-Eulerian model. However, the Eulerian-Eulerian model has no capacity of obtaining information such as particle and phase interactions, particle residence time, and particle trajectory [230]. Besides the simple assumptions of inter-particle collisions in this method make it difficult to adequately capture numerous inter-particle collisions near the tuyere and the quasi-static-regime in the deadman

region and the associated flow features[231]. Such difficulties can be overcome by one of the important Eulerian-Lagrangian methods, the discrete element method (DEM) coupled with Computational Fluid Dynamics (CFD) named CFD-DEM. In recent years, many studies have applied CFD-DEM methods to investigate the raceway's information. For example, Xu et al. [232] proposed CFD-DEM methods to study gas fluidization on fixed and fluidized beds. To comprehend raceway formation, they illustrated that this method can capture gas-solid flow characteristics ranging from large scale (such as processing equipment) to little scale features (such as each particle). Feng et al. [233] developed a 2-dimensional model to study the particle flow in the modeling of BF, finding that both solid and gas phases flow are changed spatially and temporally, in particular in the cohesive zone, which is affected by the layered ore and coke particle structure. Yuu et al. [234] compared the characteristics of the raceway such as depth and heights with experimental data and additionally reported dynamic characteristics such as the flow of solid particles, and the airflow around the raceway. Hilton and Cleary [235] used a discrete approach and observed the effect of injection velocity and bed pressure on the formation of raceway and investigate those non-spherical particles, as opposed to spherical particles, can form the raceways at higher gas input velocities. Wang and Shen [236] developed a reacting model to study raceway formation at the particle scale and discussed the impacts of several factors on raceway combustion (such as inlet velocity, temperature, and oxygen mass fraction). To examine raceway formation, Miao et al. [237] published a 2D CFD-DEM model for full-scale BF conditions and showed that in comparison to the studies in the laboratory circumstance, the raceway parameters are substantially more complicated in full-scale BF. Cui et al. [143] used a particle scale CFD-DEM method to study the raceway cavity shape and its parameters such as heat source, mass source, and chemical reactions and additionally the effect of the gas inlet velocity, size of particles, and particle discharge rate on the raceway formation. Dianyu et al. [238] also developed a 2D CFD-DEM model to analyze the effect of parameters such as particle size and oxygen enrichment on raceway formation and gasification rate. Recently, there has been an increasing interest in operating furnaces using renewable fuels, such as hydrogen, and many researchers have used CFD simulations to prove their efficiency[239, 240, 241]. Though this study does not consider

renewable fuels, its findings can be applied to such endeavors.

The present study emphasizes the superior ability of 3D models over 2D models to predict the behavior of raceways. Therefore a 3D particle-scale CFD-DEM model of a BF raceway is developed. Using radial discretization, heat and mass transfers within particles are solved, therefore the internal gradients of particles are seen. The developed model incorporates oxidation reactions within the particles and heat and mass transfer between particles and the gas. Additionally, the impact of parameters such as inlet velocity and particle mesh on raceway size and temperature distribution is discussed. In section 6.3 the governing equations of CFD and DEM models are presented along with the details of coupling techniques. In section 6.4 the results of the validation of the 3D model is presented. Then, using the comparisons between the 2D and 3D models it is argued that the inherent assumptions associated with 2D models make it unable to predict the raceway dynamics with precision. In the same section the results from the 3D model are presented and discussed. It is also shown that the discretization of the particles in the DEM model can have significant effect on the predicted size of the raceway and the gas temperature.

6.3 Model Description

XDEM software[64] is used in the current work. This software uses Lagrangian-Eulerian approach to for CFD-DEM coupling. Its multi-scale and multi-physics framework considers particles as discrete entities while fluid as a continuous medium.

6.3.1 Governing equations for discrete particles

XDEM predicts both dynamics and thermodynamics of the particulate system. The particle position, velocity and acceleration are calculated with the dynamics module of the XDEM, where as the temperature, and processes like combustion, gasification, drying etc are calculated with the conversion module of the XDEM.

	Physical constants/Greek symbols
α	Heat transfer coefficient $(W/(m^2.K))$
β	Inter-phase momentum exchange $(kg/(m^3.s))$
ϵ	Porosity
λ_f	Thermal conductivity $(W/(m.K))$
μ	Dynamic viscosity $(Pa.s)$
η	Weight of particle for porosity calculation
Ω_c	Implicitly treated drag term $(1/s)$
ρ	Density (kg/m^3)
	Operators
∂	Differential operator (-)
Δ	Difference (-)
∇	Nabla operator (-)
	Scalars
A	Surface Area
c_p	Specific Heat $(J/kg.K)$
C_d	Drag Coefficient (-)
d	Particle diameter (m)
h	Convective heat transfer coefficient $(W/(m^2.K))$
I_i	Moment of inertia $(kg.m^2)$
m	Mass (kg)
m'	Mass source $(kg/(m^3.s))$
p	Pressure (Pa)
q'	Heat source (W/m^2)
q''	Heat flux (W/m^2)
r, R	Radius (m)
Re	Reynolds number (-)
t	Time (s)
T	Temperature (K)
T_{final}	Length of simulation (s)
V	Volume (m^3)

	Subscripts
c	Cell
$cond$	Conduction
d	Drag
eff	Effective values
f	Fluid
i, j	Particle
n	Normal direction
p, P	Particle
s	Solid
rad	Radiation
t	Tangential direction
	Superscripts
n	Geometry exponent
(n)	n^{th} (time) step
$(n+1)$	n^{th} (time) step +1
	First order tensors (vectors)
$\vec{A_c}$	Acceleration on fluid cell due to explicitly treated drag term (m/s^2)
$\vec{g}$	Gravitational acceleration (m/s)
$\vec{F^c}$	Contact Forces (N)
$\vec{F^g}$	Gravitational Force (N)
$\vec{F^{ext}}$	External Forces (N)
$\vec{F_B}$	Buoyancy Force (N)
$\vec{F_D}$	Drag Force (N)
$\vec{M_{i,j}}$	Torque generated by inter-particle forces $(N.m)$
$\vec{v_f}$	Fluid velocity field
$\vec{X_i}$	Positional vector (m)
$\vec{\omega}$	Rotational velocity (rad/s)

Table 6.1: Nomenclature

Dynamics module

The Discrete Element Method (DEM) used in the dynamics module of XDEM is based on the soft sphere model. In this method, it is assumed that the particles are deformable and can overlap each other, where the magnitude of overlap is decided by the contact force using the force-displacement law. The hardness of the particle is expressed via Young's Modulus, while the particle energy dissipation is described with dampener and/or dash-pot. The translational and rotational movements of individual particles are tracked using the classical mechanics equations. A detailed description of all the terms mentioned below could be found in previous work [103]. A summary of the translational and rotational motion equations is given below: Equations of particle motion:

$$m_i \frac{d\vec{v_i}}{dt} = m_i \frac{d^2\vec{X}_i}{dt^2} = \vec{F_i^c} + \vec{F_i^g} + \vec{F_i^{ext}} \tag{6.1}$$

where $\vec{F_i^{ext}}$ is the sum of all the external forces acting on the particle, such as buoyancy forces $\vec{F_B}$ (Eq 6.25) and drag forces $\vec{F_D}$ (Eq 6.26).

$$I_i \frac{d\vec{\omega_i}}{dt} = \sum_{j=1}^{n} \vec{M_{i,j}} \tag{6.2}$$

Conversion module

The particles a modeled with pores/voids. These pores are modeled to have a gaseous mixture of different chemical species. Mass conservation equation for fluid within particles pores:

$$\frac{\partial}{\partial t}\left(\epsilon_f \rho_f\right) + \vec{\nabla} \cdot \left(\epsilon_f \rho_f \vec{v_f}\right) = m'_{s,f} \tag{6.3}$$

One dimensional transient energy conservation equations for particles:

$$\frac{\partial \rho c_p T}{\partial t} = \frac{1}{r_n}\frac{\partial}{\partial r}\left(r^n \lambda_{eff} \frac{\partial T}{\partial r}\right) - r^n \left(\vec{v}\rho_f c_{p_f} T\right) + \sum_{k=1}^{l} \dot{\omega_k} H_k \tag{6.4}$$

The mass balance and transport equation of individual fluid species within the particle pores:

$$\frac{\partial}{\partial t}\left(\epsilon_f \rho_{f,i}\right) + \nabla \cdot \left(\epsilon_f \rho_{f,i} \cdot \vec{v_f}\right) = \frac{1}{r_n}\frac{\partial}{\partial r}\left(r^n \epsilon_f D \frac{\partial \rho_{f,i}}{\partial t}\right) + m'_{s,f,i} \tag{6.5}$$

Following boundary conditions are applicable to the governing equations mentioned above:

$$-\lambda_{eff}\frac{\partial T}{\partial r}\bigg|_{r=0} = 0 \tag{6.6}$$

$$-\lambda_{eff}\frac{\partial T}{\partial r}\bigg|_{r=R} = \alpha(T_R - T_\infty) + q''_{rad} + q''_{cond} \tag{6.7}$$

$$-D_{i,eff}\ \frac{\partial \rho_i}{\partial r}\bigg|_{r=R} = \beta_i\left(\rho_{i,R} - \rho_{i,\infty}\right) \tag{6.8}$$

In the Eq 6.7, q''_{cond} and q''_{rad} are conduction and radiation heat source respectively from the neighbouring particles. The detailed description of the conduction and radiation between particles is given in B. Peters [148].

In the conversion module of XDEM, a radial discretization is considered to solve for heat & mass transfer within the particle. This radial discretization can be uniform or non-uniform, as shown in fig 6.1. In the current work, non-uniform radial discretization is utilized. The non-uniform radial discretisation allows to have smaller cell length near the particle surface that allows the model to capture the sharp temperature and mass flow gradients.

6.3.2 Governing equations for fluid

In Eulerian volumetric average method, the conservation equation of mass (Eq 6.10), momentum (Eq 6.11) and energy (Eq 6.12) are written over a representative volume, where porosity (ϵ Eq 6.9) refers to the interstitial solid space particles. These governing equations for fluids are given below. Detailed description of the porosity calculation can be found in [103], the porosity calculation in brief is as follows, where V_c is CFD cell volume, V_i is the

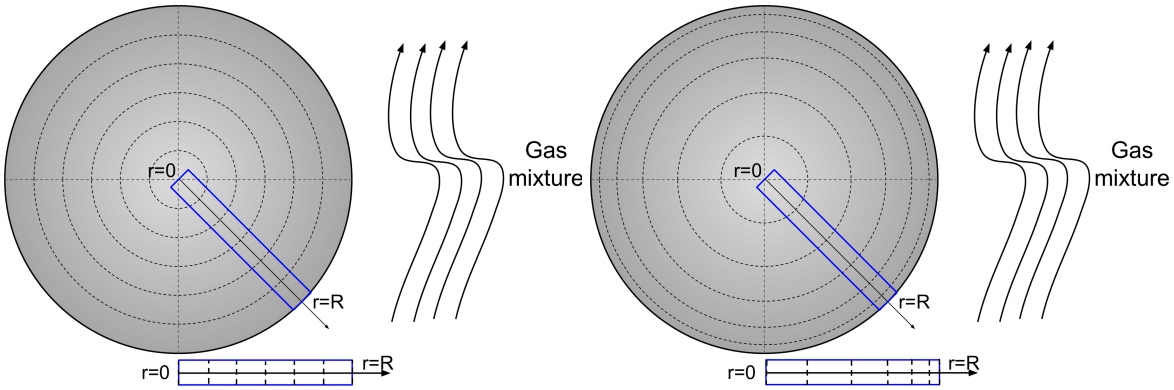

(a) Uniform discretization (b) Non-Uniform discretization

Figure 6.1: Radial discretization for heat & mass transfer within a particle

particle volume of i^{th} particle in the CFD cell and η is weight for porosity calculation:

$$\epsilon = 1 - \frac{1}{V_c} \sum_{i}^{n} \eta_i V_i \tag{6.9}$$

Conservation of mass

$$\frac{\partial}{\partial t} (\epsilon \rho_f) + \nabla \cdot (\epsilon \rho_f \vec{v}_f) = m' \tag{6.10}$$

Conservation of momentum

$$\frac{\partial}{\partial t} (\epsilon \rho_f \vec{v}_f) + \nabla \cdot (\epsilon \rho_f \vec{v}_f \vec{v}_f) = -\epsilon \nabla p + \epsilon \rho_f \vec{g} + \epsilon \rho_f \vec{A_c} + \epsilon \mu \nabla^2 \vec{v}_f - \epsilon \rho_f \Omega_c \vec{v}_{f_c} \tag{6.11}$$

Conservation of energy

$$\frac{\partial}{\partial t} (\epsilon \rho_f h_f) + \nabla \cdot (\epsilon \rho_f \vec{v}_f h_f) = \frac{\partial p}{\partial t} + \epsilon \vec{v}_f \cdot \nabla p + q' \tag{6.12}$$

Chemical reactions are also considered in the CFD solver. In a multi-species gas mixture, the mass conservation equation for a species i, is given in Eq 6.13:

$$\frac{\partial}{\partial t} \epsilon \rho_{f,i} + \nabla \cdot (\epsilon \rho_{f,i} \cdot \vec{v}_f) = m_i' \tag{6.13}$$

6.3.3 Chemical reactions

The current study focuses on the raceway and areas immediately next to raceway. In this region mainly gasification and combustion reactions are observed in the particles, the (solid phase) reactions are presented in Eq 6.14, 6.15, and 6.16. Considering the temperatures in and near raceway, the reaction 6.14 producing CO is mainly observed. Some small amount CO_2 is produced as shown in reaction 6.15, but due to high temperatures ($\geq$ 1073 K [242]) it quickly decomposes to CO as shown in gas phase reaction 6.16.
The gasification reactions are as follows:

$$\mathrm{C} + 0.5\,\mathrm{O_2} \rightarrow \mathrm{CO} \tag{6.14}$$

$$\mathrm{C} + \mathrm{O_2} \rightarrow \mathrm{CO_2} \tag{6.15}$$

$$\mathrm{C} + \mathrm{CO_2} \rightarrow 2\,\mathrm{CO} \quad \text{(Boudard's reaction)} \tag{6.16}$$

As opposed to the previous reactions, reaction 6.17 is taking place in purely gaseous state (handled by CFD solver). Due to the high temperatures in the region of interest, it is observed that the CO_2 produced from the following chemical reactions, converts back to CO according to reaction 6.16.

$$\mathrm{CO} + 0.5\,\mathrm{O_2} \rightarrow \mathrm{CO_2} \tag{6.17}$$

Generally reactions can be written as follows:

$$\sum_{i=1}^{N} \nu_i' R_i \rightleftharpoons \sum_{j=1}^{M} \nu_j'' P_j \tag{6.18}$$

where N denotes the number of reactants R_i, M denotes the number of products P_j and $\nu_{i/j}$ represents the absolute values of the corresponding stoichiometric coefficient.

$$\dot{\omega} = -\frac{1}{\nu_i'}\frac{dc_i}{dt} = \frac{1}{\nu_j''}\frac{dc_j}{dt} \tag{6.19}$$

The actual reaction rate $\dot{\omega}$ may depend on species concentrations, the available reactive surface O_{sp} and the temperature; so that in general $\dot{\omega} = f(c_i, c_j, O_{sp}, T, \ldots)$. Thus, an Arrhenius law is employed to describe the temperature dependency of the reaction rate as

$$k(T) = k_0 \, e^{\left(\frac{-E_a}{RT}\right)} \tag{6.20}$$

where $k(T)$ represents the temperature dependent rate coefficient, k_0 referred to as frequency factor and E_a denotes the activation energy.

If thermodynamic equilibrium is reached, then an equilibrium constant $K_{\mathrm{eq,c}}$, representing the thermodynamically equilibrium state, can be obtained as

$$K_{\mathrm{eq,c}}(T) = \frac{k_f(T)}{k_b(T)} = \frac{\prod_{j=1}^{M} c_{\mathrm{eq},P_j}^{\nu_j''}}{\prod_{i=1}^{N} c_{\mathrm{eq},R_i}^{\nu_i'}} \tag{6.21}$$

In the XDEM software, the equilibrium constant $K_{\mathrm{eq,c}}(T)$ is calculated as

$$K_{\mathrm{eq,c}}(T) = e^{\frac{A_{eq}}{T} + B_{eq}} \tag{6.22}$$

where A_{eq} and B_{eq} are constant values that may come from existing tables or from equilibrium diagrams of phase diagrams.

Variable	**Reaction 6.14**	**Reaction 6.17**
E_a	$149,000$	$20,129$
A_{eq}	0	$2.24e+08$
B_{eq}	0	0
Temperature Range	$273K$ to $1500K$	

Table 6.2: Chemical reaction rates

6.3.4 CFD-DEM Coupling

The CFD-DEM coupling is achieved through conventional staggered approach. In this approach, the output from one simulation (solver) is used as an input for the other. Considering current work, assume that solver S_1 is the CFD solver, and the solver S_2 is DEM solver. The fluid solver S_1 solves the momentum, mass, reactions and energy equations for the fluid. The fluid solver output such as the fluid velocity, temperature, species mass fraction etc., are then used as boundary conditions for the particles in DEM solver S_2. The DEM solver S_2 uses solution from CFD solver, to compute various source terms by computing the momentum and energy equations for particles. In the next time step, these source terms are communicated to the fluid solver S_1, which then uses the solution from n^{th} time step to get a new solution for the $(n+1)$ time step.

$$x_2^{(n+1)} = S_1^{(n)}\left(x_1^{(n)}\right) \tag{6.23}$$

In Eq 6.23, CFD solver S_1 uses old time step's boundary value (or in case of first time step it can be the boundary conditions or an initial guess), $x_1^{(n)}$to compute the values of x_2 for next time step $x_2^{(n+1)}$. During this time, DEM solver S_2 waits for CFD solver S_1 to compute solution and exchange the updated solution $x_2^{(n+1)}$.

$$x_1^{(n+1)} = S_2^{(n)}\left(x_2^{(n+1)}\right) \tag{6.24}$$

In Eq 6.24, the updated solution x_2 is used to update the solution for x_1 for the next time step. This can also be seen graphically in Fig 6.2.

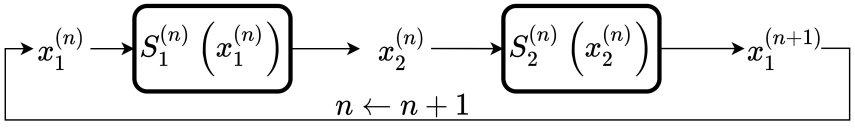

Figure 6.2: Serial Staggered Coupling Scheme

Fluid forces on particles

There are two types of fluid forces acting on the particles, namely hydro-static force and hydrodynamic force. The hydro-static force is the buoyancy force which accounts for the pressure gradient around an individual particle [108].

$$\vec{F_B} = -V_{p_i} \nabla p \tag{6.25}$$

In the Eulerian-Lagrangian approach, the hydrodynamic force corresponds to the fluid-particle interaction. This force depends on the relative velocity of the solid particle and fluid along with the forces acting due to presence of neighbouring particles. The drag force acting on the particle due the fluid for CFD-DEM approach is given as follows:

$$\vec{F_D} = \frac{\beta V_p}{(1-\epsilon)} (\vec{v_f} - \vec{v_p}) \tag{6.26}$$

The inter-phase momentum exchange β is predicted according to Gidaspow [111]. Although to cover all range of void fraction (ϵ), Wen and Yu [116] ($\epsilon \geq 0.8$) and Ergun and Orning [117] ($\epsilon < 0.8$) equations are included.

$$\beta = \begin{cases} 150\dfrac{(1-\epsilon)^2}{\epsilon}\dfrac{\mu_f}{d_p^2} + 1.75(1-\epsilon)\dfrac{\rho_f}{d_p}|\vec{v_f} - \vec{v_p}|, & \text{if} \quad \epsilon < 0.8 \\ \dfrac{3}{2}C_d\dfrac{\epsilon(1-\epsilon)^2}{d_p}\rho_f|\vec{v_f} - \vec{v_p}|\epsilon^{-2.65}, & \text{if} \quad \epsilon \geq 0.8 \end{cases} \tag{6.27}$$

where the drag coefficient C_d is given as:

$$C_d = \begin{cases} \dfrac{24}{Re}\left[1 + 0.15(Re)^{0.687}\right], & \text{if} \quad \text{Re} < 1000 \\ 0.44, & \text{if} \quad \text{Re} \geq 1000 \end{cases} \tag{6.28}$$

and the Reynolds number for the particle is given as:

$$Re = \frac{\epsilon \rho_f |\vec{v_f} - \vec{v_p}| d_p}{\mu_f} \tag{6.29}$$

Particle momentum source terms

In the fluid, the drag exerted by the solid particles is treated in semi-implicit way according to the method proposed by Xiao and Sun[118]. The explicit momentum source term $\vec{A_c}$ and implicit momentum source term Ω_c are as given in Eq 6.30

$$\vec{A_c} = \frac{1}{\rho_f V_c} \widetilde{\sum}_i B_i \vec{u_{p_i}}, \quad \Omega_c = \frac{1}{\rho_f V_c} \sum_{i=1}^{c_n} B_i \tag{6.30}$$

Particle heat and mass source terms

Fluid flow conditions such as fluid temperature, specific heat, thermal conductivity, species mass fractions are exchanged from CFD to DEM. These are used as boundary conditions for solving energy balance, mass balance and reaction equations for particles.

Based on the energy balance equations, heat loss/gain due convection or due to change in composition of particles is computed. This is used as the (explicit) heat source in fluid energy equation. Similarly, mass source and species mass fraction source are computed.

$$q_i' = h_i A_i (T_{p_i} - T_f) \tag{6.31}$$

where h_i is the heat transfer coefficient for a given particle i, which is a function of Re, Pr, λ_f, d_p and cell porosity.

As there are different phenomenon driving mass transfer, such as evaporation, mass flux due to the gradient of species concentration, species production due to chemical reactions, a generalised way to represent individual species mass source is as follows:

$$m'_{s,f,i} = (\text{Area of Mass Transfer}) \times (\text{Mass Transfer Coefficient}) \times (\text{Driving Force}) \tag{6.32}$$

The total mass transfer is summation of all the species mass transfer terms.

$$m' = \sum_i m'_{s,f,i} \tag{6.33}$$

6.3.5 Computational Procedure

A schematic for the CFD-DEM coupling is shown in fig 6.3. For the , XDEM and OpenFOAM libraries are linked together as a single executable. The simulations starts after running the executable. In the first step, DEM is initialized, where all the particles, walls, domain and XDEM mesh are created. After creating the mentioned assets, initial boundary conditions for the particles are applied. An initial porosity (ϵ) field is computed. Next CFD is initialized, where geometry and mesh is generated, boundary conditions on the fluid domain are applied, as well as porosity is made available to CFD solver, so that CFD solver takes into account the presence of particles from the first time step itself. But, these particles do not contribute to any heat or mass source terms of the fluid governing equations at the first time step. After all the required initializations, the time loop starts. The fluid governing equations are solved by the CFD solver developed with the assistance of OpenFOAM. The data transfer between DEM and CFD is done via direct read/write in memory. All the data is stored on the OpenFOAM mesh. After exchanging the data from CFD to DEM, the CFD data is used as boundary conditions for the particles. XDEM then solves the governing equations for the particles, and writes output fields such as porosity, momentum, heat, mass and species mass fraction source. After writing the data, the time loop proceeds to next time step ($T + dT$). In this time step, the data written by XDEM i.e various source terms, are injected in fluid governing equations. In this way the simulation continues until the specified end time T_{final}.

6.3.6 Simulation setup

For the simulations presented, the region of interest is only the raceway, and not the whole BF. The raceway is modeled as a 3D box of dimension $0.6m \times 0.6m \times 1.5m$. For the 2D case the cross-section dimensions remain the same ($0.6m \times 1.5m$).

The boundary conditions for the CFD and DEM are described in the Table 6.3 and 6.4 respectively. It is assumed that the particles are preheated to 1300 K and the inlet air enters at a temperature of 1500 K. Since the primary purpose of this research is to demonstrate the effects of 3D simulations and particle discretization, the particles are spherical and of the

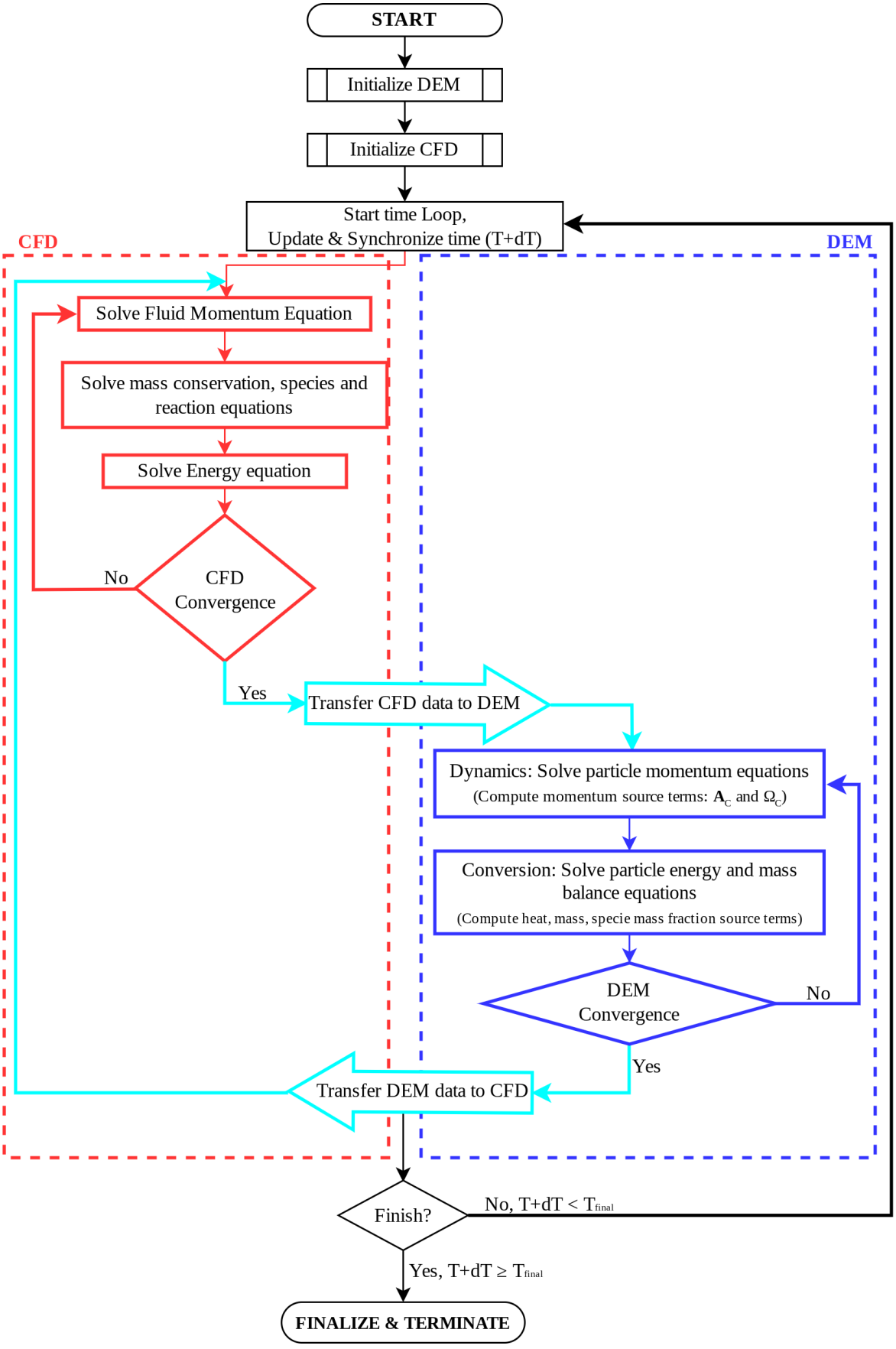

Figure 6.3: Flow chart of coupled OpenFOAM-XDEM solver showing calculation steps and exchange of data

Variable	Value
2D grid	20×50 1000 Hex elements
3D grid	$20 \times 20 \times 50$ $20,000$ Hex elements
Inlet Specie Mass fraction	
CO	$0.00\,[-]$
CO2	$0.00\,[-]$
N2	$0.79\,[-]$
O2	$0.21\,[-]$
Specie Mass fraction inside simulation domain	
CO	$0.0\,[-]$
CO2	$0.0\,[-]$
N2	$0.79\,[-]$
O2	$0.21\,[-]$
Time step length	$0.005\,s$
Simulated Time	$20.0\,s$
Temperature	
Inlet	$1500\,K$
Internal Domain	$1500\,K$
Turbulence Model	$k-\epsilon$ Reynold's Averaged Simulation (RAS)

Table 6.3: Simulation conditions for CFD

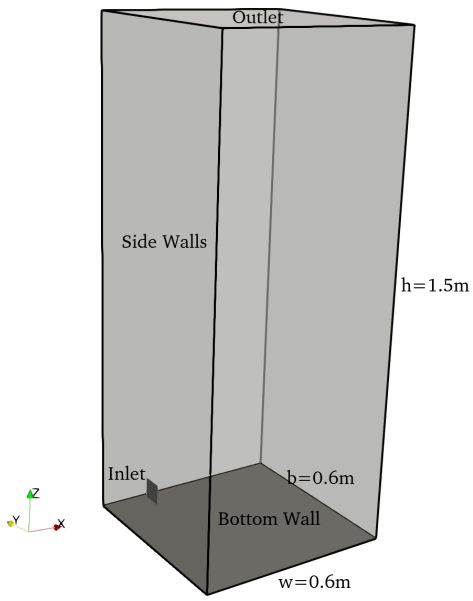

Figure 6.4: Simulation geometry and Boundaries

same size to eliminate particle shape and size effects.

6.4 Results and Discussion

6.4.1 Model validation

As it was explained in section 6.3, the CFD-DEM model used in this study is developed by coupling a CFD model in OpenFOAM and a particle system model in XDEM. The validations of the coupling have been presented in previous studies [64, 243]. For verifying the particle-scale reaction models and gas-solid reactive interactions, the resulting gas composition from the 3D model is validated against an experimental hot model [244].

Figure 6.5 shows the comparison of the simulation results for oxygen, nitrogen, and carbon monoxide against the experimental measurements. The results show that the model can predict the trend in coke combustion (oxygen consumption and carbon monoxide production) to an acceptable degree. However, there is a deviation between the predicted and measured values for oxygen and carbon monoxide which suggests and underestimated reaction rate for

Variable	Value
Particle Shape	Spherical
Particle Diameter	$0.01\,m$
Particle Density	$1111.1\,kg/m^3$
Particle Initial Temperature	$1300K$
Particle Composition	
Char (Solid)	$0.97\,[-]$
Light Ash (Solid)	$0.03\,[-]$
Number of particles	$10,000$
Particle radial discretization	5 uniform cells
Time step length	$0.005\,s$
Simulated Time	$20.0\,s$
Mechanical Properties	
Contact Model	Hertz Mindlin
Spring Constant	$100.0\,kN/m$
Viscous Contact Damping	$2420000.0\,N.s/m$
Friction Coefficient	$0.8\,[-]$
Poisson's Ratio	$0.45\,[-]$
Young's Modulus	$500000.0\,Pa/MPa$
Thermal Properties	
Thermal Conductivity	$0.47\,W/m.K$
Specific Heat	$1500\,J/kg.K$
Molar Mass	$30\,[-]$

Table 6.4: Simulation conditions for DEM

the coke combustion. The same level of deviation was also observed in previous studies [244, 238]. This deviation is rendered as acceptable considering the harsh measurement conditions inside the furnace and thus the uncertainty associated with the measurements.

6.4.2 Comparison of 2D and 3D simulations of raceway

First, we propose to study the differences between 2D and 3D simulations of the raceway. The 2D model is presented in a previous work [243]. As mentioned before, there have already been a lot of efforts in developing 2D models of the raceway and the BF. Simulations in 2D have the advantage of lower computational cost, but they come at the expense of numerical accuracy. Undoubtedly there should be a reasonable trade-off between the advantages and disadvantages. In the present work, 2D and 3D simulations are compared and the results

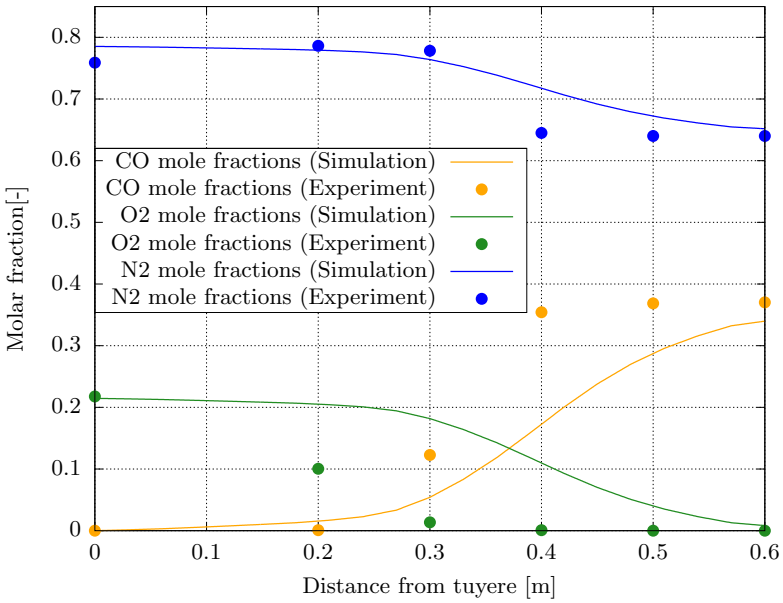

Figure 6.5: comparison of the measured and predicted gas compositions along the central axis of the tuyere

reveal a significant discrepancy in raceway behavior. In order to make a valid comparison, the 2D and 3D cases were similar in size and mesh in the x and z direction. There are also similar initial conditions, including packed bed height and particle size.

Figure 6.6 shows the comparison of the raceway cavity in 2D and 3D simulations of the dynamics of a BF raceway. It can be observed that in 2D, the raceway cavity has larger dimensions compared to the 3D results. The height and width of the raceway in the 2D case are respectively 100 cm and 38 cm, while in 3D they are respectively 30 cm and 12 cm. This notable discrepancy between the 2D and the 3D simulations can be explained by the fact that in 3D, the momentum of the inlet flow is partly consumed to expand the raceway in the third direction, depth (which reaches up to 24 cm). Whereas in 2D simulation the momentum of the inlet air is wholly saved to expanding the raceway height and width, thus resulting in an unjustifiably large raceway. The result is that in the 2D simulation, the packed bed is expanded to fill the whole available domain whereas in reality the top of the packed bed is just raised a fraction of the packed bed height. This behavior can be observed in the previous study as well [238]. This phenomenon can be confronted by defining different initial

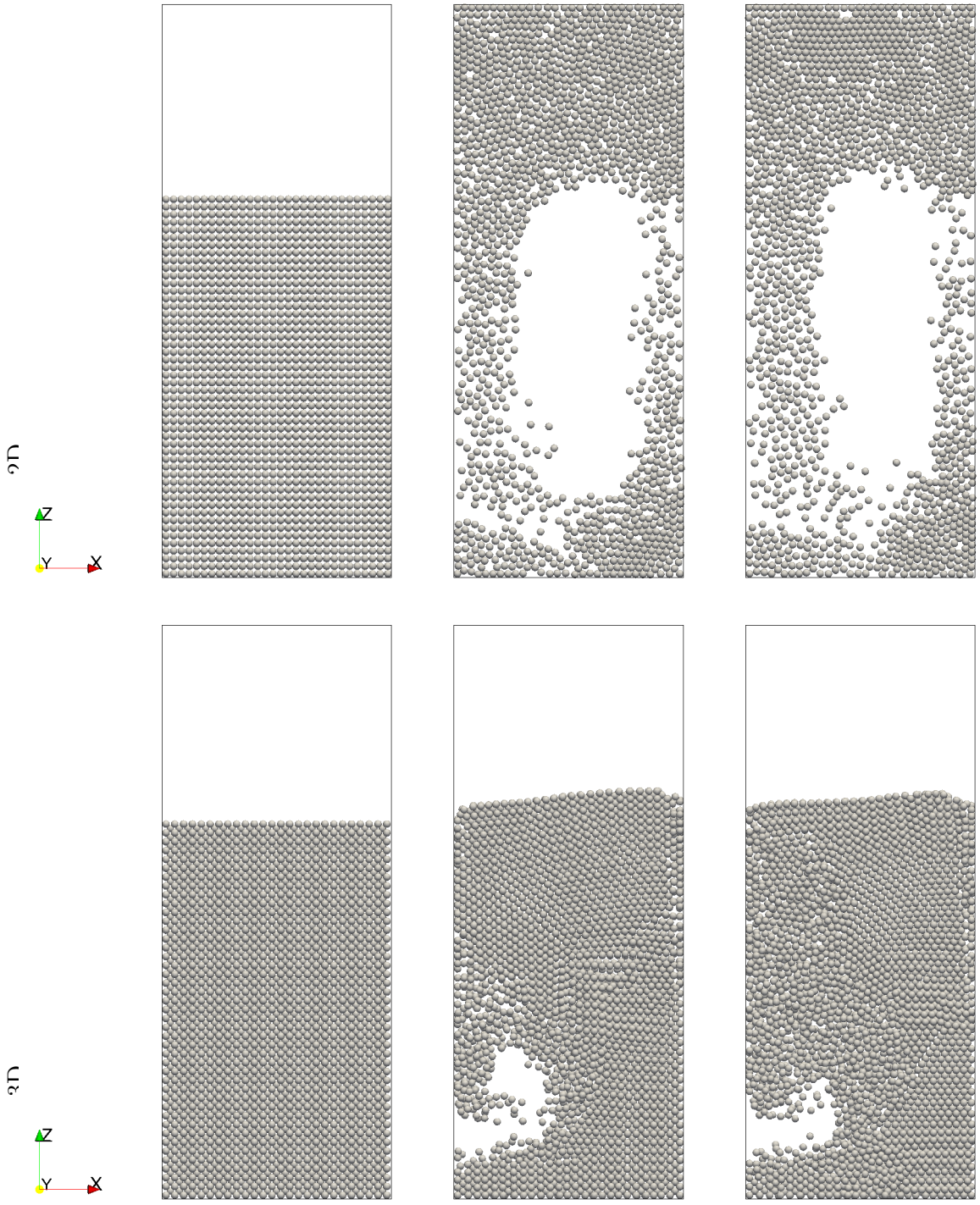

(a) t=0s (b) t=1s (c) t=5s

Figure 6.6: The 2D and 3D dynamics simulation of a blast furnace raceway at three different time steps. The 3D results are slices from the 3D packed bed cut between two XZ planes on the two sides of the inlet

or boundary conditions to constrain the packed bed height or fill the whole domain from the beginning but nevertheless, it would not change the fact that the dynamics of the packed bed and the raceway are misrepresented.

Moreover, the implicit assumption made for the 2D model by itself leads to a significant gap between the model and actual physics. The 2D simulation of the raceway assumes a symmetrical placement of the raceway in the BF. For 2D simulation to represent the real BF raceway, either the BF should be a thin slice with two raceways on the opposite sides, which is naturally far from the reality, where we have a cylindrical furnace with multiple injection inlets located on the periphery; or, the inlet of the raceway should be an open slit covering the periphery which would lead to a torus raceway in the whole furnace. None of these two cases mimick the actual physical geometry to a good approximation. Due to such observations, the previous studies have noted [231] that there should be special boundary conditions defined on the domain for the 2D or quasi-3D model to represent the physics better.

However, in a 3D simulation, the actual physics of the problem is represented more accurately. As is presented in the following sections, the raceway enlargement is more confined and the packed bed movement is very limited compared to a 2D simulation. Therefore, the significant difference between the two cases led to the conclusion that 3D simulations, despite their computational costs, provide a much more reliable insight into the physics of the raceway. Additionally, with the increasing trend in computational power and thanks to parallelization, 3D simulations are becoming more affordable.

6.4.3 Typical transport phenomena of the raceway

Figure 6.7 provides a series of snapshots from the 3D simulation of a raceway section in an operating BF. The pictures depict the raceway formation as a hot air blast is injected horizontally into the furnace via the tuyeres. Following the blast, the raceway forms in the early time steps. It first penetrates the packed bed to the maximum possible depth in a horizontal direction which is approximately 24 cm, then adopts an upward anti-clockwise direction to develop further in height and eventually reach a maximum height of 33 cm from the bottom of the furnace. As can be seen in the figures, by the time of 20 s the raceway has already adopted

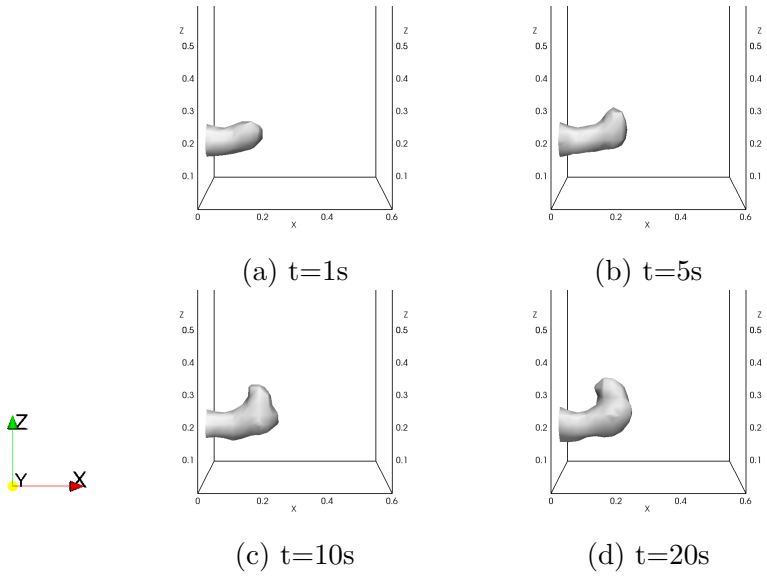

(a) t=1s (b) t=5s

(c) t=10s (d) t=20s

Figure 6.7: Topological evolution of the raceway cavity at different time steps in the 3D simulation of a BF raceway with a blast velocity of 200 m/s

a respectively steady shape and dimensions. Figure 6.8 shows the penetration profiles of the raceway through time in X-direction (depth), Z-direction (height) and Y-direction (width). This plot supports the observations in figure 6.7, by showing that the raceway dimensions achieve stability in all directions by 20 s, despite abrupt fluctuations in the beginning. However, the width of the raceway shows less stability because it is comparatively confined by the walls.

As a more clear depiction of the 3D case, figure 6.9 shows the location of the raceway and the gas flow streamlines that start from the inlet and spread all through the raceway. As can be seen in the figure, the gas flow has a high velocity inside the raceway (more than 50m/s) and as it penetrates into the packed bed, loses its momentum and its velocity decreases drastically.

6.4.4 Heat and mass distribution in the packed bed

Figure 6.10 demonstrates the particles and their respective temperature at three different time steps on horizontal and vertical slices. These horizontal and vertical slices are cut between two

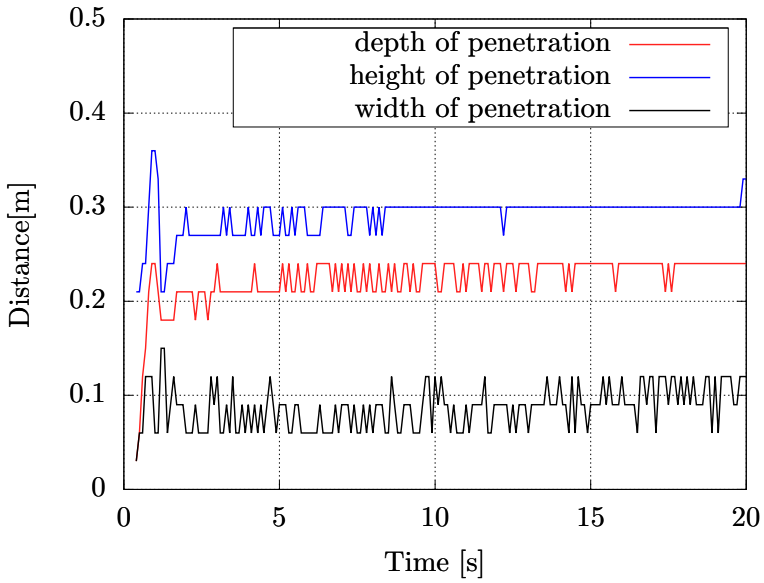

Figure 6.8: Temporal variation in depth (starting from tuyere tip in the direction of inlet flow, i.e. inlet central line) , height (starting from the bottom of the furnace in the positive z-direction) and width (starting from inlet center line in the positive y-direction) of the raceway cavity calculated based on the porosity isoline of 0.7

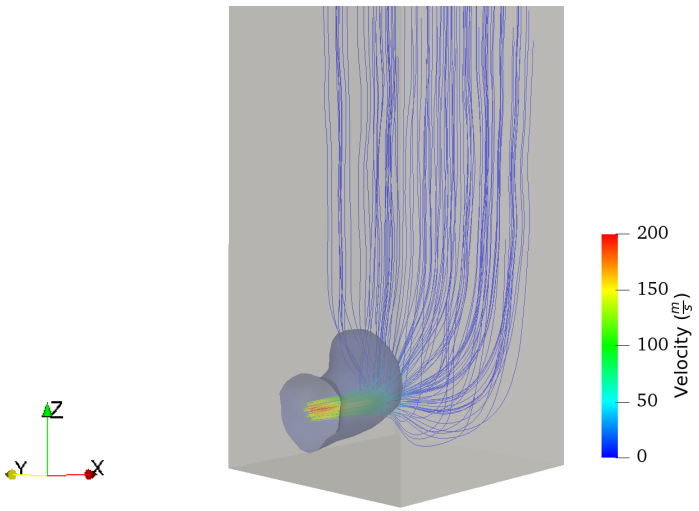

Figure 6.9: Streamlines of the flow passing through raceway for the 3D case with an inlet velocity of 200 m/s. The streamlines are colored by the flow velocity.

XY and XZ planes respectively located at Z=0.15 cm, Z=0.21 cm, and Y=0.27 cm, Y=0.33 cm. As can be seen in the XZ slices (subfigures a-c), the packed bed has increased in height because of the minor fluidization caused by the flow inside the raceway. The packed bed's top surface shows a downward slope from right to left, representing a general anti-clockwise flow flowing through the packed bed.

The particles preheated to an inital temperature of 1300 K. Figure 6.10 shows that as the raceway forms, the temperature of particles around the ring-type zone rises. The ring-type zone is the boundary of the raceway and the location where the incoming air meets the coke particles. The oxygen concentration in this zone is high, causing a high rate of the exothermic oxidation reaction with coke. Heat is produced at a faster rate when the reaction rate is higher, therefore the temperature is raised faster in the areas close to the ring-type zone.

The distribution of O_2 and CO at t=0.1 s , t=1 s and t=20 s can be seen in figure 6.11. In the initial time step (t=0 s) the mass fraction of both O_2 and CO is zero and only Nitrogen (N_2) is present(which is not shown here for the sake of brevity). As the simulation process starts, O_2 is blasted into the furnace and CO is produced. It can be observed that the raceway region is the source of O_2 and distributes it around the packed bed. This explains the correspondence of the O_2 distribution with the raceway shape. However this correspondence is very rough because some O_2 distributs into the packed bed via diffusion and convection and therefore go beyond the raceway perimeter. The O_2 concentration is maximum in the raceway and zero beyond the ring-type zone because the coke particles in the zone consume the O_2 and produce CO. Consequently, due to the outward flow direction around the raceway, CO transports away from the raceway. As a result, CO concentrations inside the raceway are lower than outside.

6.4.5 Influence of blast flow rate

Inlet velocity is a physical parameter that can be manipulated to achieve the desired outcome in the raceway. It directly affects the size of the raceway and thus the distribution of temperature and gas species. In this study, three test cases with inlet velocities of 180 m/s,

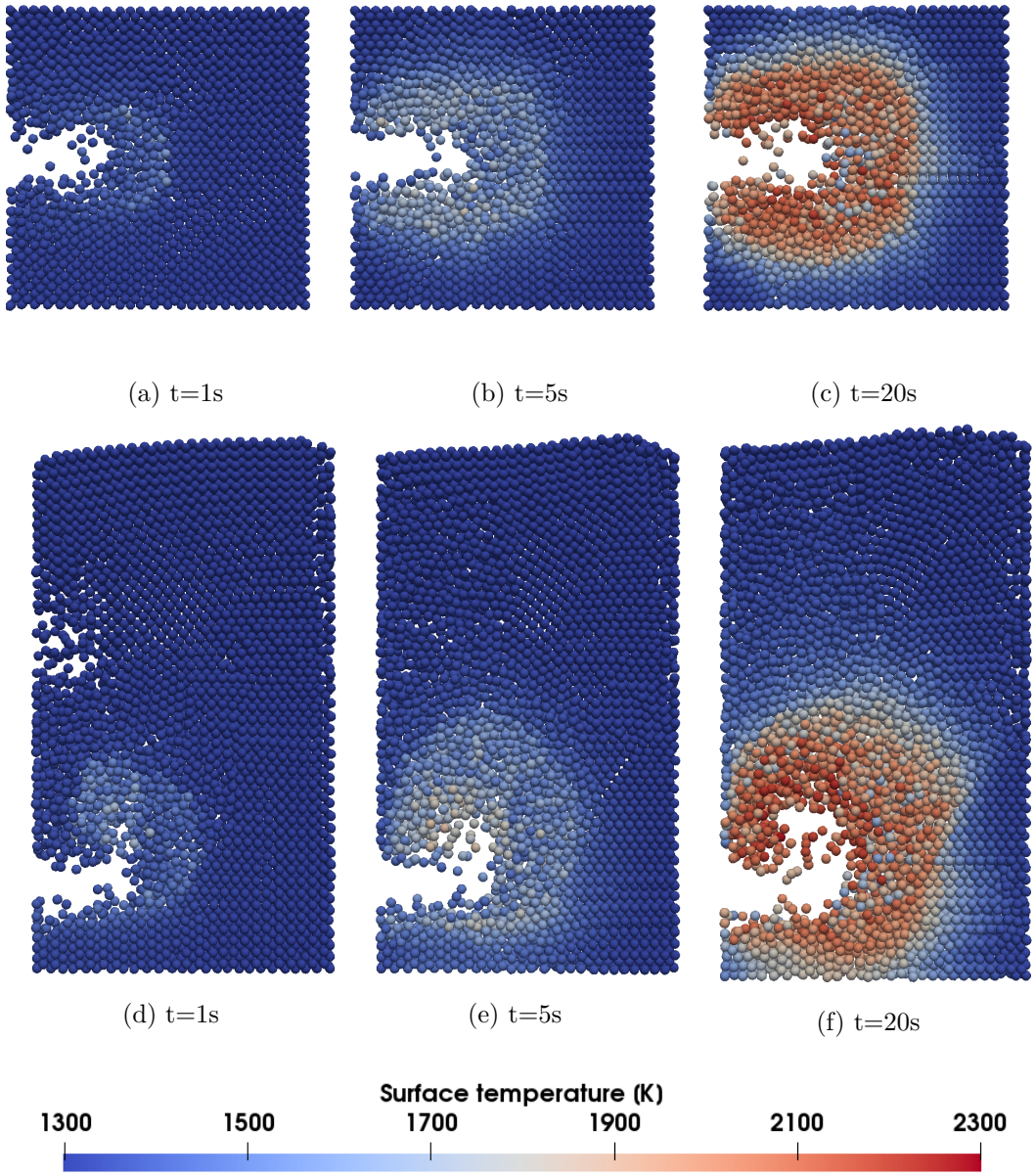

Figure 6.10: Spatial distributions of coke particles in the raceway packed bed at different time steps in a horizontal slice cut from the 3D packed bad, between two XY planes on the opposite sides of the inlet (a,b,c) and a vertical cut between two XZ planes on the opposite sides of the inlet (d,e,f). Particles are colored by the surface temperature of the particles.

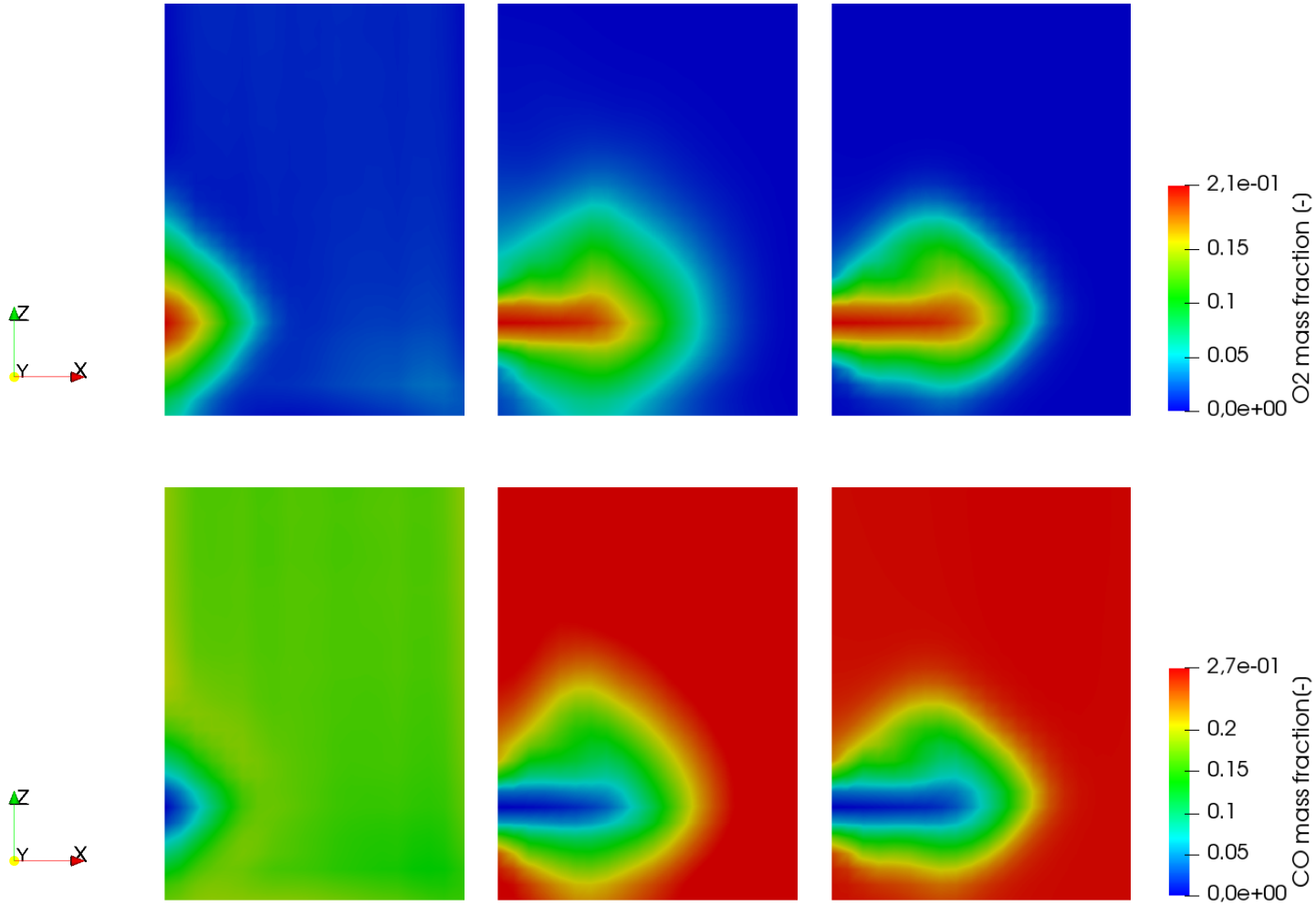

(a) t=0.1s (b) t=1s (c) t=20s

Figure 6.11: O_2 and CO mass fraction distribution in the gas (CFD) at different time steps of the 3D simulation on an XZ slice located on Y=0.3 m which passes the inlet

200 m/s, and 220 m/s are used to examine the effects of inlet velocity on raceway transport phenomena.

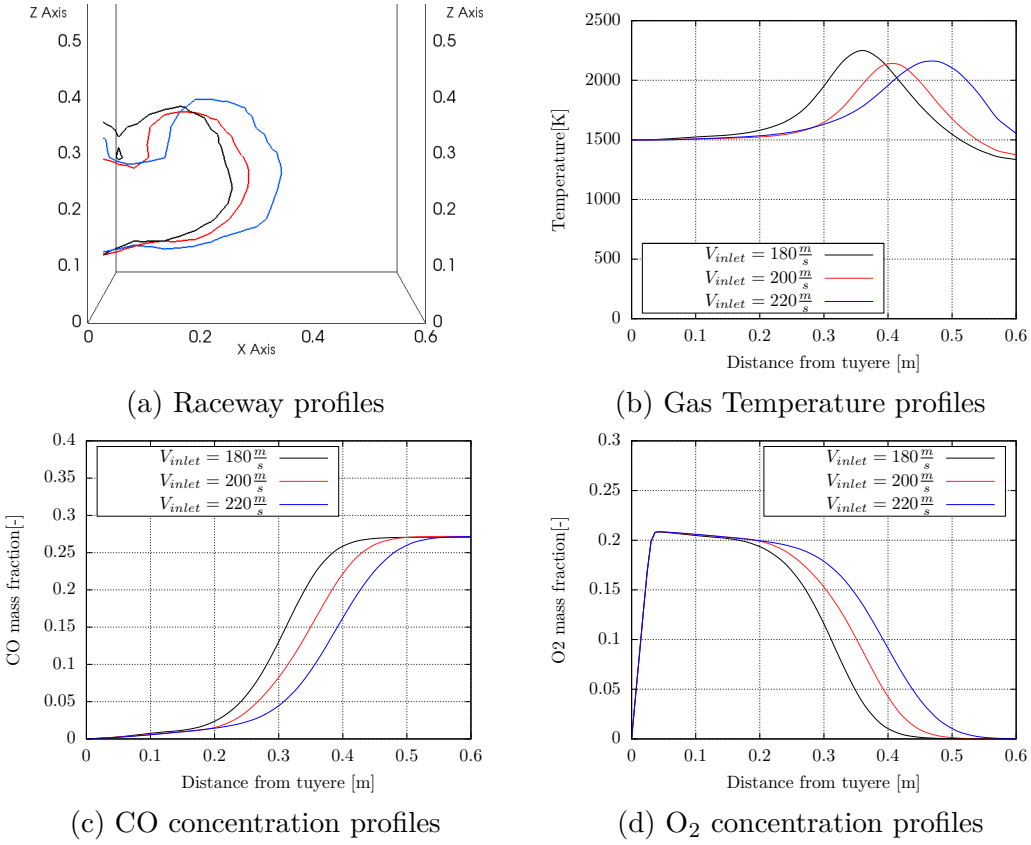

(a) Raceway profiles

(b) Gas Temperature profiles

(c) CO concentration profiles

(d) O_2 concentration profiles

Figure 6.12: Comparison of racewy profile, temperature, CO concentration and O_2 concentration along the horizontal line from the tuyere tip for three differenet velocities 180 m/s (black), 200 m/s (red) and 220 m/s (blue)

In all the cases, the initial inlet velocity is 10 m/s and it increases linearly with time, up to the desired inlet velocity (180, 200, or 220 m/s) at t=0.5 s. This gradual velocity increase was done both for the sake of stability and imitating the actual process. As can be seen in figure 6.12, increasing the inlet velocity results in a larger raceway, thus pushing the ring-type zone outward. As the raceway approaches proximate stability, the volumes of the raceway cavity for 180 m/s, 200 m/s, and 220 m/s are respectively 4.24, 4.72 and 6.56 cubic decimeters. These values are calculated based on considering the raceway as the region with

a porosity equal to or larger than 0.7.

Figure 6.12b shows the variation of temperature along the horizontal line starting from the tuyere tip. In all three cases, somewhere in the middle of the horizontal line, there is a temperature peak. The high combustion rate of the particles and the resulting heat causes the temperature to rise. Based on the raceway profiles in figure 6.12a these peaks occur in the ring-type zone which is located just outside the raceway perimeter. The same behavior can be observed in O_2 and CO concentration profiles in figure 6.12. As is expected, at the ring-type zone (for instance, between 0.2 m- 0.4 m for 180m/s case), there is a rapid consumption of oxygen, concurrent with the formation of carbon monoxide, which reaches its maximum concentration at the end of the probe line. This consistency of the temperature and concentration profiles with the raceway profile can be observed for all three inlet velocities. However, as the blast inlet velocity is increased, the ring-type zone is pushed further outward therefore the temperature peak and correspondingly the concentration profiles' inclination, occur at a further distance from the tuyere tip.

6.4.6 Heat and mass distribution within the particles

As described in section 6.3.1, the DEM model used in this study considers discretized particles. Therefore the heat and mass distributions inside the particles are considered, featuring the internal gradients of temeprature and species concentration within the particles.

Figure 6.13 compares the results between a case with 1-cell particles and a case with 5-cell particles to demonstrate the significance of particle discretization. The primary difference between a 1-cell and a 5-cell particle is that in the 5-cell case there is a gradient of species and temperature within the particle. Coke combustion is driven by oxygen which diffuses into the particle from the ambient gas. Therefore the oxygen concentration has a profile within the particle, decreasing from the surface to the center. The available oxygen concentration determines the rate of coke combustion. Therefore the combustion reaction rate will have a negative gradient from the surface to the center, resulting in more heat generation (due to the exothermic reaction of coke combustion) in the cells near to the surface. Since the particle surface temperature is higher in the 5-cell case, there is a stronger heat convection with the

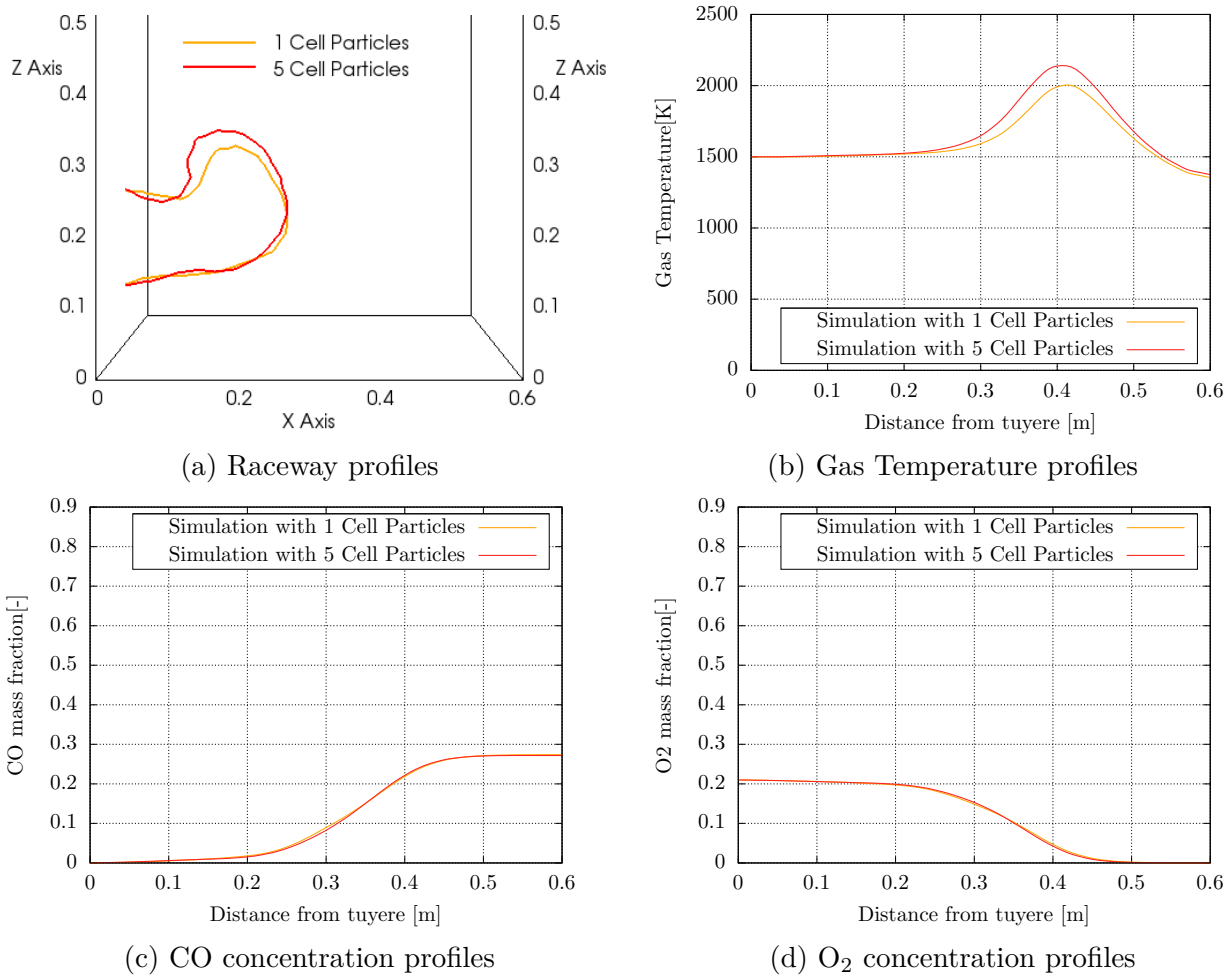

(a) Raceway profiles

(b) Gas Temperature profiles

(c) CO concentration profiles

(d) O_2 concentration profiles

Figure 6.13: Comparison of racewy profile, gas temperature, gas CO concentration and gas O_2 concentration along the horizontal line from the tuyere tip for two cases: particles with one internal cell and thus no discretization(Orange) and particles with 5 cells (Red)

surrounding ambient gas and the gas is thus hotter. This anticipation is clearly demonstrated by figure 6.13(b). The case with 5-cell particles shows a higher gas temperature peak in the ring-type zone. This higher gas temperature creates a higher pressure inside the raceway which pushes the raceway ceiling upward (as there is less resistance to vertical expansion compared to horizontal expansion which is limited by the right wall). This explains the larger raceway cavity for 5-cell particles as illustrated in figure 6.13(a).

However, it is important to note that although in the 5-cell case there is a gradient in reaction rate through the cell, the average reaction rate, or in other words the coke and oxygen consumption is almost the same in the two cases. Figures 6.13 (c) and (d) show respectively CO and O_2 concentration along the horizontal line from the tuyere tip. It can be observed that there is almost no difference between the two cases in O_2 consumption and CO production.

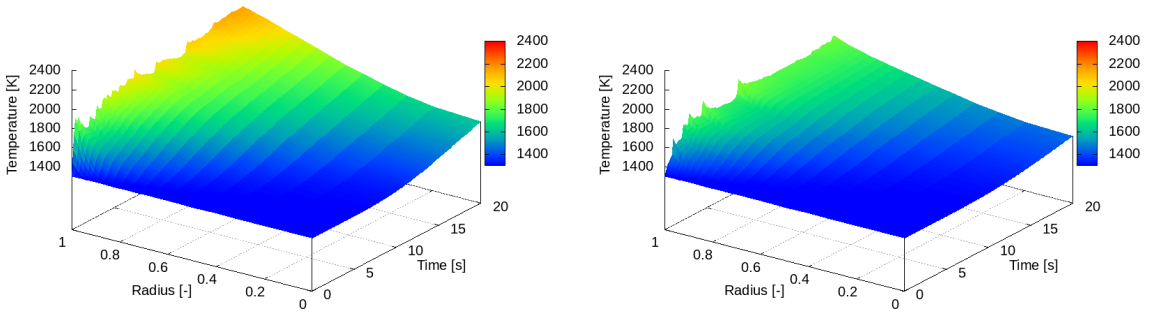

(a) inside the ring-type zone

(b) off the ring-type zone

Figure 6.14: Temporal and spatial distribution of temperature in two coke particles:(a) one, positioned inside the ring-type zone and (b) the other, further away from the ring-type zone

The aforementioned gradient of temperature can be significant in some particles that are subject to higher O_2 concentration. Figure 6.14 shows the temperature distribution over the particle radius for two different particles located at different points in the packed bed. Both of these two cases include particles with 20 cells so that this gradient is expressed more clearly. One is inside the ring-type zone, undergoing higher reaction rates and higher temperatures. The other particle, particularly in the second half of simulation, experiences lower

temperatures, suggesting that it evaded being trapped in the ring-type zone and maintained a position where heat loss and heat gain by the particle are in equilibrium.

The figures demonstrate the particle discretization which is non-uniform as it was explained in section 6.3.1. The cell adjacent to the particle surface adopts a minimum size and towards the center of the particle the cell size increases according to a geometric progression. It can be observed that in both cases there is a high gradient of temperature near the surface and this gradient increases over time, because of the low conductivity of coke. This sharp gradient would not be captured in a particle with no discretization [236, 143]. Therefore such models in which the whole particle is considered as a single element with a uniform temperature all over it, incorporate a rough temperature in the Arrhenius model and thus underestimate the reaction rates at the surface of the particle. As demonstrated in previous sections, in an application such as a BF where there is a complex inter-dependency between the heat transfer, reactions and the dynamics of the system, such gaps in the model will introduce noticeable and unacceptable errors.

6.5 Conclusion

A CFD-DEM model was developed to analyze the raceway transport phenomena in an iron-making blast furnace. The study proposed the significance of simulating the raceway in 3D. Based on the provided results, it was argued that the 2D model, due to the implicit assumptions associated with it, overestimates the raceway size. Therefore the 3D model was used to simulate the raceway and analyze the dynamical evolution of the raceway, combustion of the coke particles, and heat and species distribution in the gas flow.

It was shown that the coke combustion rate is the highest in the periphery of the raceway, known as the ring-type zone. Therefore almost all of the incoming oxygen is consumed near the ring-type zone and the particles in this region experience the highest temperatures. The discretization of the particles made it possible to analyze the heat distribution within the particles. It was shown that for the particles exposed to high oxygen concentration and high combustion rate, the surface of the particle is subjected to a relatively high temperature

gradient. Therefore, in a blast furnace where thermal conductivity of coke particles is low but temperature levels are high, using a DEM model with discretized particles is an effective strategy for preventing the underestimation of particle temperatures.

The influence of the gas inlet velocity was also investigated. It was shown that higher inlet velocity results in larger raceway cavities and more penetration into the path of the packed bed. However, the temperature ranges of the raceway and reaction rates do not follow a clear correlation with the inlet blast flow rate. These findings offer insight into the complex correlations between the dynamics and thermodynamics of the raceway.

Chapter 7

Parallel Multi-Physics Coupled Simulation of a Midrex Blast Furnace[1]

[1]The content of this chapter is published in HPCAsiaWS 2024, ACM, New York, United States-New York[3]

7.1 Abstract

Traditional steel-making is a major source of carbon dioxide emissions, but green steel production offers a sustainable alternative. Green steel is produced using hydrogen as a reducing agent instead of carbon monoxide, which results in only water vapour as a by-product. Midrex is a well-established technology that plays a crucial role in the green steel supply chain by producing direct reduced iron (DRI), a more environmentally friendly alternative to traditional iron production methods.

In this work, we model a Midrex blast furnace and propose a parallel multi-physics simulation tool based on the coupling between Discrete Element Method (DEM) and Computational Fluid Dynamics (CFD). The particulate phase is simulated with XDEM (parallelized with MPI+OpenMP), the fluid phase is solved by OpenFOAM (parallelized with MPI), and the two solvers are coupled together using the preCICE library. We perform a careful performance analysis that focuses first on each solver individually and then on the coupled application. Our results highlight the difficulty of distributing the computing resources appropriately between the solvers in order to achieve the best performance.

Finally, our multi-physics coupled implementation runs in parallel on 1024 cores and can simulate 500 seconds of the Midrex blast furnace in 1 hour and 45 minutes. This work identifies the challenge related to the load balancing of coupled solvers and makes a step forward towards the simulation of a complete 3D blast furnace on High-Performance Computing platforms.[2]

7.2 Introduction

Traditional steel-making is the biggest source of carbon dioxide emissions from industry, accounting for 7 % of global CO_2 emissions. Fortunately, there are ways to drastically cut or even eliminate steel-making emissions and meet the Paris Agreement goals, while also meeting the growing demand for steel.

[2]The content of this chapter is published in HPCAsiaWS 2024, ACM, New York, United States-New York [3]

The transition from traditional steel-making to green steel represents a revolutionary shift in the metallurgical industry. Standard steel production, largely reliant on carbon-intensive processes like the blast furnace, has long been associated with significant greenhouse gas emissions. In contrast, green steel embodies a sustainable future, emphasizing carbon neutrality and reduced environmental impact. The core of green steel production lies in using hydrogen as a clean reducing agent instead of carbon in traditional coke ovens. This process, known as hydrogen-based direct reduction, emits only water vapor as a by-product. Of course, the green iron produced this way is considered green only if the hydrogen used in the process is itself green.

Midrex is a well-established "green" technology used in the steel industry, specifically in producing direct reduced iron (DRI) or sponge iron. While it may not directly produce green steel, it plays a crucial role in the green steel supply chain by providing a more environmentally friendly alternative to traditional iron production methods.

Midrex technology is known for its:

- Use of Natural Gas: One of the hallmark features of Midrex is its reliance on natural gas as a reducing agent instead of carbon-based materials like coke. This reduces greenhouse gas emissions significantly. The process involves the conversion of iron ore pellets into highly pure and metallic DRI using a combination of natural gas and hydrogen during a transitional period until sufficient hydrogen is available.

- Lower Carbon Footprint: Compared to traditional blast furnace methods, Midrex technology has a substantially lower carbon footprint. By minimizing carbon emissions, it aligns with the goals of green steel production.

- Energy Efficiency: Midrex plants are highly energy-efficient. They can integrate renewable energy sources, such as solar or wind power, into their operations, making them more environmentally sustainable.

- Use of Renewable Hydrogen: In recent years, there has been a growing interest in using renewable hydrogen in the Midrex process. Green hydrogen, produced through elec-

trolysis powered by renewable energy sources, can further reduce the carbon footprint of DRI production.

- Reduced Environmental Impact: The Midrex process emits significantly fewer pollutants, such as sulfur dioxide and nitrogen oxides, compared to traditional steel-making methods. This contributes to cleaner air quality and reduced environmental harm.
- Flexibility and Modular Design: Midrex plants are known for their flexibility and modular design, which makes them adaptable to various production scales and locations. This adaptability can enable the decentralized production of DRI, reducing the environmental impact associated with transporting raw materials over long distances.

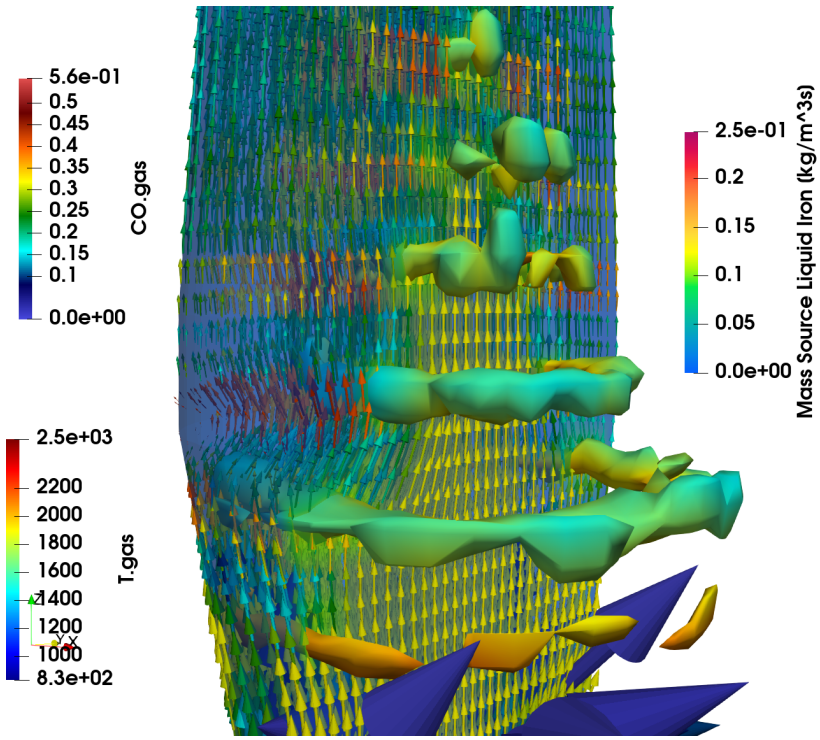

Figure 7.1: Location of the cohesive zone in a blast furnace simulated by the XDEM simulation platform.

The performance of blast furnaces is evaluated based on their thermal efficiency and harmful emissions, and it is affected by many factors, such as the furnace design and operating conditions. Numerical simulation is a more affordable and time-efficient way to optimize

blast furnace operation than expensive experimental methods. For example, as depicted in Figure 7.1, numerical simulation allows for locating the cohesive zone and thus estimating of the production of liquid iron. However, the Midrex technology in a blast furnace is a complex physical process (involving particle motion and shrinking, heat transfer, reduction, melting and slag formation, etc.) that must be carefully modeled and validated. This high level of complexity means that simulating industrial blast furnaces requires High-Performance Computing (HPC) platforms and expertise to be conducted in a reasonable time.

Our work bridges the gap between chemical engineering and high-performance numerical simulation by providing an advanced high-performance multi-physics simulation of a blast furnace. We present our numerical approach and detail the performance on a High-Performance Computing (HPC) platform. Our contributions, which are novel related to the topic of blast furnace simulations on HPC, are: (1) a parallel multi-physics CFD-DEM coupling application, based on XDEM and OpenFOAM, for the simulation of the Midrex blast furnace; (2) a thorough performance evaluation on an industrial setup, highlighting the challenges related to the load-balancing between coupled solvers.

This paper is organized as follows. First, we present an overview of the state-of-the-art related to the simulations of multi-phase flow phenomena and blast furnaces, and their execution on HPC platforms. Section 7.4 presents the physical background related to the Midrex process, its validation and parallel implementation with the coupling XDEM–OpenFOAM. A detailed performance evaluation of our solution is carried out in Section 7.5 and then followed by the Conclusion.

7.3 Related Works

Numerical methods for simulating multi-phase flow phenomena involving a solid, like a particulate phase, essentially fall into two categories: The two-fluid model is its most well-known representative, and on a macroscopic level, all phases are treated as a continuum [111]. It is a good fit for process modeling due to its simplicity in computation and effectiveness. The amount of information that can be learned about the material properties, size distribution, or

shape of individual particles, however, is significantly diminished by the concept of averaging. To compensate for this loss of information on small scales, additional constitutive or closure relations are needed.

In contrast, the Combined Continuum and Discrete Model (CCDM) treats the flow of liquids or gases as a continuum phase in the interstitial space while treating the solid phase as discrete [245, 246, 247, 248]. Because constitutive relations are excluded from the discrete description of the solid phase, basic ideas are easier to comprehend. This conclusion was reached by Zhu et al. [249] and Zhu et al. [130] while reviewing particulate flows modeled using the CCDM approach. It has undergone significant development over the past decades and treats the other continuous phases while using the Discrete Element Method (DEM) to describe the motion of the solid phase on an individual particle scale. To meet engineering requirements, current models should be expanded to include multi-phase flow behaviour and particle shapes other than spherical geometries, according to Zhu et al. [249] and Zhu et al. [130]. As a result of these efforts, discrete and continuum methods should generally be connected, enabling results to be quantified for process modeling.

At the beginning, only simple flow configurations [246, 245] were handled by the CCDM. However, Chu and Yu [250] demonstrated that the technique could also be used to model complex flow configurations that included a fluidised bed, conveyor belt, and cyclone. Similar to this, Zhou et al. [251] and Chu et al. [252] applied the CCDM approach to the complex geometry of a pulverized coal combustion [251] and Chu et al.[252] modeled the complex of magnetite particles of different sizes in a dense medium cyclone (DMC) including flow of air, water, and coal. In both instances, there was appreciably good agreement between experimental data and predictions. Fluidized beds have also been subject to the CCDM approach, according to reviews by Rowe and Nienow [253] and Feng and Yu [254]. Feng and Yu [254] described the chaotic motion of particles of various sizes in a gas-fluidized bed. See Kafuia et al. [255] for a description of discrete particle-continuum fluid modeling of gas-solid fluidized beds.

The modelling of blast furnaces has also advanced in a similar way. Shibo et al. [256] reviewed recent developments in mathematical modeling related to top charging, shaft pro-

cesses, raceway, and hearth. Their review indicates that there is still a fragmented approach for isolated regions and physical processes in the blast furnace, such as the studies of combustion in a raceway [257, 258, 259, 260]. Similar to this, Zhou et al. [261] developed numerous computational fluid dynamics (CFD) models for the shaft, raceway, and hearth in order to optimize operating conditions. These shortcomings were partially compensated by a three-dimensional CFD model developed by Lulu et al. [262]. They were successful in achieving a respectable level of agreement between measured and predicted furnace states in both industrial and experimental settings. Dong et al. [263] also employed a CFD model to identify the cohesive zone based on the temperature distribution of the ore. Shen et al. [223] identified key performance indicators like gas utilization and reduction degree using the same CFX-based CFD model. These various models each represent a particular region of a blast furnace, but they largely ignore how those regions interact. However, the current contribution represents an important first step toward a thorough modeling framework that covers the entire blast furnace.

A review by Chattopahyay et al. [264, 265] showed that computational fluid dynamics (CFD) has been employed with great success in many instances as a tool for continuous flow modeling. However, experimental results [266, 267, 268, 269, 270, 271, 272, 273, 274, 275, 276, 277] show that a pure continuous approach to the blast furnace is flawed . For a variety of engineering applications, as discussed by Yu [278], Dong et al. [279] recommend using a discrete approach to model the flow of the solid phase of particles. The CCDM method was used by Simsek et al. [280] to predict grate firing systems, but they only got qualitatively acceptable results, highlighting the need for more research.

Current CCDM approaches should be expanded to a truly multi-phase flow behaviour as carried out by [281, 282, 145, 283, 216], in contrast to the Volume-of-Fluid method and the multi-phase mixture model. In order to satisfy engineering requirements, it is also necessary to take into account particle shapes other than spherical geometries [284, 285, 286], claim Zhu et al. [249, 130] in their references. Since all derivations have been made for mono-sized particles, as stated by Feng and Yu [287], these efforts should ideally be supplemented by poly-disperse particle systems. For the purposes of process modelling, all of these initia-

tives should contribute to establishing a general connection between discrete and continuum methodologies.

Even though the CCDM methodology has been in place for more than a decade [288, 247] heat transfer prediction is still in its infancy. The heat transfer for polymerization reactions in gas-fluidised beds was predicted by Kaneko et al. [289] using the Ranz-Marshall correlation [290], but without taking conduction into account. Only in a two-dimensional spouted bed was convective transfer predicted by Swasdisevi et al. [291]. For the transport of gas-solid in horizontal pipes, Li and Mason [292, 293, 294] considered conductive heat transfer between particles. Zhou et al. [295, 296] modeled coal combustion in a gas-fluidized bed while taking into account both conductive and convective heat transfer. Although Malone and Xu [297] predicted heat transfer in liquid-fluidized beds by the CCDM method and emphasized the need for further research into heat transfer, Wang et al. [298] predicted the gas-solid flow in a high-density circulating fluidized bed with the two-fluid model. Xiang [299] found during an investigation of air on the packing structure of fine particles that his application lacks computational resources. According to a recent review by Zhou et al. [249] many approaches only take into account flow and ignore heat or mass transfer. Thus, they stated the following recommendations:

- Micro-scale: By developing a more thorough theory and experimental techniques for investigating and calculating the forces that interact with particles and fluids in various environments, we hope to strengthen the groundwork for particle scale simulation [300, 301, 302].

- Macroscale: the development of a general theory that unifies discrete and continuum methods and enables the quantification of particle scale data from DEM or DEM-based simulation in terms of (macroscopic) governing equations [303, 304, 305].

- Application: Transferring the current phenomenon simulation to process simulation is crucial for addressing actual engineering needs. In order to achieve this, it is crucial to create more trustworthy models and efficient computer codes that enable particle scale simulation to be expanded, for example, from a two-phase to a multi-phase and/or from

a simple spherical to a complex non-spherical particle system [306, 64, 307, 308].

In [309], Zhong et al. highlight that the use of CFD-DEM is not feasible for the simulation of industrial cases because it is too expensive in terms of computation and memory. Indeed, there are no reports of CFD-DEM-based simulation of a complete 3D blast furnace, even in an HPC configuration. The majority of the work used to be based on 2D models [256]. Thanks to the increasing computation power, recent studies propose 3D simulations based on sector model [310] (i.e., one-sixth of a furnace) or sub-part of the system like the raceway [2]. To alleviate the computational needs, scaled methods or coarse-grain approaches have been used for simulation with more than 2 million particles [311]. Unfortunately, authors rarely discuss their implementation, the parallelization or the performance of their simulation prototypes.

More generally, load-balancing has been identified as a critical issue for the performance of multi-physics simulations. In monolithic coupling, solvers are coupled together in a single executable which allows fast in-memory data exchange [86]. This is particularly suitable for volume-coupled problems with the use of a co-located partitioning strategy [86] which assigns the subdomains of the different solvers in the same partition to reduce costly inter-partition inter-physics data exchanges. It has been successfully applied to complex CFD-DEM coupled problems [89, 312]. Alternatively, load-balancing between coupled solvers is achieved by measuring the computational cost of each physics module and then estimating the computation weights [313] to be given to the partitioning algorithm. In partitioned coupling, the configuration is different because each solver can run on a different set of cores. Based on this, [314] builds a performance model of each solver that is used to find the optimal distribution of the computing resources between the solvers.

With the current work, we do not tackle directly load-balancing. Instead, our objective is to study the parallel execution of our Midrex blast furnace implementation and gain insight into its behaviour at large scale. The collected information will serve as a basis for further work related to load balancing.

7.4 Modelling and Implementation of the Midrex Blast Furnace

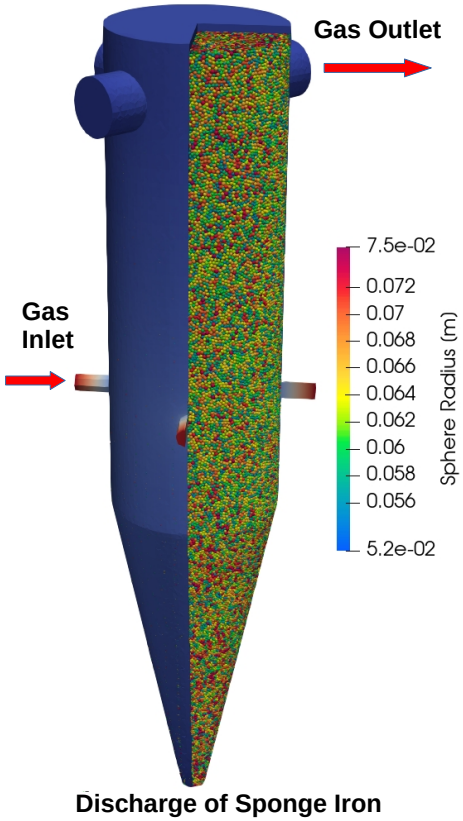

Figure 7.2: Shape a Midrex furnace filled with iron-bearing particles.

While Midrex technology itself does not directly produce steel products, its role in producing direct reduced iron is a critical step toward green steel production. The DRI produced using Midrex technology can be used as a feed-stock in electric arc furnaces (EAFs) or integrated into other steel-making processes that are more environmentally friendly compared to traditional blast furnaces. As the steel industry continues to transition toward greener and more sustainable practices, technologies like Midrex are expected to play a pivotal role in reducing the industry's carbon emissions and environmental impact, contributing to the development of a more eco-conscious steel sector. Modeling these processes provides insights into heat transfer, fluid dynamics, combustion, and chemical reactions, aiding in furnace de-

sign, efficiency enhancement, and emissions reduction. Furnace modeling stands as a dynamic field that intersects engineering, physics, chemistry, and computational science. As industries strive for efficiency, sustainability, and reduced emissions, the role of furnace modeling becomes increasingly pivotal. By addressing challenges and embracing innovative approaches, researchers and industries can collectively drive advancements in this critical realm, shaping the future of iron and steel production. The following Figure 7.2 depicts a Midrex furnace filled with iron-bearing material.

The iron oxides, Magnetite (Fe_3O_4), Hematite (Fe_2O_3), and Wüstite (FeO), undergo reduction with hydrogen and carbon monoxide on the following reaction mechanisms listed in reactions 7.1 - 7.6. In particular, reactions 7.1 - 7.3 highlight the environmental aspect of the DRI technology avoiding any formation of carbon dioxide and thus, contributing to a significant reduction of the carbon footprint. In the carburizing reaction 7.7, the iron absorbs methane to produces Cementite (Fe_3C).

Reduction with hydrogen:

$$3Fe_2O_3 + H_2 \leftrightarrow 2Fe_3O_4 + H_2O \tag{7.1}$$

$$Fe_3O_4 + H_2 \leftrightarrow 3FeO + H_2O \tag{7.2}$$

$$FeO + H_2 \leftrightarrow Fe + H_2O \tag{7.3}$$

Reduction with carbon monoxide:

$$3Fe_2O_3 + CO \leftrightarrow 2Fe_3O_4 + CO_2 \tag{7.4}$$

$$Fe_3O_4 + CO \leftrightarrow 3FeO + CO_2 \tag{7.5}$$

$$FeO + CO \leftrightarrow Fe + CO_2 \tag{7.6}$$

Carburizing reaction:

$$3Fe + CH_4 \leftrightarrow Fe_3C + 2H_2 \tag{7.7}$$

7.4.1 XDEM and OpenFOAM Coupling

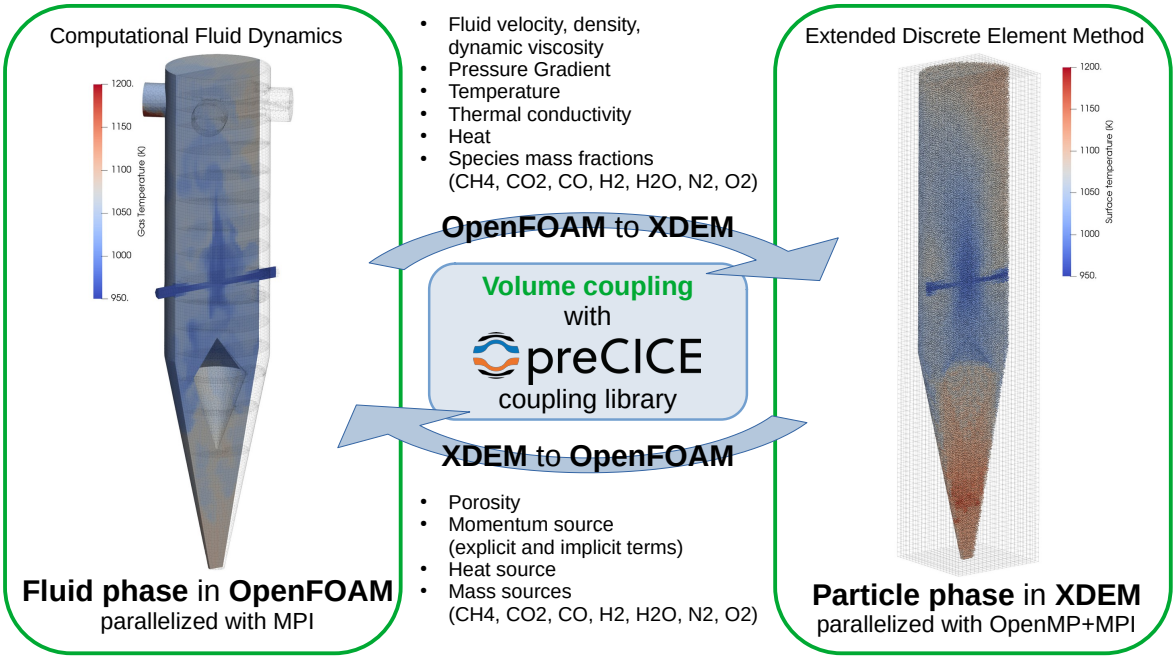

Figure 7.3: Overview of the Midrex Blast Furnace coupled simulation: The fluid phase is simulated with OpenFOAM (left); the particles are simulated with XDEM (right). The coupling is carried out by the preCICE library (middle) which exchanges the listed physical field values between the two software at every coupling time-step.

In order to describe the thermal processing of granular material such as iron reduction with the Midrex technology accurately, the particulate phase is represented by discrete entities for which the motion and the thermodynamic state are determined, while the gas phase in the void space between the particles is treated with computational fluid dynamics (CFD) as a continuum approach. Although computationally more expensive than the two-fluid approach or similar approaches solely based on continuum techniques, a coupled Euler-Lagrange coupling is superior due to its accuracy [309]. Therefore, two well-known simulation platforms are chosen for coupling, namely the extended discrete element method (XDEM) framework for the discrete phase and OpenFOAM representing CFD. Both modules exchange intensively three quantities: heat, mass and momentum.

- **Heat Exchange**: Particles are heated by the hot incoming gas of approximately 930 °C.

Thus, the gas flow transfers heat through a convective transfer to the particles meaning that particles heat up while the gas cools down. These heat quantities are exchanged between the fluid and the particles' surface [315].

- **Mass Exchange**: Particles receive hydrogen and carbon monoxide for reduction from the gas while the gas receives the products vapour and carbon dioxide from the particles. Reducing agents and products are exchanged via particle surfaces through a convective mass transfer [315].

- **Momentum Exchange**: The packed bed and in particular individual particles generate a pressure drop for the flow. Conversely, the gas flow exerts a drag force on particles that is added to other forces, e.g., gravity of the particle. Both transfer directions are accounted for by the momentum transfer [315, 118].

The above-mentioned transfer mechanisms are carried out by the preCICE library [50]. It ensures that individual particles receive the respective fluid quantities according to their position in the CFD simulation domain. Reversely, the fluid has to receive the correct particle properties e.g. surface temperature to account for the above-mentioned quantities transferred. Figure 7.3 gives an overview of the coupling between XDEM and OpenFOAM. At every coupling timestep, the preCICE coupling library communicates the values of the physical scalar and vector fields between the two solvers. Because the two simulation domains overlap (i.e., the particles are immersed within the fluid and move independently), we have a volume coupling and thus the amount of data to exchange can be quite significant.

7.4.2 Validation

The implementation of these reactions have been validated over the relevant temperature and composition range as depicted in Figure 7.4 and 7.5 using the experimental data collected from [316] and [317]. Most important is that reduction through hydrogen and carbon monoxide as reducing agents is described by two consistent reaction mechanisms with constant kinetic parameters for thermal equilibrium reactions as opposed to fitting each experiment

with an individual set of parameters. Predicted reduction degrees agree well with experimental data [316, 317] for all experiments, so these reaction mechanisms are well-suited to be applied to the Midrex furnace.

The following Figures 7.6 and 7.7 depict some representative results addressing the temperature and species distribution for the gas phase and particles. The reducing gas is injected through the side inlets to stream upward through the packed bed thus, heating the particles and providing the reducing agents meaning that the concentration of hydrogen and carbon monoxide decreases continuously towards the gas outlets. Similarly, the iron oxides of the particles are reduced according to the reactions 7.1 to 7.6 so that the particle mass fractions of iron oxide reduce and the mass fraction of iron increases. These detailed results prove the accuracy of the XDEM–CFD coupling and a thorough analysis reveals the underlying physics indispensable for an efficient design and operation.

7.4.3 Parallelisation Approach

The CFD-DEM coupling is a **volume coupling** (as opposed to a surface coupling) because the particles are located and interact with the fluid around them. That means that the amount of data exchanged is proportional to the volume of overlapping domains between CFD and DEM. As discussed in [86, 89], this can have a significant impact on the performance of the execution. Parallelization strategies for single-physics applications such as computational fluid dynamics (CFD), finite element analysis (FEM) or Lattice Boltzmann (LB) are well-developed. However, coupling two or more applications represented by parallelized software modules does not result automatically in a parallelized coupled solver [89].

In our current implementation, we rely on the preCICE coupling library [50] which is designed to support parallel applications based on domain decomposition. With preCICE, each solver is considered a black box. At the initialization, each process of each solver indicates the part of the domain (more precisely, the points of the mesh) that it is responsible for. This has many advantages: First, each solver can run in parallel using its native parallelization scheme (e.g., MPI or OpenMP). Furthermore, the preCICE library takes care of matching the overlapping subdomains between each solver and communicating the data accordingly.

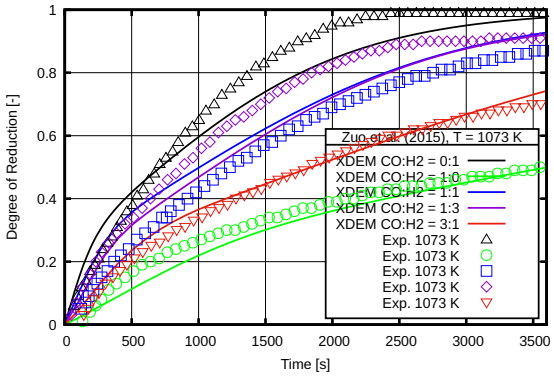

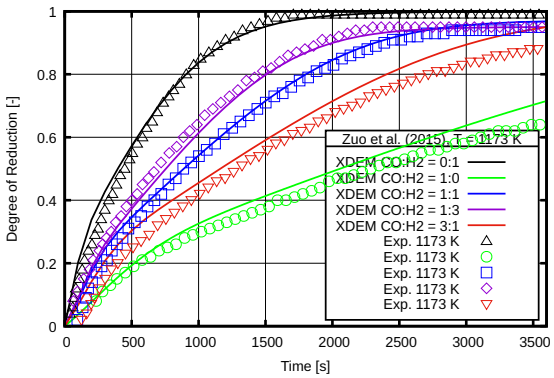

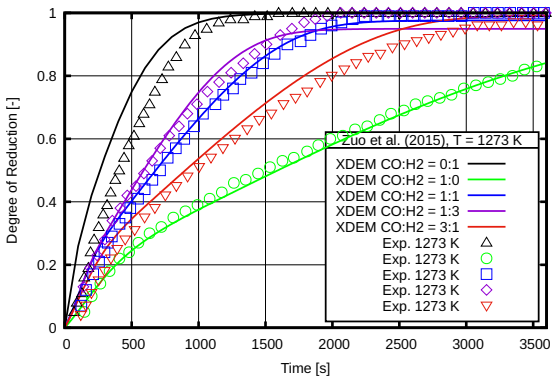

Figure 7.4: Validation of reducing reactions 7.1 to 7.3 for temperatures of 1073 K, 1173 K and 1273 K for different compositions of hydrogen and carbon monoxide in comparison with experimental data from [317].

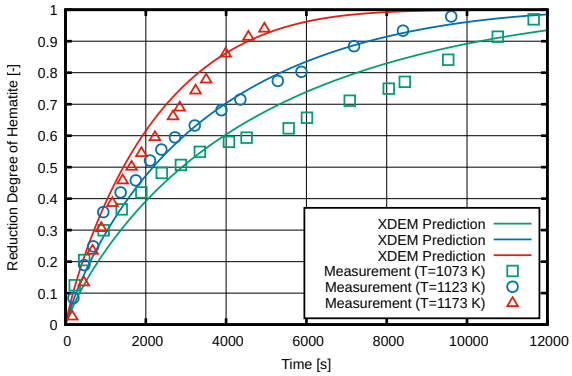

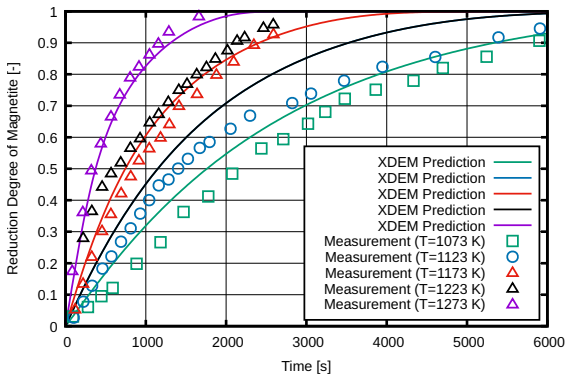

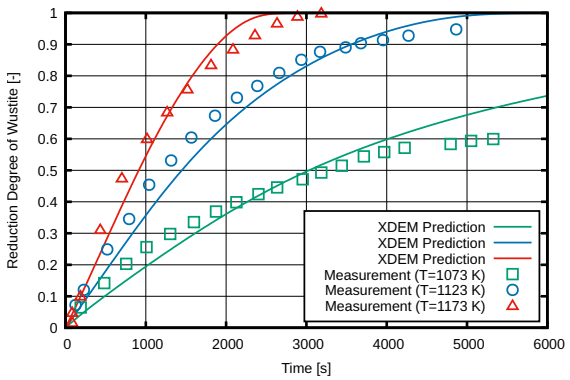

Figure 7.5: Validation of reducing reactions of Hematite, Magnetite and Wüstite for different temperatures in a pure carbon monoxide atmosphere according to reactions 7.4 to 7.6 in comparison with experimental data from [316].

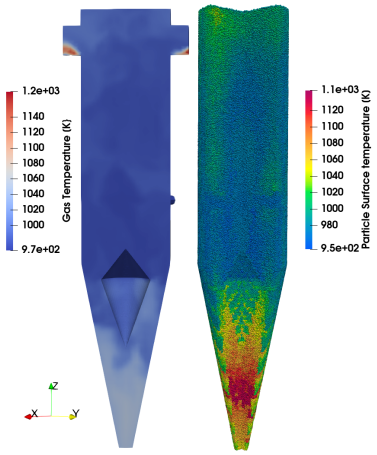

Figure 7.6: Gas and particle surface temperature distribution in a Midrex furnace.

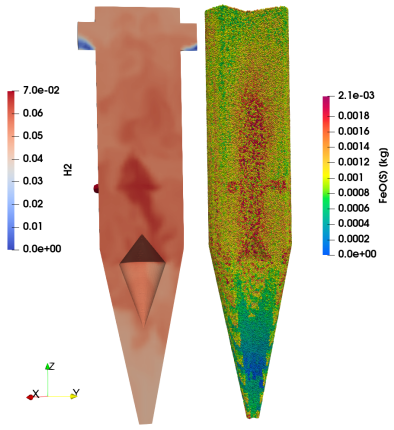

Figure 7.7: Distribution of hydrogen in the gas phase and progress of reduction represented by the partial mass of iron oxide (FeO) for the particles.

Finally, the two solvers can be executed concurrently (*parallel coupling* in the preCICE terminology) and synchronize automatically when data exchange is needed. This approach addresses the main issues highlighted in our previous works [86] and discussed in [89], namely the constraint on the partition alignment and the requirement for inter-partition inter-physics communication.

As a result, we obtain a parallel multi-physics coupled CFD-DEM solver for the Midrex blast furnace that takes advantage of two types of parallelisms [318]: With **functional decomposition**, XDEM and OpenFOAM are executed concurrently, solving respectively the particle phase and the fluid phase. With **domain decomposition**, both XDEM and OpenFOAM are executed in parallel after partitioning their respective domain. In OpenFOAM, the global CFD mesh is decomposed into smaller meshes that are distributed to computing nodes and are solved in parallel using MPI. On its side, XDEM is based on a hybrid OpenMP+MPI approach [122] in which the domain cell grid is decomposed and partitioned into subdomains in order to balance the workload. The subdomains are distributed to the processes and executed in parallel using MPI. Within each process, a fine-grain parallelization takes place at the particle level using OpenMP.

However, in this configuration, each solver runs in parallel and its workload is partitioned using its native implementation. There is no coordination for the partitioning of the two solvers that would account for their relative workload and assign the computing resources proportionally. Because of the synchronization occurring between the solvers at every coupling timestep, the slower solver will slow down the whole simulation. This is the focus of the next section.

7.5 Performance Evaluation

For the performance evaluation, we consider a Midrex blast furnace as depicted in Figure 7.2 with a total height of $32m$ and a maximum diameter of $6.5m$. It features 4 gas inlets at the mid-height and 4 gas outlets at the top and the CFD mesh is composed of 133,559 cells. The furnace is filled with 485,336 porous spherical particles with a radius between $4.5cm$ and $7.5cm$ and an internal chemical composition of 12 solid and gaseous species. In order to reduce the computational load, we use a scaling factor of 10 for the particles. This means that each simulated particle represents physical particles 10 times smaller, and the thermodynamic state is solved accordingly. In addition, for the sake of this study, the particle motion was disabled to avoid changes in the workload distribution over time.

For the software, we used OpenFOAM 7 (Git hash $3bcbaf9$), XDEM (Git hash $d03d01f$), and preCICE 2.5.0. The executions were carried out on the *Aion* cluster of the University of Luxembourg[3] which offers 354 computing nodes, each equipped with 256 GB of memory and two processors AMD Epyc ROME 7H12 2.6 GHz for a total of 128 cores per computing node. Executions were performed with exclusive access to the computing nodes and processes were bound to the computing cores using SLURM.

7.5.1 Individual Scalability of XDEM and OpenFOAM

We first study the scalability of each solver individually. We consider the coupled simulation of the Midrex blast furnace, but we measure only the time spent in each solver without

[3] `https://hpc-docs.uni.lu/systems/aion/`

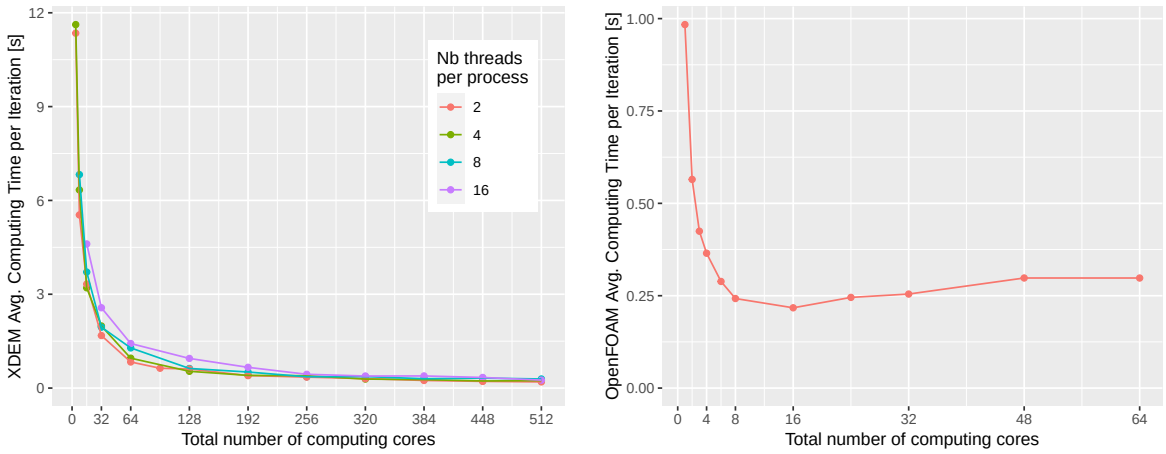

(a) Computing time spent in XDEM

(b) Computing time spent in OpenFOAM

Figure 7.8: Average iteration time spent purely in XDEM (left) and OpenFOAM (right) in function of the number of cores.

including the synchronization due to the coupling. For these executions, the processes of XDEM and OpenFOAM are assigned to distinct computing nodes with exclusive access (i.e., only XDEM processes or only OpenFOAM processes on each node). We measure the average time over 500 iterations, and we report the results in Figure 7.8. With nearly half a million particles and many chemical reactions taking place within the particles, the workload in XDEM is significant. As a result, XDEM displays good scalability with a computing time that continuously decreases up to 512 cores (i.e., four computing nodes). On the other hand, OpenFOAM shows a limited scalability, with a best performance for 16 processes and a computing time that slowly increases beyond that. This is due to the relatively small number of cells in the CFD mesh that limits the workload per process.

For an execution on a single core (not shown in the figure), XDEM requires an average of 41.2s per iteration, which is about 42 times more than for OpenFOAM in sequential (0.98s). This highlights the significant difference in workload between the two solvers.

7.5.2 Scalability of coupled XDEM–OpenFOAM

We now focus on the behaviour of the coupled execution, and we measure the coupled iteration time averaged over 500 iterations for XDEM and OpenFOAM running on different set

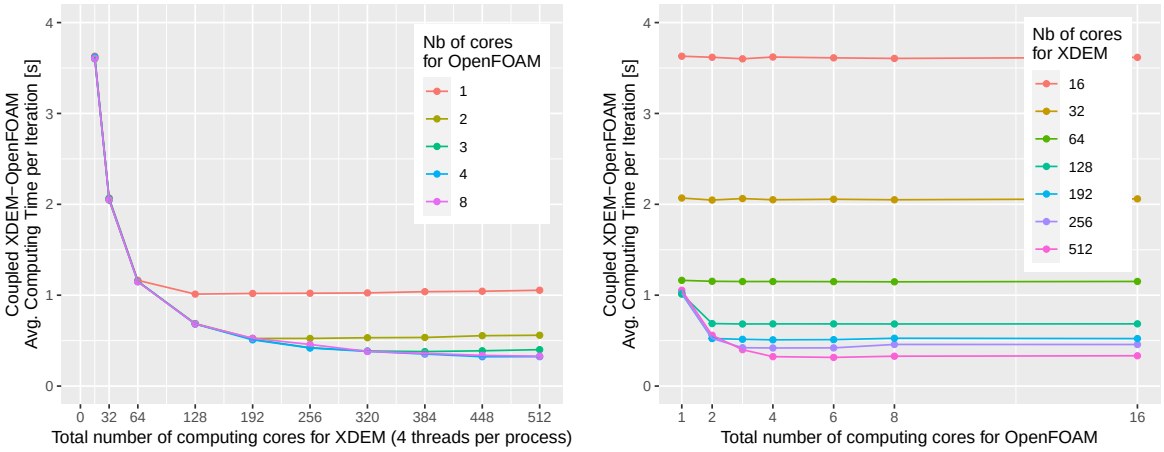

(a) In function of the number of cores assigned to XDEM

(b) In function of the number of cores assigned to OpenFOAM

Figure 7.9: Average iteration time of the coupled execution XDEM-OpenFOAM.

of computing nodes as in the previous study. The coupled iteration time includes the data exchange between the solvers and the synchronization that comes with it. The results are shown in Figure 7.9. On the left (Figure 7.9a), the coupled execution time decreases when more computing cores are added to XDEM. This is true until XDEM ceases to be the dominant solver. If OpenFOAM runs on a single core, its iteration time is around $1s$ and there is no benefit in running XDEM on more than 128 cores in this case. On the right, Figure 7.9b shows the same results from the other perspective, i.e., when increasing the number of cores for OpenFOAM. Assigning more computing resources to OpenFOAM does not reduce the iteration time while the XDEM is the dominant solver. With 128 cores or more assigned to XDEM, there is a benefit in running OpenFOAM in parallel on 2 or 4 cores.

These results show in practice the impact on the performance of the coupling synchronization. The dominant solver is the bottleneck and slows down the execution of the whole simulation. If more computing resources were to be added, they should be assigned to the dominant solver unless it has already reached its performance peak. However, it is important to notice that the dominant solver can change with the newly assigned resources and that this has to be re-evaluated if new cores have to be added again.

7.5.3 Complete Simulation of the Midrex Blast Furnace

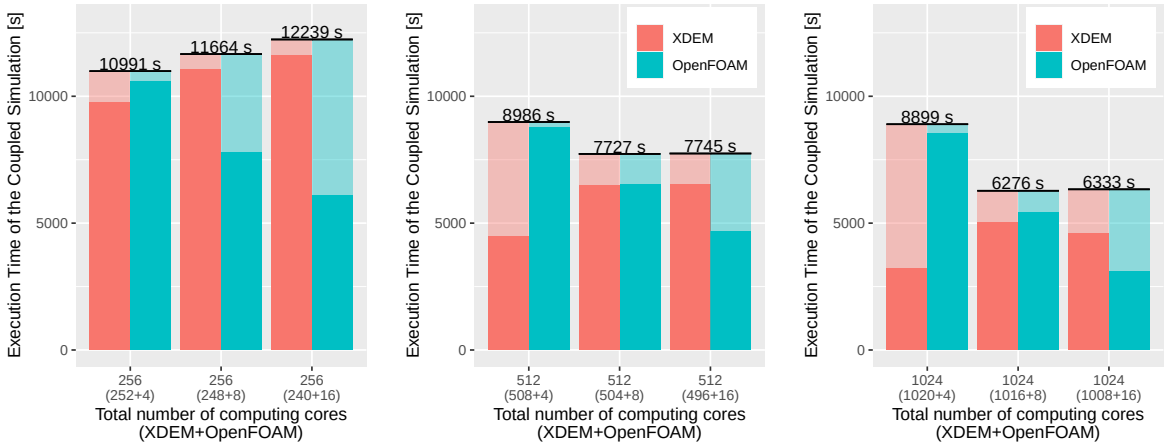

(a) Execution on 2 computing nodes.

(b) Execution on 4 computing nodes.

(c) Execution on 8 computing nodes.

Figure 7.10: Execution time for the simulation of 500s of the Midrex Blast Furnace with coupled XDEM-OpenFOAM. The bright colour represents the time actually spent in the solver and the light colour the time related to coupling communication and synchronization.

Finally, we leverage the results of our scalability studies to execute the complete simulation of the Midrex Blast Furnace for 500 seconds. In these executions, the processes of XDEM and OpenFOAM are packed together to fit the defined number of computing nodes, with all the OpenFOAM processes on the same node. In Figure 7.10, we show the total execution time of the complete simulations at a larger scale. For a given number of cores, we compare side-by-side the time spent in each solver (bright colour) and the time spent in the coupling communication and synchronization (light colour). The different Figures, from left to right (7.10a, 7.10b and 7.10c), show the performance of the coupled execution on 2, 4 and 8 computing nodes respectively.

On the left, Figure 7.10a shows the results for 2 computing nodes (256 cores) for an increasing number of cores assigned to OpenFOAM (and a slightly decreasing number of cores assigned to XDEM). We can see the switch of the workload between the solvers and how the coupled execution performance is limited by the dominant solver. We observe a similar trend with more computing resources in Figures 7.10b (512 cores) and Figure 7.10c (1024

cores), where the execution is dominated either by XDEM or OpenFOAM depending on how many cores they are assigned. The execution time increase of XDEM for the configurations (504+4) and (1016+8) appears to be linked to an unfortunate leap of the load-imbalance in the generated partitions for these specific configurations. This assumption is confirmed by a measured increase of the synchronization time between the XDEM processes at every timesteps.

Regarding the performance of the coupled execution, increasing the number of resources used to solve the problem allows speeding up the simulation if the cores are correctly distributed between the solvers. In the presented results, the best configuration is achieved with 1024 cores (for XDEM running on 1016 cores and OpenFOAM running on 8 cores) and simulates 500 seconds of the Midrex blast furnace in 1 hour and 45 minutes.

Finally, in Figure 7.10c, running the simulation with 1008 cores for XDEM and 16 cores for OpenFOAM reduces the time spent in each solver individually but it does not reduce the coupled simulation time (in comparison to the 1016+8 configuration). This leads us to believe that, at this scale, the data exchange and the coupling synchronization between the solvers are becoming a bottleneck for the performance of the coupled simulation with about 27% of the total time.

7.6 Conclusion

In this work, we focused on the Midrex blast furnace which has significant advantages in terms of energy efficiency and environmental impact. We presented our modeling and implementation based on XDEM (for the particle phases) and OpenFOAM (for the fluid phase) coupled using the preCICE library. Our implementation benefits from functional parallelism (the two solvers run concurrently) and decomposition parallelism (each solver runs in parallel with its native domain decomposition method). More precisely, XDEM relies on hybrid parallelization using MPI+OpenMPI and OpenFOAM is parallelized with MPI.

A thorough performance evaluation has been carried out to study the behaviour of the coupled system under varying numbers of cores. In the best configuration, we achieved a

coupled simulation of 500 seconds of our Midrex blast furnace in 1 hour and 45 minutes using 1024 cores.

Our work presents a detailed performance analysis of a complex real-world application employing volume coupling, and provide a concrete report that can guide the design of multi-physics load balancers. Our findings reveal a substantial work imbalance between the CFD and DEM solvers. This underscores the challenges in effectively distributing computing resources among the coupled solvers. Notably, each solver is partitioned independently and balances only the workload of its own physics domain. The load-balancing techniques currently employed fail to account for multi-solver workloads.

We made a step forward for the simulation of complex industrial processes with a multi-physics coupled CFD-DEM approach on HPC platforms. There are many remaining challenges to be addressed for the simulation of a complete 3D blast furnace. Thanks to the available computing resources, we will be able to refine our model, in particular by reducing the scaling factor and enabling the motion of particles. These improvements won't be possible without the development of advanced partitioning and load-balancing techniques for coupled multi-physics problems, which should account for the workload of each physics solver and also their dynamic behaviour.

Chapter 8

Conclusions and Recommendations

8.1 Conclusion

In this thesis, a partitioned coupling approach was proposed to couple different single-physics solvers/software so as to establish a multi-physics simulation environment. The novel 6−way momentum coupling is established between between CFD, DEM, and FEM, whereas a 2−way heat and mass transfer is established only between CFD and DEM. The partitioned coupling approach utilizes the preCICE coupling library, was developed over the complete length of the Ph.D. The momentum, heat, and mass transfer between CFD and DEM are done over volumetric meshes, whereas the momentum exchange between CFD-FEM, and DEM-FEM are done over surface meshes. The partitioned coupling approach developed throughout the Ph.D. resulted to be very versatile, and its versatility is showcased by the various problems tackled throughout the thesis.

The first two contributions in chapter 2, and 3 establish the framework required for the multi-component multi-physics simulation environment. Several numerical experiments performed validate and verify that the proposed coupling works properly. These two chapters laid the required foundation required to tackle diverse range of multi-physics applications. Additionally it lead to several related works contributed to the scientific community [3, 7].

In the fourth contribution to the thesis, the proposed coupling is utilized to its limits, where a novel fully coupled model of AWJC nozzle is established. This contribution delves into the complex interactions between the three different phases, i.e. fluid phase, particulate phase, and the nozzle solid phase. This 6−way CFD-DEM-FEM coupled numerical study allowed to thoroughly explore the complexities of particle-laden flow inside the AWJC nozzle, its complex interactions that result into unique erosion patterns consistent with the experimental observations. This study also allowed to get a deeper insight into the mechanical behavior of the AWJC nozzle under different operating conditions. This chapter significantly contributes to the scientific as well as the industrial community by modeling the AWJC nozzle with all the physics involved in the real life. This work demonstrates the need of high-fidelity numerical models do indeed lead to much deeper understanding of the complex multi-physics phenomena of erosion occurring inside the AWJC Nozzle.

The fifth contribution, utilises a 2−way CFD-DEM momentum coupling so as to study the dynamic changes in the frictional behavior of gravel in presence of melt water. This work utilises the multi-physics to successfully reproduce experiments performed to better understand rock-ice avalanche. This work proposes two different approaches to study the changes in frictional behavior, one via injection of water to emulate the water injected due to melting ice thus leading to complex, and second via ad-hoc variation of friction coefficient of the gravel. The proposed approaches yielded similar results, that are in good agreement with the experimental observations. Both the proposed approaches are scalable, and if necessary can be scaled up to simulate real size rock-ice avalanches. Nonetheless, the novel contributions of this study has opened numerical avenues for studying such disastrous phenomena.

The sixth contribution utilises a $2-way$ CFD-DEM momentum, heat and mass transfer. This work contributes to the scientific community in several ways, most significant of which is that it is the first 3D model of the raceway. This work shows significant differences as compared to the 2D model of the raceway, and correctly points out the deficiencies in the 2D model, due to several assumptions made. The 3D model captures the momentum coupling as well as the complex and dynamic thermodynamics of the blast furnace raceway.

The seventh and the final chapter of the thesis, delves into the performance analysis for the propose coupling approach. This article uses a 2−way CFD-DEM momentum, heat, and mass transfer to model the midrex furnace. Due to the large scale of the problem, this study offered the chance to study the computational performance using the HPC facilities. This work not only correctly captures the modeled physics, but also gives crucial insights into load-balancing, partitioning strategies, and detailed insights into computational costs of different aspects of the partitioned coupling approach. Additionally, this work demonstrates that by utilising the partitioned coupling approach it is possible to efficiently decompose the individual simulation domains of the individual single-physics solvers without incurring numerical instabilities.

Overall, this thesis provides crucial developments in multi-physics simulation environment. The flexibility, and versatility of the coupling approach allows to tackle diverse range of engineering applications, some of them already demonstrated in the thesis. I believe that

this work will serve as a basis of future multi-component multi-physics simulations environments.

8.2 Recommendation for future work

There are ample possibilities to further research and expand upon the work presented in the thesis. The articles presented in the current thesis have not only laid crucial foundations but also established new research directions.

The partitioned coupling approach presented in chapter 2 and 3, establishes 6−way momentum coupling between fluids, particles and solids, whereas it only establishes 2−way heat and mass transfer between fluid and particles. There is a possibility to incorporate heat and mass transfer to and fro to the solid solver (FEM). This will open up new avenues of research especially in the field of additive manufacturing. In the work of Mashhood [319], the thermal effects and stresses are studied in the process of Selective Laser Melting (SLM). The solid part is formed by melting particle bed using lasers. His model only uses boundary conditions to model the fluxes on the solid. This approximation, does not entirely capture the intricate heat exchange between the particle bed, the melted metal, and the frozen solid properly. On the other hand Aminnia [320, 321], utilizes a CFD-DEM coupled approach to study the dynamics and thermodynamics of a melt-pool. Hence, incorporating a heat and mass transfer between the solid and other two phases can open up avenues to research the SLM process in its entirety.

In the proposed CFD-DEM momentum, heat, and mass transfer, only VOF solvers can be used to model multi-phase fluid flow. This is because the momentum of all phases is treated with one equation, and only one data field is required for establishing the coupling. Although, for certain applications this is not enough, for example the SLM process mentioned above as well as when simulating the melted metal in blast furnaces. The coupling can be expanded to incorporate Euler multi-phase solver, that solves momentum and thermodynamics for each phase separately, allowing to model even more complex physics. Although, it is necessary to mind the cost of exchanging the extra fields over the coupled volumetric meshes.

The chapter 4, the foundation is laid to model the AWJC nozzle in its entirety. However, there are few things to be improved or developed. The immediate next step to the work proposed in chapter 4 will be to compute accelerated erosion using the erosion rates available in the literature and deform the AWJC nozzle solid geometry. The the 6−way CFD-DEM-FEM simulation is to be re-run with the deformed interior geometry. This will give us the beginning or new state, and the end or the eroded state of the AWJC nozzle. Additionally, it is advised to model the different components of the AWJ head separately to correct model the material properties and their mechanical response correctly. Furthermore, since it is assumed that the water-jet is stable, it is not necessary to use a computationally costly VOF solver. One can use a cheaper CFD solver as long as it can impart the same momentum on to the particles. Although, the cautionary keyword here is assumed. By using a cheaper CFD solver, the coupled simulation can be run for a longer duration, thus given better estimates of erosion and a mechanical response of the nozzle over a longer duration of time.

The work from the chapter 5, can be directly extended without the need of any new developments or research. The experiments performed [215] to study the friction behavior of rock-ice avalanche used various proportions rock and ice mixture, although thorough data was available in article for only one mixture. The same numerical simulations can be performed albeit with the different rock-ice ratios presented in the experiments. This will significantly contribute to the scientific community and additionally demonstrate the robustness of the proposed numerical approach.

As the partitioned coupling approach utilizes couples solvers/software as black box, the coupled components actually are not aware of the others. The solvers only care for the data fields being transferred. Hence, wherever necessary and/or possible the numerical models can be substitued with surrogate models. For example, Darlik [322] uses Physics Informed Neural Networks (PINNs) to reconstruct fluid fields in a biomass furnace. When simulating the biomass furnace, there is an load imbalance, where the CFD takes significantly more time. The CFD solver can be substituted in this case with a PINN solving for fluid fields, and transferring these fields to the particle solver, and so on, thus easing the load imbalance. Furthermore, preCICE allows to record the coupling data. This coupling data then can be

used through Artificial Solver Testing Environment [323] to substitute for the real solver. This enables speed up when developing and debugging new physics or cases, and removing the computational overhead.

The last but not the least, it is very important to perform preliminary performance study for large scale simulations. As the current partitioned coupling approach lifts the restrictions previously experienced when decomposing the simulations domains, it is possible to use different partitioning strategies for the individual solvers involved. Such studies will give an insight in the load balance/imbalance between the involved solvers. When tuned with proper partitioning, even if large scale, these simulations can be much faster. As several mid to large scalre applications are studied in the current work, it would be interesting to compare the performance of the new partitioned coupling approach with the legacy monolithic coupling.

Bibliography

[1] Prasad Adhav et al. “Numerical insights into rock–ice avalanche geophysical flow mobility through CFD–DEM simulation”. In: *Computational Particle Mechanics* (2024), pp. 1–17.

[2] Navid Aminnia et al. “Three-dimensional CFD-DEM simulation of raceway transport phenomena in a blast furnace”. In: *Fuel* 334 (2023), p. 126574.

[3] Xavier Besseron, Prasad Adhav, and Bernhard Peters. “Parallel Multi-Physics Coupled Simulation of a Midrex Blast Furnace”. In: *Proceedings of the International Conference on High Performance Computing in Asia-Pacific Region Workshops*. 2024, pp. 87–98.

[4] Fateme Darlik, Prasad Adhav, and Bernhard Peters. “Prediction of the biomass particles through the physics informed neural network.” In: *ECCOMAS Congress 2022-8th European Congress on Computational Methods in Applied Sciences and Engineering*. 2022.

[5] Prasad Adhav et al. “Development and Validation of Cfd-Dem Coupling Interface for Heat & Mass Transfer Using Partitioned Coupling Approach”. In: *Available at SSRN 4668107, submitted to International Communications in Heat and Mass Transfer* ().

[6] Prasad Adhav, Xavier Besseron, and Bernhard Peters. “Development of 6-way CFD-DEM-FEM momentum coupling interface using partitioned coupling approach”. In: *INENG-D-24-00303, submitted to Results in Engineering* ().

[7] Prasad Adhav, Xavier Besseron, and Bernhard Peters. “Erosion Unveiled: A 6-way Coupled CFD-DEM-FEM Analysis of Abrasive Water Jet Cutting Nozzle”. In: *POWTEC-D-23-02694, submitted in Powder Technology* ().

[8] Prasad Adhav et al. “Evaluation of erosion inside AWJC Nozzle by 6-way coupling of DEM+ CFD+ FEM using preCICE”. In: (2021).

[9] Prasad Adhav et al. “AWJC nozzle simulation by 6-way coupling of DEM+ CFD+ FEM using preCICE coupling library”. In: (2021).

[10] Prasad Adhav et al. “HEAT AND MASS TRANSFER BETWEEN XDEM & OPENFOAM USING PRECICE COUPLING LIBRARY”. In: (2022).

[11] Prasad Adhav. “Investigation of OpenFOAM-XDEM momentum coupling results for AWJC Nozzle using preCICE”. In: (2023).

[12] Xavier Besseron et al. “Toward High-Performance Multi-Physics Coupled Simulations for the Industry with XDEM”. In: *1st conference Math 2 Product (M2P) on Emerging Technologies in Computational Science for Industry, Sustainability and Innovation*. 2023.

[13] Prasad Adhav. “PhD Day-Complex Particle Laden Fluid Structure Interaction”. In: (2022).

[14] John David Anderson and John Wendt. *Computational fluid dynamics*. Vol. 206. Springer, 1995.

[15] Marwan Darwish and Fadl Moukalled. *The finite volume method in computational fluid dynamics: an advanced introduction with OpenFOAM® and Matlab®*. Springer, 2016.

[16] Olek C Zienkiewicz, Robert L Taylor, and Jian Z Zhu. *The finite element method: its basis and fundamentals*. Elsevier, 2005.

[17] Olek C Zienkiewicz and Robert L Taylor. *The finite element method for solid and structural mechanics*. Elsevier, 2005.

[18] Klaus-Jürgen Bathe. *Finite element procedures*. Klaus-Jurgen Bathe, 2006.

[19] Gerhard A Holzapfel. *Nonlinear solid mechanics: a continuum approach for engineering science*. 2002.

[20] Peter A Cundall and Otto DL Strack. “A discrete numerical model for granular assemblies”. In: *geotechnique* 29.1 (1979), pp. 47–65.

[21] Bernhard Peters. “Thermal conversion of solid fuels”. In: (2002).

[22] Shiyi Chen and Gary D Doolen. “Lattice Boltzmann method for fluid flows”. In: *Annual review of fluid mechanics* 30.1 (1998), pp. 329–364.

[23] Eugenio Oñate et al. “The particle finite element method—an overview”. In: *International Journal of Computational Methods* 1.02 (2004), pp. 267–307.

[24] Sergio Rodolfo Idelsohn et al. “Fluid–structure interaction using the particle finite element method”. In: *Computer methods in applied mechanics and engineering* 195.17-18 (2006), pp. 2100–2123.

[25] Max Roser, Hannah Ritchie, and Edouard Mathieu. “What is Moore’s Law?” In: *Our World in Data* (2023). https://ourworldindata.org/moores-law.

[26] C.A. Fourness and C.M. Pearson. *Paper metering, cutting, and reeling.* US Patent 2,006,499. July 1935. URL: `http://www.google.com/patents/US2006499`.

[27] E.V. Smith. *Liquid blasting.* US Patent 2,040,715. May 1936. URL: `http://www.google.com/patents/US2040715`.

[28] MP DuPlessis and M Hashish. “High energy water jet cutting equations for wood”. In: (1978).

[29] M Hashish. “The application of abrasive jets to concrete cutting”. In: *Proc. of 6th Int. Symp. on Jet Cutting Technology.* 1982, pp. 447–464.

[30] Mohamed Hashish. “A modeling study of metal cutting with abrasive waterjets”. In: (1984).

[31] M Hashish. “Machining of advanced composites with abrasive-waterjets”. In: *Machining composites* (1988), pp. 1–18.

[32] M Hashish, M Ramulu, and SP Raju. “Abrasive Waterjet Cutting Front Characteristics in Machining of Glass”. In: *Ceram. Trans.* 50 (1994), pp. 199–221.

[33] Jim Lorincz. “Waterjets: Evolving from macro to micro”. In: *Manufacturing Engineering* 143.5 (2009), pp. 47–53.

[34] Krzysztof Kukiełka. “Ecological aspects of the implementation of new technologies processing for machinery parts”. In: *Rocznik Ochrona Środowiska* 18 (2016), pp. 137–157.

[35] Andrzej Perec. “Experimental research into alternative abrasive material for the abrasive water-jet cutting of titanium”. In: *The International Journal of Advanced Manufacturing Technology* 97.1-4 (2018), pp. 1529–1540.

[36] Mohammad S Alsoufi. “State-of-the-art in abrasive water jet cutting technology and the promise for micro-and nano-machining”. In: *International Journal of Mechanical Engineering and Applications* 5.1 (2017), pp. 1–14.

[37] Yuvaraj Natarajan et al. “Abrasive Water Jet Machining process: A state of art of review”. In: *Journal of Manufacturing Processes* 49 (2020), pp. 271–322.

[38] A Anu Kuttan, R Rajesh, and M Dev Anand. “Abrasive water jet machining techniques and parameters: a state of the art, open issue challenges and research directions”. In: *Journal of the Brazilian Society of Mechanical Sciences and Engineering* 43 (2021), pp. 1–14.

[39] M Hashish. “Observations of wear of abrasive-waterjet nozzle materials”. In: (1994).

[40] Madhusarathi Nanduri, David G Taggart, and Thomas J Kim. “The effects of system and geometric parameters on abrasive water jet nozzle wear”. In: *International Journal of Machine Tools and Manufacture* 42.5 (2002), pp. 615–623.

[41] Chuanfu Shao et al. “Experimental and numerical investigation of abrasive water jet nozzle erosion”. In: *Powder Technology* 430 (2023), p. 119031.

[42] Andrzej Perec et al. “A study of wear on focusing tubes exposed to corundum-based abrasives in the waterjet cutting process”. In: *The International Journal of Advanced Manufacturing Technology* 104 (2019), pp. 2415–2427.

[43] Jeong-Uk Kim et al. “Nozzle Condition Monitoring System Using Root Mean Square of Acoustic Emissions during Abrasive Waterjet Machining”. In: *Journal of Manufacturing and Materials Processing* 6.2 (2022), p. 31.

[44] H Syazwani, G Mebrahitom, and A Azmir. “A review on nozzle wear in abrasive water jet machining application”. In: *IOP Conference Series: Materials Science and Engineering*. Vol. 114. 1. IOP Publishing. 2016, p. 012020.

[45] Gabriele Pozzetti and Bernhard Peters. “A numerical approach for the evaluation of particle-induced erosion in an abrasive waterjet focusing tube”. In: *Powder Technology* 333 (2018), pp. 229–242.

[46] R Kovacevic, L Wang, and YM Zhang. “Identification of abrasive waterjet nozzle wear based on parametric spectrum estimation of acoustic signal”. In: *Proceedings of the Institution of Mechanical Engineers, Part B: Journal of Engineering Manufacture* 208.3 (1994), pp. 173–181.

[47] Bostjan Jurisevic, Daniel Brissaud, and Mihael Junkar. “Monitoring of abrasive water jet (AWJ) cutting using sound detection”. In: *The International Journal of Advanced Manufacturing Technology* 24 (2004), pp. 733–737.

[48] R Pahuja and M Ramulu. “Abrasive waterjet process monitoring through acoustic and vibration signals”. In: *Proceedings of the 24th International Conference on Water Jetting*. 2018.

[49] Edoardo Copertaro, Francesco Perotti, and Massimiliano Annoni. “Operational vibration of a waterjet focuser as means for monitoring its wear progression”. In: *The International Journal of Advanced Manufacturing Technology* 116 (2021), pp. 1937–1949.

[50] Gerasimos Chourdakis et al. “preCICE v2: A sustainable and user-friendly coupling library”. In: *Open Research Europe* 2 (2022).

[51] Hans-Joachim Bungartz et al. “preCICE – A fully parallel library for multi-physics surface coupling”. In: *Computers and Fluids* 141 (2016). Advances in Fluid-Structure Interaction, pp. 250–258. ISSN: 0045-7930. DOI: https://doi.org/10.1016/j.compfluid.2016.04.003.

[52] Gerasimos Chourdakis, David Schneider, and Benjamin Uekermann. “OpenFOAM-preCICE: Coupling OpenFOAM with External Solvers for Multi-Physics Simulations”. In: *OpenFOAM® Journal* 3 (2023), pp. 1–25.

[53] Gene Hou, Jin Wang, and Anita Layton. “Numerical methods for fluid-structure interaction—a review”. In: *Communications in Computational Physics* 12.2 (2012), pp. 337–377.

[54] Woojin Kim and Haecheon Choi. “Immersed boundary methods for fluid-structure interaction: A review”. In: *International Journal of Heat and Fluid Flow* 75 (2019), pp. 301–309.

[55] Moubin Liu and Zhilang Zhang. “Smoothed particle hydrodynamics (SPH) for modeling fluid-structure interactions”. In: *Science China Physics, Mechanics & Astronomy* 62 (2019), pp. 1–38.

[56] Fei Xu et al. “On methodology and application of smoothed particle hydrodynamics in fluid, solid and biomechanics”. In: *Acta Mechanica Sinica* 39.2 (2023), p. 722185.

[57] Ramji Kamakoti and Wei Shyy. “Fluid–structure interaction for aeroelastic applications”. In: *Progress in Aerospace Sciences* 40.8 (2004), pp. 535–558.

[58] Syed Samar Abbas, Mohammad Shakir Nasif, and Rafat Al-Waked. “State-of-the-art numerical fluid–structure interaction methods for aortic and mitral heart valves simulations: a review”. In: *Simulation* 98.1 (2022), pp. 3–34.

[59] Yuri Bazilevs et al. “Computer modeling of wind turbines: 2. Free-surface FSI and fatigue-damage”. In: *Archives of Computational Methods in Engineering* 26 (2019), pp. 1101–1115.

[60] Siddharth Suhas Kulkarni et al. “Fluid-structure interaction based optimisation in tidal turbines: A perspective review”. In: *Journal of Ocean Engineering and Science* 7.5 (2022), pp. 449–461.

[61] Tajammal Abbas, Igor Kavrakov, and Guido Morgenthal. “Methods for flutter stability analysis of long-span bridges: a review”. In: *Proceedings of the Institution of Civil Engineers-Bridge Engineering*. Vol. 170. 4. Thomas Telford Ltd. 2017, pp. 271–310.

[62] AS Tijsseling. “Fluid-structure interaction in liquid-filled pipe systems: a review”. In: *Journal of Fluids and Structures* 10.2 (1996), pp. 109–146.

[63] Vincent Keim et al. “FSI-simulation of ductile fracture propagation and arrest in pipelines: Comparison with existing data of full-scale burst tests”. In: *International Journal of Pressure Vessels and Piping* 182 (2020), p. 104067.

[64] Bernhard Peters et al. “XDEM multi-physics and multi-scale simulation technology: Review of DEM–CFD coupling, methodology and engineering applications”. In: *Particuology* 44 (2019), pp. 176–193.

[65] Xiaoyu Wang et al. “Developments and applications of the CFD-DEM method in particle–fluid numerical simulation in petroleum engineering: A review”. In: *Applied Thermal Engineering* 222 (2023), p. 119865.

[66] Shibo Kuang, Mengmeng Zhou, and Aibing Yu. “CFD-DEM modelling and simulation of pneumatic conveying: A review”. In: *Powder Technology* 365 (2020), pp. 186–207.

[67] Mahmoud A El-Emam et al. “Theories and applications of CFD–DEM coupling approach for granular flow: A review”. In: *Archives of Computational Methods in Engineering* (2021), pp. 1–42.

[68] Zhenjiang Zhao et al. “Recent advances and perspectives of CFD–DEM simulation in fluidized bed”. In: *Archives of Computational Methods in Engineering* (2023), pp. 1–48.

[69] Prasad Adhav et al. “Numerical insights into Rock-Ice Avalanche Geophysical Flow Mobility through CFD-DEM simulation”. In: *Computational Particle Mechanics* (accepted 27 Nov 2023).

[70] Fanbao Chen et al. “Sand-ejecting fire extinguisher parameter sensitivity analysis based on DOE and CFD-DEM coupling simulations”. In: *Advanced Powder Technology* 33.9 (2022), p. 103719.

[71] Yong Kong, Jidong Zhao, and Xingyue Li. “Hydrodynamic dead zone in multiphase geophysical flows impacting a rigid obstacle”. In: *Powder Technology* 386 (2021), pp. 335–349.

[72] Liming Yao et al. “An optimized CFD-DEM method for particle collision and retention analysis of two-phase flow in a reduced-diameter pipe”. In: *Powder Technology* 405 (2022), p. 117547.

[73] Dan Forsström and Pär Jonsén. “Calibration and validation of a large scale abrasive wear model by coupling DEM-FEM: Local failure prediction from abrasive wear of tipper bodies during unloading of granular material”. In: *Engineering Failure Analysis* 66 (2016), pp. 274–283.

[74] Yogesh Surkutwar, Corina Sandu, and Costin Untaroiu. “Review of modeling methods of compressed snow-tire interaction”. In: *Journal of Terramechanics* 105 (2023), pp. 27–40.

[75] Boqiang Wu et al. “Numerical simulation of erosion and fatigue failure the coal gangue paste filling caused to pumping pipes”. In: *Engineering Failure Analysis* 134 (2022), p. 106081.

[76] Wei Wang et al. “Using FEM–DEM coupling method to study three-body friction behavior”. In: *Wear* 318.1-2 (2014), pp. 114–123.

[77] Seddik Shiri. “3D numerical modeling of flows on a reduced model of a ski jump spillway with an erosion pit using a coupled SPH–FEM-DEM approach”. In: *Journal of Applied Water Engineering and Research* (2023), pp. 1–13.

[78] Alessandro Leonardi et al. “Particle–fluid–structure interaction for debris flow impact on flexible barriers”. In: *Computer-Aided Civil and Infrastructure Engineering* 31.5 (2016), pp. 323–333.

[79] Chun Liu, Zhixiang Yu, and Shichun Zhao. “A coupled SPH-DEM-FEM model for fluid-particle-structure interaction and a case study of Wenjia gully debris flow impact estimation”. In: *Landslides* 18 (2021), pp. 2403–2425.

[80] LM Yao et al. “A new multi-field coupled dynamic analysis method for fracturing pipes”. In: *Journal of Petroleum Science and Engineering* 196 (2021), p. 108023.

[81] Samanthi Indiketiya, Piratheepan Jegatheesan, and Pathmanathan Rajeev. "Evaluation of defective sewer pipe–induced internal erosion and associated ground deformation using laboratory model test". In: *Canadian Geotechnical Journal* 54.8 (2017), pp. 1184–1195.

[82] R Parameshwaran, Sai Jathin Dhulipalla, and Daseswara Rao Yendluri. "Fluid-structure interactions and flow induced vibrations: a review". In: *Procedia Engineering* 144 (2016), pp. 1286–1293.

[83] Pär Jonsén et al. "A novel method for modelling of interactions between pulp, charge and mill structure in tumbling mills". In: *Minerals Engineering* 63 (2014), pp. 65–72.

[84] Simon Larsson et al. "A novel approach for modelling of physical interactions between slurry, grinding media and mill structure in wet stirred media mills". In: *Minerals Engineering* 148 (2020), p. 106180.

[85] Dong-Mei Zhang, Lei Han, and Zhong-Kai Huang. "A numerical approach for fluid-particle-structure interactions problem with CFD-DEM-CSD coupling method". In: *Computers and Geotechnics* 152 (2022), p. 105007.

[86] Gabriele Pozzetti et al. "A co-located partitions strategy for parallel CFD–DEM couplings". In: *Advanced Powder Technology* 29.12 (2018), pp. 3220–3232.

[87] Sergio R Idelsohn. *Numerical simulations of coupled problems in engineering*. Springer, 2014.

[88] Benjamin Walter Uekermann. "Partitioned fluid-structure interaction on massively parallel systems". PhD thesis. Technische Universität München, 2016.

[89] Xavier Besseron, Henrik Rusche, and Bernhard Peters. "Parallel Multi-Physics Simulation of Biomass Furnace and Cloud-based Workflow for SMEs". English. In: *Practice and Experience in Advanced Research Computing (PEARC '22)*. CE - Commission Européenne [BE]. Boston, MA, United States: Association for Computing Machinery, July 2022. DOI: 10.1145/3491418.3530294. URL: https://pearc.acm.org/pearc22/.

[90] Xavier Besseron, Prasad Adhav, and Bernhard Peters. "Parallel Multi-Physics Coupled Simulation of a Midrex Blast Furnace". In: *Proceedings of the HPC Asia 2024 Workshops*. New York, NY, United States: Association for Computing Machinery, 2024. DOI: XX.XXX/XXXXXXX.XXXXXXX.

[91] Florent Duchaine et al. "Analysis of high performance conjugate heat transfer with the openpalm coupler". In: *Computational Science & Discovery* 8.1 (2015), p. 015003.

[92] S Slattery, PPH Wilson, and R Pawlowski. "The Data Transfer Kit: A geometric rendezvous-based tool for multiphysics data transfer". In: *International conference on mathematics & computational methods applied to nuclear science & engineering (M&C 2013)*. 2013, pp. 5–9.

[93] FI Pelupessy et al. "The astrophysical multipurpose software environment". In: *Astronomy & Astrophysics* 557 (2013), A84.

[94] Francesco Di Natale et al. "A massively parallel infrastructure for adaptive multiscale simulations: modeling RAS initiation pathway for cancer". In: *Proceedings of the International Conference for High Performance Computing, Networking, Storage and Analysis*. 2019, pp. 1–16.

[95] VV Krzhizhanovskaya et al. "Preface: Twenty Years of Computational Science". In: *Lecture Notes in Computer Science* 12142 (2020).

[96] Yu-Hang Tang et al. "Multiscale universal interface: a concurrent framework for coupling heterogeneous solvers". In: *Journal of Computational Physics* 297 (2015), pp. 13–31.

[97] Derek Groen et al. "Mastering the scales: a survey on the benefits of multiscale computing software". In: *Philosophical Transactions of the Royal Society A* 377.2142 (2019), p. 20180147.

[98] Benjamin Uekermann et al. "Official preCICE adapters for standard open-source solvers". In: *Proceedings of the 7th GACM colloquium on computational mechanics for young scientists from academia*. 2017.

[99] Lucia Cheung Yau. "Conjugate Heat Transfer with the Multiphysics Coupling Library preCICE". Master's thesis. Technical University of Munich, 2016.

[100] *OpenFOAM Foundation*. URL: `https://openfoam.org`. (accessed: 2020).

[101] Guido Dhondt. *The finite element method for three-dimensional thermomechanical applications*. John Wiley & Sons, 2004.

[102] *Calculix – a free software three-dimensional structural finite element program*. URL: `http://www.calculix.de/`. (first accessed: 2020).

[103] Mehdi Baniasadi, Maryam Baniasadi, and Bernhard Peters. "Coupled CFD-DEM with heat and mass transfer to investigate the melting of a granular packed bed". In: *Chemical Engineering Science* 178 (2018), pp. 136–145.

[104] Heinrich Hertz. "Ueber die Berührung fester elastischer Körper." In: (1882).

[105] Raymond David Mindlin. "Compliance of elastic bodies in contact". In: (1949).

[106] Yutaka Tsuji, Toshitsugu Tanaka, and T Ishida. "Lagrangian numerical simulation of plug flow of cohesionless particles in a horizontal pipe". In: *Powder technology* 71.3 (1992), pp. 239–250.

[107] D Zhang and WJ Whiten. "The calculation of contact forces between particles using spring and damping models". In: *Powder technology* 88.1 (1996), pp. 59–64.

[108] Tao Zhao. *Coupled DEM-CFD analyses of landslide-induced debris flows*. Springer, 2017.

[109] Hamid Arastoopour. "Numerical simulation and experimental analysis of gas/solid flow systems: 1999 Fluor-Daniel Plenary lecture". In: *Powder Technology* 119.2-3 (2001), pp. 59–67.

[110] Renzo Di Felice and Marco Rotondi. "Fluid-particle drag force in binary-solid suspensions". In: *International Journal of Chemical Reactor Engineering* 10.1 (2012).

[111] Dimitri Gidaspow. *Multiphase flow and fluidization: continuum and kinetic theory descriptions*. Academic press, 1994.

[112] JF T Richardson. “Sedimentation and fluidization: part-1”. In: *Transactions of Institution of Chemical Engineers* 32 (1954), pp. 35–53.

[113] Links Schiller. “A drag coefficient correlation”. In: *Zeit. Ver. Deutsch. Ing.* 77 (1933), pp. 318–320.

[114] Jin Sun, Francine Battaglia, and Shankar Subramaniam. “Hybrid two-fluid DEM simulation of gas-solid fluidized beds”. In: (2007).

[115] Madhava Syamlal, William Rogers, and Thomas J OBrien. *MFIX documentation theory guide*. Tech. rep. USDOE Morgantown Energy Technology Center (METC), WV (United States), 1993.

[116] CY Wen and YH Yu. “Mechanics of fluidization”. In: *The Chemical Engineering Progress Symposium Series* 162 (1966), pp. 100–111.

[117] Sabri Ergun and Ao Ao Orning. “Fluid flow through randomly packed columns and fluidized beds”. In: *Industrial & Engineering Chemistry* 41.6 (1949), pp. 1179–1184.

[118] Heng Xiao and Jin Sun. “Algorithms in a robust hybrid CFD-DEM solver for particle-laden flows”. In: *Communications in Computational Physics* 9.2 (2011), pp. 297–323.

[119] Isaak E Idelchik. “Handbook of hydraulic resistance”. In: *Washington* (1986).

[120] RB Bird, WE Stewart, and EN Lightfoot. *Transport Phenomena, 2nd Edn. New York, NY: John Wilwe & Sons*. 2007.

[121] *preCICE Coupling Library official page*. URL: `www.precice.org`. (accessed: 2020).

[122] A. W. Mainassara Chekaraou et al. “Hybrid MPI+OpenMP Implementation of eXtended Discrete Element Method”. In: *2018 30th International Symposium on Computer Architecture and High Performance Computing (SBAC-PAD)*. Sept. 2018, pp. 450–457. DOI: `10.1109/CAHPC.2018.8645880`.

[123] Gerasimos Chourdakis. “A general OpenFOAM adapter for the coupling library preCICE”. MA thesis. Technical University of Munich, Oct. 2017. URL: `https://www5.in.tum.de/pub/Chourdakis2017_Thesis.pdf`.

[124] Stefan Turek and Jaroslav Hron. *Proposal for numerical benchmarking of fluid-structure interaction between an elastic object and laminar incompressible flow*. Springer, 2006.

[125] Mark Michael, Frank Vogel, and Bernhard Peters. "DEM–FEM coupling simulations of the interactions between a tire tread and granular terrain". In: *Computer Methods in Applied Mechanics and Engineering* 289 (2015), pp. 227–248.

[126] H Nakashima and A Oida. "Algorithm and implementation of soil–tire contact analysis code based on dynamic FE–DE method". In: *Journal of Terramechanics* 41.2-3 (2004), pp. 127–137.

[127] David A Horner, John F Peters, and Alex Carrillo. "Large scale discrete element modeling of vehicle-soil interaction". In: *Journal of engineering mechanics* 127.10 (2001), pp. 1027–1032.

[128] Shahab Golshan et al. "Review and implementation of CFD-DEM applied to chemical process systems". In: *Chemical Engineering Science* 221 (2020), p. 115646.

[129] Benedikt Schott, Christoph Ager, and Wolfgang A Wall. "Monolithic cut finite element–based approaches for fluid-structure interaction". In: *International Journal for Numerical Methods in Engineering* 119.8 (2019), pp. 757–796.

[130] HP Zhu et al. "Discrete particle simulation of particulate systems: a review of major applications and findings". In: *Chemical Engineering Science* 63.23 (2008), pp. 5728–5770.

[131] Andrew Hobbs. "Simulation of an aggregate dryer using coupled CFD and DEM methods". In: *International Journal of Computational Fluid Dynamics* 23.2 (2009), pp. 199–207.

[132] F Sudbrock et al. "Convective drying of agitated silica gel and beech wood particle beds—experiments and transient DEM-CFD simulations". In: *Drying technology* 33.15-16 (2015), pp. 1808–1820.

[133] Patiwat Khomwachirakul et al. “Simulation of flow and drying characteristics of high-moisture particles in an impinging stream dryer via CFD-DEM”. In: *Drying technology* 34.4 (2016), pp. 403–419.

[134] Viktor Scherer et al. “Coupled DEM–CFD simulation of drying wood chips in a rotary drum–Baffle design and model reduction”. In: *Fuel* 184 (2016), pp. 896–904.

[135] Matthias Börner, Andreas Bück, and Evangelos Tsotsas. “DEM-CFD investigation of particle residence time distribution in top-spray fluidised bed granulation”. In: *Chemical Engineering Science* 161 (2017), pp. 187–197.

[136] Daoyin Liu, Changsheng Bu, and Xiaoping Chen. “Development and test of CFD–DEM model for complex geometry: A coupling algorithm for Fluent and DEM”. In: *Computers & Chemical Engineering* 58 (2013), pp. 260–268. ISSN: 0098-1354. DOI: https://doi.org/10.1016/j.compchemeng.2013.07.006.

[137] Clarissa B Fonte, JA Oliveira Jr, and Lucilla C de ALMEIDA. “DEM-CFD coupling: mathematical modelling and case studies using ROCKY-DEM® and ANSYS Fluent®”. In: *Proceedings of the 11th International Conference on CFD in the Minerals and Process Industries, CSIRO, Melbourne, Australia*. 2015, pp. 7–9.

[138] Christoph Goniva et al. “Open source CFD-DEM modelling for particle-based processes”. In: *11th International Conference on Computational Fluid Dynamics in the Minerals and Process Industries*. 2015.

[139] Kristin Kerst et al. “CFD-DEM simulations of a fluidized bed crystallizer”. In: *Chemical Engineering Science* 165 (2017), pp. 1–13.

[140] Maryam Askarishahi, Mohammad-Sadegh Salehi, and Stefan Radl. “Full-physics simulations of spray-particle interaction in a bubbling fluidized bed”. In: *AIChE Journal* 63.7 (2017), pp. 2569–2587.

[141] Gerasimos Chourdakis et al. “Coupling OpenFOAM to different solvers, physics, models, and dimensions using preCICE”. en. In: *14th OpenFOAM Workshop*. Duisburg, Germany, July 2019. URL: https://www.conftool.com/ofw14/index.php?page=browseSessions%5C&form_session=26%5C&presentations=show.

[142] Patrick Schmidt et al. “Simulation of flow in deformable fractures using a quasi-Newton based partitioned coupling approach”. In: *Computational Geosciences* (2022). ISSN: 15731499. DOI: 10.1007/s10596-021-10120-8.

[143] Jiaxin Cui, Qinfu Hou, and Yansong Shen. “CFD-DEM study of coke combustion in the raceway cavity of an ironmaking blast furnace”. In: *Powder Technology* 362 (2020), pp. 539–549.

[144] Christian Bruch, Bernhard Peters, and Thomas Nussbaumer. “Modelling wood combustion under fixed bed conditions”. In: *Fuel* 82.6 (2003), pp. 729–738.

[145] Amir Houshang Mahmoudi, Florian Hoffmann, and Bernhard Peters. “Application of XDEM as a novel approach to predict drying of a packed bed”. In: *International Journal of Thermal Sciences* 75 (2014), pp. 65–75.

[146] Amir Houshang Mahmoudi et al. “An experimental and numerical study of wood combustion in a fixed bed using Euler–Lagrange approach (XDEM)”. In: *Fuel* 150 (2015), pp. 573–582.

[147] Amir Houshang Mahmoudi, Florian Hoffmann, and Bernhard Peters. “Semi-resolved modeling of heat-up, drying and pyrolysis of biomass solid particles as a new feature in XDEM”. In: *Applied Thermal Engineering* 93 (2016), pp. 1091–1104.

[148] Bernhard Peters. *Thermal conversion of solid fuels*. eng. International series on developments in heat transfer Vol. 15 15. Southampton: WIT Press, 2003. ISBN: 1-85312-953-4.

[149] Hans-Joachim Bungartz et al. “preCICE–a fully parallel library for multi-physics surface coupling”. In: *Computers & Fluids* 141 (2016), pp. 250–258.

[150] E Achenbach. “Heat and flow characteristics of packed beds”. In: *Experimental thermal and fluid science* 10.1 (1995), pp. 17–27.

[151] Volker Gnielinski. “New equations for heat and mass transfer in turbulent pipe and channel flow”. In: *International chemical engineering* 16.2 (1976), pp. 359–367.

[152] Jian Yang et al. “Experimental analysis of forced convective heat transfer in novel structured packed beds of particles”. In: *Chemical engineering science* 71 (2012), pp. 126–137.

[153] Noriaki Wakao and Seiichirō Kagei. *Heat and mass transfer in packed beds*. Vol. 1. Taylor & Francis, 1982.

[154] Bernhard Peters et al. “Measurements and particle resolved modelling of heat-up and drying of a packed bed”. In: *Biomass and Bioenergy* 23.4 (2002), pp. 291–306.

[155] *Foam Extend v3.2*. URL: `https://openfoamwiki.net/index.php/Installation/Linux/foam-extend-3.2`. (accessed: 2020).

[156] Josef Petek. *Experimentelle Untersuchung der Pyrolyse in inerter und reaktiver Atmosphäre unter den Bedingungen der Wurfbeschickung*. na, 1998.

[157] Bernhard Peters and Christian Bruch. “Drying and pyrolysis of wood particles: experiments and simulation”. In: *Journal of analytical and applied pyrolysis* 70.2 (2003), pp. 233–250.

[158] AM Jethe and LM Thakare. “Appraisal and Assessment of Hydraulic Geometry and Development of Potholes on Bedrock Channel of Kukadi River, Maharashtra, India”. In: *Indian Journal of Science and Technology* 16.35 (2023), pp. 2822–2834.

[159] O.J. Carl. *Method for cutting up plastic and semi-plastic masses*. US Patent 2,881,503. Apr. 1959. URL: `http://www.google.com/patents/US2881503`.

[160] RK Thakur and KK Singh. “Abrasive waterjet machining of fiber-reinforced composites: A state-of-the-art review”. In: *Journal of the Brazilian Society of Mechanical Sciences and Engineering* 42 (2020), pp. 1–25.

[161] David A Summers. *Waterjetting technology*. CRC Press, 2003.

[162] Andreas W Momber and Radovan Kovacevic. *Principles of abrasive water jet machining*. Springer Science & Business Media, 2012.

[163] Paul Etchells. “Cutting head design lowers abrasive waterjet cutting costs”. In: *Aircraft Engineering and Aerospace Technology* 69.2 (1997), pp. 147–150.

[164] Bo Assarsson. “Robotized waterjet cutting”. In: *Industrial Robot: An International Journal* 21.1 (1994), pp. 12–17.

[165] Mohamed Hashish. *Abrasive-Waterjet Machining of Composites*. 2008.

[166] HT Liu and E Schubert. “Micro abrasive-waterjet technology”. In: *Micromachining techniques for fabrication of micro and nano structures* (2012), pp. 205–233.

[167] Gustav Hultgren et al. “Fatigue probability model for AWJ-cut steel including surface roughness and residual stress”. In: *Journal of Constructional Steel Research* 179 (2021), p. 106537.

[168] Xiaochen Chen et al. “Experiment and simulation research on abrasive water jet nozzle wear behavior and anti-wear structural improvement”. In: *Journal of the Brazilian Society of Mechanical Sciences and Engineering* 39 (2017), pp. 2023–2033.

[169] Mingming Du et al. “Numerical research on multi-particle movements and nozzle wear involved in abrasive waterjet machining”. In: *The International Journal of Advanced Manufacturing Technology* 117 (2021), pp. 2845–2858.

[170] Mingming Du et al. “Numerical research on kerf characteristics of abrasive waterjet machining based on the SPH-DEM-FEM approach”. In: *The International Journal of Advanced Manufacturing Technology* 111 (2020), pp. 3519–3533.

[171] Zhongtan Li et al. “Numerical simulation and experimental verification of heterogeneous granite impacted by abrasive water jet based on SPH-FEM coupling algorithm”. In: *Powder Technology* 416 (2023), p. 118233.

[172] S Anwar, DA Axinte, and AA Becker. “Finite element modelling of abrasive waterjet milled footprints”. In: *Journal of Materials Processing Technology* 213.2 (2013), pp. 180–193.

[173] TN Deepu Kumar and DS Srinivasu. “Integration of CFD simulated abrasive waterjet flow dynamics with the material removal model for kerf geometry prediction in overlapped erosion on Ti-6Al-4V alloy”. In: *Simulation Modelling Practice and Theory* (2023), p. 102788.

[174] T Matsumura, T Muramatsu, and S Fueki. “Abrasive water jet machining of glass with stagnation effect”. In: *CIRP annals* 60.1 (2011), pp. 355–358.

[175] Gabriele Pozzetti and Bernhard Peters. “LES-VOF simulations of a pure water jet developing inside an AWJC nozzle: preliminary observations and guidelines”. In: *Proceedings of 2017 WJTA-IMCA* (2017).

[176] Zhe Lv et al. “Investigation on flow field of ultrasonic-assisted abrasive waterjet using CFD with discrete phase model”. In: *The International Journal of Advanced Manufacturing Technology* 96 (2018), pp. 963–972.

[177] Xinping Long et al. “Numerical investigation on the internal flow and the particle movement in the abrasive waterjet nozzle”. In: *Powder Technology* 314 (2017), pp. 635–640.

[178] Zhengrong Qiang et al. “CFD research on particle movement and nozzle wear in the abrasive water jet cutting head”. In: *The International Journal of Advanced Manufacturing Technology* 95 (2018), pp. 4091–4100.

[179] Zhibo Li et al. “Simulation and Optimization of the Nozzle Section Geometry for a Suspension Abrasive Water Jet”. In: *Machines* 10.1 (2021), p. 3.

[180] Tolga Susuzlu. “Development and evaluation of ultra high pressure waterjet cutting”. In: (2008).

[181] Edoardo Copertaro et al. “Focusing tube operational vibration as a means for monitoring the abrasive waterjet cutting capability”. In: *Journal of Manufacturing Processes* 59 (2020), pp. 1–10.

[182] Stewart Cant. “SB Pope, Turbulent Flows, Cambridge University Press, Cambridge, UK, 2000, 771 pp.” In: *Combustion and Flame* 125.4 (2001), pp. 1361–1362.

[183] Edin Berberović et al. “Drop impact onto a liquid layer of finite thickness: Dynamics of the cavity evolution”. In: *Physical Review E* 79.3 (2009), p. 036306.

[184] Y Isomoto Oka, K Okamura, and T Yoshida. "Practical estimation of erosion damage caused by solid particle impact: Part 1: Effects of impact parameters on a predictive equation". In: *Wear* 259.1-6 (2005), pp. 95–101.

[185] David Alexander. "Urban landslides". In: *Progress in Physical Geography* 13.2 (1989), pp. 157–189.

[186] Marcel Hürlimann, Ramon Copons, and Joan Altimir. "Detailed debris flow hazard assessment in Andorra: a multidisciplinary approach". In: *Geomorphology* 78.3-4 (2006), pp. 359–372.

[187] Dan H Shugar et al. "A massive rock and ice avalanche caused the 2021 disaster at Chamoli, Indian Himalaya". In: *Science* 373.6552 (2021), pp. 300–306.

[188] Xuanmei Fan et al. "Imminent threat of rock-ice avalanches in High Mountain Asia". In: *Science of The Total Environment* 836 (2022), p. 155380.

[189] Shiva P Pudasaini and Kolumban Hutter. *Avalanche dynamics: dynamics of rapid flows of dense granular avalanches*. Springer Science & Business Media, 2007.

[190] Rosanna Sosio et al. "Modelling rock avalanche propagation onto glaciers". In: *Quaternary Science Reviews* 47 (2012), pp. 23–40.

[191] Mario Germán Trujillo-Vela et al. "An overview of debris-flow mathematical modelling". In: *Earth-Science Reviews* (2022), p. 104135.

[192] Stuart B Savage and Kolumban Hutter. "The motion of a finite mass of granular material down a rough incline". In: *Journal of fluid mechanics* 199 (1989), pp. 177–215.

[193] Stuart B Savage and Kolumban Hutter. "The dynamics of avalanches of granular materials from initiation to runout. Part I: Analysis". In: *Acta Mechanica* 86.1-4 (1991), pp. 201–223.

[194] Olivier Pouliquen and Yoel Forterre. "Friction law for dense granular flows: application to the motion of a mass down a rough inclined plane". In: *Journal of fluid mechanics* 453 (2002), pp. 133–151.

[195] Roger P Denlinger and Richard M Iverson. “Granular avalanches across irregular three-dimensional terrain: 1. Theory and computation”. In: *Journal of Geophysical Research: Earth Surface* 109.F1 (2004).

[196] Dominique Laigle and Philippe Coussot. “Numerical modeling of mudflows”. In: *Journal of hydraulic engineering* 123.7 (1997), pp. 617–623.

[197] Hiroshi Takebayashi and Masaharu Fujita. “Numerical simulation of a debris flow on the basis of a two-dimensional continuum body model”. In: *Geosciences* 10.2 (2020), p. 45.

[198] Maurice A Biot. “Theory of propagation of elastic waves in a fluid-saturated porous solid. II. Higher frequency range”. In: *The Journal of the acoustical Society of america* 28.2 (1956), pp. 179–191.

[199] Richard M Iverson and Roger P Denlinger. “Flow of variably fluidized granular masses across three-dimensional terrain: 1. Coulomb mixture theory”. In: *Journal of Geophysical Research: Solid Earth* 106.B1 (2001), pp. 537–552.

[200] SP Pudasaini, Y Wang, and K Hutter. “Modelling debris flows down general channels”. In: *Natural Hazards and Earth System Sciences* 5.6 (2005), pp. 799–819.

[201] E Bruce Pitman and Long Le. “A two-fluid model for avalanche and debris flows”. In: *Philosophical Transactions of the Royal Society A: Mathematical, Physical and Engineering Sciences* 363.1832 (2005), pp. 1573–1601.

[202] Shiva P Pudasaini. “A general two-phase debris flow model”. In: *Journal of Geophysical Research: Earth Surface* 117.F3 (2012).

[203] Shiva P Pudasaini and Martin Mergili. “A multi-phase mass flow model”. In: *Journal of Geophysical Research: Earth Surface* 124.12 (2019), pp. 2920–2942.

[204] Shiva P Pudasaini and Jan-Thomas Fischer. “A mechanical model for phase separation in debris flow”. In: *International Journal of Multiphase Flow* 129 (2020), p. 103292.

[205] Tuo Wang et al. “A review of methods, applications and limitations for incorporating fluid flow in the discrete element method”. In: *Journal of Rock Mechanics and Geotechnical Engineering* 14.3 (2022), pp. 1005–1024.

[206] Richard M Iverson and David L George. “A depth-averaged debris-flow model that includes the effects of evolving dilatancy. I. Physical basis”. In: *Proceedings of the Royal Society A: Mathematical, Physical and Engineering Sciences* 470.2170 (2014), p. 20130819.

[207] Tong Shan and Jidong Zhao. “A coupled CFD-DEM analysis of granular flow impacting on a water reservoir”. In: *Acta Mechanica* 225 (2014), pp. 2449–2470.

[208] Wen-Jie Xu et al. “Study on landslide-induced wave disasters using a 3D coupled SPH-DEM method”. In: *Bulletin of Engineering Geology and the Environment* 79 (2020), pp. 467–483.

[209] Wen-Jie Xu and Xue-Yang Dong. “Simulation and verification of landslide tsunamis using a 3D SPH-DEM coupling method”. In: *Computers and Geotechnics* 129 (2021), p. 103803.

[210] T Zhao, GT Houlsby, and S Utili. “Investigation of submerged debris flows via CFD-DEM coupling”. In: *IS-Cambridge, geomechanics from micro to macro. Taylor and Francis Group, Cambridge* (2014), pp. 497–502.

[211] Xingyue Li and Jidong Zhao. “Dam-break of mixtures consisting of non-Newtonian liquids and granular particles”. In: *Powder Technology* 338 (2018), pp. 493–505.

[212] Alexander M Taylor-Noonan et al. “Influence of Pore Fluid on Grain-Scale Interactions and Mobility of Granular Flows of Differing Volume”. In: *Journal of Geophysical Research: Earth Surface* 127.12 (2022), e2022JF006622.

[213] Jun Fang et al. “A new insight into the dynamic impact between geophysical flow and rigid barrier”. In: *Computers and Geotechnics* 148 (2022), p. 104790.

[214] Yong Kong et al. “How Flexible, Slit and Rigid Barriers Mitigate Two-Phase Geophysical Mass Flows: A Numerical Appraisal”. In: *Journal of Geophysical Research: Earth Surface* 127.6 (2022), e2021JF006587.

[215] D Schneider et al. “Frictional behavior of granular gravel–ice mixtures in vertically rotating drum experiments and implications for rock-ice avalanches”. In: *Cold Regions Science and Technology* 69.1 (2011), pp. 70–90.

[216] Gabriele Pozzetti and Bernhard Peters. “A multiscale DEM-VOF method for the simulation of three-phase flows”. In: *International Journal of Multiphase Flow* 99 (2018), pp. 186–204.

[217] L Jing et al. “Extended CFD–DEM for free-surface flow with multi-size granules”. In: *International journal for numerical and analytical methods in geomechanics* 40.1 (2016), pp. 62–79.

[218] Kitware Inc Sandia National Labs and Los Alamos National Labs. *Paraview: Parallel visualization application*. URL: `http://paraview.org`. (accessed: 2023).

[219] Qi Zhang et al. “Comprehensive assessment of energy conservation and CO2 emissions mitigation in China’s iron and steel industry based on dynamic material flows”. In: *Applied Energy* 209 (2018), pp. 251–265.

[220] Jose Adilson de Castro, Cyro Takano, and Jun-ichiro Yagi. “A theoretical study using the multiphase numerical simulation technique for effective use of H2 as blast furnaces fuel”. In: *Journal of Materials Research and Technology* 6.3 (2017), pp. 258–270.

[221] XU Chunbao Charles and Da-qiang Cang. “A brief overview of low CO2 emission technologies for iron and steel making”. In: *Journal of Iron and Steel Research, International* 17.3 (2010), pp. 1–7.

[222] Wenqiang Sun et al. “Material and energy flows of the iron and steel industry: Status quo, challenges and perspectives”. In: *Applied Energy* 268 (2020), p. 114946.

[223] Yansong Shen et al. “Three-dimensional modeling of flow and thermochemical behavior in a blast furnace”. In: *Metallurgical and Materials Transactions B* 46.1 (2015), pp. 432–448.

[224] S Dong et al. “Characterization of tuyere-level core-drill coke samples from blast furnace operation”. In: *Energy & fuels* 21.6 (2007), pp. 3446–3454.

[225] Yoshiyuki MATSUI et al. “Analyses on blast furnace raceway formation by micro wave reflection gunned through tuyere”. In: *ISIJ international* 45.10 (2005), pp. 1432–1438.

[226] GSSRK Sastry, GS Gupta, and AK Lahiri. “Cold model study of raceway under mixed particle conditions”. In: *Ironmaking & steelmaking* 30.1 (2003), pp. 61–65.

[227] Sastry GSSRK. “Void formation and breaking in a packed bed”. In: *ISIJ international* 43.2 (2003), pp. 153–160.

[228] Ruixuan Zhang et al. “Image-based flame detection and combustion analysis for blast furnace raceway”. In: *IEEE Transactions on instrumentation and measurement* 68.4 (2019), pp. 1120–1131.

[229] SS Mondal, SK Som, and SK Dash. “Numerical predictions on the influences of the air blast velocity, initial bed porosity and bed height on the shape and size of raceway zone in a blast furnace”. In: *Journal of Physics D: Applied Physics* 38.8 (2005), p. 1301.

[230] Xiaoping Qiu et al. “A simplified two-fluid model coupled with EMMS drag for gas-solid flows”. In: *Powder technology* 314 (2017), pp. 299–314.

[231] WJ Yang, ZY Zhou, and AB Yu. “Discrete particle simulation of solid flow in a three-dimensional blast furnace sector model”. In: *Chemical Engineering Journal* 278 (2015), pp. 339–352.

[232] BH Xu et al. “A numerical and experimental study of the gas-solid flow in a fluid bed reactor”. In: *Powder Handling & Processing* 13.1 (2001), pp. 71–76.

[233] Yu-Qing Feng et al. “Numerical study of gas-solid flow in the raceway of a blast furnace”. In: *steel research international* 74.9 (2003), pp. 523–530.

[234] Shinichi Yuu, Toshihiko Umekage, and Masatomo Kadowaki. “Numerical simulation of particle and air velocity fields in raceway in model blast furnace and comparison with experimental data (cold model)”. In: *ISIJ international* 50.8 (2010), pp. 1107–1116.

[235] JE Hilton and PW Cleary. “Raceway formation in laterally gas-driven particle beds”. In: *Chemical engineering science* 80 (2012), pp. 306–316.

[236] Shuai Wang and Yansong Shen. “CFD-DEM modelling of raceway dynamics and coke combustion in an ironmaking blast furnace”. In: *Fuel* 302 (2021), p. 121167.

[237] Zhen Miao et al. “CFD-DEM simulation of raceway formation in an ironmaking blast furnace”. In: *Powder technology* 314 (2017), pp. 542–549.

[238] E Dianyu et al. “Particle-scale study of coke combustion in the raceway of an ironmaking blast furnace”. In: *Fuel* 311 (2022), p. 122490.

[239] Yuting Zhuo, Zhongjie Hu, and Yansong Shen. “CFD study of hydrogen injection through tuyeres into ironmaking blast furnaces”. In: *Fuel* 302 (2021), p. 120804.

[240] Tao Li et al. “Numerical Simulation Study on the Effects of Co-Injection of Pulverized Coal and Hydrochar into the Blast Furnace”. In: *Sustainability* 14.8 (2022), p. 4407.

[241] Tyamo Okosun, Samuel Nielson, and Chenn Zhou. “Blast Furnace Hydrogen Injection: Investigating Impacts and Feasibility with Computational Fluid Dynamics”. In: *JOM* 74.4 (2022), pp. 1521–1532.

[242] Thomas Fred Eric Rhead and Richard Vernon Wheeler. “CCXXVI.—The effect of temperature on the equilibrium 2CO⇌CO 2+ C”. In: *Journal of the Chemical Society, Transactions* 97 (1910), pp. 2178–2189.

[243] Edder Rabadan Santana, Gabriele Pozzetti, and Bernhard Peters. “Application of a dual-grid multiscale CFD-DEM coupling method to model the raceway dynamics in packed bed reactors”. In: *Chemical Engineering Science* 205 (2019), pp. 46–57.

[244] Hiroshi Nogami, Hideyuki Yamaoka, and Kouji Takatani. “Raceway design for the innovative blast furnace”. In: *ISIJ international* 44.12 (2004), pp. 2150–2158.

[245] Yutaka Tsuji, Toshihiro Kawaguchi, and Toshitsugu Tanaka. “Discrete particle simulation of two-dimensional fluidized bed”. In: *Powder technology* 77.1 (1993), pp. 79–87.

[246] BPB Hoomans et al. “Discrete particle simulation of bubble and slug formation in a two-dimensional gas-fluidised bed: a hard-sphere approach”. In: *Chemical Engineering Science* 51.1 (1996), pp. 99–118.

[247] BH Xu and AB Yu. “Numerical simulation of the gas-solid flow in a fluidized bed by combining discrete particle method with computational fluid dynamics”. In: *Chemical Engineering Science* 52.16 (1997), pp. 2785–2809.

[248] B. H. Xu and A. B. Yu. “Comments on the paper “Numerical simulation of the gas-solid flow in a fluidized bed by combining discrete particle method with computational fluid dynamics?-Reply”. In: *Chemical Engineering Science* 53 (1998), pp. 2646–2647.

[249] H. P. Zhu et al. “Discrete particle simulation of particulate systems: Theoretical developments”. In: *Chemical Engineering Science* 62 (2007), pp. 3378–3396.

[250] K. W. Chu and A. B. Yu. “Numerical simulation of complex particle-fluid flows”. In: *Powder Technology* 179 (2008), pp. 104–114.

[251] H. Zhou et al. “DEM-CFD simulation of the particle dispersion in a gas-solid two-phase flow for a fuel-rich/lean burner”. In: *Fuel* 90 (2011), pp. 1584–1590.

[252] K. W. Chu et al. “CFD-DEM study of the effect of particle density distribution on the multiphase flow and performance of dense medium cyclone”. In: *Minerals Engineering* 22 (2009), pp. 893–909.

[253] P. N. Rowe and A. W. Nienow. “Particle mixing and segregation in gas fluidized beds—A review”. In: *Powder Technology* 15 (1976), pp. 141–147.

[254] Y. Q. Feng and A. B. Yu. “An analysis of the chaotic motion of particles of different sizes in a gas fluidized bed”. In: *Particuology* 6 (2008), pp. 549–556.

[255] K. D. Kafuia, C. Thornton, and M. J. Adams. “Discrete particle-continuum fluid modelling of gas-solid fluidised beds”. In: *Chemical Engineering Science* 57 (2002), pp. 2395–2410.

[256] S. Kuang, Z. Li, and A. Yu. “Review on Modeling and Simulation of Blast Furnace”. eng. In: *Steel research international* 89.1 (2018), 1700071–n/a. ISSN: 1611-3683.

[257] S. Wang and Y. Shen. “CFD-DEM modelling of raceway dynamics and coke combustion in an ironmaking blast furnace”. eng. In: *Fuel (Guildford)* 302 (2021), pp. 121167–. ISSN: 0016-2361.

[258] T. Grejtak, S. Wang, and J. Shao. “Modeling of a Blast Furnace with Both CFD and Thermodynamics Principles”. eng. In: *Applied Mechanics* 3.3 (2022), pp. 1019–1039. ISSN: 2673-3161.

[259] H. Tang et al. “Modeling Coal/coke Combustion Behavior in Tuyere-raceway-dripping Zone in Blast Furnace”. eng. In: *Procedia Engineering* 102 (2015), pp. 1583–1592. ISSN: 1877-7058.

[260] A.G. Radjuk, A.E. Titlianov, and M.M. Skripalenko. “Computer simulation of temperature field of blast furnace’s air tuyere”. eng ; rus. In: *Computer Research and Modeling* 9.1 (2017), pp. 117–125. ISSN: 2076-7633.

[261] C. Zhou et al. “Comprehensive Numerical Modeling of the Blast Furnace Ironmaking Process”. eng. In: *JOM (1989)* 68.5 (2016), pp. 1353–1362. ISSN: 1047-4838.

[262] L. Jiao et al. “Three-Dimensional Modeling of an Ironmaking Blast Furnace with a Layered Cohesive Zone”. eng. In: *Metallurgical and materials transactions. B, Process metallurgy and materials processing science* 51.1 (2020), pp. 258–275. ISSN: 1073-5615.

[263] D. Fu et al. “CFD modeling of multiphase reacting flow in blast furnace shaft with layered burden”. eng. In: *Applied thermal engineering* 66.1-2 (2014), pp. 298–308. ISSN: 1359-4311.

[264] K. Chattopadhyay, M. Isac, and R. I. L. Guthrie. "Applications of Computational Fluid Dynamics (CFD) in iron- and steelmaking: Part 1". In: *Ironmaking and Steelmaking* 37.8 (2010), pp. 554–561.

[265] K. Chattopadhyay, M. Isac, and R. I. L. Guthrie. "Applications of Computational Fluid Dynamics (CFD) in iron- and steelmaking: Part 2". In: *Ironmaking and Steelmaking* 37.8 (2010), pp. 562–569.

[266] G. S. Gupta et al. "A cold model study of liquid flow in the Blast Furnace lower zone". In: *6th AusIIM Extractive Metallurgy Conference, Brisbane, 3-6 July 1994*. 1994, pp. 295–301.

[267] G. Gupta, J. D. Litster, and V. R. Rudolph. "Model Studies of Liquid Flow in the Blast Furnace Lower Zone". In: *Journal of Iron And Steel Research, International* 36 (1996), pp. 32–39.

[268] G. Gupta et al. "Nonwetting Flow of a Liquid Through a Packed Bed With Gas Cross-Flow". In: *Metallurgical and Materials Transactions B* 28B (1997), pp. 597–604.

[269] D. Y. Liu, G. X. Wang, and J. D. Litster. "Unsaturated Liquid Percolation Flow Through Nonwetted Packed Beds". In: *AIChE Journal* 48 (2002), pp. 953–962.

[270] P.J. Mackey and N.A. Warner. "Studies in the vaporization of mercury in irrigated packed beds". In: *Chemical Engineering Science* 28 (1973), pp. 2141–2154.

[271] N. Standish. "Dynamic holdup in liquid metal irrigated packed beds". In: *Chemical Engineering Science* 23 (1968), pp. 51–56.

[272] G. X. Wang et al. "Modeling the Discontinuous Liquid Flow in a Blast Furnace". In: *Metallurgical and Materials Transactions B* 28B (1997), pp. 333–342.

[273] G. X. Wang et al. "Experimental and Numerical Simulation of Discrete Liquid Flow in a Packed Bed". In: *Chemical Engineering Science* 52 (1997), pp. 4013–4019.

[274] G. X. Wang et al. "Model study of liquid flow in blast furnace lower zone". In: *Iron and Steel Institute of Japan (ISIJ-International)* 37 (1997), pp. 573–582.

[275] N. A. Warner. “Liquid metal irrigation of a packed bed”. In: *Chemical Engineering Science* 11 (1959), pp. 149–160.

[276] J. Yagi. “Mathematical Modeling of the Flow of Four Fluids in a Packed Bed”. In: *Journal of Iron And Steel Research, International* 33 (1993), pp. 619–639.

[277] D. Y. Liu, S. Wijeratne, and J. D. Litster. In: *Scand. J. Metall.* 26 (1998), p. 79.

[278] A. B. Yu. “Encyclopedea of Condensed Matter Physics”. In: ed. by G. F. Bassani. Elsevier, 2005. Chap. Powder Processing: Models and Simulations, pp. 401–414.

[279] Xuefeng Dong et al. “Modelling of Multiphase Flow in a Blast Furnace: Recent Developments and Future Work”. In: *ISIJ International* 47.11 (2007). 3, pp. 1553–1570.

[280] E. Simsek et al. “Numerical simulation of grate firing systems using a coupled CFD/discrete element method (DEM)”. In: *Powder Technology* 193 (2009), pp. 266–273.

[281] M. Mohseni et al. “Biomass drying in a vibrating fluidized bed dryer with a Lagrangian-Eulerian approach”. In: *International Journal of Thermal Sciences* 138 (2019), pp. 219–234. ISSN: 1290-0729. DOI: https://doi.org/10.1016/j.ijthermalsci.2018.12.038. URL: http://www.sciencedirect.com/science/article/pii/S1290072917314011.

[282] A. H. Mahmoudi, F. Hoffmann, and B. Peters. “Detailed numerical modeling of pyrolysis in a heterogeneous packed bed using XDEM”. en. In: *Journal of Analytical and Applied Pyrolysis* 106 (2014), 9–20. URL: http://hdl.handle.net/10993/15828.

[283] A. H. Mahmoudi et al. “Modeling of the biomass combustion on a forward acting grate using XDEM”. -. In: *Chemical Engineering Science* 142 (2016), pp. 32–41. DOI: 10.1016/j.ces.2015.11.015. URL: http://hdl.handle.net/10993/33156.

[284] M. Wu et al. “A forcing fictitious domain method to simulate fluid-particle interaction of particles with super-quadric shape”. In: *Powder Technology* 360 (2020), pp. 264–277. ISSN: 0032-5910. DOI: https://doi.org/10.1016/j.powtec.2019.09.088. URL: https://www.sciencedirect.com/science/article/pii/S0032591019308198.

[285] A. H. Mahmoudi et al. “Numerical study of the influence of particle size and packing on pyrolysis products using XDEM”. en. In: *International Communications in Heat & Mass Transfer* 71 (2016), pp. 20–34. DOI: 10.1016/j.icheatmasstransfer.2015.12.011. URL: http://hdl.handle.net/10993/33157.

[286] Mohammad Mohseni, Bernhard Peters, and Mehdi Baniasadi. “Conversion analysis of a cylindrical biomass particle with a DEM-CFD coupling approach”. In: *Case Studies in Thermal Engineering* 10 (2017), pp. 343–356. ISSN: 2214-157X. DOI: https://doi.org/10.1016/j.csite.2017.08.004. URL: https://www.sciencedirect.com/science/article/pii/S2214157X17301387.

[287] Y. Q. Feng and A. B. Yu. “Assessment of model formulations in the discrete particle simulation of gas-solid flow”. In: *Industrial & Engineering Chemistry Research* 43 (2004), pp. 8378–8390.

[288] Y. Tsuji, T. Kawaguchi, and T. Tanaka. “Discrete Particle Simulation of Two-dimensional Fluidized Bed”. In: *Powder Technol.* 77.79 (1993).

[289] Y. Kaneko, T. Shiojima, and M. Horio. “DEM simulation of fluidized beds for gas-phase olefin polymerization”. In: *Chemical Engineering Science* 54 (1999), p. 5809.

[290] W. E. Ranz and W. R. Marshall. “Evaporation from drops”. In: *Chemical Engineering Progress* 48 (1952), p. 141.

[291] T. Swasdisevi et al. “Prediction of gas-particle dynamics and heat transfer in a two-dimensional spouted bed”. In: *Advanced Powder Technology* 16 (2005), p. 275.

[292] J. T. Li and D. J. Mason. “A computational investigation of transient heat transfer in pneumatic transport of granular particles”. In: *Powder Technology* 112 (2000), p. 273.

[293] J. T. Li and D. J. Mason. “Application of the discrete element modelling in air drying of particulate solids”. In: *Drying Technology* 20 (2002), p. 255.

[294] J. T. Li, D. J. Mason, and A. S. Mujumdar. “A numerical study of heat transfer mechanisms in gas-solids flows through pipes using a coupled CFD and DEM model”. In: *Drying Technology* 21 (2003), p. 1839.

[295] H. Zhou, G. Flamant, and D. Gauthier. “DEM-LES of coal combustion in a bubbling fluidized bed. Part I: gas-particle turbulent flow structure”. In: *Chemical Engineering Science* 59 (2004), p. 4193.

[296] H. Zhou, G. Flamant, and D. Gauthier. “DEM-LES simulation of coal combustion in a bubbling fluidized bed. Part II: coal combustion at the particle level”. In: *Chemical Engineering Science* 59 (2004), p. 4205.

[297] K. F. Malone and B. H. Xu. “Particle-scale simulation of heat transfer in liquid-fluidised beds”. In: *Powder Technology* 184 (2008), pp. 189–204.

[298] X. Wang et al. “A Revised Drag Force Model and the Application for the Gas-Solid Flow in the High-density Circulating Fluidized Bed”. In: *Applied Thermal Engineering* 31.14-15 (2011), pp. 2254–2261.

[299] J. Xiang. “The effect of air on the packing structure of fine particles”. In: *Powder Technology* 191 (2009), pp. 280–293.

[300] S. Hassanzadeh Saraei and B. Peters. “Immersed boundary method for considering lubrication effects in the CFD-DEM simulations”. In: *Powder Technology* (2023), p. 118603. ISSN: 0032-5910. DOI: https://doi.org/10.1016/j.powtec.2023.118603. URL: https://www.sciencedirect.com/science/article/pii/S003259102300387X.

[301] M. Baniasadi et al. “Experimental and numerical investigation into the softening Behavior of a packed bed of iron ore pellets”. In: *Powder Technology* 339 (2018), pp. 863–871. ISSN: 0032-5910. DOI: https://doi.org/10.1016/j.powtec.2018.08.035. URL: https://www.sciencedirect.com/science/article/pii/S003259101830665X.

[302] C. Introini et al. “A mass conservative Kalman filter algorithm for thermo-computational fluid dynamics”. en. In: *Materials (ISSN 1996-1944)* (n.d.): *Uncertainties and Randomness*. URL: http://hdl.handle.net/10993/36124.

[303] F. Qi et al. “DEM simulation of dense granular flows in a vane shear cell: Kinematics and rheological laws”. In: *Powder Technology* 366 (2020), pp. 722–735. ISSN: 0032-5910. DOI: https://doi.org/10.1016/j.powtec.2020.03.008. URL: https://www.sciencedirect.com/science/article/pii/S0032591020301984.

[304] T. Rosemann et al. “Comparison of numerical schemes for 3D lattice Boltzmann simulations of moving rigid particles in thermal fluid flows”. In: *Powder Technology* 356 (2019), pp. 528–546. ISSN: 0032-5910. DOI: https://doi.org/10.1016/j.powtec.2019.07.054. URL: https://www.sciencedirect.com/science/article/pii/S0032591019305467.

[305] C. Introini et al. “Development of a Data-Driven Approach based on Kalman filtering for CFD Reactor Analysis”. en. In: *PHYSOR 2018* (2018). URL: http://hdl.handle.net/10993/36125.

[306] Bernhard Peters. “The extended discrete element method (XDEM) for multi-physics applications”. In: *Scholarly Journal of Engineering Research* (2013).

[307] B. Peters. “Characterization of Municipal Solid Waste Combustion in a Grate Furnace”. en. In: *Waste Management* vol. 23/8 (2003), pp. 689–701. URL: http://hdl.handle.net/10993/6019.

[308] B. Peters et al. “Enhanced Thermal Process Engineering by the Extended Discrete Element Method (XDEM)”. en. In: *Universal Journal of Engineering Science* 1 (2013), pp. 139–145. URL: http://hdl.handle.net/10993/11445.

[309] W. Zhong et al. “CFD Simulation of Dense Particulate Reaction System: Approaches, Recent Advances and Applications”. In: *Chemical Engineering Science* 140 (Feb. 2016), pp. 16–43. DOI: 10.1016/j.ces.2015.09.035.

[310] W. J. Yang, Z. Y. Zhou, and A. B. Yu. “Discrete Particle Simulation of Solid Flow in a Three-Dimensional Blast Furnace Sector Model”. In: *Chemical Engineering Journal* 278 (Oct. 2015), pp. 339–352. DOI: 10.1016/j.cej.2014.11.144.

[311] D. Xu, S. Wang, and Y. Shen. “An Improved CFD-DEM Modelling of Raceway Dynamics and Coke Combustion in an Industrial-Scale Blast Furnace”. In: *Chemical Engineering Journal* 455 (Jan. 2023), p. 140677. DOI: 10.1016/j.cej.2022.140677.

[312] A. Zhu et al. “A Dynamic Load Balancing Algorithm for CFD–DEM Simulation with CPU–GPU Heterogeneous Computing”. In: *Powder Technology* 428 (Oct. 2023), p. 118782. DOI: 10.1016/j.powtec.2023.118782.

[313] A. Niemöller et al. “Dynamic Load Balancing for Direct-Coupled Multiphysics Simulations”. In: *Computers & Fluids* 199 (Mar. 2020), p. 104437. DOI: 10.1016/j.compfluid.2020.104437.

[314] A. Totounferoush et al. “A Data-Based Inter-Code Load Balancing Method for Partitioned Solvers”. In: *Journal of Computational Science* 51 (Apr. 2021), p. 101329. DOI: 10.1016/j.jocs.2021.101329.

[315] R. B. Bird, W. E. Stewart, and E. N. Lightfoot. *Transport Phenomena*. John Wiley & Sons, 1960.

[316] T. Murayama, Y. Ono, and Y. Kawai. “Step-Wise Reduction of Hematite Pellets with CO-CO_2 Gas Mixtures”. In: *Transactions of the Iron and Steel Institute of Japan* 18.9 (1978), pp. 579–587. DOI: 10.2355/isijinternational1966.18.579.

[317] Hb. Zuo et al. “Reduction Kinetics of Iron Oxide Pellets with H2 and CO Mixtures”. In: *International Journal of Minerals, Metallurgy, and Materials* 22.7 (July 2015), pp. 688–696. DOI: 10.1007/s12613-015-1123-x.

[318] Ian Foster. *Designing and Building Parallel Programs: Concepts and Tools for Parallel Software Engineering*. USA, 1995.

[319] Muhammad Mashhood et al. “Developing the AM G-code based thermomechanical finite element platform for the analysis of thermal deformation and stress in metal additive manufacturing process”. In: *Journal of Mechanical Science and Technology* (2023), pp. 1–10.

[320] Navid Aminnia, Alvaro Antonio Estupinan Donoso, and Bernhard Peters. “Developing a DEM-Coupled OpenFOAM solver for multiphysics simulation of additive manufacturing process”. In: *Scipedia. com* (2022).

[321] Navid Aminnia. “CFD-XDEM coupling approach towards melt pool simulations of selective laser melting”. In: (2023).

[322] Fateme Darlik and Bernhard Peters. “Reconstruct the biomass particles fields in the particle-fluid problem using continuum methods by applying the physics-informed neural network”. In: *Results in Engineering* 17 (2023), p. 100917.

[323] *Artificial Solver Testing Environment (ASTE)*. URL: `https://github.com/precice/aste`.

[324] Open Cascade. “Salome: The open source integration platform for numerical simulation”. In: *Open source on www. salome-platform. org* (2005).

Appendix A

Performance Analysis

A.1 AWJC Nozzle performance

The AWJC nozzle fluid mesh is generated using a python script for Salome [324]. The mesh size could be controlled by number of divisions, and different meshes are generated from very coarse to fine. A preliminary simulation until 0.003 s is run without tracking performance, so as to establish water-jet stability inside the simulation domain. This also ensures that the computational load is closer to that seen in the coupled AWJC nozzle simulations. The figure A.1 shows the time taken for different meshes to solve for 10 time steps.

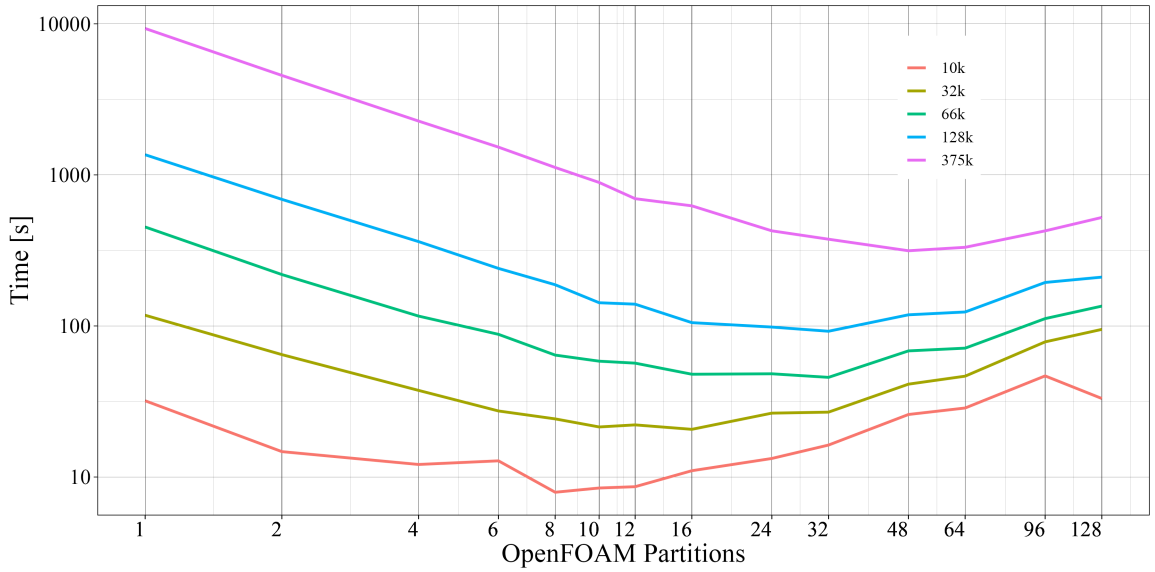

Figure A.1: Performance comparison for pure OpenFOAM simulation for different AWJC Nozzle meshes